The evolution of Late Quaternary alluvial landscapes in northern Oman

Samuel Woor

St Cross College



Thesis submitted for the degree of Doctor of Philosophy

Trinity Term 2023

Abstract

Dryland fans predominately preserve signals of Late Quaternary (350-0 ka) climatic variability within their stratigraphy because of hydrological changes in their feeding catchments. Their morpho-dynamics are also the product of various other non-climatic controls, such as catchment morphology, geology and depositional setting. The mountain front fans of the Hajar Mountains, south-east Arabia, have been shown to aggrade under more sustained streamflow during periods of insolation maxima which coincide with intensified monsoon rainfall, as well as their diverse morphologies indicating complex, non-climatic controls on their evolution. Better understandings of the ways in which landscapes respond to changes in boundary conditions is important in the context of contemporary climate change, as well as understanding long-term human-environment interactions. However, previous palaeoenvironmental and morphological studies have been concentrated in the very north and south of the range.

Today, the Hajar is also environmentally distinct, relative to other regions of the Arabian Peninsula, in that it receives high amounts of rainfall and is a centre of rich biological endemism. The growing body of dated palaeoenvironmental sites available from alluvial fans and other landforms in the Hajar suggest that the region has remained more hydrologically active than surrounding lowlands during more arid periods in the Late Quaternary. Despite this, there has been no prior attempt to synthesise these environmental data for the Arabian Peninsula and compare palaeoenvironmental heterogeneity between different regional settings.

This thesis addresses these knowledge gaps by 1) providing new, dated records of fan aggradation in the central Hajar; 2) conducting a systematic survey of fan and catchment morphology across the Hajar range, and 3) constructing the first database which critically assesses geochronological data for the entire Arabian Peninsula over the last 20 ka.

The fans of the central Hajar record aggradation in line with orbital (primarily precessional) forcing over the last 300 ka. Taken together with alluvial records from the wider region, Hajar fan aggradation provides the longest and most continuous terrestrial record of environmental and climatic change in south-east Arabia. Fan morphologies are strongly controlled by their diverse catchment morphologies and lithologies, with smaller, steeper catchments comprised of less erodible rocks producing smaller, steeper fans. Fans in more complex depositional settings, such as coastlines, have weaker relationships with catchment morphology due to greater external influences. The new data also show that aggradation continued to occur during more arid periods, primarily within catchment settings, but to a lesser degree under more ephemeral flow conditions. Combined with other palaeoenvironmental archives from the Hajar, these findings support hypotheses of more continuous hydrological activity in mountain catchments despite reductions in monsoon rainfall. Therefore, the Hajar, and other uplands in Arabia, appear to be more resilient to regional aridity than lowlands. These findings have important implications for interpreting increasingly complex palaeoenvironmental and archaeological data from south-east Arabia which seemingly conflict with regional-scale palaeoclimate archives.

Acknowledgements

A huge thanks is owed to my supervisors Professor David Thomas, Dr Julie Durcan, Dr Sallie Burrough and Dr Ash Parton. I am incredibly grateful for your unwavering support, trust and patience despite how tough the last three years have been for everyone throughout the Covid-19 pandemic. You've navigated me through all of this, continually challenged me to become a better scientist and have believed in me when I haven't had much belief in myself. If I ever find myself in a supervisory position, I hope to set the example you have been to me. I have thoroughly enjoyed working with you all.

My co-authors (and friends!), Dr Anya Leenman and Dr Catherine Buckland, also provided valuable expertise which has contributed to this research. Thanks to Dr Jean-Luc Schwenninger who kindly retrieved my data from our elderly gamma spectrometer. I also thank Professor Heather Viles and the OxRBL group, Dr Mitch D'Arcy and Professor Olav Lian for your wisdom and broadening my scientific horizons even further.

This research has been possible with financial support from the Science and Engineering in Arts, Heritage and Archaeology Centre for Doctoral Training through the Engineering and Physical Sciences Research Council. Fieldwork was also supported by Professor Simon Underdown's Beatrice de Cardi Award from the Society of Antiquaries and I thank him and Dr Sam Smith for their assistance in the field. I also acknowledge St Cross College for funding additional training activities during my DPhil and all the excellent facilities and technical staff in the School of Geography.

I thank Dr John Lynch, the tutors and students at St Catz for welcoming me to such a wonderful academic community. My friends in Geography, St Cross and further afield, including Ella, Marcus, Maike, Rosie, Anca, Callum, Alex, Kenta, Mirna, Marco, Dom, Clara, Michael, Angie, Hope, Ella TF, Sophie, Hattie, Camilla and Ellie, made sure that I had plenty of fun along the way. Jasper, I am grateful for our morning runs, despite not always being that grateful whilst we're doing them! To

the Ipswich boys, Chris, Ben, Sam, Lawrence, Michael and Conan, I promise that I will now get a ‘proper’ job.

Emily, thank you for being an excellent housemate and friend throughout this process. I’m certain that Tim and I have converted you to being a geographer. Dr Tim Baxter has been a constant source of inspiration, support and distraction (molehills) throughout this process and I can’t imagine having done it without him. I can’t wait to think up some more hair-brained ideas over a pint soon…

Lastly, I couldn’t have done this without the support of my family. I thank my sisters, Charlotte and Elizabeth, for reminding me during the stressful times that, at the end of the day, it’s ‘just sand’. To my parents, Jane and Martin, thank you for your love and being such superb role models. I hope you’re looking forward to me scrounging off you over the summer as much as I am!

Table of contents

Abstract i

Acknowledgements iii

Table of contents v

List of figures xi

List of tables xvii

List of equations xix

List of abbreviations xxi

List of units xxiii

1 | Introduction, aims and thesis structure 1

1.1 Introduction 3

1.2 Aims and objectives 5

1.3 Thesis structure 7

2 | Alluvial fans, south-east Arabia and the Hajar Mountains 11

2.1 Introduction 13

2.2 Alluvial fans 13

2.2.1 Controls on fan morphology and dynamics 14

2.2.2 Fans as geoproxies of palaeoenvironmental and palaeoclimatic change 23

2.3 South-east Arabia and the Hajar Mountains 28

2.3.1 Regional setting 28

2.4 Late Quaternary climatic and environmental change in south-east Arabia 37

2.4.1 Marine cores and speleothem: palaeoclimate archives of IOSM variability 38

2.4.2 Geoproxy records in the Arabian Peninsula and the Hajar Mountains 42

2.5 Non-climatic controls on Hajar fan morpho-dynamics 48

2.6 Key points from Chapter 2 50

3 | Methods 53

3.1 Introduction 55
3.2 New records of fan aggradation from the central Hajar 55
3.2.1 Field sampling, site selection and location 55
3.2.2 Luminescence dating 60
3.2.3 Hierarchical cluster analysis of regional age data 71
3.3 Understanding the non-climatic controls on Hajar fan morpho-dynamics 72
3.3.1 Geomorphological mapping of fans and catchments 72
3.3.2 Fan and catchment morphometric variables 75
3.4 Building a database of geoproxy ages for Arabia over the last 20 ka 76
4 | The aggradation of alluvial fans in response to monsoon variability over the last 300 ka in the Hajar Mountains, south-east Arabia (Paper 1) 79
4.1 Paper abstract 81
4.2 Introduction 83
4.2.1 The IOSM model of precessionally-paced alluvial fan aggradation in the Hajar 83
4.3 Regional setting and sampling site selection 86
4.3.1 Wadi Sahtan and the Rustaq fan 87
4.3.2 The Ibri and Dhank fans 88
4.4 Methods 90
4.4.1 Luminescence dating 90
4.4.2 Sedimentology 92
4.5 Results 92
4.5.1 Chronology 92
4.5.2 Sedimentary descriptions and chronostratigraphic relationships 96
4.6 Discussion 101
4.6.1 Palaeoenvironmental interpretation 101
4.6.2 Hajar alluvial fans as sensitive records of IOSM rainfall 108
4.7 Conclusions 112

5 | Morphology and controls of the mountain front fan systems of the Hajar Mountains, south-east Arabia (Paper 2) 115

5.1 Paper abstract 117

5.2 Introduction 119

5.2.1 Alluvial fan morphometry 119

5.2.2 Hajar Mountain fans and previous morphometric work 121

5.3 Regional setting 123

5.3.1 Geological setting 123

5.3.2 Geomorphological and climatological setting 125

5.4 Methods 127

5.4.1 Mapping 127

5.4.2 Fan and catchment morphometric variables 131

5.5 Results 131

5.5.1 Summary of fan and catchment mapping and general characteristics 131

5.5.2 Fan morphology 134

5.5.3 Interactions with distal environments 137

5.5.4 Fan-catchment morphometric relationships 139

5.6 Discussion 147

5.6.1 Catchment controls 147

5.6.2 Base level controls 150

5.6.3 Long-term controls: climate change and tectonics 152

5.6.4 Summary of the controls on mountain front fan morphology along the Hajar 156

5.6.5 Implications at the global and planetary scale: comparisons with other fans 158

5.7 Conclusions 162

6 | Assessing the robustness of geochronological records from the Arabian Peninsula: A new synthesis of the last 20 ka (Paper 3) 165

6.1 Paper abstract 167

6.2 Introduction 168

6.3 Arabian climate variability 170
6.3.1 IOSM variability over the past 20 ka 171
6.3.2 The ‘wet’ vs ‘dry’ narrative 172
6.4 The SCAPE database 174
6.4.1 Types of record 175
6.4.2 Sub-regions, sites and individual records 176
6.4.3 Geochronological metadata 180
6.5 Geochronological quality assurance 182
6.5.1 Sources of uncertainty in OSL and ^{14}C dating 182
6.5.2 Quality assurance criteria 182
6.6 Arabia geochronology quality assessment 186
6.7 Sub-regional palaeoenvironmental variability 190
6.7.1 The Nefud 190
6.7.2 The Arabian Gulf/N Rub’al Khali 194
6.7.3 The Hajar Mountains 197
6.7.4 The Arabian Sea Coast 199
6.7.5 The Rub’al Khali 201
6.7.6 Western Arabia 201
6.7.7 Southern Arabia 203
6.8 Discussion 205
6.8.1 The role of regional climatic factors in Arabian palaeoenvironmental change 206
6.8.2 The role of wider environmental factors in Arabian palaeoenvironmental change 207
6.9 Conclusions 209
7 | Discussion and conclusions 213
7.1 Introduction 215
7.2 New records of fan aggradation from the central Hajar Mountains 215
7.2.1 Field sampling approach and determining the timing of fan aggradation 215

7.2.2 The IOSM as the driver of fan aggradation in the Hajar Mountains 216

7.3 Controls on Hajar fan aggradation outside of climate 218

7.3.1 Using remote sensing and GIS to build a database of fan and catchment morphometric variables for Hajar fans 218

7.3.2 The non-climatic controls on Hajar fan morphology 219

7.3.3 Comparing the Hajar fans with other dryland contexts 221

7.4 Comparing Hajar geoproxy records to other regions of Arabia 224

7.4.1 The status of Arabian geochronology and geoproxy records for the last 20 ka 224

7.4.2 Synthesising palaeoenvironmental data from across Arabia: how does the Hajar compare? 225

7.4.3 Implications for archaeology 227

7.5 Summary 229

7.6 Future research 230

7.6.1 Further developing Hajar alluvial fan deposits as geoproxies 230

7.6.2 The role of geology in controlling Hajar fan morphology and a global fan morphometric database 231

7.6.3 Expanding the SCAPE database and testing palaeoclimate models 232

8 | References 233

9 | Appendix A: Evaluating the effectiveness of heavy liquid density separation in isolating K-feldspar grains using alluvial sediments from the Hajar Mountains, Oman (Paper 4) 279

10 | Appendix B: Supplementary material for Chapters 3 and 4 (Paper 1) 299

11 | Appendix C: Supplementary material for Chapter 5 (Paper 2) 321

12 | Appendix D: Supplementary material for Chapter 6 (Paper 3) 329

13 | Appendix E: Statement of authorship 337

List of figures

Figure 2.1. Examples of the diversity of terrestrial and extra-terrestrial alluvial fans. **(a)** Mountain-front fans in Death Valley, California, USA, often considered the 'archetype' fans (Harvey, 2011). **(b)** Tributary-junction fans along the Nubra River, Ladakh, north-western India. **(c)** The Panj River fan being extensively used for agriculture on the border of Tajikistan and Afghanistan. **(d)** The megafans of the Himalayas, northern India, where they meet the Ganges River. **(e)** Coastal fans in the cold environment of northern Nunavut, north-eastern Canada, situated in an inlet of Baffin Bay. **(f)** Alluvial fans in Mojave Crater, Xanthe Terra, Mars. **(g)** Channels draining to the Elivagar Flumina fan bajada located near Titan's equator with a sand sea of linear dunes located in the top right of the image. Images **a - e** were acquired from Google Earth Pro. Image **f** was acquired on 27th March 2015 by the High-Resolution Image Science Experiment (HiRISE), made available through the University of Arizona's HiRISE Catalogue (https://www.uahirise.org/catalog/). Image **g** was acquired from the synthetic aperture radar (SAR) instrument aboard the Cassini Orbiter and is reproduced from Radebaugh et al. (2018). 15

Figure 2.2. Fan-catchment morphometric measurements for selected fan studies from the literature for a range of different climatic, geological and planetary settings: Petuniabukta, Svalbard (Norway; Tomczyk, 2021); Adventdalen, Svalbard (Norway; De Haas et al., 2015); Sao Vincente, Cape Verde (Stokes and Gomes, 2020); Pin Valley, northern India (Shoshta and Marh, 2021); Gulf of Corinth, Greece (Karymbalis et al., 2018); the Danehkoshk anticline, Iran (Bahrami, 2013); the Betic Cordillera, Spain (Viseras et al., 2003); the San Juan River, Argentina (Milana and Ruzycki, 1999); the High Atlas Mountains, Morocco (Stokes and Mather, 2015); assorted terrestrial megafans (Arzani, 2012: references therein); craters on Mars (Moore and Howard, 2005) and Titan (Birch et al., 2016). **(a)** The positively correlated fan area vs. catchment area relationship ($Fa = 0.20Ca^{0.76}$; R^2=0.70). **(b)** The negatively correlated fan gradient vs. catchment area relationship ($Fg = 0.14Ca^{-0.28}$; R^2=0.41). Data from 930 individual fans in total. 18

Figure 2.3. Standardised residuals for the Fa v. Ca and Fg v. Ca relationships shown in Figure 2.2, plotted by fan location. Clusters emerge, likely controlled by factors such as catchment geology, fan setting, tectonics etc. Data references are the same as Figure 2.2. 21

Figure 2.4. (a) Stratigraphic models for debris-flow driven fans (the 'Trollheim' type) and fluvially-driven fans (the 'Scott' type). **(b)** Long-profile stratigraphic model for a generic fluvial fan. N:G refers to net to gross ratio: the ratio of the cumulative thickness of deposits relative to their volume. **(a)** Reproduced from Harvey (2011), **(b)** reproduced from Moscariello (2018). 25

Figure 2.5. The Arabian Peninsula, showing coastal uplands, the interior Rub' al Khali desert, speleothem and marine core records and the major faults associated with the Arabian Plate boundaries and along the Hajar. Red arrows indicate the direction of plate movement, with the collisional zone in the north denoted by the Makran Subduction Zone (MSZ). Palaeolithic archaeological sites are also marked (from Nicholson et al., 2020). South-east Arabia is delineated with the blue box. Key locations discussed in the text are labelled. 29

Figure 2.6. The alluvial fans of the Hajar Mountains. **(a)** The urbanised fan at Ras Al-Khaimah in the north-western UAE forming part of the northern interior bajada. **(b)** The large megafans of central Oman extending westwards to the Rub' al Khali and Umm as Samim and south-eastwards to the Wahiba Sands. **(c)** Inverted sinuous palaeochannels preserved on the megafans shown in **(b)**. **(d)** The bajada along the Batinah Coast, draining north-eastwards from the Hajar Mountains. **(e)** The smaller coastal fans forming in the rocky inlets of the Musandam Peninsula in the northern Hajar. **(f)** The fans situated between the Hajar Mountain front and the Wahiba Sands in the south of the range. This image shows an example of a fan prograding telescopically beyond an intersection point. Imagery from Google Earth Pro. 33

Figure 2.7. Average monthly rainfall over south-east Arabia during: **(a)** June, July and August and **(b)** January, February and March from 1970-2000. **(a)** Shows the concentration of precipitation along the southern coast of Oman and the Hajar Mountains in response to the IOSM, the onshore direction of which is denoted by the blue arrows in the Arabian Sea. The red dashed line denotes the approximate position of the inter-tropical convergence zone (ITCZ), although paradigm of the coupling between the ITCZ and monsoon rain belt may be overly simplistic (e.g. Nicholson, 2018). **(b)** Shows the dominance of the MLWs from November-April, bringing rainfall to the north-eastern part of the region as denoted by the blue arrows. The ITCZ retreats to the southern Indian Ocean during winter months due to the reversal of the monsoon winds. Data from WorldClim 2 (Fick and Hijmans, 2017). 35

Figure 2.8. Palaeoclimate data from south-east Arabia. **(a)** The Hoti Cave speleothem record (Fleitmann et al., 2003b). Examples of marine core proxies from the Arabian Sea: **(b)** bromine XRF counts (Ziegler et al., 2010), **(c)** percentage of G. Bulloides (Anderson and Prell, 1993), **(d)** the Summer Monsoon Factor (SMF; solid line) and Summer Monsoon Stack (SMS; dashed line) composite proxies (Clemens and Prell, 2003). **(e)** Summer insolation at 30°N (Berger and Loutre, 1991). **(f)** LR04 global benthic δ18O stack (Lisiecki and Raymo, 2005). Blue bars denote peaks in IOSM rainfall based on the Hoti Cave speleothem record and the SMF/SMS record from the Arabian Sea, after Caley et al. (2011). 39

Figure 2.9. The number of geoproxy records with either luminescence or radiocarbon chronologies within 0-20 ka published in south-east Arabia. 44

Figure 3.1. (a) The Hajar Mountains of northern Oman and the north-eastern UAE showing regional geomorphological features and key sites with previously dated alluvium using OSL and radiocarbon: 1: Atkinson et al. (2013); 2: Purdue et al. (2019); 3: Mueller et al. (2022); 4: Parton et al. (2013); 5: Parton et al. (2015a); 6: Moraetis et al. (2020); 7: Hoffmann et al. (2015); 8: Blechschmidt et al. (2009) and 9: Beuzen-Waller et al. (2022). Other regional palaeoenvironmental sites are shown, including palaeolake deposits from: 10: Parker et al. (2006); 11: Preston et al. (2015); 12: Rosenberg et al. (2012) and 13: Fuchs and Buerkert (2008), as well as 14: the Hoti Cave speleothem (Burns et al., 2001). 'JA' denotes Jebel Ahkdar. **(b)** The study sites both east (OM20/2-5) and west (OM20/6-12) of the Hajar drainage divide. Sites OM20/2-4 are valley-fill deposits along Wadi Sahtan in the lower reaches of the mountain catchment feeding the Rustaq fan. Sites OM20/5-12 are alluvial fan deposits. Major drainage networks and mountain catchments are delineated by the blue and black lines, respectively. 56

Figure 3.2. Elevation profiles and sampled sites along (a) Wadi Sahtan and the Rustaq fan, (b) Wadi Al Ayn and the Ibri fan and (c) Wadi Dhank and the Dhank fan. 58

Figure 3.3. Fieldwork in January 2020. Images a-c were taken at sites along Wadi Sahtan and the Rustaq fan, images d-g on the Ibri and Dhank fans. **(a)** Site OM20/3 showing a basal unit of finely laminated, ponded sediments. **(b)** Site OM20/4 showing bedded gravels and cobbles comprising the upper conglomerates. **(c)** Site OM20/5 viewed laterally showing various braided channel fills bounded by floodplain deposits. **(d)** Looking out across the cobbled surfaces of the Ibri fan near its apex. **(e)** Site OM20/11 on the Dhank fan showing weakly bedded fluvial and aeolian sands overlying coarser channel deposits. **(f)** Site OM20/6 within the central channel fill unit of which (red arrow) a well-preserved pre-historic hand-axe was found **(g).** 59

Figure 3.4. Measurement results for an aliquot of sample OM20/12/1. **(a)** The TL signal resulting from the sample cut-heat following a 6.8 Gy test dose, showing the characteristic 110°C peak of quartz. **(b)** The natural OSL signal (Ln) in blue and the corresponding test signal (Tn) in orange showing the characteristic rapid decay or 'fast dominated' signal. **(c)** The dose response curve for the aliquot built by plotting sensitivity corrected luminescence (Lx/Tx)for multiple SAR cycles against the laboratory administered dose. The dashed orange line is the Ln/Tn value used to interpolate the De which is ~15 Gy. **(d)** The Tx/Tn ratio used to monitor sensitivity change throughout the SAR repeats. The dashed orange line represents unity. 68

Figure 3.5. (a) Dendrogram of clustered ages. Each age is represented by a number (1-90) and paired with its nearest neighbour at the bottom of the plot. Coloured boxes show the groups defined based on similarity (k = 9). **(b)** Average silhouette widths for different k values (1-10). K = 9 (dashed vertical line) gives the highest average silhouette width, so was chosen as the most optimum place to cut the dendrogram. 72

Figure 3.6. Flowchart of the input data and processing steps used to map fans and catchments to produce the dataset analysed in Chapter 5. Data processing was undertaken in ArcMap 10.8 and Google Earth pro. Chapter 5 provides a more detailed overview of data sources and resolutions. 74

Figure 3.7. Comparison between delineating fans based on 1984 imagery **(a)** and 2022 imagery **(b)** in the north-western Hajar. Urbanisation has made it more difficult to delineate the same fans in some areas of the mountain front, therefore using historic imagery is important to help ensure accurate mapping. 75

Figure 3.8. The re-calibration of sample Pa 1996 from the Al Hawa lake basin in Yemen using the IntCal20 calibration curve (blue line) and the OxCal software. The red distribution shows the uncalibrated age of 6850 ± 115 ^{14}C years and the grey distribution the interpolated (calibrated) age of 7746 ± 189 cal yrs BP. Data is originally from Lézine et al. (2007) and is included in the SCAPE database (see Chapter 6). 77

Figure 4.1. (a) The circulation of the Indian Ocean Monsoon system and the position of the inter-tropical convergence zone (ITCZ) during summer months. **(b)** The circulation of the Indian Ocean Monsoon system and position of the ITCZ during winter months. Key palaeoclimate records are shown, including Hoti Cave, located in the Hajar Mountains. Redrawn from Fleitmann and Matter (2009). The red boxes indicate the extent of south-east Arabia, shown in **(c)** and **(d)**. **(c)** Mean rainfall in south-east Arabia during summer months (June-August). The red line denotes the approximate position of the ITCZ, blue arrows denote the onshore flow of the IOSM. **(d)** Mean rainfall in south-east Arabia during winter months (January-March). Blue arrows denote the influx of moisture from Mediterranean westerlies. Rainfall data for 1970-2000 from WorldClim 2 (Fick and Hijmans, 2017). 84

Figure 4.2. (a) The location of sampled sites east of the Hajar drainage divide along Wadi Sahtan (OM20/2-4) and in the proximal part of the Rustaq fan (OM20/5). **(b)** The locations of sites OM20/2-4 in Wadi Sahtan, with valley-fill sequences exposed by the incised channel. **(c)** The main channel of Wadi Sahtan taken from site OM20/3. **(d)** Site OM20/5 showing the sampling locations of samples OM20/5/1 and -/2 from sand units inter-stratified with gravelly channel-fill deposits. 89

Figure 4.3. (a) The location of sampled sites west of the Hajar drainage divide on the Ibri and Dhank fans. **(b)** Sites OM20/8, -/10 and -/11 in the medial-distal part of the Dhank fan where fan surfaces begin to become obscured by Rub' al Khali dunes. **(c)** Site OM20/6 showing the sampling locations of OM20/6/1 and -/3 in floodplain deposits, bounding channel conglomerate and bedded gravel material. **(d)** Site OM20/12 showing the sampling location of sample OM20/12/1 within floodplain deposits, bounded by channel gravels above and below, and an in-situ gamma spectrometry measurement being taken following OSL sampling. 90

Figure 4.4. (a) An example OSL signal for an aliquot of sample OM20/3/3, and the dose response curve measured for the same signal **(b)**. Below are abanico plots showing example De distributions for **(c)** the broadly gaussian sample OM20/3/3 and **(d)** the positively skewed sample OM20/11/3. The central age model (CAM) and minimum age models (MAM) of Galbraith et al. (1999) are displayed as well as relative overdispersion (OD). A CAM-derived final De was used to derive a final age for sample OM20/3/3 **(c)**, whilst a MAM-derived final De was used for **(d)** OM20/11/3 (Table 4.1). 93

Figure 4.5. Stratigraphic logs of sites from the eastern Hajar (OM20/3-5). See Fig.4.2 for site locations. 99

Figure 4.6. Stratigraphic logs of sites from the western Hajar (OM20/6-12). Note the change of scale for sites OM20/11, -/10 and -/8. See Fig.4.3 for sampling site locations. 101

Figure 4.7. Palaeoenvironmental records from the Hajar Mountains. For alluvial and lacustrine records, blue symbols denote wetter conditions than present and orange symbols denote similar or drier conditions to present, based on the interpretations of original authors. **a:** Alluvial records: Dalongeville (1999); Blechschmidt et al. (2009); Farrant et al. (2012); Atkinson et al. (2013); Parton et al. (2015a); Hoffmann et al. (2015); Purdue et al. (2019); Moraetis et al. (2020); Mueller et al. (2022); Beuzen-Waller et al. (2022); this study. **b:** Lacustrine records: Aqabah (Parton et al., 2013); Maqta (Fuchs and Buerkert, 2008); Wahala (Preston et al., 2015); Awafi (Parker et al., 2006); Saiwan (Rosenberg et al., 2012). Ages from this study are marked by black diamonds. **c:** The Hoti Cave speleothem record (Fleitmann et al., 2011). Marine proxy records from the Arabian Sea: **d:** bromine XRF counts (Ziegler et al., 2010) and **e:** the IOSM factor and stack (Clemens and Prell, 2003). **f:** June insolation at 30°N (Berger and Loutre, 1991). **g:** Global δ18O data from the LR04 benthic stack (Lisiecki and Raymo, 2005). The vertical blue bars denote periods of fan and lake aggradation, identified by a hierarchical cluster analysis conducted on age data from alluvial and lacustrine settings interpreted as being indicative of wetter conditions (see Appendix B for further details). The width of each bar is the interquartile range of each resulting age group. Grey bars denote periods of fan aggradation which are more speculative due to few data points. 103

Figure 5.1. Schematic diagram showing the morphology of a typical unconfined fan in a mountain front setting and key morphometric parameters utilised in previous studies such as fan area (F_a), width (F_w), length (F_l) and gradient (F_g) and typical catchment characteristics. 120

Figure 5.2. (a) The global distribution of dryland fan morphometric studies (see Appendix C for references and locations). The Global Aridity Index (UNEP, 1997) is a function of annual precipitation, temperature and evapotranspiration (data from Trabucco and Zomer, 2018). Fan morphometric studies in **(b)** the SW USA in California (CA) and Nevada (NV), **(c)** southern Spain, **(d)** Greece and SW Asia. The red box denotes the Hajar Mountain region of the UAE and northern Oman, detailed in Figure 5.3. 121

Figure 5.3. (a) Regional geology and geomorphology of the Hajar Mountains, south-east Arabia, showing major thrusts zones, lithological groups and principle landform types (geology redrawn from Corradetti et al., 2020). The exhumed domes of the Arabian Proximal Domain are as follows: Hawasina Window (Musandam; MU), Jabal Akdhar (JA) and Saih Hatat (SH). Four key areas of the mountain front were studied: 1) the Musandam Peninsula (MP), 2) the Rub' al Khali (RK), 3) the Wahiba Sands (WS) and 4) the Batinah Coast (BC). **(b)** Cross sectional elevation profile from the interior bajada to the Makran Subduction Zone in the Arabian Sea. 124

Figure 5.4. Hajar mountain front fans in Oman (January 2020). Landscape views of fan surfaces highlight their very low gradient, with **(a)** and **(b)** showing fan surfaces near Rustaq on the Batinah Coast and near Ibri on the interior bajada, respectively. **(a)** Shows the activation of a shallow surface channel in response to recent rainfall. **(c)** Older fan material has been incised by more recent streamflow, revealing internal architecture. **(d)** Fan surfaces are mantled by desert pavements showing varying degrees of clast varnishing. **(e)** At their medial-distal extents, interior-draining fans are overtopped by Rub' al Khali dune systems (shown by the view of the fan surface, foreground, over-topped by large linear dunes, background). 127

Figure 5.5. (a) Fan systems along the interior mountain front of the Hajar Mountains depicted in Landsat 8 true-colour imagery (bands 432) and **(b)** false-colour imagery (bands 642). Landsat false-colour imagery **(c)** is compared with L-band PALSAR **(d)** for radar-bright fans along the northern Batinah Coast. Landsat false-colour imagery of fan surfaces **(e)** is obscured by overtopping dunes, however L-band PALSAR imagery **(f)** is able to penetrate shallow sand veneers, although areas of radar-dark deep dunes remain. 130

Figure 5.6. (a) Overview of fans mapped in this study, with their apex points shown (red dots). **(b)** Smaller fans were observed in the Musandam Peninsula, with the smallest **(c)** located around the rugged northern coastline. **(d)** Coastal

fans also drain to the Batinah Coast. **(e)** The Wahiba Sands fans. **(f, g)** Examples of the large range of scales of Rub' al Khali fans. 133

Figure 5.7. (a) Very few fans surveyed displayed 'typical' planform morphology (Fig.5.1). Fans are laterally confined by each other, coalescing into elongated bajadas, principally along **(b)** the Rub' al Khali mountain front, **(c)** Batinah Coast and **(d)** Wahiba region in the southern Hajar. **(e)** The fans of the Musandam Peninsula do not form bajadas, being confined laterally by bedrock. **(f)** Larger fans display backfilling into catchment areas along the Rub' al Khali and Batinah Coast mountain fronts. 136

Figure 5.8. Example long profiles are shown for distally **(a)** unconfined and **(b)** fluvially confined fans along the Rub' al Khali and Wahiba Sands bajadas. Smaller fans show steeper profiles than larger fans. Dune encroachment on fans produces a superimposed topography, whilst erosion by axial channels results in sharp, erosive profiles at fan toes. The shaded area in **(a)** denotes the scale of **(b).** 137

Figure 5.9. The offshore bathymetry of **(a)** the Batinah Coast and **(b)** south-western Musandam Peninsula. **(a)** Also shown: examples of small rias and an onshore (Fig.5.10) and offshore sediment core BMB-1 (referred to in the discussion). **(c, d)** Longprofiles for selected fans, including the continental shelf, show low distal gradients are not achieved until below modern sea level (MSL). Toe steepening is observed where fans intersect with the coastal zone. Global mean sea level (GSL) estimates at 50 ka are also marked with standard deviations (Spratt and Lisiecki, 2016). 138

Figure 5.10. (a-c) Historical Google Earth Engine imagery reveals numerous drowned channel systems or rias at fan toes, which have been modified by marine processes forming semi-open and closed lagoons behind spits along the distal extents of Batinah Coast fans. **(d)** An exposed pit section from the coastal zone showing highly calcareous silt/sand deposits overlying fan conglomerates and gravels, indicating previous fan extent (Image credit: A. Parton). Locations marked in Fig.5.9. 139

Figure 5.11. (a) The Umm as Samim is a large interior drainage basin fed by fan drainage networks. **(b)** L-band PALSAR imagery reveals that the basin and fan toes are geomorphologically diverse. **(c)** Lobate structures contrasting with the sabkha floor are interpreted as shallow shoreline features. **(d)** Large fan systems form fan deltas where they disgorge into the basin, indicating a low energy environment under periods of wetter climate. 140

Figure 5.12. Selected morphometric regressions for the mapped fans and their catchments discussed in the text. Colours in the key respond to the four study areas: Musandam Peninsula (MP), Rub' al Khali (RK), Wahiba Sands (WS) and Batinah Coast (BC). The black regression line in each plot reflects the relationship for all studied fans. R^2 values are shown corresponding to each study area as well as the all fans case. See Tables 5.4-5.6 for summary statistics from the regression relationships. 143

Figure 5.13. Standardised residual plots of the fan area vs. catchment area and fan gradient vs. catchment area relationships by **(a)** fan location, **(b)** catchment lithological group; Arabian Proximal Domain (APD), ophiolite (OPH), slope and basin (SB) or post nappe units (PN) (see Fig.5.3a for geological map), and **(c)** distal confinement either by coastal and fluvial processes or topographic barrier, or fans which are unconfined. Bar charts on the right show the percentage of fans by each classification group for each of the four plotting positions on the residual plots. 146

Figure 5.14. Fans typical of each study area along Hajar Mountain fronts and their key controls. **(a)** Musandam Peninsula, **(b)** Rub' al Khali, **(c)** Wahiba Sands, **(d)** Batinah Coast. 157

Figure 5.15. (a) Comparison of the fan area vs. catchment area and **(b)** fan gradient vs. catchment area relationships derived in this study for Hajar Mountain front fans, with studies from other terrestrial dryland and extra-terrestrial contexts. Note: the gradients in **(b)** reproduced from the literature have been derived by the original authors using different methodologies. See Appendix C for regression coefficients, R^2 values, locations and references. MP: Musandam Peninsula, RK: Rub' al Khali, BC: Batinah Coast, WS: Wahiba Sands. 162

Figure 6.1. The principle modern climate circulations around Arabia: Indian Ocean Summer Monsoon (IOSM), African Monsoon (AM) and Mid-Latitude Westerlies (MLWs). Speleothem **(a-c)** and marine core **(d-g)** palaeoclimate archives of the IOSM in south-eastern Arabia and the Arabian Sea are also shown (see Appendix D for the names and references for **a-g**)..... 171
Figure 6.2. The structure of the database and the metadata it contains..... 174
Figure 6.3. (a) All sites included in the database showing the predominate palaeoenvironmental interpretations of the age records they contain (1-138), as well as regional palaeoclimate and sea level archives (a-i). Sub-regional divisions of the Arabian Peninsula are shown. See Appendix D for a table listing the details of each numbered site. **(b)** The eastern portion of the Arabian Gulf/Northern Rub'al Khali sub-region. **(c)** The northern portion of the Arabian Sea Coast sub-region. d: The western portion of the Southern Arabia sub-region..... 178
Figure 6.4. Temporal trends in published luminescence and radiocarbon dates from palaeoenvironmental sites from the Arabian Peninsula (1970-2020)..... 179
Figure 6.5. Geochronological quality assurance criteria for green, amber and red luminescence and radiocarbon dates with both 'Geomorphic' and 'Sample' considerations for each technique. After the approach of Small et al. (2017). ... 185
Figure 6.6. Classified records by landform type and 1 ka time-slice intervals at the Peninsula (A) and sub-regional (B) scales. Records have been placed into time-slices based on central age estimates. 189
Figure 6.7. (a) Sites with records attaining GREEN and AMBER classifications referred to in the following sub-regional syntheses. Site numbers refer to 'Assessed site number' included as a table in Appendix D. **(b)** The eastern Arabian Gulf/Northern Rub'al Khali sub-region. **(c)** The northern portion of the Arabian Sea Coast and Hajar Mountains sub-regions. **(d)** The western portion of the Southern Arabia sub-region..... 191
Figure 6.8. All GREEN and AMBER age records from the database displayed by landform type and included in the following sub-regional syntheses. Site numbers refer to sites listed in Appendix D. Sub-region abbreviations are as Figure 6.7. Palaeoclimate and sea level archives from around the Arabian Peninsula are shown (**a-i**; see Appedix D). **(j)** Summer insolation at 30°N (Berger and Loutre, 1991). The Arabian Holocene Humid Period (AHHP) is marked at ~10-6 ka (Petraglia et al., 2020)..... 193
Figure 7.1. (a) Comparison between mean catchment slope and mean fan area by lithological group. **(b)** Comparison between mean catchment slope and mean fan gradient by lithological group. Error bars represent the standard errors of the means. Labels denote lithological groups: ophiolite (OPH), slope and basin deposits (SB), post-nappe deposits (PN) and the Arabian Proximal Domain (APD)..... 221
Figure 7.2. (a) Coefficient x and exponent y for the F_a v. C_a relationships from this study and the wider literature for dryland fans. **(b)** Coefficient x and exponent y for the F_g v. C_a relationships from this study and the wider literature for dryland fans. The grey shaded areas denote the expected range of values for mountain-front fans after Harvey (2011). Fans are categorised by location and setting. Fans from this study use the following abbreviation: Musandam Peninsula (MP); Rub' al Khali (RK); Wahiba Sands (WS); Batinah Coast (BC). 223
Figure 7.3. R^2 values from the F_a v. C_a and F_g v. C_a regression relationships reported in this study and the literature. The dashed black line shows unity. The grey shaded area denotes the group of strongest relationships reported for mountain-front fans. Figure legend the same as Fig.7.2. 224
Figure 7.4. The key findings from Papers 1-3 (Chapters 4-6) discussed in Chapter 7, summarised relative to a refined model of Hajar landscape response to precessionally-paced climatic forcing ('Climate state') throughout the Late Quaternary for an interior fan system. The numbered findings map onto the numbers shown in the diagrams ('Landscape response'). 229

List of tables

Table 1.1. Overview of the structure of the research chapters comprising this thesis. 8

Table 2.1. The key passive and active controls on fan morphology and dynamics, with examples of studies where these controls have been suggested to be important for fan evolution. 16

Table 2.2. Summary of the previous studies using Hajar alluvial deposits as geoproxies with the key aggradation periods dated and the inference of the original authors based on chronological and sedimentary evidence. The 14C ages of Dalongeville (1999) have been re-calibrated using the IntCal20 calibration curve (see Section 3.4 for more details). 45

Table 3.1. The locations and descriptions of sites located east of the Hajar drainage divide, along the lower reaches of Wadi Sahtan's catchment and the proximal part of the Rustaq fan. Luminescence sampling information is also shown, including whether samples were taken as a tube or block (see Section 3.2.2). [a] Samples where in-situ gamma spectrometry was conducted. [b] Samples which did not yield enough quartz for dating, thus were abandoned. 61

Table 3.2. The locations and descriptions of sites located west of the Hajar drainage divide, in the proximal part of the Ibri fan and both proximal and medial-distal parts of the Dhank fan on the central interior bajada. Luminescence sampling information is also shown, including whether samples were taken as a tube or block (see section 3.2.2). a Samples where in-situ gamma spectrometry was conducted. b Samples which did not yield enough quartz for dating, thus were abandoned. c Samples of little relevancy to the thesis narrative as the underlying sample showed they dated to the historical period so were also abandoned. 62

Table 3.3. The SAR protocol (Murray and Wintle, 2003). 67

Table 4.1. Luminescence age results, including: the sampling depth, grain size, soil radionuclide concentrations (measured using ICP-MS), total environmental dose rate and its components, number of aliquots accepted out of total measured, relative overdispersion (OD), the age model applied for De calculation, final De and resulting age reported with 1σ errors. CAM: central age model (Galbraith et al. 1999), MAM: minimum age model (Galbraith and Laslett, 1993). Values are reported to 2 decimal places, with calculations made prior to rounding. For the two samples considered saturated, the minimum De and age are reported to the nearest integer. 95

Table 4.2. Grain size data from the <2 mm fractions of the samples taken for luminescence dating, calculated using the GRADISTAT software (version 9.1; Blott and Pye, 2001). 96

Table 4.3. Summaries of site location, luminescence age results and sedimentary interpretations for units discussed in the text. 104

Table 5.1. The free data sources employed in this study with product type, acquisition period, resolution and a link to where they were sourced from. 129
Table 5.2. Fan and catchment morphometric variables (e.g. area) and qualitative characteristics (e.g. lithology). 132
Table 5.3. Summary statistics of fan and catchment morphometric parameters. 135
Table 5.4. Summary of selected regressions between morphometric variables for all fans in the dataset (displayed in Fig.5.12). Bold p-values denote statistically significant relationships at the 95% confidence level. 142
Table 5.5. Summary of F_a v. C_a regression relationships for each study area (displayed in Fig.5.12). Bold p-values denote statistically significant relationships at the 95% confidence level. 142
Table 5.6. Summary of F_g v. C_a regression relationships for each study area (displayed in Fig.5.12). Bold p-values denote statistically significant relationships at the 95% confidence level. 142
Table 6.1. Summary of the landform types recorded in the database from the published literature with a general description of the geomorphological, sedimentological and biological features they commonly exhibit. 177
Table 6.2. Sub-regional summary of sites and landform types of individual chronological records within the database. 179
Table 6.3. Summary of the common sources of uncertainty in luminescence dating and examples from the database where these issues have been discussed. 183
Table 6.4. Summary of the common sources of uncertainty in radiocarbon dating relating to sample considerations and reservoir effects. Examples of studies where these issues have been discussed are included from the database. 184
Table 6.5. Descriptions of the quality assurance 'traffic-light' classifications devised by Small et al. (2017) and applied to SCAPE 184
Table 6.6. Number of records attaining each dating method quality level, by sub-region 187

List of equations

Equation 2.1. The power-law relationship between fan area and catchment area. 17

Equation 2.2. The power-law relationship between fan gradient and catchment area. 17

Equation 2.3. Melton's ruggedness index (Melton, 1965). 20

Equation 3.1. The calculation of a luminescence age. 64

List of abbreviations

^{10}Be	Berilium-10
^{14}C	Carbon-14 (radiocarbon)
^{26}Al	Aluminium-26
^{90}Sr	Strontium-90
^{90}Y	Yttrium-90
AHHP	Arabian Holocene Humid Period
AI	Accumulation intensity
ALOS PALSAR	Advanced Land Observation Satellite Phased Array type L-band Synthetic Aperture Radar
APD	Arabian Proximal Domain
ASM	African Summer Monsoon
ASTCs	Arabian Sea tropical cyclones
BC	Batinah Coast
BIC	Bayesian information criterion
C_a	Catchment area
CAM	Central age model
C_e	Catchment elevation
C_g	Catchment gradient
C_{mr}	Catchment Melton's ruggedness index
C_r	Catchment relief
D_e	Equivalent dose
DEM	Depth elevation model
D_r	Environmental dose rate
DRAC	Dose Rate and Age Calculator
DRT	Dose recovery test
F_a	Fan area
F_{ae}	Fan apex elevation
F_g	Fan gradient
Fig.	Figure
F_l	Fan length
FMM	Finite mixture model
F_r	Fan relief
F_{ra}	Ratio of fan relief to area
F_{te}	Fan toe elevation
GEBCO	General Bathymetric Chart of the Oceans
GSL	Global sea level
H_2O_2	Hydrogen peroxide
HCl	Hydrochloric acid
HF	Hydroflouric acid
HiRISE	High Resolution Imaging Experiment
ICP-MS	Inductively-coupled plasma mass spectrometry
IOSM	Indian Ocean Summer Monsoon
IR	Infra-red
IRSL	Infra-red stimulated luminescence

ITCZ	Inter-tropical conversion zone
JA	Jebel Akhdar
K	Potassium
LGM	Last glacial maximum
LOI	Loss on ignition
L_n	Natural luminescence signal
MAM	Minimum age model
MIS	Marine isotope stage
MLWs	Mid-latitude westerlies
MP	Musandam Peninsula
MRE	Marine reservoir effect
MSL	Modern sea level
MSZ	Makran subduction zone
OPH	Ophiolite
OSL	Optically stimulated luminescence
pIR-IR	Post infrared-infrared
PMIP	Palaeoclimate Model Intercomparison Project
PN	Post-nappe
RGB	Red green blue
RK	Rub' al Khali
RSL	Relative sea level
RSCZ	Red Sea convergence zone
RST	Red Sea trough
SAR protocol	Single aliquot regenerative dose protocol
SB	Slope and basin
SCAPE	Synthesising Chronologies for Arabian Palaeoenvironments
SEM	Scanning electron microscopy
SMF	Summer monsoon factor
SMS	Summer monsoon stack
SPT	Sodium polytungstate
Th	Thorium
TL	Thermoluminescence
T_n	Natural luminescence test signal
TT-OSL	Thermally transferred optically stimulated luminescence
T_x	Regerated luminescence test signal
U	Uranium
VPDB	Vienna Pee Dee Belemnite
WS	Wahiba Sands
XRF	X-ray flourescence
α	Alpha radiation
β	Beta radiation
γ	Gamma radiation
$\delta^{13}C$	Ratio of carbon-12 and carbon-13
$\delta^{18}O$	Ratio of oxygen-16 and oxygen-18
ΔR	Marine reservoir correction factor
σ	Standard deviation

List of units

$^{0}/_{00}$	Per mille (parts per thousand)
^{14}C years	Radiocarbon years
AD	Anno Domini (since the birth of Christ)
BC	Before the birth of Christ
cal ka BP	Calendar years (thousands) before present (1950 AD)
cm yr^{-1}	Centimetres per year
GHz	Gigahertz
Gy	Grays
Gy ka^{-1}	Grays per thousand years
ka	Thousand years
km	Kilometres
km^2	Kilometres squared
m	Metres
m asl	Metres above sea level
ma	Million years
mm	Millimetres
mm yr^{-1}	Millimetres per year
nm	Nanometres
ppm	Parts per million
s	Seconds
S*k*	Kurtosis
W/m^2	Watts per metre squared
µm	Micrometre
σ	Skewness
°	Degrees
°C	Degrees Celsius

1 | Introduction, aims and thesis structure

1.1 Introduction

Sediment routing systems, the dynamic pathways that shift sediment from where it is sourced to down-system sinks where it is stored over geological timescales, are key for understanding past landscape change (Allen, 2017). These interconnected systems are comprised of multitudes of temporary repositories of sediment within hillslopes, alluvial fans, rivers, lakes, floodplains, deltas and aeolian dunes. The formation and erosion of these landforms is controlled by a complex array of factors, so that their morphology and the sediments comprising them have the potential to preserve signals of changing environmental conditions through time. However, making sense of these signals and what they tell us about past environmental change is reliant on our ability to detect and interpret them, as well as relate them to discrete periods of time.

A principle driver of landscape change is climate variability which can be observed at multiple temporal scales. Over Quaternary timescales (the last 2.6 ma), Croll-Milankovitch forcing has resulted in numerous periodic shifts in global temperature and rainfall which have occurred gradually over tens of thousands of years. Earth's low-latitude desert belts have been shown to be strongly influenced by variability in the latitudinal positions and intensities of monsoon systems at precessional timescales (~23 ka), with major palaeoenvironmental changes linked to long-term rainfall variability (e.g. De Menocal et al., 2000).

In the Arabian Peninsula, which is the focus of this thesis, the last 20 years has seen an explosion in the number of studied geomorphological archives of Quaternary palaeoenvironmental change, facilitated by the availability of appropriate dating techniques. These include rivers and fans (e.g. Parton et al., 2015a), lakes and wetlands (e.g. Parker et al., 2016), dunes (e.g. Preusser et al., 2002) and coastal landforms such as mangroves and relict beaches (e.g. Lézine et al., 2002). High-resolution palaeoclimate archives such as marine cores from the Arabian Sea (e.g. Clemens and Prell, 2003) and speleothem from caves (e.g. Nicholson et al., 2020) are also available, providing 'master' records of climate variability from biological and isotopic proxies over recent geological

time (Thomas, 2013). These higher-resolution archives are inevitably useful for understanding long-term climatic forcing, but it is the geomorphological archives which provide information about the smaller-scale landscape responses to these changes. The information that landforms provide about landscape evolution and palaeoenvironmental change is not only useful for better understanding the variability of geomorphological systems in response to climatic change, but also for contextualising the complexity of social-environmental interactions over the long-term (Petraglia et al., 2020).

Quaternary environmental change in south-east Arabia has attracted much research attention due to the availability of high-resolution speleothem and marine core data, and a diverse suite of geomorphological archives. Of particular interest are the Hajar Mountains in northern Oman and the United Arab Emirates (UAE) due to their long-term interaction with the Indian Ocean Summer Monsoon (IOSM). Today, the mountains are located on the periphery of the region affected by these strong seasonal rains, but Quaternary palaeoclimate records suggest that they have periodically received much higher rainfall due to a northward shifting of the rain belt (e.g. Burns et al., 2001; Fleitmann and Matter, 2009). This long-term climatic variability has had important implications for the region's hydrology, with periods of higher rainfall resulting in more sustained seasonal drainage activation and the stabilisation of dunes (e.g. Blechschmidt et al., 2009; Thomas and Bailey, 2019; Mueller et al., 2022). These wetter intervals have also been linked to periods of hominid dispersal out of Africa and into south-east Arabia (Armitage et al., 2011), although new archaeological data from the Hajar Mountains suggest this regional climatic model is overly simplistic (Bretzke et al., 2022).

The extensive alluvial deposits that are found in intra-montane valleys and on the flanks of the Hajar Mountains are key sources of palaeoenvironmental data in the region. In the Hajar, alluvial chronologies have shown that periods of fan building coincide with higher IOSM rainfall (e.g. Atkinson et al., 2013; Farrant et al., 2012; Moraetis et al., 2020). It has also been suggested that

Hajar fans provide more sensitive records of climate than nearby speleothems, which do not capture the full record of monsoon variability (Parton et al., 2015a). This is because they record periods of fan building during times when speleothem show no growth, but marine records evidence a strengthened IOSM.

Alluvial fans are complex landforms which respond to changes in climate, but their processes and morphology are also governed by other factors such as setting, tectonics, geology and the morphology of their catchments (Harvey, 2011). The morphologies of the Hajar fans and catchments are diverse, spanning a large range of sizes and forms. Therefore, they provide an excellent natural laboratory for studying the controls on sediment production, supply and storage within a mountainous, dryland context. As such, the Hajar fans have great potential as both records of changing environmental and climatic conditions in their catchments, but also for understanding the wider controls on long-term landscape evolution in alluvial settings.

Despite these boons, the response of Hajar alluvial fans to both climatic and non-climatic controls is still poorly constrained as palaeoenvironmental and geomorphological studies are narrowly concentrated in the north-west of the range. A wider regional synthesis of Quaternary geomorphological records and the quality of the geochronology underpinning them is also lacking for Arabia, making it difficult to compare palaeoenvironmental histories between the Hajar and other regions of the Peninsula. Being able to consider landscape heterogeneity across a broader spatial scale is important for understanding whether the Hajar Mountains are environmentally distinct, with implications for contextualising Quaternary ecological and archaeological shifts within the region.

1.2 Aims and objectives

This thesis seeks to address these knowledge gaps, with the **overall aim being to improve records of the timing and controls on alluvial system evolution in the Hajar Mountains and to compare**

palaeoenvironmental change in the Hajar to its adjacent regions. This aim will be met with three research objectives, each divided into three sub-objectives:

Objective 1: To produce new records of alluvial fan aggradation for settings in the central interior and eastern bajadas of the Hajar Mountains, by:

- Taking a field sampling approach across individual sites to build an integrated record of Late Quaternary environmental change.
- Dating periods of fan aggradation using luminescence.
- Testing whether the timing of aggradation phases from these settings align with the existing model of precessionally-paced incursions of the IOSM.

Objective 2: To identify additional, non-climatic controls on Hajar Mountain alluvial fan morphology and evolution, by:

- Using remote sensing and GIS to build a database of mountain-front fan-catchment morphometric data at the mountain-range scale.
- Assessing the spatial variability of different controls throughout the Hajar range.
- Comparing these data with those for other dryland fans.

Objective 3: To critically assess Hajar geoproxy records, improving interpretation of landscape responses to climatic and wider environmental controls during the Late Quaternary and how this compares with other regions of Arabia, by:

- Constructing the first database of geoproxy records with geochronological control over the last 20 ka for the entire Arabian Peninsula.
- Critically re-assessing geochronological data in an attempt to reduce noise from potential dating issues.

- Synthesising these data for different regions of the Arabian Peninsula, including the Hajar Mountains, to determine the variability in the nature, timing and drivers of palaeoenvironmental changes at the landscape scale.

Each thesis objective is represented by a research paper, ordered by the increasing spatial scale of their coverage. First is a field and dating study of a suite of individual fan systems; second, a remote sensing study of mountain-front fan morphology around the Hajar range; and third, a landscape-scale synthesis comparing different regional palaeoenvironmental records across the whole Arabian Peninsula.

The overall aim will be achieved using a diverse array of methods, including luminescence dating, field stratigraphy, remote sensing, database creation and the re-assessment of legacy data.

1.3 Thesis structure

The three papers each represent a chapter in the thesis, sitting within a total of seven chapters that provide the coherence of a thesis. The overall structure is as follows:

Chapter 1, 'Introduction and thesis structure', provides background context to this thesis and outlines the overall structure and papers constituting this work.

Chapter 2, 'Alluvial fans, south-east Arabia and the Hajar Mountains', provides a deeper review of the literature on, firstly, the definition of alluvial fans, the controls on their processes and morphology and interpreting and dating their stratigraphy as palaeoenvironmental archives. Second, it introduces the geological, geomorphological and climatic context of south-east Arabia and the Hajar Mountains. It will then give an overview of the regional literature on high resolution palaeoclimate archives, geoproxy records and previous work conducted on the controls on Hajar fan evolution throughout the Late Quaternary. Following this, **Chapter 3, 'Methods',** provides justification and background information on the methods used throughout this thesis, in additional detail to the methodology sections of the individual papers.

The main body of the thesis is comprised of the three research papers, the details of which are outlined in Table 1.1. A fourth, technical paper is included in Appendix A. **Chapter 4 (paper 1), 'Alluvial fan response to monsoon variability over the last 300 ka in the Hajar Mountains, south-east Arabia',** aims to establish whether the model of monsoon-paced fan aggradation observed in previous studies is applicable for fan systems in the central interior and east of the Hajar Mountains. An approach applying luminescence dating and field stratigraphic interpretations determines periods of aggradation for fans in the central and eastern Hajar Mountains. Results show that aggradation phases do align with periods of higher IOSM rainfall inferred from other palaeoenvironmental and palaeoclimatic records from the region. However, deposits indicative of flash flooding are coincident with periods of drier climate, suggesting that only the largest flood events are able to result in down-fan sediment transport during precipitation minima at orbital timescales.

Table 1.1. Overview of the structure of the research chapters comprising this thesis.

Chapter number	Paper number	Paper title	Journal	Date published
4	1	Alluvial fan response to monsoon variability over the last 300 ka in the Hajar Mountains, south-east Arabia	Quaternary Science Reviews	June 2023 *(submitted)*
5	2	Morphology and controls of the mountain-front fan systems of the Hajar Mountains, south-east Arabia	Earth-Science Reviews	February 2023
6	3	Assessing the robustness of geochronological records from the Arabian Peninsula: A new synthesis of the last 20 ka	Global and Planetary Change	February 2022
9 (Appendix A)	4	Evaluating the effectiveness of heavy liquid density separation in isolating K-feldspar grains using alluvial sediments from the Hajar Mountains, Oman	Quaternary Geochronology	August 2022

Chapter 5 (paper 2), 'Morphology and controls of the mountain-front fan systems of the Hajar Mountains, south-east Arabia', focuses on the controls on fan morphology in the region, specifically

testing the influence of catchment morphology, geology, base-level change and fan setting. Long-term climatic (established in Chapter 4) and tectonic processes are also considered. To achieve this, a dataset of 438 fans is generated using remote sensing and GIS and then analysed using standard regression techniques. Results show that all factors are influential, but the degree to which is dependent on where across the mountain range the fan is located. This paper also provides the largest dataset of dryland alluvial fan morphometry available in the literature and comparisons are drawn between the morphometric relationships generated in this study and from other dryland contexts.

Chapter 6 (paper 3), 'Assessing the robustness of geochronological records from the Arabian Peninsula: A new synthesis of the last 20 ka', provides a larger-scale synthesis of palaeoenvironmental changes across different sub-regions of the Arabian Peninsula, including the Hajar Mountains. To achieve this, a database of dated geomorphological records is compiled and the data filtered based on an assessment of its geochronological robustness; the first time such a database has been made available for the Arabian Peninsula. These records are then synthesised by each sub-region in the context of their regional-scale climatic and smaller-scale geomorphological controls. Variability in the responses of different sites, regions and geomorphic systems emerge. Mountainous regions such as the upland catchments of the Hajar show less strong coupling with changes in regional climate. It concludes by discussing the importance of these contextual geomorphic controls on environmental change and the implications they have for hydrological heterogeneity, landscape habitability and archaeology over the last 20 ka.

Chapter 7, 'Discussion and conclusions', summarises the findings of the three papers presented in this thesis in the context of the research aim and objectives. It will also consider the broader implications of these findings and what topics emerge for future research.

The Appendices contain supplementary information for all of the work presented in this thesis. **Appendix A** is a paper **('Evaluating the effectiveness of heavy liquid density separation in isolating**

K-feldspar grains using alluvial sediments from the Hajar Mountains, Oman') relevant in the context of **Chapter 3** but not central to the thesis narrative. **Appendix B** provides additional information on the luminescence dating methodology and results outlined in **Chapters 3** and **4**. **Appendix C** provides additional regression statistics from analyses and the morphometric data from the literature used in **Chapter 5**. **Appendix D** gives an overview of the records compiled from the literature included in the database presented in **Chapter 6. Appendix E** contains a Statement of Authorship signed by all co-authors of papers constituting this thesis.

2 | Alluvial fans, south-east Arabia and the Hajar Mountains

2.1 Introduction

This chapter provides context for the research presented in this thesis. What alluvial fans are, the key controls on their morpho-dynamics and their utility as geoproxies of past climate change are outlined first. Second, the geological, geomorphological and modern climatic context of south-east Arabia and the Hajar Mountains are introduced. Third, the current understanding of palaeoclimate variability in south-east Arabia and the established signals preserved in alluvial sediments in the region are discussed. The chapter concludes by considering previous work on the wider controls on Hajar fan morphology that influence their long-term evolution.

2.2 Alluvial fans

Alluvial fans are conically-shaped depositional landforms (Fig.2.1). They form where sediment transfer, either through fluvial or gravity-driven processes, passes from a relatively confined channel setting to a less-constrained hillslope setting. The decrease in energy when flows become unconfined results in the deposition of sediment in the radial splays which are typical of fan morphology (Harvey, 2011). These transitions from zones of higher to lower confinement typically occur at the outlets of steep mountain-front catchments (e.g. Bull, 1964), or where tributaries meet an axial river system (e.g. Stokes and Mather, 2015). Alluvial fans can therefore be grouped into two broad categories: mountain-front fans (Fig.2.1a) and tributary-junction fans (Fig.2.1b). Where numerous fans coalesce, they form low-gradient plains called bajadas (Fig.2.1a, d, g) and occur at a range of scales with the largest fans (or 'megafans') having planform areas of 10^3 – 10^5 km^2 and lengths of >100 km (Fig.2.1d; Hartley et al., 2010).

Alluvial fans have been studied in numerous dryland settings globally, but most prominently in the arid south-western USA (e.g. Bull, 1962; 1977; Denny, 1965; Hooke, 1967; 1968; 1977; Harvey, 2005) and southern Spain (e.g. Harvey, 1990; 1999; Silva et al., 1992; Mather et al., 2000; Viseras et al., 2003). Low-latitude dryland fans are very visible due to having only very patchy vegetation cover, or none at all, and are often the products of periods of higher rainfall during the Late Quaternary

(e.g. Fig.2.1a, b; e.g. ; Abrams and Chadwick, 1994; Harvey, 2004; D'Arcy et al., 2017). However, they are not limited to hot deserts, and are also found in humid-temperate environments (e.g. Wells and Harvey, 1987; Chakraborty et al., 2010; Opalka et al., 2022; e.g. Fig.2.1d) and in glacial and peri-glacial environments (e.g. Legget et al., 1966; Cable et al., 2018; Tomczyk, 2021; e.g. Fig.2.1e). Alluvial fans are also not limited to Earth, having been observed in remote sensing imagery from Mars (e.g. Moore and Howard, 2005; Morgan et al., 2022; e.g. Fig.2.1f) and Saturn's moon, Titan (e.g. Birch et al., 2016; Radebaugh et al., 2018; e.g. Fig.2.1g).

Alluvial fans act as important stores of sediment as part of the source-to-sink sediment routing system. This means that they buffer the cascade of sediment produced in upland catchments, in part controlling the rate of its movement to down-system sinks (Harvey, 2010). They are important for human societies as water sources (either from channels or groundwater) and so are commonly exploited for agriculture or settlement, especially in drylands where they may have more reliable sources of water than other areas (e.g. Fig.2.1c). The sedimentary stratigraphy and relict morphologies that they preserve can also serve as archives of palaeoenvironmental information (e.g. Parton et al., 2015a), as will be discussed later. They also pose challenges for society, being dynamic landforms prone to flash flooding and debris flows (e.g. Mollaei et al., 2018; Leenman et al., 2021).

2.2.1 Controls on fan morphology and dynamics

The morphology and dynamics of alluvial fans are controlled by five key factors: 1) the feeding catchment, 2) the setting of the fan, 3) whether the fan has been subject to changes in distal base level, 4) climatic changes over Quaternary timescales and, 5) either ongoing or previous tectonic processes (Table 2.1). Harvey (2011) groups these factors into 'passive' and 'active' controls. Passive factors (catchment and fan setting) are those that essentially do not change over the timescale of fan formation (the Late Quaternary being the focus of this thesis), thereby exerting what can be thought of as a constant control. However, active controls (changes in base level, climate and

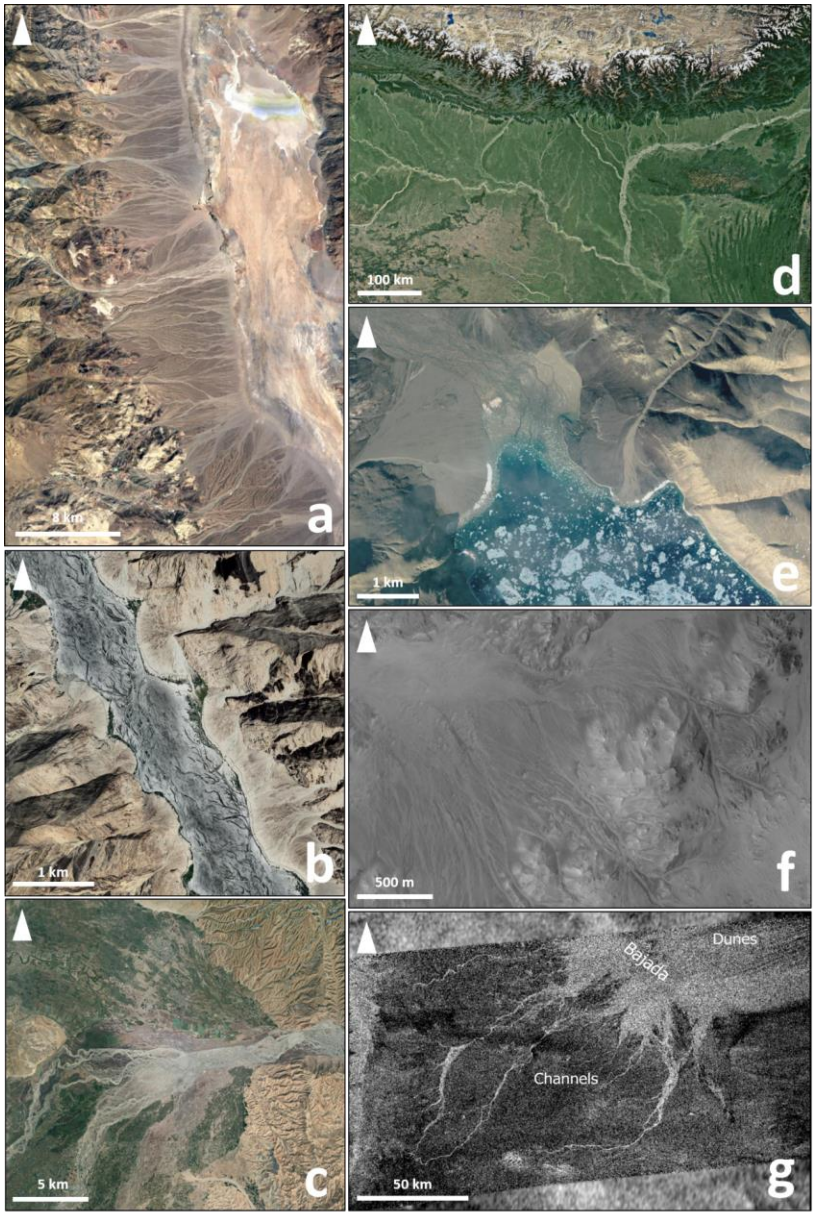

Figure 2.1. Examples of the diversity of terrestrial and extra-terrestrial alluvial fans. **(a)** Mountain-front fans in Death Valley, California, USA, often considered the 'archetype' fans (Harvey, 2011). **(b)** Tributary-junction fans along the Nubra River, Ladakh, north-western India. **(c)** The Panj River fan being extensively used for agriculture on the border of Tajikistan and Afghanistan. **(d)** The megafans of the Himalayas, northern India, where they meet the Ganges River. **(e)** Coastal fans in the cold environment of northern Nunavut, north-eastern Canada, situated in an inlet of Baffin Bay. **(f)** Alluvial fans in Mojave Crater, Xanthe Terra, Mars. **(g)** Channels draining to the Elivagar Flumina fan bajada located near Titan's equator with a sand sea of linear dunes located in the top right of the image. Images **a - e** were acquired from Google Earth Pro. Image **f** was acquired on 27th March 2015 by the High-Resolution Image Science Experiment (HiRISE), made available through the University of Arizona's HiRISE Catalogue (https://www.uahirise.org/catalog/). Image **g** was acquired from the synthetic aperture radar (SAR) instrument aboard the Cassini Orbiter and is reproduced from Radebaugh et al. (2018).

Table 2.1. The key passive and active controls on fan morphology and dynamics, with examples of studies where these controls have been suggested to be important for fan evolution.

Control	Key points	Literature examples
Passive controls		
Catchment	• Aspects of fan morphology scale with aspects of catchment morphology, such as area and topography. • Fan area scales positively with catchment area, fan gradient scales negatively with catchment area (Fig.2.2). • Catchment morphology controls depositional processes on fans (e.g. fluvial or debris-flow dominated). • Catchment geology is an important control on sediment production and therefore fan building.	Morphometric relationships widely demonstrated for fans. Classical studies are from the south-western USA (e.g. Denny, 1965; Hooke, 1968; Bull, 1977) and southern Spain (e.g. Silva et al., 1992; Harvey, 2002; Harvey et al., 1999). Fan morphometric relationships have been shown to be modified by the erodibility of catchment geology in Death Valley, south-western USA (Hooke and Rohrer, 1977).
Fan setting	• The depositional location of the fan influences morphology. • Fans in unconfined, mountain-front settings are typically larger and have stronger regression relationships with catchment morphology. • Fans in confined settings, such as tributary junctions, are typically smaller and have weaker fan-catchment regression relationships.	Mountain-front fans in the Wadi al Bih region of the UAE are larger and have stronger relationships with their catchments than fans in tributary junction settings (Al-Farraj and Harvey, 2005). Weak regression relationships also reported for tributary junction fans along the Dades River, Morocco (Stokes and Mather, 2015).
Active controls		
Base level change	• The level that the fan toe grades to can be variable through time, for example due to sea level variability or distal lake level fluctuations. • Increasing base level results in fan aggradation, whilst a drop in base level results in incision. • Fan foreshortening and steepening often results from processes acting on their toes, such as wave action in coastal settings.	Incision and progradation occurred on the Stillwater fans in Nevada, south-western USA, following the desiccation of Lake Lahontan (Harvey, 2002). Foreshortening and steeping of fans observed in the coastal setting of the Cabo de Gata region of southern Spain due to sea level highstands during the Late Quaternary (Harvey et al., 1999).
Climatic change	• Climate is the key control of periods of drainage activity, resulting in sediment mobility from catchments to fans. • Considered the predominate signal preserved in fan sedimentary archives globally, although signals are variable (Harvey, 2011).	How fans adjust to climatic change is variable between settings. E.g., Himalayan megafans record widespread incision during periods of intensified monsoon rainfall during the Late Quaternary (Goodbred Jr, 2003), whereas aggradation is reported during wetter periods for eastern Australian systems (Nanson et al., 1992).
Tectonics	• Tectonic processes result in the uplift of catchments, modulating climatically-paced activity. • Can also be an active control on fan morphology by inducing base-level changes or active faulting altering fan morphology.	Variable tectonic activity in the valleys of the Betic Cordillera, southern Spain, results in variable fan morphology as tectonic subsidence controls accommodation space for fan development (Viseras et al., 2003). Fans in the Gobi desert, southern Mongolia have undergone post-depositional modification by thrust-faulting (Owen et al., 1997).

tectonic processes) are those that change, sometimes many times, over the timescale of interest, and therefore the nature and magnitude, relative to other controls, of their influence is not constant.

Fans are fundamentally the products of their feeder catchments as this is where all the sediment contributing to fan building originates. Catchments exert intrinsic controls on the volume and rate of sediment production through their size, topography and geological characteristics. The morphometric characteristics of fans can be statistically related to those of their catchments through the use of power-law regression relationships (e.g. Bull, 1962). The most fundamental of these relationships are 1) fan area vs. catchment area (Equation 2.1) and 2) fan gradient vs. catchment gradient (Equation 2.2; Al-Farraj and Harvey, 2005):

Equation 2.1. The power-law relationship between fan area and catchment area.

$$F_a = xC_a^y$$

Equation 2.2. The power-law relationship between fan gradient and catchment area.

$$F_g = xC_a^y$$

Where F_a is planform fan area, F_g is fan gradient, C_a is planform catchment area and coefficient x and exponent y define the relationship between the catchment morphometric variable and that of the fan.

Equations 2.1 and 2.2 have been extensively applied in the alluvial fan literature, with Equation 2.1 consistently giving a positive relationship and Equation 2.2 giving a negative relationship (e.g. Bull, 1977; Harvey et al., 1999; Mokarram et al., 2014; Stokes and Gomes, 2020; Fig.2.2). Larger catchments produce larger fans because they produce greater volumes of sediment (Fig.2.2a; Allen and Hovius, 1998). The negative relationship reported throughout the literature for Equation 2.2 (Fig.2.2b) is the result of transport process thresholds, whereby smaller catchments are more likely to have higher sediment-to-water ratios, resulting in sediment mobilisation by debris flows and thus steeper depositional gradients on the fan (Harvey, 1987). On the other hand, larger catchments

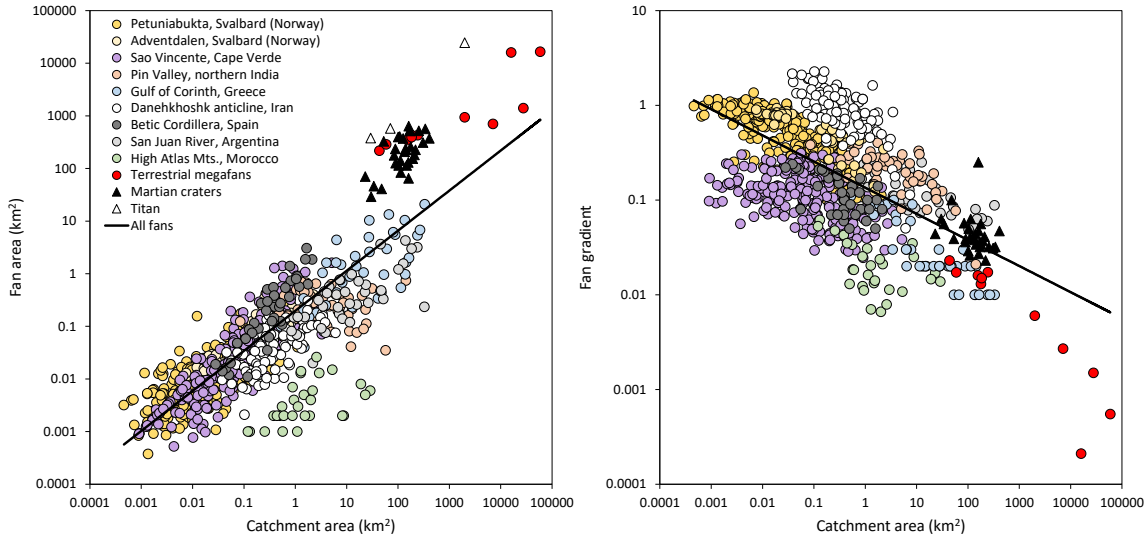

Figure 2.2. Fan-catchment morphometric measurements for selected fan studies from the literature for a range of different climatic, geological and planetary settings: Petuniabukta, Svalbard (Norway; Tomczyk, 2021); Adventdalen, Svalbard (Norway; De Haas et al., 2015); Sao Vincente, Cape Verde (Stokes and Gomes, 2020); Pin Valley, northern India (Shoshta and Marh, 2021); Gulf of Corinth, Greece (Karymbalis et al., 2018); the Danehkoshk anticline, Iran (Bahrami, 2013); the Betic Cordillera, Spain (Viseras et al., 2003); the San Juan River, Argentina (Milana and Ruzycki, 1999); the High Atlas Mountains, Morocco (Stokes and Mather, 2015); assorted terrestrial megafans (Arzani, 2012: references therein); craters on Mars (Moore and Howard, 2005) and Titan (Birch et al., 2016). **(a)** The positively correlated fan area vs. catchment area relationship ($Fa = 0.20Ca^{0.76}$; $R^2=0.70$). **(b)** The negatively correlated fan gradient vs. catchment area relationship ($Fg = 0.14Ca^{-0.28}$; $R^2=0.41$). Data from 930 individual fans in total.

have lower sediment to water ratios, meaning sediment mobilisation is more likely to occur through fluvial processes that have lower depositional gradients.

Coefficient *x* and exponent *y* from Equations 2.1 and 2.2 vary between studies, attributed to the effects of variability in contextual factors such as source area geology, tectonic history and fan setting (e.g. Kostaschuk et al., 1986; Allen and Hovius, 1998; Mills, 2000; Giles, 2010). However, linking these factors to values of *x* and *y* is difficult due to 1) the difficulties in quantifying factors like tectonic history into a single metric and, 2) their complex interplay in reality (e.g. Whipple and Trayler, 1996). Based on research from dryland fans, *x* and *y* typically range between 0.1 - 2.1 and

0.7 - 1.1, respectively, for the fan area vs. catchment area relationship and 0.03 - 0.17 and -0.15 - -0.35 for the fan gradient vs. catchment area relationship (Harvey, 2011; Fig.2.2).

The strength of these relationships, reported as an R^2 statistic, varies depending on the coupling of fans to their catchments relative to other controlling factors. The relative influence of catchment morphology on fan morphology can vary both between the parameters assessed and between fans in different contexts. For instance, the fan area vs. catchment area relationship is typically stronger than the fan gradient vs. catchment area relationship (Fig.2.2; e.g. Silva et al., 1992; Al-Farraj and Harvey, 2005; Harvey, 2005; Karymbalis et al., 2018). Fans in unconfined, mountain-front settings typically have stronger regression relationships with their catchments than fans in confined settings such as tributary junctions. For example, Stokes and Mather (2015) report weak R^2 statistics of 0.27 and 0.21 for the fan area vs. catchment area and fan gradient vs. catchment area relationships, respectively, for fans forming at tributary junctions along the Dades River in the High Atlas Mountains of Morocco (Fig.2.2). In these settings, other factors external to the catchment, such as the erosive influence of an axial river system, are also important controls on resulting fan morphology (Leeder and Mack, 2001). Fans in more complicated contexts also have regression relationships with values of *x* and *y* (Equations 2.1, 2.2) which fall to the extreme ends or outside of the expected ranges suggested by Harvey (2011) (e.g. Milana and Ruzycki, 1999; Al-Farraj and Harvey, 2005; Stokes and Mather, 2015), although there is likely a bias effect with these 'typical' ranges as most of the literature comes from dryland and mountain-front settings (Stokes and Gomes, 2020).

Equations 2.1 and 2.2 apply to numerous different morphological variables which can be measured for fans and their catchments. Outside of catchment area, topographic variables of the feeding catchment often produce strong relationships with properties of the fans at their outlets. These variables often include mean catchment gradient, elevation (the difference between the maximum

elevation of the catchment and that of the fan apex) and Melton's ruggedness index (e.g. Tomczyk, 2021; Karymbalis et al., 2022), defined as:

Equation 2.3. Melton's ruggedness index (Melton, 1965).

$$C_{mr} = C_r C_a^{-0.5}$$

where C_{mr} is Melton's ruggedness index (Melton, 1965), C_r is catchment relief and C_a is catchment area. Typically, these catchment topographic variables produce negative relationships with fan area and positive relationships with fan gradient (e.g. Melton, 1965; Kostaschuk, 1987; Marchi et al., 1993; Guzzetti et al., 1997; Tomczyk, 2021; Karymbalis et al., 2022). Therefore, steeper and more rugged catchments produce smaller, steeper fans because of the sediment transport processes they are likely to generate. The relationship between Melton's ruggedness index and fan gradient in particular has been shown to be a good discriminator of whether fans are formed by fluvial or debris flow processes, with multiple studies using these relationships to define process thresholds (e.g. De Scally and Owens, 2004; Karymbalis et al., 2022).

Catchment geology is a key control on fan development which modulates the statistical relationships previously outlined. This is because catchment rock type and its weathering history are important controls on sediment production for fan building (e.g. Bull, 1964; Al-Farraj and Harvey, 2005; Stokes and Mather, 2015). However, it is difficult to quantify and thus include in statistical relationships such as Equations 2.1 and 2.2, with the same applying to the other factors discussed throughout this section except catchment morphometric variables. Due to this, plotting the residuals of Equations 2.1 and 2.2 has been used widely to help identify the controls of non-quantifiable variables such as catchment geology (e.g. Silva et al., 1992; Harvey et al., 1999; Harvey, 2002; 2005; Al-Farraj and Harvey, 2005; Stokes and Mather, 2015; Stokes and Gomes, 2020; Tomczyk, 2021; Fig.2.3). The plotting positions of the example data shown in Figure 2.3 are likely to be, at least in part, controlled by catchment geology, although other controls such as fan setting and tectonics are probably also important.

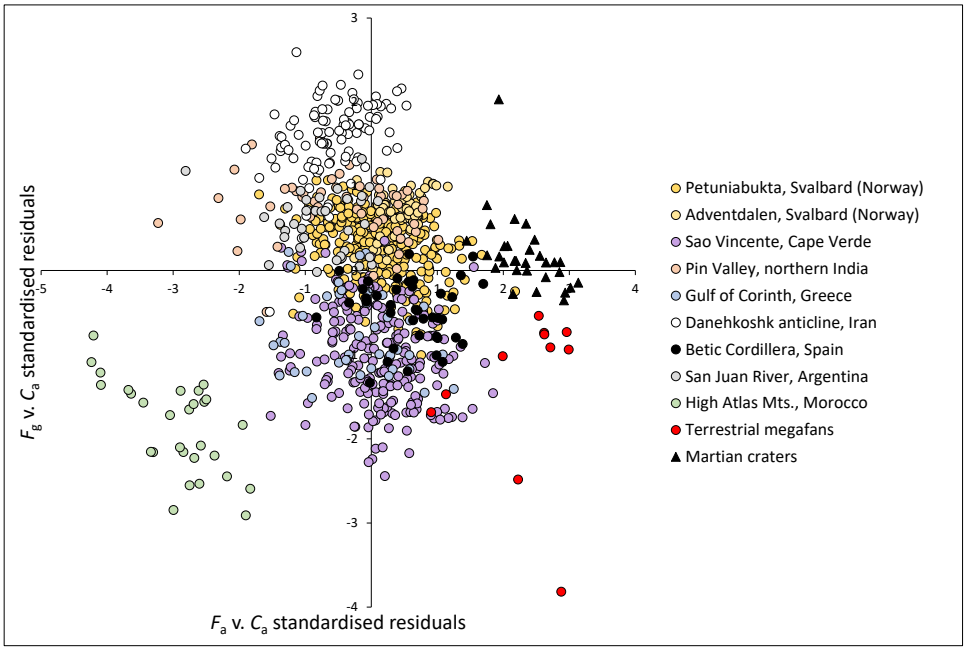

Figure 2.3. Standardised residuals for the Fa v. Ca and Fg v. Ca relationships shown in Figure 2.2, plotted by fan location. Clusters emerge, likely controlled by factors such as catchment geology, fan setting, tectonics etc. Data references are the same as Figure 2.2.

Changes in base level can have a significant influence on fan morphology. Base-level change is often the result of highstands in either lake or sea levels where fans are located on the margins of lacustrine basins or along coastlines, respectively (e.g. Hayward, 1985; Harvey et al., 1999; Robustelli et al., 2005). Lake-level variability, for example, has been shown to control distal processes on the Stillwater fans of the southwestern USA, with lowstands resulting in distal incision and progradation and highstands causing distal aggradation (Harvey, 2002). Base-level changes also result in the alteration of long-profile and planform fan morphology, for instance through the foreshortening and steepening of coastal fans due to the erosion of their toes during periods of higher sea level, as has been observed for fans on Sao Vincente, Cape Verde (Stokes and Gomes, 2020). Tectonic processes can also influence base level, with ongoing subsidence in sedimentary basins being a key control on the accommodation space available for fan building (e.g. Whipple and Trayler, 1996; Viseras et al., 2003; Rodgers and Gunatilaka, 2003; Davis et al., 2021).

Fans preserve responses to climatic change within their sedimentary architecture and morphologies (e.g. Maizels and McBean, 1990; D'Arcy et al., 2017; Terrizzano et al., 2017), with climatic change widely reported in the literature to be the dominant driver of fan dynamics (Harvey, 2011). However, the ways in which fans respond are complex, with multiple, and conflicting, conceptual models for different regions. Much of the classical fan literature holds that fan aggradation occurs during periods of higher rainfall as more sediment is produced and mobilised from catchments, with incision linked to transport-limited arid periods (Lecce, 1990). The dominant aggradation or incision on fans depends on the ratio of water to sediment in flows from the catchment which, whilst climatically driven, is also modulated by factors such as catchment morphology and vegetation cover (Blair and McPherson, 1994).

As such, the signals of climatic change recorded by fans are spatially variable. For example, the fans of southern Spain record the opposite response to the classical model whereby they aggrade during colder and drier periods and incise during warmer and wetter periods (e.g. Harvey, 1984; Harvey, 1987; Harvey, 1996). Harvey (1996) suggests that incision could result during periods of higher rainfall due to increased vegetation growth in upland catchments, limiting sediment transport and generating stream flows with greater erosive capacity. Such diverse responses make it difficult to ascribe any one model of climatic change responses to alluvial fans as a collective, requiring detailed regional or even catchment-scale interpretation of stratigraphic sequences and, underpinning this, good chronometric control (Dorn, 1994).

Lastly, tectonics play key long-term roles in fan evolution and morphology. Whilst Harvey (2011) groups tectonics with the active controls, he also notes that they can be thought of as passive in some circumstances as well. In the passive sense, tectonics ‘set the stage’ for fan development through producing the sharp topographic differences between uplands and depositional lowlands and the relief characteristics of the catchment (Bowman, 2019). For example, Ritter et al. (1995) suggest that, for fans in south-western Montana, tectonic processes are responsible for producing

relief and accommodation space but sedimentation on the fans is a climatically-driven process. As an active control, tectonic faulting can deform fans, leading to changes in their morphologies such as the production of scarps which can be used to reconstruct subsidence and uplift histories (e.g. Mousavi et al., 2021; Davis et al., 2021). As previously mentioned, the subsidence of lowlands is an important control on base level and the accommodation space for fan building. For example, Viseras et al. (2003) showed that for fans in the Betic Cordillera of southern Spain, subsidence-driven base-level change exerts an important control on resulting fan planform and long-profile morphologies. Active tectonics can also result in changes to the feeder catchments of fans, such as by increasing the area of drainage networks through river capture (e.g. Mather et al., 2000).

2.2.2 Fans as geoproxies of palaeoenvironmental and palaeoclimatic change

Fans adjust in response to these active controls. As such, they have the potential to record signals of past control variability within their morphologies and sedimentary stratigraphy (Bowman, 2019). In this sense, alluvial fans can act as geomorphological records of palaeoenvironments by preserving features relating to past base-level, tectonic and climatic changes. Thomas (2013) terms such archives of palaeoenvironmental change 'geoproxies': the evidence of Quaternary terrestrial environmental variability found through the analysis of landforms. Being highly dynamic landforms with multiple interacting controls, ascertaining what is driving a signal of, for example, fan aggradation can be challenging. From the literature, understandings of what changes in external forcing fans preserve usually relies on the comparison between dated records of fan development and other regional proxy records (e.g. Dorn, 1994; Ritter et al., 1995; Harvey, 2004). However, it has been widely demonstrated that the principal signal preserved in phases of fan building and incision correlate with long-term climatic variability (e.g. Owen et al., 1997; Suresh et al., 2007; Parton et al., 2015a; Terrizzano et al., 2017; D'Arcy et al., 2017; Bartz et al., 2020; Winsemann et al., 2022), which is modulated by other, secondary, signals such as tectonics and base-level change (the latter of which is often itself the product of climate or tectonics).

The nature of fan deposition through one or more active and avulsing lobes means that they can preserve palaeoenvironmental information in both vertical stratigraphy and through assemblages of relict surfaces. Relict surfaces are the result of periods of fan aggradation and are subject to incision during periods of lower sediment production or transport from catchments. In drylands in particular, these relict surfaces are often visible due to limited vegetation cover and are mantled by desert pavements and rock varnish (McFadden et al., 1987; Al-Farraj and Harvey, 2000; Walk et al., 2022). Different weathering extents and rock varnish development on the relict surfaces of fans allows for different phases of fan activity to be identified. This was quantitatively demonstrated by D'Arcy et al. (2018) for fans in the south-west USA, with the degree of reflectance from fan surfaces in multi-spectral satellite data correlating with their known ages.

Fan stratigraphy reveals both fan deposition and the environmental context of these periods. There are two common stratigraphic sequence types observed from sections through alluvial fans (Harvey, 2011), following the facies descriptions of Miall (1977; Fig.2.4a). These provide a useful framework for identifying the processes of fan aggradation and their drivers. The first is the 'Trollheim Type', comprised of coarse and poorly sorted debris flow units, without discernible bedding, inter-stratified with structureless gravels deposited by sheetflooding or channel flows (Fig.2.4a). Trollheim Type sequences are common on gravity-driven fans where debris flows are more likely (e.g. Moscariello, 2018). Second is the 'Scott Type', comprised of sheet and channel fill gravels interstratified with sand units (Fig.2.4a). Scott Type sequences are typical of fluvial fans where deposition occurs in channelised or overbank settings as a result of stream flow (e.g. Nichols and Fisher, 2007).

Fan stratigraphy is also internally variable, with facies changing down-fan (Figure 2.4b) . Near the fan apex, deep and coarse channel fills dominate the sedimentary architecture, becoming thinner in the medial fan where overbank channel deposits show evidence of palaeosol development (e.g. Sinha et al., 2014). At the low-gradient toes of fluvially-dominated fans, channel fills are very thin

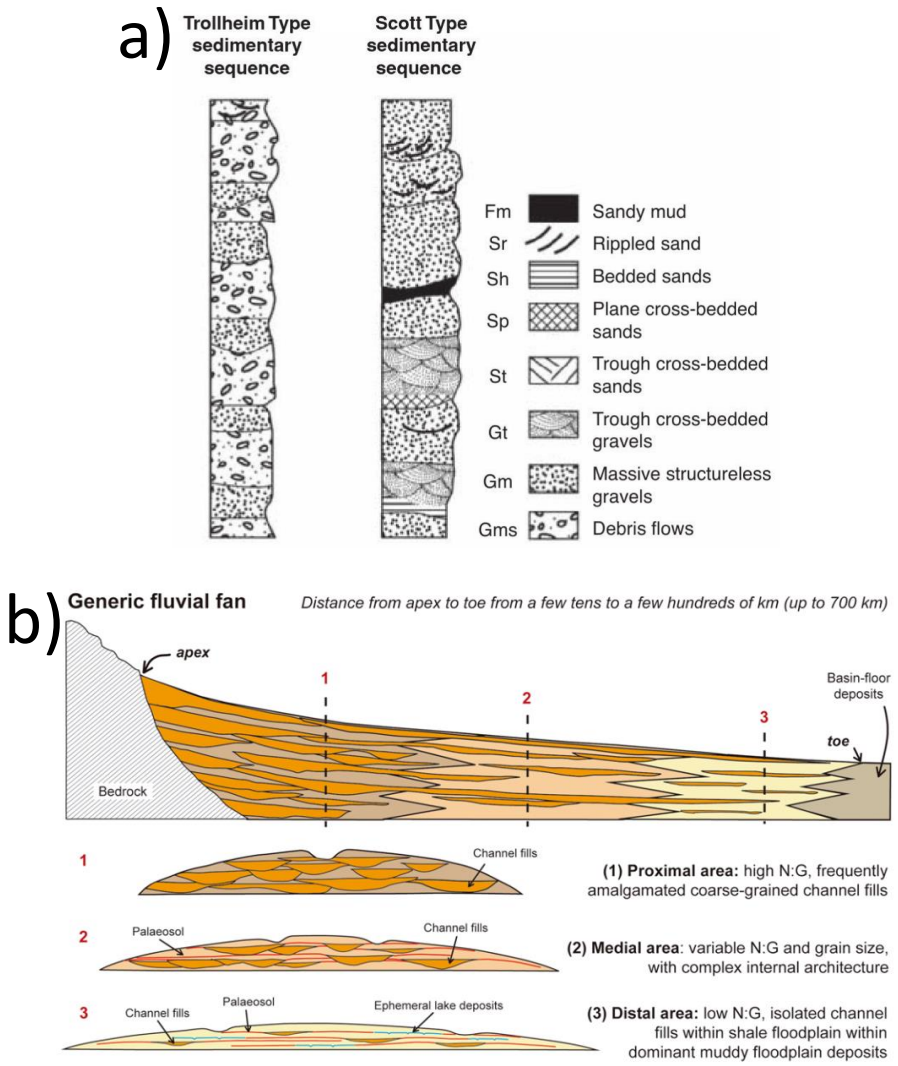

Figure 2.4. (a) Stratigraphic models for debris-flow driven fans (the 'Trollheim' type) and fluvially-driven fans (the 'Scott' type). **(b)** Long-profile stratigraphic model for a generic fluvial fan. N:G refers to net to gross ratio: the ratio of the cumulative thickness of deposits relative to their volume. **(a)** Reproduced from Harvey (2011), **(b)** reproduced from Moscariello (2018).

and sheet deposits of gravels and sands are common due to the washout of sediments past intersection points (e.g. Thalmeier et al., 2021). Ponded wetland or lacustrine sediments may also punctuate the stratigraphy, forming as a result of low flow energy in an increasingly distributed drainage network down-fan (e.g. Horton and DeCelles, 2001).

Stratigraphic variability across fans due to their position within the source-to-sink sediment routing system can make reconstructing complete records of palaeohydrological changes difficult. Deposits

left by avulsing, braided channel systems for instance can be problematic as they do not simply deposit sequentially on the fan surface as, for example, sediments in a lake would. Instead, the loci of deposition will change over time with changing hydrological conditions and relict deposits will be eroded and either reworked on the fan or transmitted to the sedimentary basin or axial river system (Bristow and Best, 1993). Overprinted on this is the noise introduced by other external (e.g. tectonics and base-level change) and internal controls on fan sedimentation which can vary through time and between fans (Harvey, 2012). This can make field sampling challenging and often means that a three-dimensional approach of integrating multiple sites across space needs to be taken to build a representative picture of the preserved signals (e.g. Ballantyne and Whittington, 1999; Hornung et al., 2010; Kober et al., 2013; Harries et al., 2019; McClain et al., 2021).

Underpinning the palaeoenvironmental interpretation of fans is absolute chronology. Fans are usually comprised of coarse-grained sediments and deposition can span long periods that scale with fan size. The largest megafans may have developed over periods of up to 10^7 years (Mather et al., 2017). This can make dating challenging using radiocarbon techniques due to the limit on radiocarbon dating being ~50,000 years (Wood, 2015), as well as fan sediments typically preserving little organic material. However, where organic matter is preserved there have been successful applications of radiocarbon dating, such as charcoal layers (e.g. Jull and Geertsema, 2006) or organic-rich bulk sediments (e.g. Ratnayaka et al., 2019). The characteristics of the weathering of relict fan surfaces have also been applied as dating techniques, such as Schmidt-hammer exposure age dating whereby the relative strength of surface clasts are used as a proxy for exposure time (McEwen et al., 2020; Matthews and Winkler, 2022) and the widths of weathering fractures on surface clasts (e.g. D'Arcy et al., 2015), although these methods still rely on an absolute chronology for calibration.

Cosmogenic nuclides and luminescence techniques are the most commonly applied dating methods to Quaternary fans. Cosmogenic nuclide dating involves the measurement of isotopes such as ^{10}Be

and ^{26}Al from surface boulder samples which are produced through exposure to cosmic rays (e.g. Nishiizumi et al., 2005; Sarıkaya et al., 2015; Dühnforth et al., 2017). These techniques are very useful for measuring time since the abandonment of relict fan surfaces and they can also be applied to measure burial time (e.g. Zhao et al., 2017), with a range of 10^2-10^7 years depending on the isotope (Schaefer et al., 2022). However, cosmogenic techniques are best applied to large boulders which are unlikely to have been remobilised and deposited in various locations along the fan-catchment system as this can produce erroneously old ages of surface abandonment.

Luminescence dating techniques, such as the optically stimulated luminescence (OSL) signal of quartz or the infrared-stimulated luminescence (IRSL) signal of feldspar, calculate the time since burial of minerals (Rhodes, 2011; see Section 3.2.2 for more detail). Sand lenses within fan deposits are ideal targets for luminescence dating as they are typically abundant in sand-sized grains of quartz and feldspar (e.g. Porat et al., 1997; Rittenour, 2008; Singh et al., 2016). Whilst sand lenses are relatively easy to sample in the field and require less laboratory preparation, gravel deposits can also be targeted and coarse sand retrieved by sieving (e.g. Kenworthy et al., 2014; Mueller et al., 2022). Progress has also been made in recent years in the dating of fluvial cobbles using luminescence techniques (Jenkins et al., 2018; Ishii et al., 2022; Ou et al., 2022), potentially broadening the range of target materials available in alluvial fan contexts. The upper age limit on luminescence dating is normally ~200 ka, however this is dependent on the local geological context and fans have been dated up to ~1 ma using luminescence techniques (e.g. Blechschmidt et al., 2009).

Luminescence and cosmogenic nuclide techniques can both suffer from problems of signals being the product of prior periods of either burial or exposure (inheritance; Mather et al., 2017), however they have a significant advantage over radiocarbon techniques in that they are able to directly date geomorphological events. With radiocarbon dating, the dated event is the time of death of an organism, which is assumed to be contemporaneous with burial (Small et al., 2017). Therefore,

luminescence and cosmogenic nuclide dating methods, in conjunction with sedimentological analyses, may be more appropriate for answering questions about the controls and timings of fan deposition and abandonment. This being said, 'toolbox' approaches of multiple geochronological methods are often useful to be able to target different aspects of fans and other fluvial deposits where appropriate (e.g. DeLong and Arnold, 2007; Rizza et al., 2019; Moreno et al., 2021).

2.3 South-east Arabia and the Hajar Mountains

The Hajar Mountains run through northern Oman and the UAE in south-east Arabia (Fig.2.5) and are host to extensive alluvial fan and valley-fill deposits. These alluvial archives, along with other landforms, form an increasingly complex record of palaeoenvironmental change from geoproxies in the region. As outlined in the previous section, interpreting fan records relies on an understanding of their geological, geomorphological and climatic contexts. This section will outline the regional context of south-east Arabia in terms of present conditions, as well as the drivers of Late Quaternary climatic change and resulting environmental responses.

2.3.1 Regional setting

Geology

Covering around 3,000,000 km^2, the Arabian sub-continent is the largest peninsula in the world (Al-Hemoud et al., 2022). It has formed as the result of the spreading rift axes of the Gulf of Aden and Red Sea in the south and west, respectively, separating the Arabian Plate from the Nubian Shield and Somali Block of the north-eastern margins of the African Plate (Bosworth et al., 2005). To the

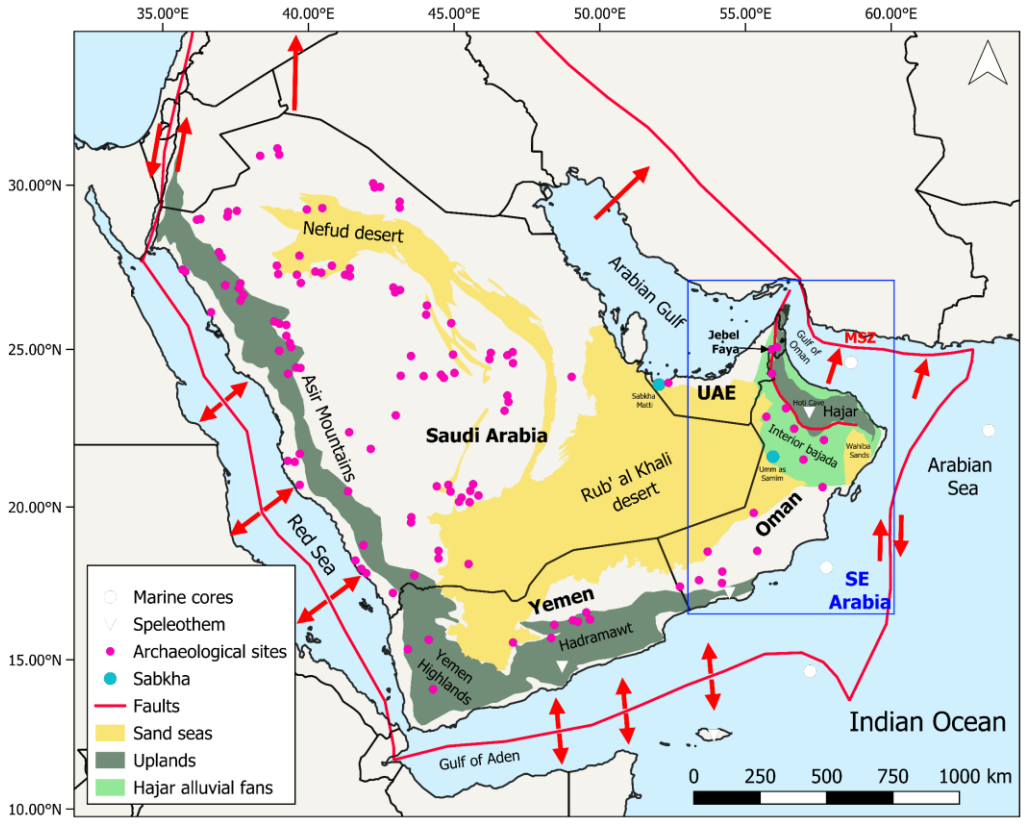

Figure 2.5. The Arabian Peninsula, showing coastal uplands, the interior Rub' al Khali desert, speleothem and marine core records and the major faults associated with the Arabian Plate boundaries and along the Hajar. Red arrows indicate the direction of plate movement, with the collisional zone in the north denoted by the Makran Subduction Zone (MSZ). Palaeolithic archaeological sites are also marked (from Nicholson et al., 2020). South-east Arabia is delineated with the blue box. Key locations discussed in the text are labelled.

north and north-east, the Arabian Plate is colliding with the Eurasian Plate, generating the active orogeny forming the Zagros Fold-Thrust Belt which spans south-eastern Turkey, northern Iraq and western and southern Iran (Zebari et al., 2019). The majority of the Arabian Peninsula is comprised of Precambrian igneous and metamorphic rocks which form the Arabian Shield, dating up to 900 ma (Powers et al., 1966; Nehlig et al., 2002).

The northwards movement of the Arabian Plate at a rate of ~4 cm yr^{-1} (DeMets et al., 1990) into the Eurasian Plate is an important control on the structural geology of south-east Arabia. This convergent plate boundary is located in the Makran Subduction Zone (MSZ), located 200 km to the

north of the Hajar range in the Arabian Sea (Hansman et al., 2017; Fig.2.5). Two collisions are responsible for the uplift of the Hajar. The first was a Late Cretaceous continent-ocean collision between the Arabian Plate and the Tethyan Ocean which commenced from at least 104 ma with the obduction of the Semail ophiolite, ancient oceanic crust, onto the continental crust of the Arabian Plate (Guilmette et al., 2018), forming the principle lithological group of the Hajar Mountains (Searle and Cox, 1999). The second was the continent-continent collision with the Eurasian Plate causing the culmination of the Musandam Peninsula in the northern Hajar during the Late Cenozoic (~22 ma) and the uplift of the Zagros Mountains in Iran (Ali et al., 2018). Slower uplift continues to the present rates of 0.1-0.89 mm yr^{-1} recorded by raised marine terraces in the south-eastern Hajar during the Mid Quaternary (Hoffmann et al., 2020). Contrasting this, subsidence is evident in the Musandam Peninsula since their culmination which, along with eustatic sea level rise during the Quaternary, has formed the drowned *khors* (fjords) of northern Oman (Searle, 2019).

Geomorphology

South-east Arabia's geomorphology is varied and contrasting. The northern and southern coastlines along the Arabian Gulf and Arabian Sea, respectively, are characterised by flat, low-elevation sabkha. The largest of these coastal salt-flats is Sabkha Matti on the border between the UAE and Saudi Arabia, covering 2,950 km^2 (Fig.2.5; Saeed et al., 2020). The Rub' al Khali ('*Empty Quarter*') occupies the sedimentary basin in the interior of south-east Arabia (Fig.2.5). It is the largest active sand sea in the world, spanning 600,000 km^2 in total, with aeolian dune types in south-east Arabia including linear dunes towards the north-west and barchanoid forms in central and southern areas (Goudie et al., 2000). Inland sabkha are also common in the Rub' al Khali, occupying interdune areas fed by groundwater and small amounts of meteoric rainfall. The largest of these inland sabkha is the Umm as Samim ('*Mother of Poisons*') which is located in the eastern Rub' al Khali on the border between Oman and Saudi Arabia (Fig.2.5).

The British explorer Sir Wilfred Thesiger visited the Umm as Samim in 1949 and was likely the first westerner to see it (Fookes et al., 2019). Thesiger (1950a) described the Umm as Samim as a place of hazardous quicksand:

> *"Ahead of us a tawny waste stretched out to blend at an indeterminable distance with a dust-laden sky and nothing, neither stick nor stone, broke its dull monotony. This was the quicksand of the Umm [as] Samim… I am myself convinced that it is the only dangerous quicksand in southern Arabia. Camels can be lost after rain on many of the salt flats… for they are unable to move if they sink in a couple of feet and then they die of starvation; but I believe that it is only in Umm [as] Samim that they could be engulfed".*

By contrast, the Wahiba Sands is a smaller sand sea spanning 12,500 km^2 situated between the central Arabian Sea coastline to the south and the southern Hajar Mountains to the north and is characterised by linear dunes running north to south (Alsharhan et al., 2020).

The Hajar Mountains run from central Oman, passing through the north-eastern UAE up to the Musandam Peninsula, which forms the northern tip of south-east Arabia and is also part of Oman (Fig.2.5). Hajar means '*solid rock*' and the mountains are comprised of rugged, often sparsely vegetated slopes of exposed rock, rising to their highest points at Jebel Akhdar and Jebel Shams (~3000 m asl) in the central Hajar. These high-relief, high-gradient uplands give rise to landforms relating to fluvial and hill slope process regimes.

The Hajar are drained by systems of narrow *wadis* (typically ephemeral rivers) which range from being boulder- to sand-bedded channels (Zwemer, 1907). In their mountainous catchment settings, sequential periods of aggradation and incision have produced complex systems of terraces which preserve deep valley-fill sequences (e.g. Al-Farraj and Harvey, 2000), as well as small, steep tributary-junction fans (Al-Farraj and Harvey, 2005). These wadi systems drain roughly eastwards and westwards from the central spine of the Hajar, following the range's arcuate curvature.

Where the Hajar wadis emerge at mountain fronts, they have formed substantial alluvial fans. Predominately, the fans of the Hajar are the result of fluvial processes as they are comprised of the sheet flood and channelised gravel-sand deposits formed by avulsing, braided streamflow (Al-Farraj

and Harvey, 2005; Blechschmidt et al., 2009; Mueller et al., 2022). Thus, they are more likely to present sequences with litho-facies resembling 'Scott type' fans (Fig.2.4a; Harvey, 2011). Typically, they are telescopic forms whereby they prograde in an active lobe downstream of an intersection point (Al-Farraj and Harvey, 2005). This means that the feeding channel forms a trench in the upper sections of the fan, dissecting a relict surface, before emerging onto the fan surface in its medial-distal reaches and depositing sediment via overbank processes (e.g. Fig.2.6f; Hooke, 1967).

These fans coalesce to form extensive low-gradient bajadas that radiate from the mountain fronts as gravel plains. The two main bajadas have formed in the continental interior of the mountains as well as within their arcuate curve. In the interior, fans range from the smaller (10^1 km^2) and highly urbanised features of the north-western UAE (Fig.2.6a) to the large megafans (10^4 km^2) of the southern Hajar in central Oman (Fig.2.6b; Al-Farraj and Harvey, 2005; Blechschmidt et al., 2009). Interior fans terminate in the Rub' al Khali basin, although often their distal extremities have become obscured by more recent dune migration.

On describing the Bedouin people, the historical nomadic inhabitants of the Arabian Peninsula, Thesiger (1950b) describes the interior bajada situated between the mountains and the dunes of the Rub' al Khali:

> *"[The Bedouin] live in the desert… in country which, judged by ordinary standards, is waterless. This applies to the equally barren, broken limestone mountains near the southern coast, the flat, featureless gravel plains, and to the sands of the Empty Quarter itself…"*

This description by Thesiger of a place which is 'waterless' by 'ordinary standards' is somewhat ironic, given the formation of these features by fluvial processes. The Hajar mountain-front fans preserve extensive geomorphological evidence of a more intense hydrological regime in the past. For example, in their distal settings, the interior fans preserve the remnants of freshwater wetlands and lakes (Parker et al., 2006; Rosenberg et al., 2012; Parton et al., 2013), typical of the low-energy hydrological environments associated with the terminations of fluvial fans (Fig.2.4b; Moscariello,

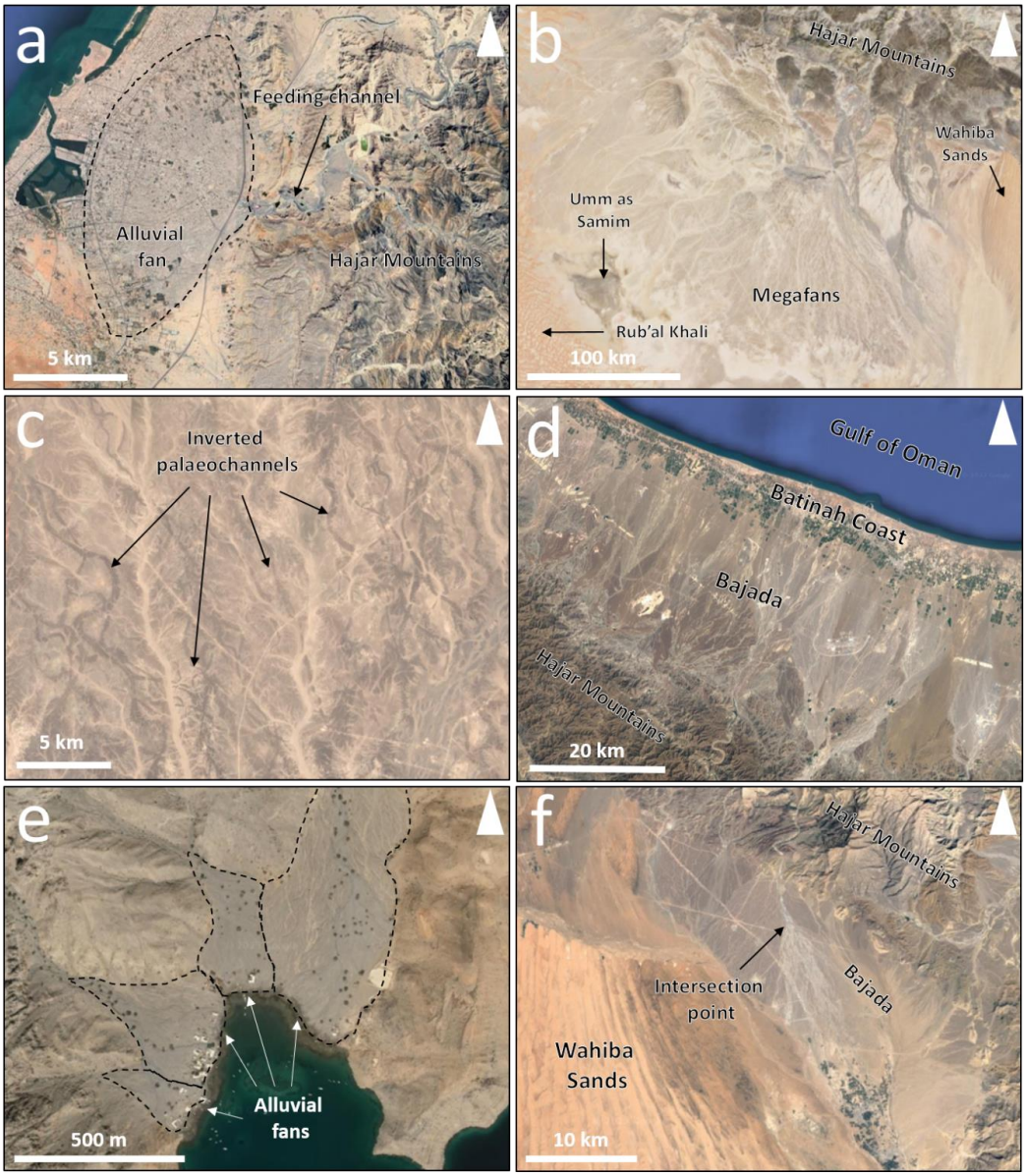

Figure 2.6. The alluvial fans of the Hajar Mountains. **(a)** The urbanised fan at Ras Al-Khaimah in the north-western UAE forming part of the northern interior bajada. **(b)** The large megafans of central Oman extending westwards to the Rub' al Khali and Umm as Samim and south-eastwards to the Wahiba Sands. **(c)** Inverted sinuous palaeochannels preserved on the megafans shown in **(b)**. **(d)** The bajada along the Batinah Coast, draining north-eastwards from the Hajar Mountains. **(e)** The smaller coastal fans forming in the rocky inlets of the Musandam Peninsula in the northern Hajar. **(f)** The fans situated between the Hajar Mountain front and the Wahiba Sands in the south of the range. This image shows an example of a fan prograding telescopically beyond an intersection point. Imagery from Google Earth Pro.

2018). The large megafans of the southern Hajar also preserve sinuous, inverted palaeochannels on their surfaces, the product of the exhumation of channel fill deposits by the fluvial and aeolian stripping of surrounding, more erodible sediments (Fig.2.6c; Maizels and McBean, 1990).

The second main bajada forms the Batinah Coastal Plain which has developed between the eastern Hajar Mountain front and the Gulf of Oman coastline in northern Oman (Fig.2.6d). Mountain-front alluvial fans are also apparent in the coastal setting of the rocky inlets of the Musandam Peninsula to the north (Fig.2.6e), as well as along the axial river setting of Wadi Batha north of the Wahiba Sands to the south (Fig.2.6f).

Modern climate and hydrology

South-east Arabia's climate is today characterised by aridity and hyper-aridity. However, considerable temporal and spatial variability exists within this, especially in the Hajar Mountains. Convective storms generate short-lived and sporadic rainfall events, but are most likely to occur in summer (Kwarteng et al., 2009). More sustained precipitation is the product of three main seasonal rain-bearing systems: 1) the Indian Ocean Monsoon during the summer, 2) westerly Mediterranean depressions during the winter and, 3) tropical cyclones in the Arabian Sea. These are summarised as follows:

Indian Ocean Summer Monsoon (IOSM): a seasonally-reversing system of rain-bearing, onshore winds which blow from the southern Indian Ocean towards the coastlines of Oman and western India during summer months (Fig.2.7a). In Oman, the summer monsoon rainfall which falls on the southern coastal plains and uplands is called khareef (*autumn*). The Hajar Mountains also receive some monsoon rain, although this is more limited compared with southern Oman (Babikir, 1985). The winds reverse during winter, blowing towards the southern Indian Ocean (Fig.2.7b). The system is driven by the pressure cells generated by the land-sea thermal contrast which exists between the Indian Ocean and the Indian sub-continent (Molnar et al., 1993).

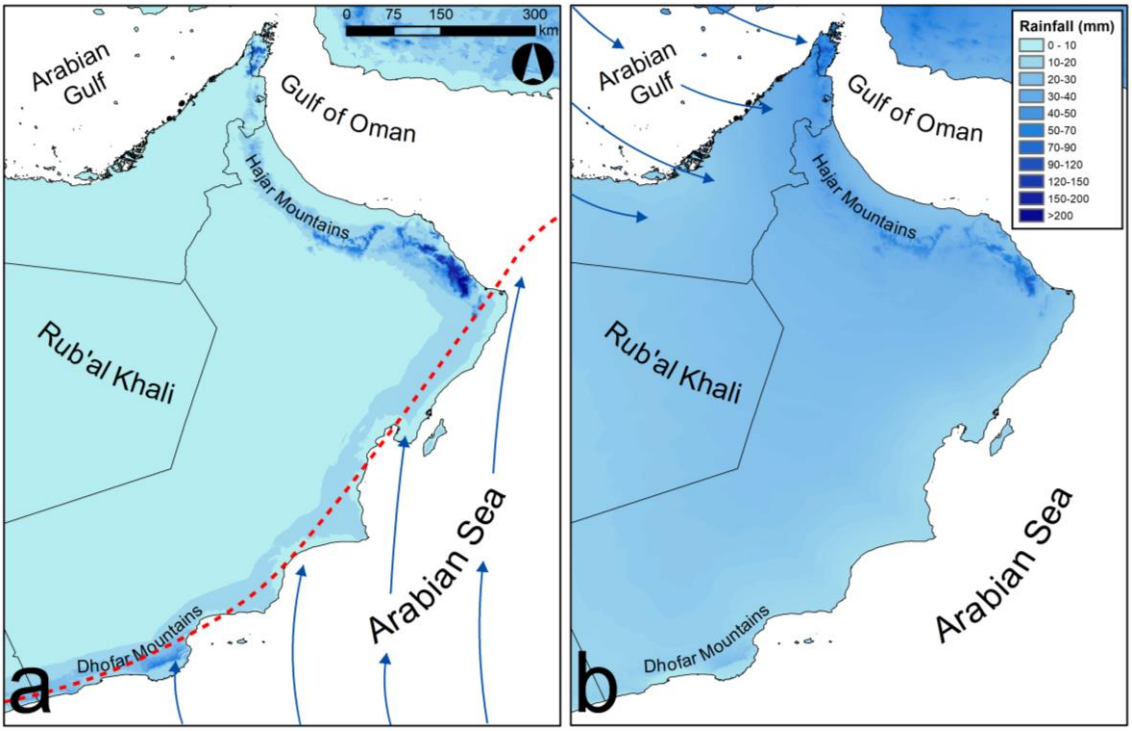

Figure 2.7. Average monthly rainfall over south-east Arabia during: **(a)** June, July and August and **(b)** January, February and March from 1970-2000. **(a)** Shows the concentration of precipitation along the southern coast of Oman and the Hajar Mountains in response to the IOSM, the onshore direction of which is denoted by the blue arrows in the Arabian Sea. The red dashed line denotes the approximate position of the inter-tropical convergence zone (ITCZ), although paradigm of the coupling between the ITCZ and monsoon rain belt may be overly simplistic (e.g. Nicholson, 2018). **(b)** Shows the dominance of the MLWs from November-April, bringing rainfall to the north-eastern part of the region as denoted by the blue arrows. The ITCZ retreats to the southern Indian Ocean during winter months due to the reversal of the monsoon winds. Data from WorldClim 2 (Fick and Hijmans, 2017).

Mid-latitude westerlies (MLWs): during winter months, MLWs drive the migration of extra-tropical cyclonic depressions eastwards from the Mediterranean to the Arabian Gulf region (Weyhenmeyer, 2000; Saeed and Almazroui, 2019). These storms track into the Hajar Mountains, bringing precipitation to mountain catchments (Fig.2.7b; Fryberger et al., 2016). Known as *seif* rains, these systems can extend as far as central and southern Oman (Kwarteng et al., 2009).

Arabian Sea tropical cyclones (ASTCs): rainfall is also provided to the south and east of the region, principally the Hajar Mountains and southern coastline of Oman, by tropical cyclones which track westwards across the Arabian Sea and Gulf of Oman (Kwarteng et al., 2009). The Arabian Sea has

two main cyclone seasons: from May-June and October-November with the highest occurrence likelihood in June, however these systems have high inter-annual variability (Soltanpour et al., 2021). Tropical cyclones bring short lived periods of high rainfall, often triggering flash flooding in the Hajar Mountains (e.g. Terry et al., 2022).

Mountainous areas in south-east Arabia are much wetter than interior lowlands. The southern uplands of Dhofar and the Salalah coastal plain receive rainfall from the IOSM concentrated in June-August, resulting in the highest absolute recorded monthly precipitation in south-east Arabia (60-70 mm; Kwarteng et al., 2009). However, in terms of average yearly rainfall, the highest amount is recorded at Sayq in the Hajar Mountains (330.15 mm yr^{-1}), compared to 184.58 mm yr^{-1} for the Dhofar Mountains (Kwarteng et al., 2009).

The relatively high amount of rainfall received by the Hajar Mountains, compared to other areas of south-east Arabia, has important implications for regional hydrology, biodiversity and human settlement. Travellers to south-east Arabia have noted the Hajar as climatically and environmentally exceptional relative to more arid lowlands. Following an ascent of Jebel Akhdar whilst staying in the village of Saik in the central Hajar, Miles (1901) wrote:

"I had hardly returned to my cottage… when a violent thunderstorm with hail and heavy rain burst upon us and lasted for some time. The rain on the rocky plateau above soon concentrated in the watercourses, and the tumultuous cascades that began to tumble down the steep walls of the chasm afforded a fine spectacle. The people informed me they had already had several smart showers, and that there was generally a fair amount of rain during the monsoon".

Ephemeral wadi activation in response to Hajar rainfall is a common occurrence. Events such as that witnessed by Miles (1901) occur during winter months as a result of MLW rainfall, or in summer from intense convective storms and the onshore monsoon winds. However, they are unlikely to transmit downstream to the mountain fronts due to rapid transmission loss (Shahin, 2007). Groundwater also plays a key role in generating streamflow in the Hajar, with the few perennial stream systems being maintained by springs rather than direct meteoric input for most of the year.

However, these springs are not independent from climate as they are recharged by meteoric rainfall events in both winter and summer months (Stanger, 1986). Miles (1901) also described the interplay between groundwater, rainfall events and topography in Hajar fluvial systems:

> *"… Wadi Semail is fed by innumerable springs and rivulets, and is swelled after rain by the tributary, but transient streams poured into it by the ravines and torrents… The source of the river is in Jebel Akhdar, and the flow is intolerably fast, but without any sudden falls to Semail, from whence the descent is more slow and gradual."*

The reference to Jebel Akhdar by Miles is significant. Elevation is a strong control on precipitation in south-east Arabia, with the high amounts of rainfall occurring in the Hajar at least in part due to the orographic effect they exert as a topographic barrier. For example, Muscat, located at sea level, received average annual rainfall of 75 mm yr^{-1} whereas Jebel Akhdar received an average of 250-400 mm yr^{-1} between 1977-2003, attributable to its elevation between 400-3000 m asl (Kwarteng et al., 2009). This is important for the region's flora and fauna, with the Hajar being a significant area of endemism in south-east Arabia (Ghazanfar, 1992; Patzelt et al., 2014; Mateiciucová et al., 2023).

2.4 Late Quaternary climatic and environmental change in south-east Arabia

There are two broad strands of information from which inferences of past climatic and environmental variability can be made in south-east Arabia. These are 1) marine cores and speleothems which provide proxies of palaeoclimate change and, 2) geoproxies which provide often noisier signals of past environmental change at much smaller spatial scales (Fig.2.5). Palaeoclimate archives preserve signals which often relate more directly to past climate change, such as biological or isotopic proxies, whereas palaeoenvironmental archives from geoproxies preserve sedimentary signals related to the often more complex controls on landforms of which climate may be one. This non-linear relationship between climatic forcing and the resulting response of sedimentary systems can result in signal 'shredding', whereby higher frequency signals are less likely to be preserved in the record (Jerolmack and Paola, 2010). Teasing out inferences of what signals are preserved in

geoproxies therefore requires careful interpretation of their geomorphological contexts (e.g. Thomas, 2013; Walsh et al., 2022b).

This section will outline the palaeo-records which currently exist in the literature for south-east Arabia, firstly from Arabian Sea marine cores and speleothem from northern and southern Oman, and, secondly, from alluvial deposits across the Hajar Mountains.

2.4.1 Marine cores and speleothem: palaeoclimate archives of IOSM variability

The climate of south-east Arabia has varied over Quaternary timescales, including periods of considerably greater rainfall than today. High-resolution palaeoclimate archives show evidence of periodic northwards migrations and intensifications of the IOSM which are precessionally-paced (~23 ka), driven by insolation maxima (Berger and Loutre, 1991).

Marine cores from the Arabian Sea record isotopic, sedimentological, geochemical and biological proxies at high temporal resolution, providing long records of climatic change throughout the Quaternary. These proxies evidence periods of higher biological productivity in the Arabian Sea, reduced terrigenous sediment flux and higher rainfall during precessional maxima (Fig.2.8). These changes in proxies through time have been attributed to the northwards displacement and intensification of the monsoon rain belt over the Arabian Sea (e.g. Sirocko et al., 1993; Cullen et al., 2000; Clemens and Prell, 2003; Ziegler et al., 2010; Caley et al., 2011; Fig.2.8).

There are also two speleothem records from Oman. The Hoti Cave speleothem, located in the central Hajar Mountains, extends over ~330 ka (Fig.2.5; Neff et al., 2001; Burns et al., 2001; Fleitmann et al., 2003b). The Qunf Cave speleothem located in southern Oman, by contrast, only spans the last ~10 ka (Fleitmann et al., 2003a; Fleitmann and Matter, 2009). Speleothem growth rings are formed as calcium carbonate precipitates out of groundwater percolating into caves in karst landscapes. Periods of higher rainfall result in periods of greater speleothem growth and they can be reliably dated using U-series techniques (e.g. Dayem et al., 2010). The isotope $\delta^{18}O$ is the most widely used

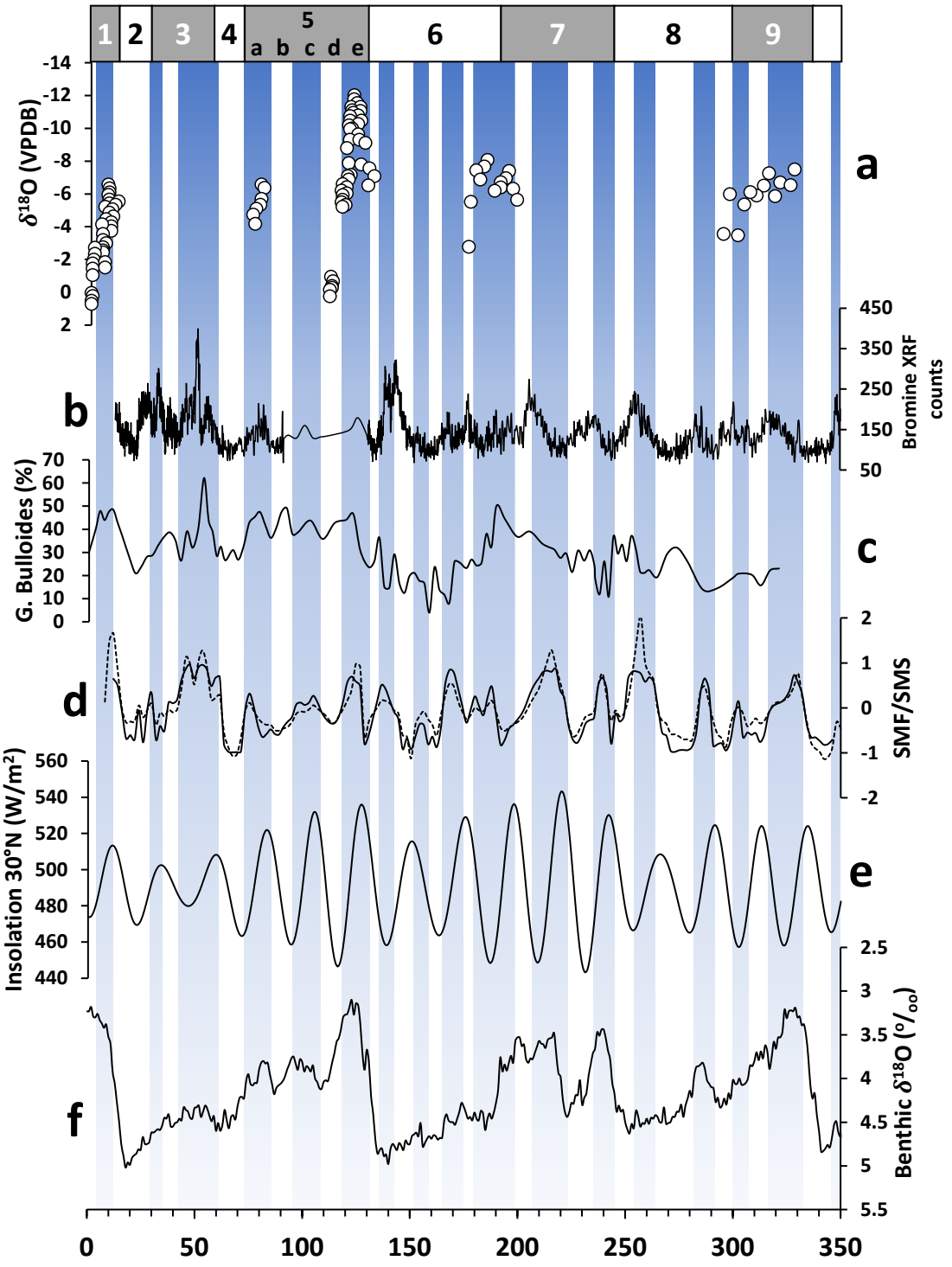

Figure 2.8. Palaeoclimate data from south-east Arabia. **(a)** The Hoti Cave speleothem record (Fleitmann et al., 2003b). Examples of marine core proxies from the Arabian Sea: **(b)** bromine XRF counts (Ziegler et al., 2010), **(c)** percentage of G. Bulloides (Anderson and Prell, 1993), **(d)** the Summer Monsoon Factor (SMF; solid line) and Summer Monsoon Stack (SMS; dashed line) composite proxies (Clemens and Prell, 2003). **(e)** Summer insolation at 30°N (Berger and Loutre, 1991). **(f)** LR04 global benthic δ18O stack (Lisiecki and Raymo, 2005). Blue bars denote peaks in IOSM rainfall based on the Hoti Cave speleothem record and the SMF/SMS record from the Arabian Sea, after Caley et al. (2011).

speleothem proxy for reconstructing past precipitation. The isotopic composition of groundwater entering caves is often in equilibrium with precipitation, as is the case in both Hoti and Qunf Caves (Fleitmann and Matter, 2009). In the context of south-east Arabia, the concentrations of precipitate δ^{18}O are strongly controlled by the moisture source: either from the Indian Ocean (via the IOSM) or the Mediterranean (via the MLWs; Nicholson et al., 2020). More negative δ^{18}O values indicate the dominance of the Indian Ocean source, whilst less negative values indicate the northerly, Mediterranean source (Fleitmann and Matter, 2009). For a detailed recent review of the analysis and interpretation of speleothem in Arabia, see Nicholson et al. (2020).

The speleothem record of south-east Arabia shows: 1) periods of increased rainfall (based on the rapid precipitation of growth layers) and, 2) that during these periods of increased rainfall, the Indian Ocean was the principle moisture source (based on more negative δ^{18}O values; Burns et al., 2001; Fleitmann et al., 2003b; Nicholson et al., 2020). Throughout the last 350 ka the periods of more intense IOSM precipitation in southeast Arabia align with periods of IOSM intensification recorded by the marine proxies, driven by insolation maxima (Fig.2.8).

The speleothem record is not simply a product of precessional variability, however. Nicholson et al. (2020) show that periods of more intense rainfall recorded in the Hoti Cave speleothem align with global ice volumes as they show close correspondence with global benthic δ^{18}O data recording northern hemisphere glacial variability (Lisiecki and Raymo, 2005; Fig.2.8).

Hoti Cave records higher IOSM rainfall centred at ~310 ka or within Marine Isotope Stage (MIS) 9c, 200 ka (MIS 7), 130 ka (MIS 5e), 80 (MIS 5a) and 10-6 ka (MIS 1; the Early-Mid Holocene; Fleitmann et al., 2003b; Fig.2.8). Mukalla Cave in southern Oman also records an intensification of the IOSM during the Early Holocene (Fleitmann et al., 2003a). During intervening periods of insolation minima or higher global ice volume, these speleothems show a reduction or a paucity of calcite accumulation as well as less negative δ^{18}O values, indicating a less intense, more southerly IOSM rain belt and the dominance of a Mediterranean, MLW-driven moisture source (Fleitmann and

Matter, 2009). For example, between 10.1-6.3 ka, the Hoti Cave speleothem has an isotopic composition indicative of a southern moisture source with highly negative $\delta^{18}O$ values (relative to present), with a mean of -4.78 $^{0}/_{00}$ VPDB. Between 6.3-5.2 ka, the isotopic composition was less negative than during the 10.1-6.3 ka period (-3.2 $^{0}/_{00}$ VPDB), but still more negative than present (-2.1 $^{0}/_{00}$ VPDB) which indicates the increasing proportion of winter rainfall delivered by MLWs to groundwater composition and the waning of the IOSM's contribution (Fleitmann et al., 2022).

Based on the highest resolution speleothem data from the Holocene, the latitudinal shifts of the IOSM rain belt were time-transgressive processes. The onset of wetter conditions occurred earlier at lower latitudes, with increasingly more negative $\delta^{18}O$ values recorded during the Terminal Pleistocene (~12 ka) from Moomi Cave on the island of Socotra (located off the southern coast of Arabia; Van Rampelbergh et al., 2013). The Qunf and Hoti Cave speleothem do not show more negative $\delta^{18}O$ values until later, with the onset of wetter conditions at Hoti (the most northerly of the speleothem) lagging behind Qunf by ~400 years (Fleitmann and Matter, 2009). Hoti Cave then displays a rapid decrease in IOSM rainfall at ~6.3 ka whereas the decline in IOSM rainfall in the Qunf record is more gradual, showing the progressive displacement of the monsoon rain belt to more southerly latitudes (Fleitmann and Matter, 2009).

Whilst the speleothem record does corroborate the majority of periods of increased IOSM intensity visible in the marine records from the Arabian Sea over the last 350 ka, there are notable periods which do not record higher rainfall. For example, peaks in monsoon intensity in line with insolation maxima centred at ~100 ka (within MIS 5c) and ~50 ka (within MIS 3) do not have the corresponding rapid speleothem growth or highly negative $\delta^{18}O$ values associated with other insolation peaks (Fig.2.8). A potential reason for this could be the precipitation threshold needed to trigger speleothem growth which has been estimated for Hoti Cave to be >300-350 mm yr^{-1} (Fleitmann et al., 2011). Therefore, lower amplitude increases in precipitation may not be preserved in the record. The scale of the speleothem record preserved should also be considered. Caves with

smaller contributing catchments may only record periods with the highest precipitation levels, whereas caves with larger catchments may amplify the signal of smaller relative increases in rainfall (Sorin et al., 2010).

2.4.2 Geoproxy records in the Arabian Peninsula and the Hajar Mountains

Alongside these high-resolution palaeoclimate records, geoproxies permit the reconstruction of hydrological variability at smaller spatial scales (Thomas, 2013). This is crucial for understanding *landscape* change in drylands such as south-east Arabia. In turn, this is important for resolving thresholds of response to external forcing and building a picture of past environments relevant for establishing the context of palaeobiogeographical and anthropological dynamics (Bull, 1991; Parton et al., 2015b).

In dryland contexts where biological and isotopic proxies are often rare relative to temperate environments due to poor preservation and low amounts of pollen production, geoproxies have provided crucial information about hydro-climatic variability throughout the Late Quaternary. South-east Arabia has a growing number of records for which luminescence and radiocarbon dating facilitate absolute chronologies (Fig.2.9). These records include: palaeolakes and wetlands (e.g. Fuchs and Buerkert, 2008; Rosenberg et al., 2012; Parker et al., 2016), coastal deposits such as beach ridges, mangroves and sabkha (e.g. Zander et al., 2007; Berger et al., 2013; Beuzen-Waller et al., 2019), dunes (e.g. Goudie et al., 2000; Preusser et al., 2002; Leighton et al., 2013), spring deposits such as tufas (e.g. Clark and Fontes, 1990; Mervine et al., 2015) and alluvial fan and river deposits (e.g. Blechschmidt et al., 2009; Parton et al., 2015a; Beuzen-Waller et al., 2022).

Synthesising complex landform records can be challenging due to issues of scale, sampling biases and the reliability of the geochronological data which underpin them often making them appear seemingly contradictory, especially when compared to regional-scale palaeoclimate archives (Thomas, 2013). Despite these issues, synthesising these records in a way which is sensitive to considerations of their specific contexts and controls as well as critical of their chronological data

has been shown to be useful for interpreting environmental variability at the landscape scale (e.g. Thomas and Burrough, 2012; Thomas and Burrough, 2016; Small et al., 2017; Walsh et al., 2022b). There have been previous syntheses of palaeoenvironmental data from south-east Arabia and the Arabian Peninsula more broadly (e.g. Glennie and Singhvi, 2002; Parker and Goudie, 2008; Preusser, 2009; Preston and Parker, 2013; Lézine et al., 2014), however they did not have the benefit of the wealth of legacy data now available from geoproxy records.

As such, there has been a prevailing narrative of the Arabian Peninsula being either 'wet' or 'dry' at certain periods of the Late Quaternary, based on the large-scale of the palaeoclimate archives outlined in Section 2.3.1. However, this broad, binary narrative is being challenged by a growing body of ecological and archaeological data which suggests the existence of hydro-climatic refugia during more arid intervals of the Quaternary (Fig.2.5; e.g. Rose et al., 2019; Petraglia et al., 2020; Bretzke et al., 2022; Mateiciucová et al., 2023). The Hajar Mountains have been suggested to be a refugia, based on archaeological finds at the Jebel Faya rock shelter, located on the interior Hajar bajada, which do not date to periods of Hoti Cave speleothem formation (Fig.2.5; e.g. Armitage et al., 2011; Bretzke et al., 2022). These hypotheses have important implications for debates around hominin demographic shifts and occupation within dryland contexts, with Arabia situated at the 'crossroads of continents' between Africa and Eurasia (Petraglia et al., 2015). Therefore, there is a need to reassess legacy and more recent geoproxy data to permit inter-regional comparisons of palaeoenvironmental change for Arabia and move beyond the binary narrative of large scale palaeoclimate archives. This rationale informs the objectives of Chapter 6 (Section 1.2).

Although few date to the last 20 ka (Fig.2.9), Hajar alluvial fan deposits form a key geoproxy record in south-east Arabia throughout the Late Quaternary. As discussed in section 2.2.1, the dominant

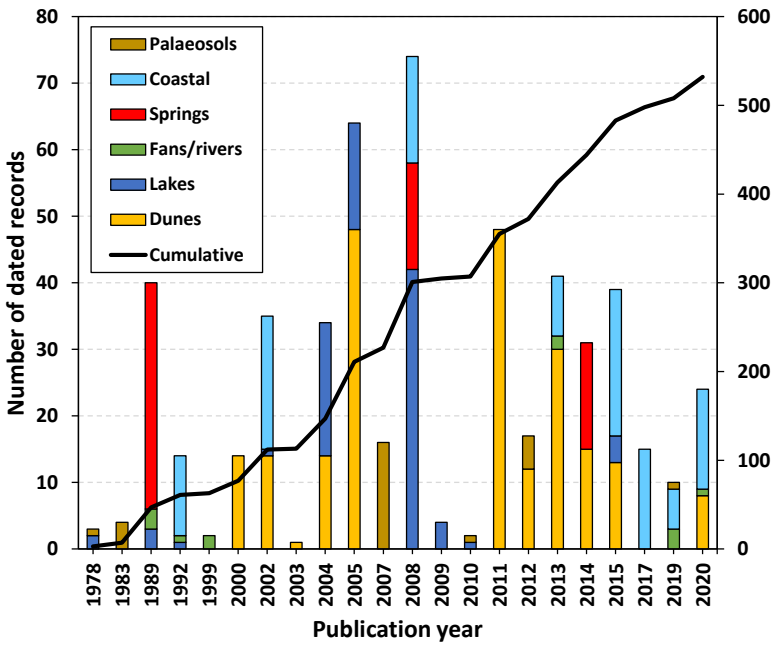

Figure 2.9. The number of geoproxy records with either luminescence or radiocarbon chronologies within 0-20 ka published in south-east Arabia.

signal preserved by Hajar alluvial fan sediments appears to be Quaternary climatic variability (Al-Farraj and Harvey, 2000). Over the last 300 ka, the key aggradation periods which have been identified in the literature are ~240-200 ka, 160-150 ka, 130-75 ka, 60-40 ka and 12-6 ka (Table 2.2). Within the 130-75 ka period (MIS 5), fan aggradation ages typically fall during either 135-120 ka (MIS 5e) or 90-75 ka (MIS 5a). These periods correspond with periods of increased IOSM rainfall, as shown in the previously discussed marine and speleothem records (e.g. Fleitmann et al., 2003b; Caley et al., 2011). A model of fan aggradation being driven by precessionally-paced increases in IOSM rainfall as a result of insolation maxima has, therefore, been established in the literature (Parton et al., 2015a).

Table 2.2. Summary of the previous studies using Hajar alluvial deposits as geoproxies with the key aggradation periods dated and the inference of the original authors based on chronological and sedimentary evidence. The 14C ages of Dalongeville (1999) have been re-calibrated using the IntCal20 calibration curve (see Section 3.4 for more details).

Reference	Location	Geomorphological setting	Dating technique	Type of deposit	Aggradation period(s)	Climatic/environmental interpretation
Dalongeville (1999)	Mleiha, UAE	Northern interior bajada	^{14}C (shells)	Fluvial silts, incised by modern channel.	5.8-4.7 cal ka BP	Increased flow conditions, wetter than present during Mid-Holocene.
Preusser et al. (2002)	Wahiba Sands, Oman	Southern interior bajada (underlying dunes)	OSL	Fluvial sands and conglomerates underlying aeolian deposits (aeolian deposits were dated using OSL).	>100 ka	Increased flow conditions during MIS 5e (130-120 ka).
Blechschmidt et al. (2009)	Southern Hajar megafans, Oman	Southern interior bajada	OSL	Fluvial sands preserved in different levels of fan terraces.	45 ka 200-240 ka 320 ka 410 ka 750-600 ka 900-800 ka	Increased flow, wetter than present during mid-MIS 3, MIS 7, MIS 9 and MIS 11. Ages older than 500 ka are difficult to interpret due to large uncertainties. Most likely drivers of wetter conditions are interglacial conditions and peaks in IOSM rainfall.
Farrant et al. (2012)	Remah, UAE	Northern interior bajada	OSL	Fluvial sands.	60-50 ka	Increased flow, wetter than present during early MIS 3.
Parton et al. (2013)	Aqabah, UAE	Northern interior bajada	OSL	Distal fluvio-lacustrine silt-sands, interstratified with aeolian sediments (targeted for OSL dating to provide bracketing ages on lacustrine deposits)	~60 ka	Increased flow, wetter than present during early MIS 3. However, flow increases were still intermittent, shown by aeolian sediments interstratified with fluvio-lacustrine sediments.
Atkinson et al. (2013)	Tawi Asmar, UAE Al Ain, UAE	Northern interior bajada	OSL	Fluvial sands interstratified with aeolian deposits exposed at two sites.	Tawi Asmar: 12-13 ka 114-75 ka Al Ain: 130-115 ka 90-76 ka	Increased flow, wetter than present during MIS 5e, 5a and the Early Holocene. Flow likely seasonal rather than perennial, based on fining up sequences, but extended into the Rub' al Khali.
Parton et al. (2015a)	Al Sibetah, UAE	Northern interior bajada	OSL	Fluvial sands, floodplain deposits exposed in a quarry site through the fan's stratigraphy.	55 ka 130-75 ka	Increased flow, wetter than present during MIS 6, MIS 5 and early MIS 3. Phases of stream channel activation coincide with periods of soil and grassland development on fan surfaces.

					160-150 ka	
Hoffmann et al. (2015)	Wadi Mistal, Oman	Valley-fill, catchment draining towards Batinah Coast mountain front	OSL	Fluvio-lacustrine silt sands deposited in landslide-damned lake.	60-40 ka	Climate similar to present conditions in the Hajar, based on identification of 112 fining up sequences representing intense, intermittent rainfall events.
Moraetis et al. (2020)	Wadi Shkar, Oman	Valley-fill, catchment draining towards Batinah Coast mountain front	OSL	Fluvial sand unit within conglomerate material.	160 ka	Climate wetter than present, resulting in higher streamflow and fan aggradation during a short-lived wetter period in MIS 6.
Mueller et al. (2022)	Wadi Iddayyah, UAE Wadi Dhaid, UAE	Northern interior bajada	OSL	Fluvial sands across multiple sites along two wadi systems.	3.5-0 ka 20 ka 43-34 ka 160-135 ka	Increased flow, wetter than present during late MIS 3 and MIS 6, however aggradation likely occurred as the result of intermittent flow events during MIS 2 and the Late Holocene under arid to hyper-arid climates similar to present.
Beuzen-Waller et al. (2022)	Wadi Dishshah, Oman	Valley-fill, catchment draining towards interior mountain front	OSL/^{14}C (charcoal)	Fluvial sands from multiple sites along a wadi exposure.	2.8 ka 6.2-5.5 ka 11.3 ka 26.5 ka	The earliest events likely occurred under more arid conditions during MIS 2 and is indicative of high-energy streamflow. The Early Holocene deposit occurred at the transition from lower to higher rainfall. The Mid Holocene shows a decrease in streamflow, indicative of waning rainfall. During the Late Holocene, the system becomes characterised by deposition as a result of intense, short-lived flood events.

Thomas (2013) established five principles for utilising geoproxies to their fullest potential in investigations of Quaternary palaeoenvironmental and climatic change:

1. Drawing on modern process studies to inform interpretations of relict landforms;
2. Ensuring they are underpinned by the highest-quality geochronological data;
3. Interpreting landforms in terms of their site-specific contexts;
4. Integrate multiple records across a landscape, rather than just individual sites;
5. Careful comparison between geoproxies and other palaeoenvironmental and climatic records.

Alluvial fan and river deposits in the Hajar are ideally suited to meeting these criteria. Firstly, there has been a large body of work focused on the interpretation of alluvial sedimentary stratigraphy based on both modern and palaeo-studies in many different settings (e.g. Miall, 1977; Blair and McPherson, 1994; Harvey et al., 1999; Hartley et al., 2010). Secondly, numerous studies have demonstrated the applicability of luminescence techniques to date aggradation periods from the coarse sand deposits of Hajar alluvial systems (e.g. Blechschmidt et al., 2009; Parton et al., 2015a; Hoffmann et al., 2015). The characteristics of the region's dose rates (to be discussed in more detail in Section 3.2.2) means that it is possible to calculate very old ages in some locations, permitting very long records to be established (>300 ka), although large uncertainties make it difficult to interpret these ages (e.g. Blechschmidt et al., 2009; Table 2.2). The alluvial fans and valley-fill sequences of the Hajar are also spatially extensive, offering an opportunity to integrate records from numerous sites.

Lastly, when compared to the Hoti Cave speleothem record, Hajar alluvial fans appear to preserve signals of higher rainfall over their catchments during periods not preserved in the speleothem record. For example, numerous fans record aggradation from 60-40 ka (MIS 3; e.g. Blechschmidt et al., 2009; Farrant et al., 2012; Parton et al., 2015a; Mueller et al., 2022; Table 2.2), a period of higher IOSM rainfall also captured in Arabian Sea marine cores (e.g. Clemens and Prell, 2003; Caley et al.,

2011; Fig.2.8). Parton et al. (2015a) suggest that this discrepancy is due to the proposed threshold of 300-350 mm yr^{-1} of rainfall required to trigger speleothem growth in Hoti Cave (Nicholson et al., 2020). Based on this, they further suggest that Hajar fans are potentially more sensitive records to relatively lower-amplitude perturbations in regional climate than the Hoti Cave speleothem.

Despite the utility provided by the existing record from Hajar fan and river sediments, there are also challenges of interpretation. More recent data record aggradation events in channels during times of insolation minima and reduced IOSM precipitation in south-east Arabia, such as during hyper-arid MIS 2 and the Late Holocene (Table 2.2; Mueller et al., 2022; Beuzen-Waller et al., 2022). There are also other periods of time during which fan aggradation may be expected due to increased IOSM rainfall and other geoproxies, such as lakes, recording enhanced hydrological activity like 110-100 ka (MIS 5c; Rosenberg et al., 2012), yet are not captured in the existing alluvial record.

The existing record of alluvial aggradation in the Hajar is also spatially biased. Most of the prior work (six of the ten papers reported in Table 2.2) has been conducted on the mountain-front fans of the north-eastern UAE. Including the study by Blechschmidt et al. (2009) on the megafans of central Oman, then seven of the ten are located on the interior bajada, concentrated in the very northern and southern parts. Few studies have considered the signals preserved in catchment settings, the central interior bajada, or the Batinah Coast bajada located to the east of the Hajar Mountains (Fig.6d). This, along with the previous critiques, calls into question the wider spatial applicability of the precessionally-driven model of fan aggradation. There is also a growing pre-historic archaeological record of human occupation in the central Hajar (Parton and Bretzke, 2020), but a geoproxy record of hydrological conditions within the local landscape is, at present, non-existent. These considerations inform the research objectives of Chapter 4 (Section 1.2).

2.5 Non-climatic controls on Hajar fan morpho-dynamics

Based on the research compiled in the previous section, climate as a key control on fan aggradation in the Hajar Mountains has been long established. However, as outlined in Section 2.2.1., fans have

multiple different controls which contribute to their formation, morphology and long-term evolution. It is important to also consider these other controls, outside of climate, for the Hajar Mountain fans to build a more holistic understanding of landscape evolution in south-east Arabia.

Catchment morphology, geology, base-level change and ongoing long-term tectonic processes are all likely important for determining fan morphology in the region (Table 2.1). To date, the only quantitative investigation of fan-catchment morphological relationships in the Hajar Mountains was undertaken by Al-Farraj and Harvey (2005) in the Musandam region of the north-east UAE around Wadi al Bih. They collected data for both mountain-front and tributary junction fans in the region, showing that fan area and gradient were more strongly related to catchment area for fans formed at the mountain front, using the regression analysis approach discussed in Section 2.2.1 (Equations 2.1 and 2.2; e.g. Fig.2.2). They also showed that catchment geology was an important factor mediating these fan-catchment morphometric relationships through residual analysis (e.g. Fig.2.3).

Whilst fans do not appear to preserve a signal of long-term tectonics in terms of the timings of their aggradation phases, tectonics has been shown to be the main control on the availability of accommodation space for fan formation in the Hajar. For example, the interior foreland basin in which the western bajada's megafans have formed is controlled by the central forebulge axis of the Hajar (Rodgers and Gunatilaka, 2003), allowing larger, unconfined fans to develop in contrast to other mountain fronts where accommodation space is more limited.

Base-level variability is also likely to be an important factor in fan evolution, with many fans around the Hajar Mountains located adjacent to the Arabian Gulf and Gulf of Oman coastlines. Global sea levels have been variable throughout the Quaternary (e.g. Spratt and Lisiecki, 2016) and morphometric studies have shown that coastal fans record evidence of these changes in their distal morphology, for example becoming steepened and foreshortened as a result of sea-level rise (Harvey et al., 1999; Stokes and Gomes, 2020). Hajar fans are likely to be sensitive to sea-level variability as fluvial conglomerate deposits are reported to underly coastal deposits along the

Arabian Gulf and Batinah coasts, evidencing deposition during periods of lower sea levels (e.g. Macklin et al., 2012; Pain and Abdelfattah, 2015). Base-levels have also varied over the long-term where fans are located adjacent to axial drainage systems, influencing the incision and aggradation of fans grading to them (Scharf et al., 2019). The Hajar is also geologically complex, comprised of a variety of primarily carbonate and basaltic rock types resulting from various stages of uplift and exposure over the last ~100 ma since the Late Cretaceous (Searle, 1988). Catchment geology has been shown to be a key control on fan morphology in other settings (Table 2.1), so it is likely an important controlling factor across the Hajar beyond the local focus of Al-Farraj and Harvey (2005).

Al-Farraj and Harvey (2005) remains the only study of fan-catchment morphometric relationships for Hajar Mountain fans and, while useful, it is spatially limited to just a small portion of the overall mountain range. Therefore, it does not account for differences between the contrasting catchment, tectonic and depositional settings within which fans are situated along different mountain fronts around the Hajar (e.g. Fig.2.6). This necessitates the generation of a larger dataset of fan-catchment morphometric variables for the Hajar. Improvements in the accessibility and resolution of remote sensing data could serve as a viable means to achieve this, as has been demonstrated in other studies of the controls on fans which generate large datasets (>100 fans/catchments; e.g. Stokes and Gomes, 2020; Tomczyk, 2021; Morgan et al., 2022). These gaps in the literature inform the objectives of Chapter 5.

2.6 Key points from Chapter 2

In summary, the major points arising from the literature reviewed are:

- Alluvial fans have both passive (catchment and depositional setting) and active (base-level variability, climatic change and tectonics) controls. However, climate variability over Quaternary timescales seems to be the principal control in many dryland settings. They therefore have a lot of potential to act as geoproxies of past climatic and environmental variability from the sedimentary signals they preserve.

- The Hajar Mountains in south-east Arabia have been subject to periodic climate variability throughout the Late Quaternary due to changes in the latitudinal position and intensity of the IOSM.
- The extensive alluvial fans and valley-fills of the Hajar attest to periodic changes in rainfall over their mountain catchments, recording aggradation phases which align with periods of higher IOSM intensity shown in marine cores.
- There are, however, some problems with this model:
    - Fans and catchment settings also seem to record aggradation during times of reduced IOSM intensity in some locations, as well as some periods of increased IOSM intensity which are within dating limits not being recorded by previous work (e.g. ~100 ka).
    - Previous work has focused heavily on the northern and southern interior bajadas, despite the large spatial extent of alluvial sediments in the region.
- The non-climatic controls on Hajar alluvial fan morphology and evolution, such as catchment morphology, geology, depositional settings, base-level variability and tectonics are poorly constrained except for a small area in the north-west of the range. However, understanding these broader controls, outside of just climate, is fundamental for better explaining the long-term evolution of alluvial landscapes in south-east Arabia.
- The Hajar region of south-east Arabia, as well as the Arabian Peninsula more broadly, lacks syntheses of geoproxy data considering the complex controls on geomorphological systems and rigorous assessment of the quality of the geochronological data underpinning them. This is important for building landscape-scale palaeoenvironmental reconstructions and making comparisons between different regions, as has been implemented in other drylands.

3 | Methods

3.1 Introduction

This chapter will outline and justify the methods used to meet the objectives of this thesis. Methods will be outlined in three sections, in the order in which they are used, and detailed, in the research papers that make up chapters 4-6.

3.2 New records of fan aggradation from the central Hajar

3.2.1 Field sampling, site selection and location

The objective of Chapter 4, to produce new records of fan aggradation on the central interior and eastern parts of the Hajar to test its timing relative to increased IOSM precipitation, focusses on fieldwork conducted in Oman during January 2020.

As discussed in the literature review (Section 2.3.2), three spatial attributes exist within the previously published alluvial fan aggradation research in the Hajar region. Analyses have primarily focused on fans on the interior bajada, particularly on fans in either the very north (e.g. Gebel et al., 1989; Dalongeville, 1999; Farrant et al., 2012; Atkinson et al., 2013; Parton et al., 2013; 2015a; Mueller et al., 2022) or very south of the bajada (e.g. Maizels, 1987; 1990; Maizels and McBean, 1990; Blechschmidt et al., 2009; Fig.3.1a). By contrast, few studies have considered systems which drain eastwards towards the Batinah Coast and there are no studies of aggradation on the central interior bajada.

Considering these spatial attributes, this thesis targeted sites located in three under-sampled areas: 1) the interior central bajada, 2) catchment valley-fill settings and 3) the Batinah Coast bajada. Sites within each were chosen based on access and the exposure of sand-sized material for OSL sampling. Two main sampling locations were chosen following field reconnaissance and pre-fieldwork surveying of the region using Google Earth (Fig.3.1). On the east of the Hajar drainage divide, the lower reaches of Wadi Sahtan and the proximal setting of the Rustaq fan on the Batinah Coast. On the west of the Hajar drainage divide, proximal and medial-distal settings of the Ibri and Dhank fans

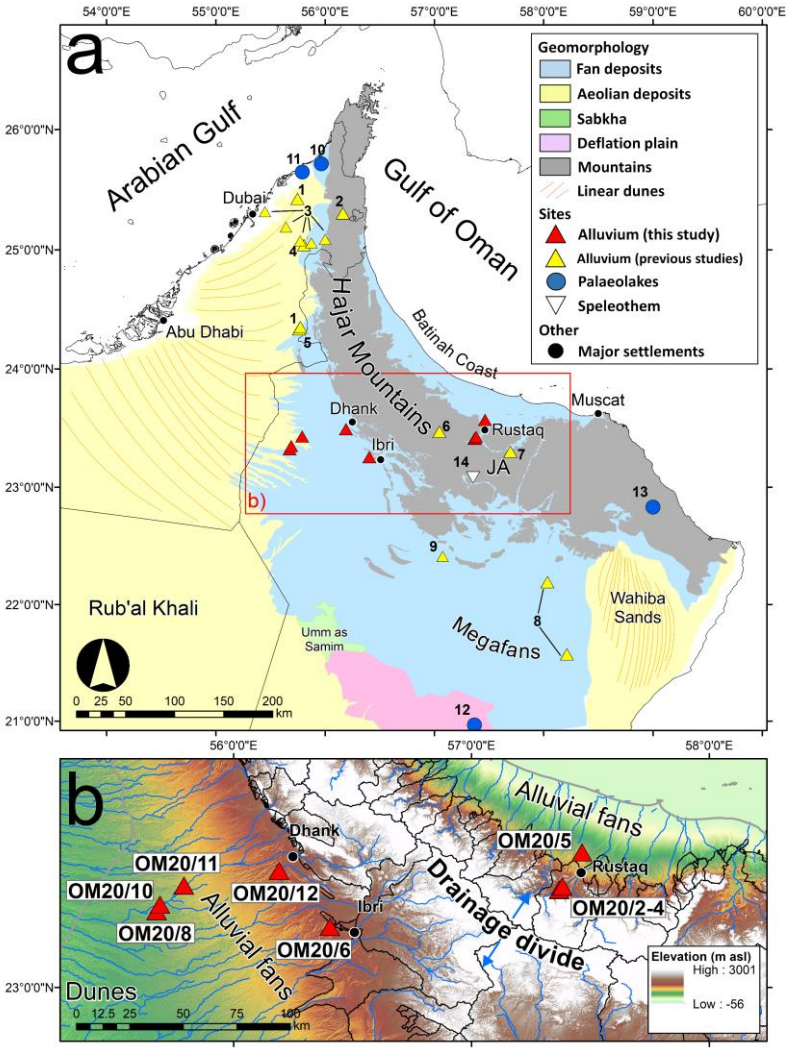

Figure 3.1. (a) The Hajar Mountains of northern Oman and the north-eastern UAE showing regional geomorphological features and key sites with previously dated alluvium using OSL and radiocarbon: 1: Atkinson et al. (2013); 2: Purdue et al. (2019); 3: Mueller et al. (2022); 4: Parton et al. (2013); 5: Parton et al. (2015a); 6: Moraetis et al. (2020); 7: Hoffmann et al. (2015); 8: Blechschmidt et al. (2009) and 9: Beuzen-Waller et al. (2022). Other regional palaeoenvironmental sites are shown, including palaeolake deposits from: 10: Parker et al. (2006); 11: Preston et al. (2015); 12: Rosenberg et al. (2012) and 13: Fuchs and Buerkert (2008), as well as 14: the Hoti Cave speleothem (Burns et al., 2001). 'JA' denotes Jebel Ahkdar. **(b)** The study sites both east (OM20/2-5) and west (OM20/6-12) of the Hajar drainage divide. Sites OM20/2-4 are valley-fill deposits along Wadi Sahtan in the lower reaches of the mountain catchment feeding the Rustaq fan. Sites OM20/5-12 are alluvial fan deposits. Major drainage networks and mountain catchments are delineated by the blue and black lines, respectively.

which form part of the central interior bajada were investigated.

Site descriptions

Wadi Sahtan and the Rustaq fan

Draining the primarily sedimentary rocks forming the western portion of Jebel Ahkdar in the central Hajar, Wadi Sahtan runs eastwards and exits these steeper uplands at the mountain front located near Rustaq. Under today's arid climate, the wadi does not flow for most of the year. However, winter rainfall from the north-west does result in seasonal channel activity which is most likely to occur in the upper reaches (Shahin, 2007). Near the apex of the Rustaq fan, Wadi Sahtan incises through thick alluvial valley fills, exposing sequences up to 20 m deep in the reach sampled. These expose interstratified units of fluvial material which range in size from fine silty-sand to large cobbles (up to 40 cm in length). Four sites were sampled in the lower reaches of the mountain catchment of Wadi Sahtan (OM20/2-4; Table 3.1; Fig.3.2a; Fig.3.3a, b).

Where Wadi Sahtan exits its mountain catchment at the mountain front near Rustaq, it forms a large, low gradient alluvial fan which extends ~36 km to the Arabian Sea coastline to the north-east, forming part of the Batinah Coast bajada. The relict surfaces of the fan are mantled with a well-developed desert pavement and it is incised with numerous smaller wadi systems. These form shallower sections than are found in the trenched upper part of the system, ranging from ~1-5 m. Exposures in the fan setting also show interstratified alluvial deposits of finer silty-sands and conglomerates, although the cobbles forming conglomerates show a reduction in particle size compared to those observed in the catchment. One site was sampled near the apex of the fan (OM20/5; Table 3.1; Fig.3.2a; Fig.3.3c).

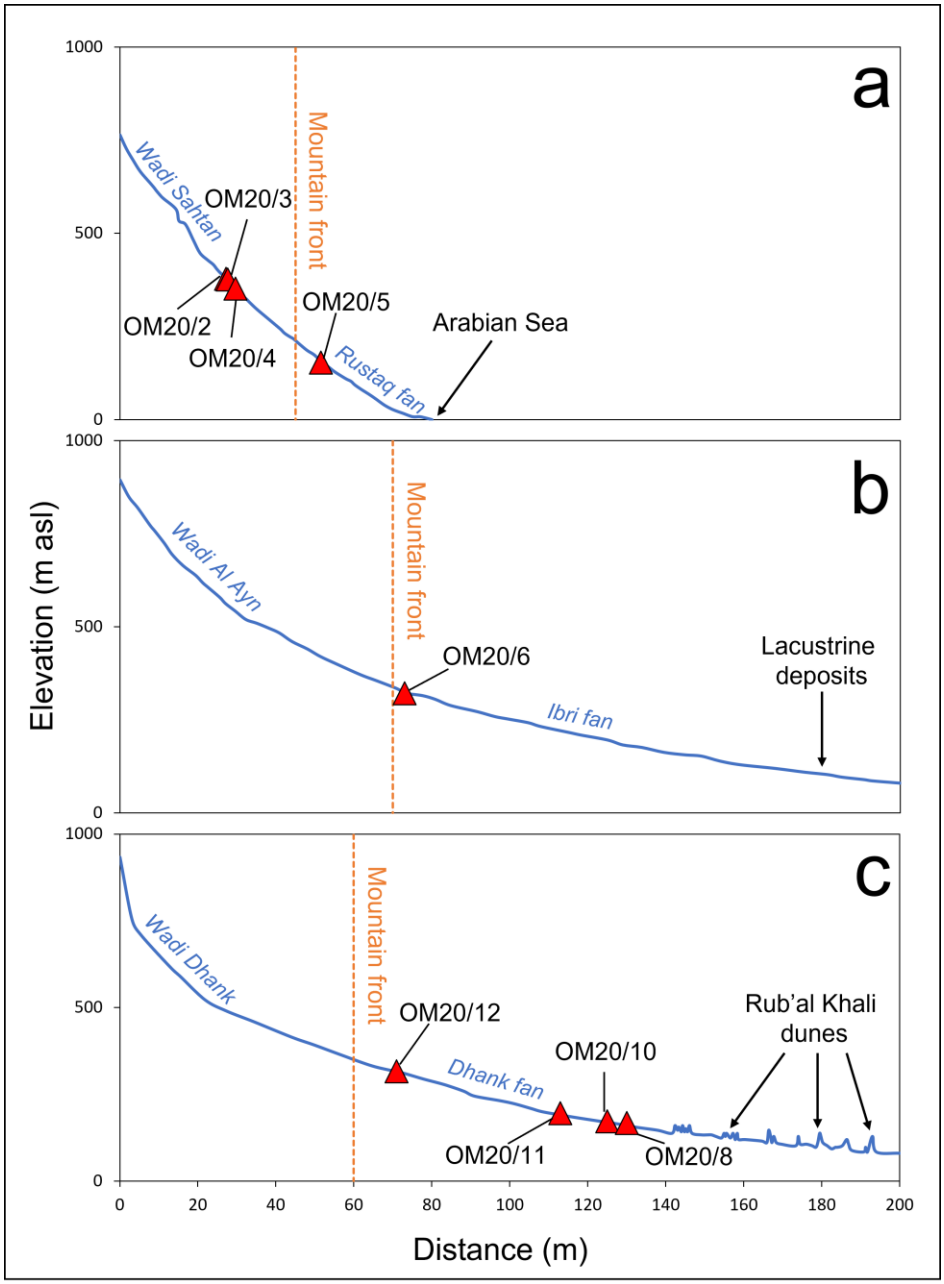

Figure 3.2. Elevation profiles and sampled sites along (a) Wadi Sahtan and the Rustaq fan, (b) Wadi Al Ayn and the Ibri fan and (c) Wadi Dhank and the Dhank fan.

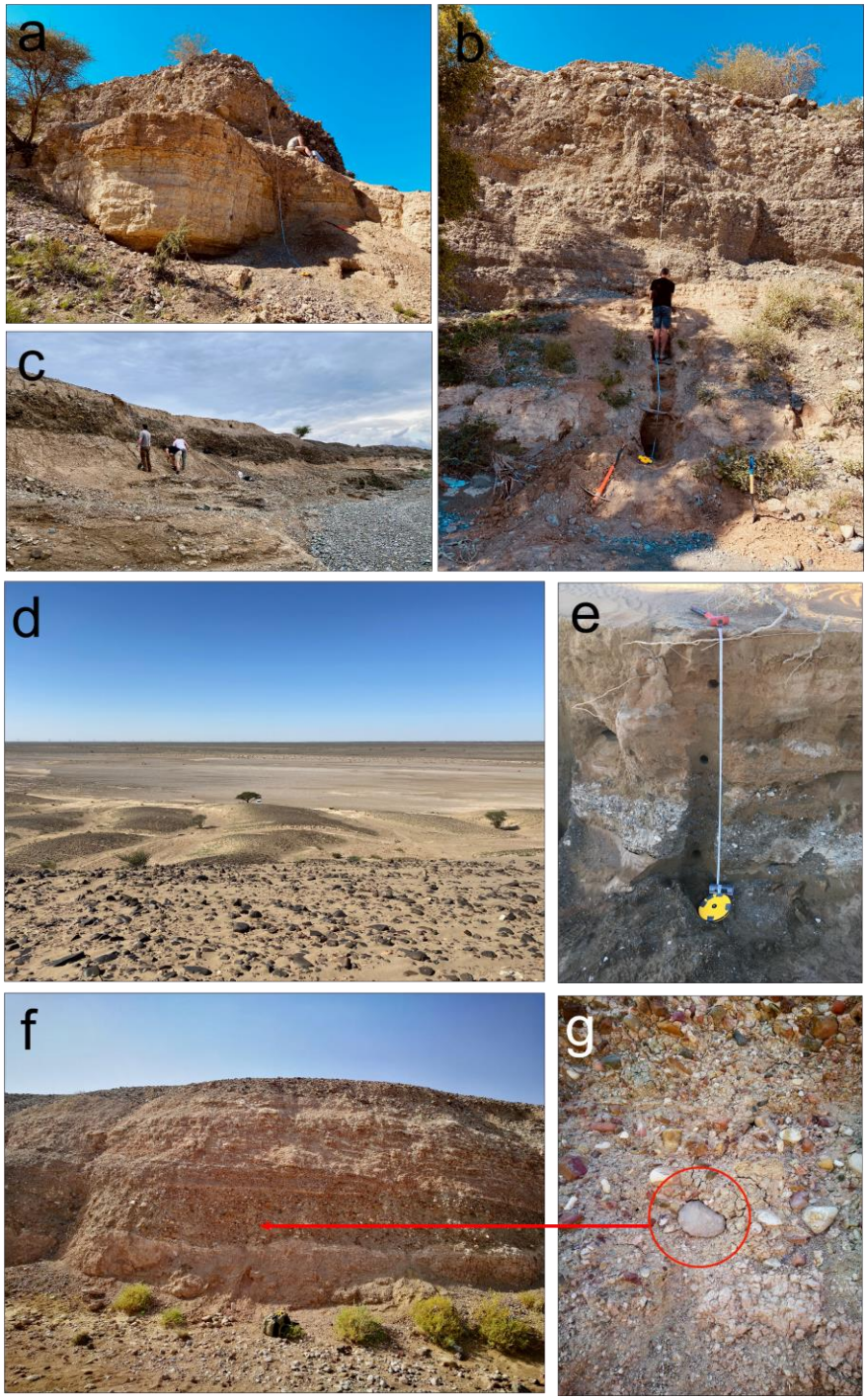

Figure 3.3. Fieldwork in January 2020. Images a-c were taken at sites along Wadi Sahtan and the Rustaq fan, images d-g on the Ibri and Dhank fans. **(a)** Site OM20/3 showing a basal unit of finely laminated, ponded sediments. **(b)** Site OM20/4 showing bedded gravels and cobbles comprising the upper conglomerates. **(c)** Site OM20/5 viewed laterally showing various braided channel fills bounded by floodplain deposits. **(d)** Looking out across the cobbled surfaces of the Ibri fan near its apex. **(e)** Site OM20/11 on the Dhank fan showing weakly bedded fluvial and aeolian sands overlying coarser channel deposits. **(f)** Site OM20/6 within the central channel fill unit of which (red arrow) a well-preserved pre-historic hand-axe was found **(g).**

The Ibri and Dhank fans

The sites on the interior central bajada are located on the large fans which emanate from the towns of Ibri and Dhank at the mountain front (Fig.3.3d). These fans are fed by large catchments that drain the mixed lithologies comprising the Semail ophiolite which makes up the central Hajar, as well as the Hawasina nappe and post-nappe carbonates which are exposed along the mountain front of the interior arc of the Hajar (Glennie et al., 1973). These fans extend ~120-140 km from the mountain front to the Rub' al Khali sand sea (Fig.3.2b, c), with the Dhank fan surface becoming partially obscurred by the more recent deposition of aeolian dunes extending eastwards from the interior in their medial-distal reaches (Fig.3.2c). Similar to observations on the eastern side of the Hajar, these fan surfaces are also mantled with well-developed desert pavements. They also preserve inverted palaeochannel features in their more proximal areas.

The incision of more recent episodes of channel flow through older deposits has created exposures similar to those sampled in proximal locations on the Rustaq fan. However, these sections become shallower downfan as channels near intersection points. Two sites were sampled in proximal locations (OM20/6 and -/12) and three sites were sampled in medial-distal settings where fan surfaces begin to become obscurred by dune encroachment (OM20/8-11; Table 3.2; Fig.3.2b, c; Fig.3.3e-g).

3.2.2 Luminescence dating

To constrain the age of fan aggradation across these sites, OSL dating was used to provide ages for twenty samples which will be presented and discussed in more detail in Chapter 4. This section will briefly introduce the background to OSL dating and provide additional detail of the methods and protocols used.

Table 3.1. The locations and descriptions of sites located east of the Hajar drainage divide, along the lower reaches of Wadi Sahtan's catchment and the proximal part of the Rustaq fan. Luminescence sampling information is also shown, including whether samples were taken as a tube or block (see Section 3.2.2). [a] Samples where in-situ gamma spectrometry was conducted. [b] Samples which did not yield enough quartz for dating, thus were abandoned.

Site	Location		Elevation (m asl)	Description	Luminescence sample code	Sampling method	Depth (m)
	Latitude	Longitude					
Wadi Sahtan							
OM20/2	23.41 N	57.35 E	397	Downstream from OM20/1. 15.5 m section although the basal 8 m are obscured by scree. A sand lens is exposed at 7.5 m (OM20/2/1) with a sharp contact with overlying gravels which coarsen upwards into a similar conglomerate unit to OM20/1.	OM20/2/1	Tube	7.20
OM20/3	23.41 N	57.37 E	393	Downstream from OM20/2. 17 m section with basal gravels overtopped by ~6 m of fine, laminated silt-sands (OM20/3/5-3). This unit has a sharp contact with an overlying sand lens (OM20/3/2-1) which coarsens upwards into gravels and eventually the same conglomerates exposed at the previous sites.	OM20/3/1[b]	Tube	10.30
					OM20/3/2[b]	Tube	10.80
					OM20/3/3	Block	12.30
					OM20/3/4[b]	Block	13.30
					OM20/3/5[b]	Block	15.80
OM20/4	23.43 N	57.38 E	337	Downstream from OM20/3. 10.5 m section with the basal 2.5 m consisting of interstratified sand lenses and thin sheets of gravel (OM20/4/5-1). There is a sharp contact above with coarser gravels which grade upwards into the same unit of conglomerate material as observed at previous sites.	OM20/4/1[a]	Tube	8.50
					OM20/4/2	Tube	8.75
					OM20/4/3[a, b]	Tube	9.25
					OM20/4/4	Tube	9.60
					OM20/4/5[a]	Tube	10.40
Rustaq fan							
OM20/5	23.55 N	57.46 E	189	5.75 m exposure of a basal gravel unit overlain by a sharp contact with 2.5 m of finer, laminated silt-sands (OM20/5/3-2). This is overlain by coarse gravel channel fills, numerous of which are evident laterally along the exposure. Above is a thin sand lens (OM20/5/1) with the unit topped by a thin layer of cobbles forming the desert pavement of the relict fan surface.	OM20/5/1[a]	Tube	0.35
					OM20/5/2[a]	Block	2.60
					OM20/5/3[a]	Block	4.50

Table 3.2. The locations and descriptions of sites located west of the Hajar drainage divide, in the proximal part of the Ibri fan and both proximal and medial-distal parts of the Dhank fan on the central interior bajada. Luminescence sampling information is also shown, including whether samples were taken as a tube or block (see section 3.2.2). a Samples where in-situ gamma spectrometry was conducted. b Samples which did not yield enough quartz for dating, thus were abandoned. c Samples of little relevancy to the thesis narrative as the underlying sample showed they dated to the historical period so were also abandoned.

Site	Location		Elevation (m asl)	Description	Luminescence sample code	Sampling method	Depth (m)
	Latitude	Longitude					
Ibri fan							
OM20/6	23.25 N	56.40 E	337	6 m section exposed by modern wadi incision. A basal palaeosol unit (OM20/6/3-2) with evidence of thick lenses of diagenetic mineral growth is overlain by a sharp contact with gravel channel fills which are evident laterally across the exposure. There is another sharp contact above with more floodplain deposits with evidence of soil development (OM20/6/1), again overlain by more conglomerate material.	OM20/6/1[a]	Block	1.50
					OM20/6/2[b]	Block	4.05
					OM20/6/3[a]	Block	4.80
Dhank fan							
OM20/8	23.32 N	55.68 E	169	The remnants of a ~2 m pit exhumed for road building in the medial-distal part of the fan excavated and cleaned by hand. Basal unit is comprised of very cemented, pale silt-sands (OM20/8/2). This is overlain by a thin sheet of gravels and the upper unit (OM20/8/1) is composed of gravelly-sands.	OM20/8/1[a]	Tube	0.50
					OM20/8/2[a]	Block	0.90
OM20/10	23.35 N	55.69 E	189	~2 m section dug through a dune (OM20/10/1-2) overtopping the fan surface, exposing the upper 0.75 m of a modern playa in the medial-distal portion of the Dhank fan. Underlying playa sediments are composed of silty-sand with fine laminations (OM20/10/3).	OM20/10/1[c]	Tube	1.00
					OM20/10/2[c]	Tube	1.45
					OM20/10/3	Tube	1.80
OM20/11	23.43 N	55.79 E	193	2 m section through a small bar laterally eroded by the modern wadi channel on the Dhank fan, upstream of site OM20/10. The section is comprised of a number of sand lenses (OM20/11/1-3) interstratified with a lower gravel channel fill and upper, thinner gravel lenses. The section is topped by a thin veneer of aeolian sand.	OM20/11/1	Tube	0.30
					OM20/11/2	Tube	0.75
					OM20/11/3	Tube	1.40
OM20/12	23.49 N	56.20 E	305	4 m section dug into the proximal part of the fan with cobbles and gravels cemented in a calcareous matrix at the base, interrupted by a thin lens of fine silt-sans (OM20/12/2). There is a sharp overlying contact with coarser conglomerate material above, before silt-sands resume fining upwards (OM20/12/1). The section is topped with another layer of cobbles forming the overlying desert pavement.	OM20/12/1[a]	Block	0.30
					OM20/12/2[a]	Block	2.60

Background

Luminescence dating involves the measurement of charge trapped within the crystals of dosimetric minerals, primarily quartz and potassium-rich feldspar, allowing the calculation of the time since grains were last exposed to heat or light (Aitken, 1985). It does not refer to one technique, but rather a family of techniques which include optical and thermal luminescence of different mineral types. For the purposes of this thesis, the OSL dating of quartz will be the focus. This is because the OSL signal of quartz is rapidly reset with sunlight exposure and is thermally stable over Late Quaternary timescales (Godfrey-Smith et al., 1988) and previous work has shown that the OSL signal of quartz is appropriate for dating Hajar alluvium (e.g. Blechschmidt et al., 2009; Atkinson et al., 2013; Parton et al., 2015a). The infrared-stimulated stimulated luminescence (IRSL) signal of feldspar can also be used for dating and it is sometimes preferable to quartz as it 1) has a higher luminescence intensity than quartz which is useful when quartz OSL signals are dim; and 2) has a higher saturation point than quartz so can be used to date older samples (Huntley and Lamothe, 2001). However, the feldspar IRSL signal is subject to anomalous fading: the loss of charge over time which must be corrected for (Wintle, 1973), unless a post-IR IR (pIRIR) protocol is used (Buylaert et al., 2012). Furthermore, the ultra-mafic geology of the Hajar region is not conducive to the production of feldspars, limiting their potential as a chronometer in these settings (Woor et al., 2022; Appendix A).

Dosimetric minerals are exposed to naturally occurring, ionising radiation from surrounding sediments due to the decay of radionuclides such as Uranium (U), Thorium (Th), and Potassium (K), as well as from extra-terrestrially sourced cosmic rays (e.g. Aitken, 1985; Prescott and Hutton, 1994; 1998). Defects (ion vacancies) in the crystal lattices of dosimeters such as quartz act as ‘traps’ for charge separated from ions within the crystal due to exposure to this naturally occurring radiation (e.g. Aitken 1985; McKeever et al., 1985; Itoh et al., 2002). Exposure to energy (in the form of heat or light), releases the trapped charge from the trap, and recombination of this charge with a parent

ion can result in the production of a photon, and therefore the production of luminescence (e.g. Aitken 1985).

Luminescence dating utilises the production of luminescence in response to exposure to ionisation as the basis for age calculation (Huntley et al., 1985). The rate of exposure to ionising radiation is termed the environmental dose rate (D_r) and forms the denominator of the age equation (Equation 3.1). The laboratory dose required to reproduce the observed luminescence signal is termed the equivalent dose (D_e), and this is the numerator of the age equation (Equation 3.1). Therefore, age calculation can be summarised by:

Equation 3.1. The calculation of a luminescence age.

$$Age\ (ka) = \frac{Equivalent\ dose\ (Gy)}{Environmental\ dose\ rate\ (Gy\ ka^{-1})}$$

OSL dating is a very useful technique for providing age control in alluvial settings, relative to other geochronological techniques (e.g. radiocarbon dating) for a number of reasons. Firstly, coarse-grained fluvial sediments do not typically preserve organic remains, limiting the applicability of radiocarbon dating but they do commonly yield quartz-bearing coarse sand fractions (Rittenour, 2008). Secondly, luminescence permits the dating of deposition directly so is potentially more robust in terms of seeking to date past hydrological activity. Lastly, it has a larger age range than radiocarbon dating, with quartz typically providing ages up to 100-200 ka (Wintle, 2008), relative to the younger upper limit of radiocarbon (~50 cal ka BP; Wood, 2015). This last point is especially relevant for Hajar fan sediments, for which previous luminescence dates are commonly >50 ka and have been derived up to ~900 ka (Blechschmidt et al., 2009).

Laboratory sample preparation and D_e measurement protocol

Luminescence samples were collected in the field by hammering opaque plastic tubes into sediments or, where sediments were highly indurated, chiselled out as blocks (Tables 3.1, 3.2). Blocks and tubes were wrapped in light-tight plastic for transport to the laboratory. Samples were

opened under subdued orange light conditions in the laboratory and the light exposed ends of tubes and the edges of block samples were removed. These light exposed sediments were retained for dose rate and grain size analyses. Inner light sensitive sediments were submerged in 37% HCl to remove carbonate and 30% H_2O_2 to remove organic material. Samples were then sieved to various grain-size fractions within the range of 90-250 µm. Density separation using sodium polytungstate (SPT) was then carried out at densities of 2.72 g cm^{-3} (to remove heavy minerals) and 2.62 g cm^{-3} (to isolate quartz) as the density of quartz is 2.65 g cm^{-3} (Wintle, 1997). Isolated quartz was then chemically etched using 40% HF for 45 minutes to remove the alpha (α) irradiated outer 8-10 µm (Roberts, 2007). Etching should also dissolve feldspar contaminants (Porat et al., 2015). The prepared quartz grains were mounted on aluminium discs (9.8 mm diameter) using silicone oil. The yield of quartz was variable across the samples and samples which yielded too little quartz for dating were abandoned (Table 3.2).

Small aliquots (2 mm diameter) were used for all analyses. Small aliquots are appropriate for fluvial sediments which can suffer from issues of partial bleaching: the insufficient removal during transport of a previous luminescence signal. This can be particularly problematic within turbid water columns or short-lived flood events where light exposure is limited (Wallinga, 2002; Rittenour, 2008). Using larger sample sizes can obscure the true distribution of D_es due to signal averaging effects between hundreds or thousands of grains. This potentially makes it difficult to detect issues such as partial bleaching which affect age model selection (Duller, 2008). Single-grain measurements give the highest-resolution appraisals of D_e scatter; however, single-grain signal brightness and yield tests carried out 180-210 µm quartz grains from three samples suggested that this approach would be inappropriate for this project. Whilst the yield of grains giving >90% of the total luminescence signal was adequate (10-20%), OSL signals in response to a 50 Gy laboratory dose were generally dim with <5.5% of grains giving signals of >100 OSL counts per 0.01 s (details and results are available in Appendix B). The finer-grained nature of some samples as well as low quartz yields from separation meant that there was little quartz in the 180-210 µm fraction

appropriate for single-grain measurement for many of the samples. Therefore, a small aliquot approach is justified in this context and follows previous applications of OSL to Hajar alluvium (e.g. Blechschmidt et al., 2009; Hoffmann et al., 2015; Mueller et al., 2022).

D_es were measured using the single aliquot regenerative dose (SAR) protocol (Murray and Wintle, 2000; 2003; Wintle and Murray, 2006). The luminescence sensitivity of quartz crystals (or the magnitude of luminescence emitted in response to radiation dose) can change throughout the SAR measurement protocol due to heating and irradiation. Pre-heating samples is necessary to remove potentially unstable charge from low-energy traps (Aitken, 1985; Fig.3.4a). The SAR protocol corrects for these sensitivity changes by normalising signals to the luminescence produced in response to a fixed radiation dose (the test dose) measured throughout the sequence (Table 3.3). Following the measurement of the natural signal (L_n) and test signal (T_n; Fig.3.4b), aliquots are irradiated with a known dose of radiation which is regenerated through the same measurement procedure and normalised to a test dose. The ratio of subsequent test signals (T_x) against the first test signal (T_n) is used to monitor sensitivity change throughout the regeneration cycles (Fig.3.4d). These regeneration cycles are repeated at progressively higher doses to build a dose response curve of normalised luminescence against dose (Table 3.3). The D_e is then interpolated from the dose response curve using the L_n/T_n ratio (Fig.3.4c). Depending on the yield of quartz during preparation, 32-113 aliquots were measured for each sample.

Pre-heat plateau and dose recovery tests were also performed to decide an appropriate pre-heat temperature. These procedures test the appropriateness of the SAR protocol to recover a known dose from samples as heating can change the luminescence sensitivity (Wintle and Murray, 2006). Results showed that the SAR protocol was able to recover a known dose and that 220° is an appropriate pre-heat temperature for the samples measured in this thesis (Appendix B). The SAR protocol also has an in-built set of quality control measurements which inform rejection criteria

Table 3.3. The SAR protocol (Murray and Wintle, 2003).

Measurement step	Treatment	Observation
1) Regeneration dose	Aliquots irradiated with a known amount of radiation, increasing with each SAR cycle.	-
2) Pre-heat	Samples heated to remove unstable charge.	-
3) Measurement of natural or regenerated OSL signal	Samples stimulated with blue light for 40 s at 125°C to measure the OSL emission. The first measurement is termed the 'natural' which is the OSL signal as found in nature. Subsequent or 'regenerated' measurements are those which are measured following the administering of a known laboratory dose of radiation to samples.	L_n (natural) or L_x (regenerated).
4) Test dose	A known amount of radiation is given to samples. With each SAR cycle, the test dose remains constant and is used to normalise regenerated signals to build the dose response curve.	-
5) Cut-heat	Fulfils the same purpose as the pre-heat.	-
6) Measurement of the test signal	Sample is again stimulated with light for 40 s at 125°C to measure the OSL signal resulting from the test dose.	T_n (following the measurement of the natural luminescence signal) or T_x (following a regeneration dose).
7) Repeat	SAR cycles are repeated typically 4 or 5 times following the measurement of the natural signal. Each regenerated signal (L_x) (step 3) is divided by the test signal (T_x) (step 6) and plotted against the administered dose (step 1) in order to build a dose response curve.	-

used to screen resulting measurement data (Murray and Wintle, 2003). These measures include checking for the contamination of samples by IR-sensitive minerals (IR-OSL depletion ratio), the reproducibility of OSL signals (recycling ratio) and the transfer of charge from deeper OSL traps (recuperation test). These criteria are detailed in Section 4.3.1 and results given in Appendix B.

Age model selection

From the aliquots measured for each sample and passing rejection criteria, a representative D_e from the D_e distribution needs to be calculated through the application of a statistically appropriate age model. Resulting D_e measurements were combined for each sample using either a central age model (CAM) or minimum age model (MAM; Galbraith et al., 1999). The choice depended on the shape of the D_e distribution, with samples showing broadly gaussian distributions being calculated

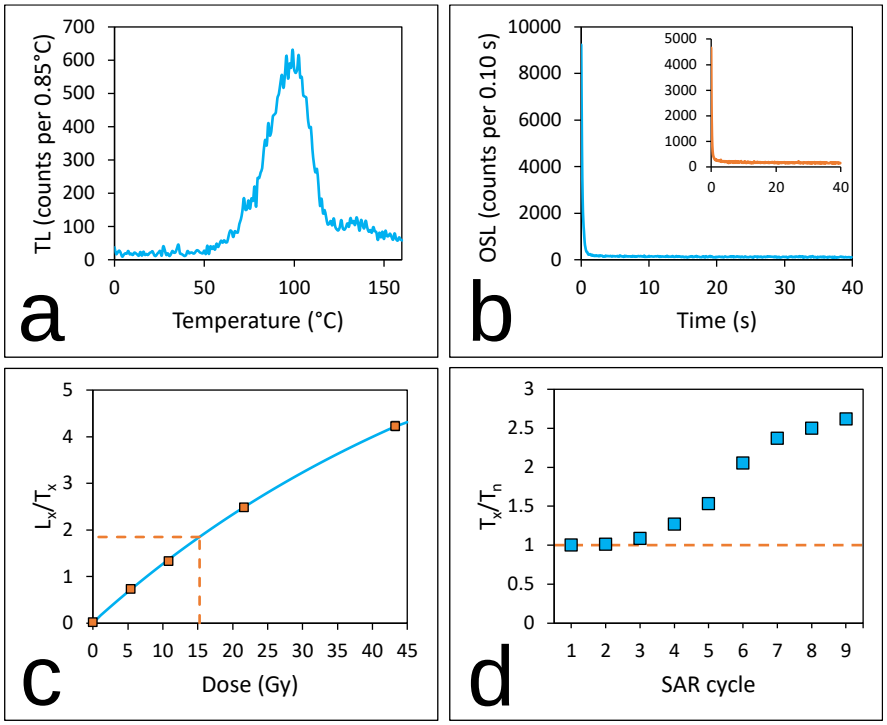

Figure 3.4. Measurement results for an aliquot of sample OM20/12/1. **(a)** The TL signal resulting from the sample cut-heat following a 6.8 Gy test dose, showing the characteristic 110°C peak of quartz. **(b)** The natural OSL signal (Ln) in blue and the corresponding test signal (Tn) in orange showing the characteristic rapid decay or 'fast dominated' signal. **(c)** The dose response curve for the aliquot built by plotting sensitivity corrected luminescence (Lx/Tx)for multiple SAR cycles against the laboratory administered dose. The dashed orange line is the Ln/Tn value used to interpolate the De which is ~15 Gy. **(d)** The Tx/Tn ratio used to monitor sensitivity change throughout the SAR repeats. The dashed orange line represents unity.

with CAM, essentially a weighted mean of D_es (Galbraith and Roberts, 2012). Gaussian dose distributions indicate that partial bleaching is less likely to be significant in samples from fluvial contexts (e.g. Blechschmidt et al., 2009). MAM, by contrast, calculates a D_e based on a truncated distribution which biases the outcome towards lower values. This is appropriate where partial bleaching may be suspected, for example in positively skewed distributions with a distinct younger population of D_es (e.g. Rodnight et al., 2006), which is common in fluvial and fan settings (e.g. Wallinga et al., 2001). Examples of both types of D_e distributions are included in Section 4.4.1 and

all age model results and D_e distributions are available in Appendix B. Age models were calculated using the R 'Luminescence' package (Kreutzer et al., 2017).

D_r calculation

For the coarse grain dating of quartz, the environmental dose rate is the rate at which dose accumulates in the dated minerals and can be calculated by measuring three separate dose rates. These are: 1) the beta (β) dose rate, 2) the gamma (γ) dose rate principally derived from soil radionuclides, and 3) the cosmic dose rate contributed from the bombardment of Earth's surface by cosmic rays (Aitken, 1985). For quartz, the alpha (α) dose rate is assumed to have been removed because the α irradiated outer layers of the mineral grains are removed during the etching process. An infinite matrix assumption is used to calculate β and γ dose rates where all the energy being emitted by homogeneous sediment is also being absorbed by the sediment within ranges specific to each type of radiation (~2 mm for β and ~30 cm for γ; Guerin et al., 2012).

β dose rates were calculated by measuring the concentrations of radionuclides in the bulk sediments removed from luminescence samples. Inductively-coupled plasma mass spectrometry (ICP-MS) was used to measure concentrations of ^{238}U, ^{232}Th and ^{40}K which were converted into infinite matrix β dose rates using the conversion factors of Guérin et al. (2011). ICP-MS measurement of bulk sediment from luminescence samples is an appropriate method for calculating β dose rates as the range of β radiation is very small, so is likely to be contributed from very close to the measured quartz grains (Bailey et al., 2003).

For the majority of samples, γ dose rates were measured in the field using a portable Canberra InSpector 1000 gamma spectrometer with a NaI crystal probe. This is a more appropriate approach than using ICP-MS for γ dose rate calculation where samples are taken from thin sand units near coarser conglomerate material (Bailey et al., 2003) where infinite matrix assumptions cannot be made for the ~30 cm range of γ rays (Aitken, 1985). The instrument was calibrated prior to fieldwork using the Oxford blocks (Rhodes and Schwenninger, 2007) and the γ spectrum for U, Th, and K was

measured for ~1 hour at each sampled unit. Due to logistical constraints in the field, it was not possible to conduct in-situ gamma spectrometry at all luminescence sampling locations. Therefore, samples taken from contexts that were potentially more complex in terms of dose rate calculation (e.g. clastic inclusions or close proximity to stratigraphic boundaries) were prioritised as these were judged as more likely to be affected by complexities in the γ radiation field which would not be captured using ICP-MS. Where in-situ gamma spectrometry was not conducted, radionuclides measured with ICP-MS were used to calculate infinite matrix γ dose rates using the conversion factors of Guérin et al. (2011), however these results are likely to be accurate due to samples being from homogeneous units > 30 cm from stratigraphic boundaries (see Appendix B for results and discussion of these methods).

The Dose Rate and Age Calculator (DRAC; Durcan et al., 2015) was used to calculate final dose rates. Attenuation factors were used to correct for an estimated water content of 5±2% (Zimmerman, 1971), grain size (Mejdahl, 1979), etching depth (Bell, 1979) and carbonate contents (Nathan and Mauz, 2008; Appendix B). Water content follows previous estimations applied when dating Hajar alluvium and fluvial sediments from drylands more broadly (e.g. Telfer and Thomas, 2007; Parton et al., 2015a). Cosmic dose rates were calculated using the method of Prescott and Hutton (1994), based on the overburden depth above the sample, latitude and longitude and altitude. Without independent chronology, an assumption has to be made about overburden depth remaining constant throughout burial history which may not necessarily be true for dryland fans subject to periodic aggradation. However, resulting ages are insensitive to varying calculated cosmic dose rates by ±20% (Appendix B).

DRAC was also used to calculate final age results, combining the selected D_e model results and D_r values as per Equation 3.1 with uncertainties propogated in quadrature. D_r and final age results are presented in Section 4.4.1.

3.2.3 Hierarchical cluster analysis of regional age data

Chapter 4 presents the results of the dating procedures outlined in the previous section within the context of other alluvial records from the region. Taken together, these records alongside those from lacustrine basins record periods of higher hydrological activity in the past across the Hajar. However, the data are noisy and it is difficult to identify clusters objectively when testing ideas of periodicity. Cluster analysis is a statistical approach for identifying groups within a dataset and has been previously applied to inventories of luminescence ages (e.g. Kalinska et al., 2022). It offers a more objective means of identifying periods of fan and lacustrine activity than a qualitative assessment of ages.

Luminescence and radiocarbon ages from this study and the literature were filtered to only include those from sedimentary contexts interpreted by the original authors as representative of more sustained streamflow conditions or lake highstands, relative to present (n = 90; table provided in Appendix B). Any ages relating to deposits interpreted as being the result of ephemeral flooding events under relatively drier climate conditions where disregarded (e.g. examples in Rosenberg et al., 2012; Mueller et al., 2022; Chapter 4). Euclidean distance was computed as a measure of similarity between central age values. Euclidean distance values were used to inform hierarchical clustering, whereby each member of the dataset is paired with its most similar neighbour, with groups then paired with most similar groups and so on until all values are incorporated. This can be represented as a dendrogram (Fig.3.5a) whereby each level represents a different number of clusters (k).

The average silhouette approach offers a means of deciding the most appropriate value of k at which to cut the dendrogram, whereby the k value with the highest average silhouette score defines the point at which groups are the most different to each other whilst being the most internally similar. The silhouette score of k = 9 is the highest, meaning that eight groups is the optimum for this dataset (Fig.3.5b). Analysis was conducted using the ‘cluster’, ‘factoextra’ and ‘dendextend’

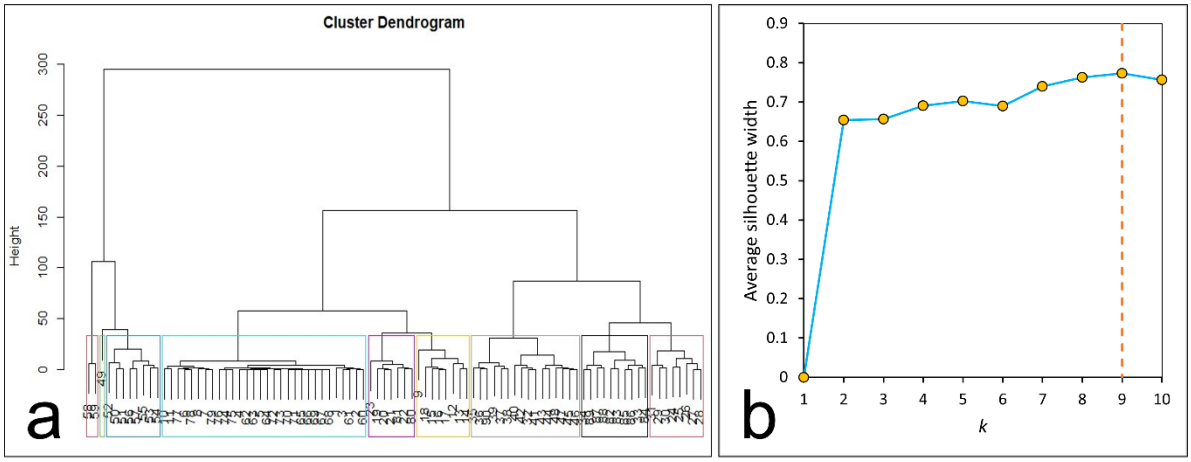

Figure 3.5. (a) Dendrogram of clustered ages. Each age is represented by a number (1-90) and paired with its nearest neighbour at the bottom of the plot. Coloured boxes show the groups defined based on similarity (k = 9). **(b)** Average silhouette widths for different k values (1-10). K = 9 (dashed vertical line) gives the highest average silhouette width, so was chosen as the most optimum place to cut the dendrogram.

packages in R Studio. The mean ages for each cluster and their quartile ranges are given in Appendix B and plotted in Fig.4.8 (Section 4.5.1).

3.3 Understanding the non-climatic controls on Hajar fan morpho-dynamics

To address research objective 2, an understanding of the contribution of factors other than climate to regional mountain-front fan morphology and dynamics is important. Following methods applied widely in the literature (e.g. Bull, 1977; Silva et al., 1992; Harvey, 1992; 1999; Mather et al., 2000; Stokes and Mather, 2015), and to a small region of the northern Hajar (Al-Farraj and Harvey, 2005), two approaches were used: 1) the remote sensing and geographical information systems (GIS) mapping of fans and catchments, and 2) statistical analysis of regression relationships between fan and catchment morphology. Further methodological details are discussed in Section 5.3.

3.3.1 Geomorphological mapping of fans and catchments

A purely remote sensing approach was taken for three reasons (Fig.3.6). First, the scale of this study warrants a desk-based approach as it maps >400 fans spanning the whole Hajar range. Second, the fans in the Hajar can be $>10^4$ km^2 in planform area, posing logistical challenges for field-based

morphometric measurements. Third, a multi-remote sensing product approach allows detection of features that may be challenging to identify in the field, such as delimiting the boundaries of individual fans in complex, coalescing settings or where fans are over-topped by dunes.

Fan mapping

Following the approach of Stokes and Gomes (2020), mapping was initially carried out using Google Earth Pro (Fig.3.6). Outputs were compared with historic imagery (dating back to 1984) available from Google Earth Engine Timelapse where fan surfaces have become obscured by more recent urban development (Fig.3.7). The resulting shape file was then imported into ArcMap 10.8 and cross-referenced against Landsat 8 false-colour imagery (RGB: 642), the ALOS World 3D-30 m digital elevation model (DEM) and radiometric and terrain-corrected Advanced Land Orbiting Satellite 1 Phased Array L-band Synthetic Aperture Radar (ALOS PALSAR). A Lee speckle filter was applied to SAR imagery to reduce backscatter noise (Lee, 1981) and units were converted from linear backscatter intensity to decibels to aid image interpretation (Fig.3.6).

Catchment mapping

Fan-feeding catchments were delineated using the ArcMap 10.8 Hydrology Toolkit (Fig.3.6). The ALOS World 3D-30 m DEM was filled and the resulting DEM used to generate a flow direction raster. From this, a flow accumulation raster was produced to isolate areas of high and low accumulation corresponding to the stream network. Pour-points were placed at the intersection between the apexes of fans and the feeding streams and used to inform the watershed tool to delineate catchments. The resulting catchment raster was converted into a polygon shapefile for further analysis.

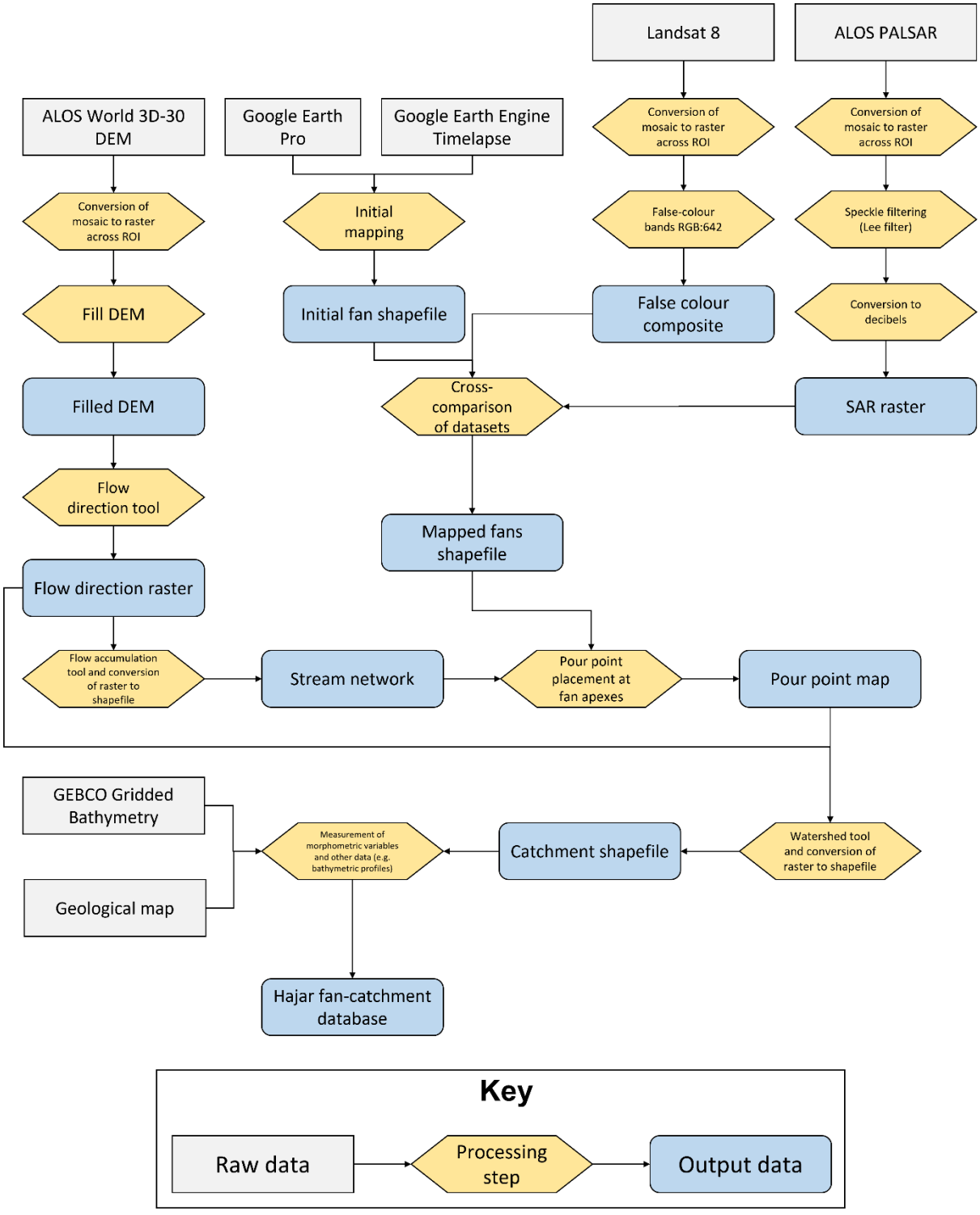

Figure 3.6. Flowchart of the input data and processing steps used to map fans and catchments to produce the dataset analysed in Chapter 5. Data processing was undertaken in ArcMap 10.8 and Google Earth pro. Chapter 5 provides a more detailed overview of data sources and resolutions.

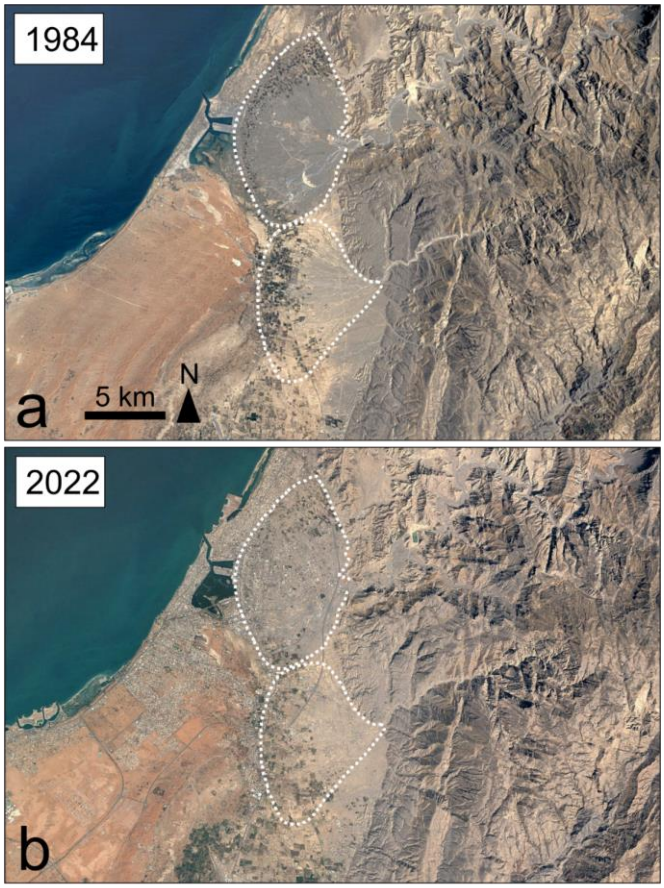

Figure 3.7. Comparison between delineating fans based on 1984 imagery **(a)** and 2022 imagery **(b)** in the north-western Hajar. Urbanisation has made it more difficult to delineate the same fans in some areas of the mountain front, therefore using historic imagery is important to help ensure accurate mapping.

3.3.2 Fan and catchment morphometric variables

Morphometric variables for fans, such as planform area (km^2), axial gradient and length (km), and for catchments, such as planform area (km^2), relief (m asl) and Melton's ruggedness index (Melton, 1965), were measured using ArcMap 10.8 using the fan and catchment polygons (Fig.3.7; full details of these variables are given in Section 5.3.2). Results were used to calculate power-law regression relationships between fan and catchment morphometric characteristics, outlined in section 2.2.1 (Equations 2.1 and 2.2).

Un-quantifiable variables are also important controls on resulting fan morphology, such as catchment geology and fan setting (Harvey, 2011; Table 2.1). These variables were also recorded in

the dataset through the visual inspection of remote sensing data and a geological map of the Hajar (see Corradetti et al., 2020; Fig.3.7). The influence of these variables on fan morphology was assessed by plotting the residuals of the fan area vs. catchment area and fan gradient vs. catchment area regression relationships (e.g. Silva et al., 1992). This allowed the identification of fans which are 1) larger and steeper, 2) larger and flatter, 3) smaller and flatter and 4) smaller and steeper than expected by these key regression relationships and what controls these patterns across the Hajar range (e.g. Fig.2.3).

3.4 Building a database of geoproxy ages for Arabia over the last 20 ka

To meet research objective 3 which aims to compare palaeoenvironmental changes in the Hajar region to other regions of Arabia, a databasing approach was used to compile sites with chronologically constrained palaeoenvironmental records from across the Hajar region and the wider Arabian Peninsula which would facilitate comparison. Individual luminescence and radiocarbon ages were compiled with their environmental interpretations and screened against a set of quality control criteria. Radiocarbon ages (57% of the database) were also re-calibrated using the most recent calibration curve (IntCal20; Reimer et al., 2020; Fig.3.8). What were deemed to be the best quality ages were then included in the environmental synthesis. The result was the Synthesising Chronologies for Arabian PalaeoEnvironments (SCAPE) database, detailed background, results and discussion of which are included in Chapter 6.

SCAPE is divided into four sections, each with various metadata which are expanded upon in Section 6.3. A summary of the sites included within the database is also attached in Appendix D and the full database can be downloaded as an Excel spreadsheet here:

https://doi.org/10.1016/j.gloplacha.2022.103748.

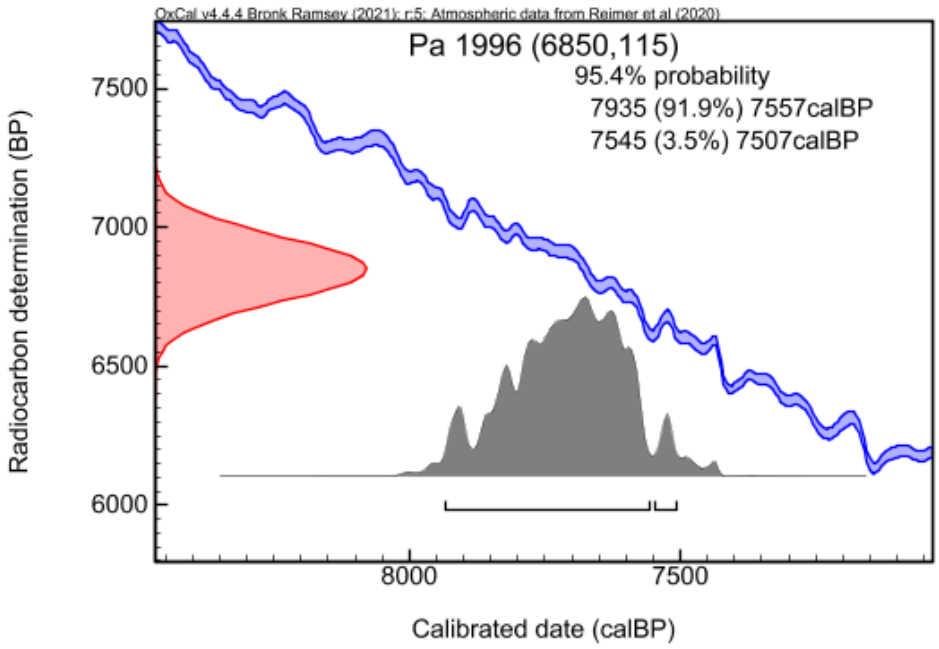

Figure 3.8. The re-calibration of sample Pa 1996 from the Al Hawa lake basin in Yemen using the IntCal20 calibration curve (blue line) and the OxCal software. The red distribution shows the uncalibrated age of 6850 ± 115 ^{14}C years and the grey distribution the interpolated (calibrated) age of 7746 ± 189 cal yrs BP. Data is originally from Lézine et al. (2007) and is included in the SCAPE database (see Chapter 6).

4 | The aggradation of alluvial fans in response to monsoon variability over the last 300 ka in the Hajar Mountains, south-east Arabia (Paper 1)

Authorship: Sam Woor, David Thomas, Julie Durcan, Sallie Burrough, Ash Parton

This chapter is based on a research paper of the same name, submitted to the journal Quaternary Science Reviews, June 2023. A number of changes have been made to the version in this chapter to ensure continuity of text and avoid over-duplication of background material in the thesis. This chapter meets Research Objective 1 (Section 1.2).

4.1 Paper abstract

New sites are presented from across the central interior bajada and the mountain-front of the Batinah Coastal plain in the Hajar Mountains, Oman, which record Late Quaternary alluvial aggradation. Luminescence ages show fans aggraded at 300 ka, 149 ka, 133 ka, 85 ka, 60-30 ka and 8 ka (during Marine Isotope Stages 9, 6, 5e, 5a, 3 and 1, respectively) in line with periods of increased monsoon rainfall. These units show sedimentary evidence of more sustained streamflow conditions than present, with conglomerates, channel sands and stabilised floodplain deposits. Episodes of aggradation also occurred at 91 ka (MIS 5b), 65 ka (MIS 4) and from 4-1 ka (the Late Holocene), out of keeping with this model of IOSM-paced aggradation. These deposits are found in markedly different depositional contexts. Based on their sedimentary facies, these events are interpreted to be the result of ephemeral flow under a more arid climate. Up-stream, mountainous, catchment areas were more hydrologically active during periods of broader regional aridity, relative to downstream alluvial fans. Like today, only the largest flash floods were capable of transmitting sediment from mountain catchments to fans during these drier intervals, accounting for seeming conflicts in the palaeoenvironmental record presented here, as well as in the wider literature from the region.

These findings emphasise the importance of careful consideration of the landscape context of sedimentary records contributing to palaeoenvironmental analyses. Data are synthesised with previous studies of fan aggradation from the region, demonstrating that alluvial sediments in the Hajar preserve the most continuous and sensitive record of palaeoclimate and environmental

change in south-east Arabia during the Late Quaternary. These signals are adding increasing nuance to understandings of water availability and the response of regional hydrological systems to climate change throughout the Late Quaternary.

4.2 Introduction

Today, south-east Arabia is characterised by an arid to hyper-arid climate, with the northerly extent of IOSM rainfall only reaching the southern coast of Arabia (Fig.4.1). However, South-east Arabia has experienced considerable palaeoclimatic and palaeoenvironmental variability through the Late Quaternary. Marine sediment cores from the Arabian Sea (e.g. Sirocko et al., 1993; Overpeck et al., 1996; Clemens and Prell, 2003; Ziegler et al., 2010; Caley et al., 2011b) and speleothem records from the Hajar Mountains (e.g. Fleitmann et al., 2003; Burns et al., 1998; 2001) have been used to infer that the periodic, northwards displacement and intensification of the IOSM has resulted in periods of higher rainfall in south-east Arabia (Fig.4.1). Inferences from palaeoclimate archives are further supported by modelling studies which show higher rainfall over south-east Arabia periodically during the last 130 ka (Jennings et al., 2015). These periodic incursions of the IOSM are driven by increases in insolation oscillating at precessional (~23 ka) timescales (Parton et al., 2015b).

These high-resolution palaeoclimate archives offer a regional signal of Quaternary precipitation variability. Establishing landscape-scale responses to external forcing, especially in regions of significant environmental variability, requires proxy data that has a higher spatial and temporal resolution. Geomorphological records of environmental change, termed geoproxies (Thomas and Burrough, 2012), offer a means for understanding landscape responses to both regional-scale climatic drivers and smaller-scale controls throughout the Late Quaternary (Thomas, 2013).

4.2.1 The IOSM model of precessionally-paced alluvial fan aggradation in the Hajar

Fluvial sediments in the form of palaeochannel and floodplain deposits are useful records of palaeoenvironmental change in the region. The Hajar Mountains, which run from northern Oman to the Musandam Peninsula in the northern UAE, have extensive alluvial deposits, forming valley-fill sequences within mountain catchments and large fans which extend both to the Arabian Sea and the interior Rub' al Khali desert (Woor et al., 2023). The classic model of dryland fan response

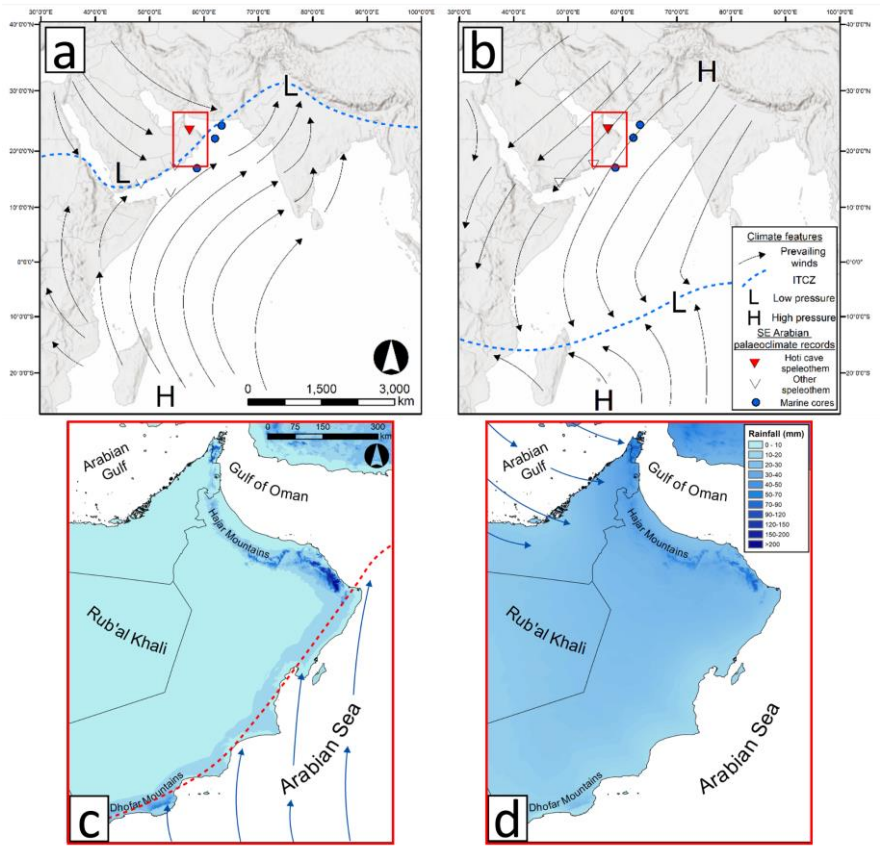

Figure 4.1. (a) The circulation of the Indian Ocean Monsoon system and the position of the inter-tropical convergence zone (ITCZ) during summer months. **(b)** The circulation of the Indian Ocean Monsoon system and position of the ITCZ during winter months. Key palaeoclimate records are shown, including Hoti Cave, located in the Hajar Mountains. Redrawn from Fleitmann and Matter (2009). The red boxes indicate the extent of south-east Arabia, shown in **(c)** and **(d)**. **(c)** Mean rainfall in south-east Arabia during summer months (June-August). The red line denotes the approximate position of the ITCZ, blue arrows denote the onshore flow of the IOSM. **(d)** Mean rainfall in south-east Arabia during winter months (January-March). Blue arrows denote the influx of moisture from Mediterranean westerlies. Rainfall data for 1970-2000 from WorldClim 2 (Fick and Hijmans, 2017).

to Quaternary climatic variability is that they aggrade during periods of higher rainfall as sediment supply increases from their catchments, juxtaposed with becoming net incisional during periods of greater aridity when systems become transport-limited leading to the abandonment of relict surfaces (Lecce, 1990; Blair and McPherson, 1994; Harvey, 2011). The response of fans to climatic change does, however, vary somewhat depending on the specific contexts of their feeding catchments (Blair and McPherson, 1994).

To date, fan paleoenvironmental analyses in the Hajar have focused on the fans of the eastern UAE and the large megafans in central Oman. They record periods of sediment deposition under more sustained channel flow conditions, in-sync with precessionally-paced periods of IOSM intensification (e.g. Blechschmidt et al., 2009; Atkinson et al., 2013; Parton et al., 2013; 2015a; Mueller et al., 2022). This conforms to the general model of sediment aggradation during wetter periods, which also aligns with higher monsoon intensity recorded in marine core records (Clemens and Prell, 2003), and sediment incision during drier periods (Harvey, 2004). Herein, the precessionally-paced Hajar fan aggradation in response to higher rainfall from a more northerly, intensified IOSM is referred to as the 'IOSM model'.

Within the IOSM model, eight periods of fan aggradation have been attributed to higher IOSM rainfall over the last 300 ka based on luminescence and radiocarbon dating studies of fan sediments and their terminal lacustrine basins. These occur at ~12-6 ka, 60-40 ka, 90-76 ka, 110-100 ka, 135-120 ka, 160-150 ka, 200-180 ka and 240-220 ka (e.g. Dalongeville, 1999; Parker et al., 2006; Blechschmidt et al., 2009; Farrant et al., 2012; Rosenberg et al., 2012; Parton et al., 2013; Atkinson et al., 2013; Hoffmann et al., 2015; Preston et al., 2015; Parton et al., 2015a; Moraetis et al., 2020; Mueller et al., 2022; Beuzen-Waller et al., 2022). The climatic drivers of these last two periods however, as well as older records of fan aggradation dated as far back as 900 ka (Blechschmidt et al., 2009), are more speculative due to the larger uncertainties on older luminescence ages. In these cases, the timing of fan aggradation and has been linked with higher rainfall during peak interglacial conditions (Blechschmidt et al., 2009).

These dated periods of proposed hydrological intensification are further supported by other environmental records from the region, such as the Hoti Cave speleothem isotopic record from the central Hajar (e.g. Fleitmann et al., 2003; Fig.3.1). The speleothem record does not, however, record all the wetter phases represented in fan aggradation and marine core records, for example no growth is recorded during MIS 3 (60-30 ka; Fleitmann et al., 2003).

Previous fan investigations have focused on the northern interior Hajar bajada in the UAE (e.g. Farrant et al., 2012; Parton et al., 2013; 2015; Mueller et al., 2022) and the large megafans of the southern Hajar bajada (Blechschmidt et al., 2009). Fans along the Batinah Coastal plain east of the Hajar, the interior central bajada and valley-fill sequences within their mountain source areas have received limited or no palaeoenvironmental analysis compared to those described above (Fig.3.1). The MIS 3 chronology presented by Hoffmann et al. (2015) for Wadi Mistal remains the only study of alluvial aggradation for systems draining east of the Hajar drainage divide to the Batinah Coast.

There is a growing body of age data from alluvial sediments around the Hajar which appear at odds with the regional IOSM model. Beuzen-Waller et al. (2022) date deposition in Wadi Dishah, located at the mountain front of the southern Hajar, to 26.6 ± 1.8 ka, falling within MIS 2, a dry phase in the IOSM model. The Maqta Oasis, located in the central Hajar, records continuous, gradual deposition within a wetland environment throughout the arid Last Glacial Maximum and Terminal Pleistocene (20-12 ka; Fuchs and Buerkert, 2008). Similarly, numerous aggradation events are recorded in alluvial fans along the interior mountain front of the UAE from 20-16 ka and again during the arid Late Holocene (3.5-1.6 ka; Mueller et al., 2022). These age data come from sedimentary units which are interpreted by the original authors as indicative of more ephemeral streamflow conditions. This suggests that careful sedimentary interpretations, as well as considerations of sampling location within large alluvial systems, are important for making climatic inferences in these contexts. Gathering data from areas of the Hajar for which no prior studies have been undertaken can, therefore, provide a means for testing the climatic controls on sediment systems.

4.3 Regional setting and sampling site selection

The large, mountain-front alluvial fans of the Hajar coalesce into two principal bajadas in the continental interior draining to the Rub' al Khali desert, as well as along the Batinah Coast parallel to the Arabian Sea. These bajadas are fed by drainage from mountain catchments, the direction of which is controlled by the watershed which runs along the spine of the Hajar (Fig.3.1).

Sites were selected with exposures of fluvial deposits located across mountain-front fans on the central interior bajada and along a feeder channel and proximal part of a fan on the eastern mountain front. This sampling strategy aimed to build as complete a record of aggradation as possible, considering the spatial variability in fan deposition. Sites comprised four from the eastern-draining Wadi Sahtan and the alluvial fan emanating from its apex at Rustaq on the Batinah Coastal plain (sites OM20/2-5; Fig.4.2), and five sites from the interior fans of the central bajada (OM20/6-12; Fig.4.3). These two main study areas will be summarised in the following sections. For more details of study sites, the reader is referred back to Section 3.2.1.

4.3.1 Wadi Sahtan and the Rustaq fan

Wadi Sahtan drains north-east from a catchment in the central Hajar, forming an alluvial fan with an apex located near the town of Rustaq and extending down to the Arabian Sea coast (Fig.4.2a). The catchment is primarily composed of sedimentary geological units including sandstones and Jurassic carbonates which form the western portions of Jebel Ahkdar (Rousseau et al., 2005). The channel of Wadi Sahtan incises through valley-fill alluvium in the lower reaches of the catchment (Fig.4.2b, c), exposing deep (~20 m) sections of fluvial sediments. These range in size from silty-sands to clast-supported conglomerates composed of large cobbles. Sites OM20/3 and OM20/4 are located along these exposed valley-fills, on the opposite side of the wadi to the Hayy al-Sarh Neolithic archaeological site which occupies an upper terrace (Bretzke et al., 2018). A fourth site, OM20/2 was also sampled just upstream from OM20/3 at the same sand unit as OM20/3/1 and -3/2. However, due to sampling within close proximity (<20 cm) to a conglomerate unit and the lack of field gamma spectrometry at this site, the sample is not presented as part of this analysis (see Appendix B). Downstream, Wadi Sahtan passes through a gap in the mountain front near Rustaq, resulting in the deposition of a large alluvial fan on the Batinah Coast. The fan is incised by smaller stream networks, exposing shallow (typically 1-5 m) sections of fluvial deposits such as site OM20/5 (Fig.4.2d).

4.3.2 The Ibri and Dhank fans

West of the Hajar drainage divide, large megafans emanate from apexes located at the towns of Ibri and Dhank on the interior mountain front (Fig.4.3a). These fans are more extensive than the Rustaq fan on the other side of the range and have formed in the foreland basin of the Hajar mountains which provides considerably more accommodation space than the much narrower Batinah Coastal zone (Rodgers and Gunatilaka, 2003). The fans are fed by large catchments draining mixed geologies composed of the Semail ophiolite, but also the limestones of the Hawasina nappes and the younger carbonates of the post-nappe units which outcrop at the mountain front (Glennie et al., 1973; Corradetti et al., 2020). The Ibri and Dhank fans coalesce, forming a low-gradient plain stretching to the Rub' al Khali, with incised channels exposing sections of fluvial sands and gravels (Fig.4.3c, d). Sites OM20/6 and OM20/12 are located close to the fan apexes at the mountain front (Fig.4.3c, d). OM20/6 is near the Ibri mountain-front rock shelter site, which shows evidence of Pleistocene human occupation (Parton and Bretzke, 2020). Sites OM20/8-11 are located in the medial-distal portion of the Dhank fan where fan surfaces begin to become obscured by aeolian sediments (Fig.4.3b).

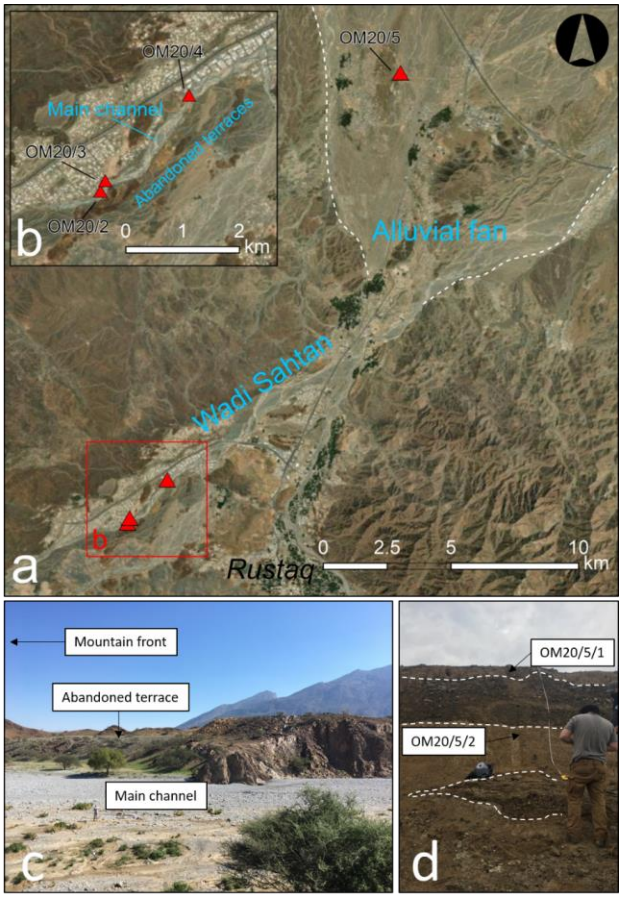

Figure 4.2. (a) The location of sampled sites east of the Hajar drainage divide along Wadi Sahtan (OM20/2-4) and in the proximal part of the Rustaq fan (OM20/5). **(b)** The locations of sites OM20/2-4 in Wadi Sahtan, with valley-fill sequences exposed by the incised channel. **(c)** The main channel of Wadi Sahtan taken from site OM20/3. **(d)** Site OM20/5 showing the sampling locations of samples OM20/5/1 and -/2 from sand units inter-stratified with gravelly channel-fill deposits.

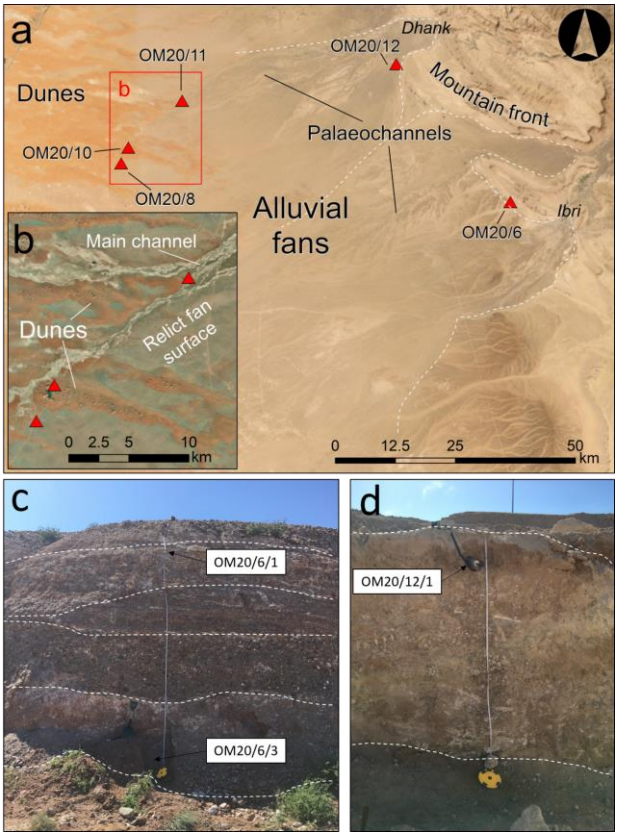

Figure 4.3. (a) The location of sampled sites west of the Hajar drainage divide on the Ibri and Dhank fans. **(b)** Sites OM20/8, -/10 and -/11 in the medial-distal part of the Dhank fan where fan surfaces begin to become obscured by Rub' al Khali dunes. **(c)** Site OM20/6 showing the sampling locations of OM20/6/1 and -/3 in floodplain deposits, bounding channel conglomerate and bedded gravel material. **(d)** Site OM20/12 showing the sampling location of sample OM20/12/1 within floodplain deposits, bounded by channel gravels above and below, and an in-situ gamma spectrometry measurement being taken following OSL sampling.

4.4 Methods

4.4.1 Luminescence dating

Luminescence dating samples were collected from units of fluvial sands from channel fill or overbank deposits using either opaque tubes hammered into sections or, where sediments were highly cemented, chiselled out as blocks. Samples were wrapped in light-tight plastic for transport to the laboratory. Samples were analysed at the Oxford Luminescence Dating (OLD) Laboratory, University of Oxford. Under orange light conditions, light-exposed sediments were removed from the ends of tube samples and the outer surfaces of blocks. Sediments were then treated with 37%

HCl and 30% H_2O_2 to remove carbonate and organic material, before undergoing sieving and density separation to isolate medium-coarse grained quartz. The quartz was then etched with 40% HF for 45 minutes and mounted on 9.8 mm aluminium discs as small aliquots of 2 mm diameter. Ultra-violet quartz OSL signals were measured using Risø TL/OSL luminescence readers fitted with blue-light emitting diodes (470 nm) and calibrated $^{90}Sr/^{90}Y$ beta sources, following the SAR protocol (Wintle and Murray, 2006; Murray and Wintle, 2003). OSL signals were measured at 125°C for 40 s. A preheat temperature of 220°C and a cutheat of 160°C was used for all samples following pre-heat plateau and dose recovery tests (Appendix B). The rejection criteria used to screen resulting D_e measurements included OSL IR depletion ratios (Duller, 2003), recycling and recuperation ratios (Murray and Wintle, 2000), a test signal (T_n) greater than 3σ above background levels, and the fast ratio of Durcan and Duller (2011; Appendix B).

Environmental dose rates were calculated using the Dose Rate and Age Calculator (DRAC, version 1.2; Durcan et al., 2011). Inductively-coupled plasma mass spectrometry (ICP-MS) was used to measure ^{238}U, ^{232}Th and ^{40}K concentrations to calculate beta and gamma dose rates and, for samples where infinite matrix assumptions could not be made with respect to the gamma dose rate, in-situ gamma spectrometry was measured with an InSpector Canberra 1000 portable gamma spectrometer which was calibrated using the Oxford blocks prior to measurement (Rhodes and Schwenninger, 2007). The conversion factors of Guérin et al (2011) were used to convert radionuclide concentrations into infinite matrix dose rates, and attenuation factors including etching depth (Bell, 1979), grain size range (Guerin et al., 2012) and an estimated water content of 5±2% were accounted for. An additional attenuation factor accounting for the carbonate content of samples following the approach outlined by Nathan and Mauz (2008) was also applied and is detailed in Appendix B.

4.4.2 Sedimentology

Facies interpretations were undertaken in the field to determine streamflow conditions at the time of deposition, for example whether deposition was occurring under more sustained flow conditions or under similar, flashy flows relative to present. Interpretations made for similar fluvial, or 'Scott-type', fans and braided stream facies in the region as well as other dryland contexts provided a basis for these observations (e.g. Miall, 1977; Atkinson et al., 2013; Parton et al., 2015a; Bowman, 2019; Mueller et al., 2022; Walsh et al., 2022). Fluvial fans are those on which deposition is primarily driven by braided-stream processes as opposed to more viscous debris flows (Harvey, 2011).

To compliment field sedimentological interpretations, bulk sediment was also extracted from the luminescence dating samples for grain size analysis. Analysis was carried out using a laser granulometer (Malvern Mastersizer 2000), with samples undergoing ultra-sonic displacement for 30 s before analysis commenced to ensure particle disaggregation. The characteristics of each grain size distribution were calculated from measurements made on three subsamples, enabling average particle size distributions to be determined. The GRADISTAT software (version 9.1) was used to calculate the percentages of sands (63 μm - 2 mm) and silts and clays (<63 μm) from these distributions, as well as modal grain size, sorting and skewness statistics (Blott and Pye, 2001).

4.5 Results

4.5.1 Chronology

In total, twenty samples were dated using quartz OSL luminescence signals (Table 4.1; Appendix B). In general, luminescence signals tended to be dominated by the fast component, yielding fast ratios of >20 (Durcan and Duller, 2011; Appendix B). An example natural signal for an aliquot of sample OM20/3/3 is shown in Fig.4.4a. The proportion of aliquots of samples from Wadi Sahtan and the Rustaq fan which failed rejection criteria were higher than western samples (Table 4.1; Appendix B). This is primarily due to failing the OSL IR depletion ratio, indicating contamination by infra-red

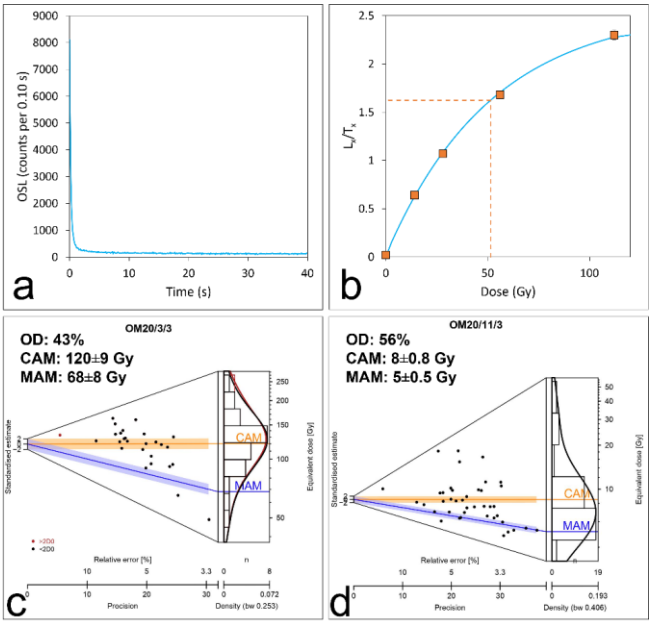

Figure 4.4. (a) An example OSL signal for an aliquot of sample OM20/3/3, and the dose response curve measured for the same signal **(b)**. Below are abanico plots showing example De distributions for **(c)** the broadly gaussian sample OM20/3/3 and **(d)** the positively skewed sample OM20/11/3. The central age model (CAM) and minimum age models (MAM) of Galbraith et al. (1999) are displayed as well as relative overdispersion (OD). A CAM-derived final De was used to derive a final age for sample OM20/3/3 **(c)**, whilst a MAM-derived final De was used for **(d)** OM20/11/3 (Table 4.1).

sensitive minerals, such as feldspar (Duller, 2003). Two samples had >25% of D_es either in or close to saturation (samples OM20/4/1 and OM20/5/2), therefore are ascribed a minimum age based on the central age model (CAM) D_e due to the potential truncation of the dose distribution (Table 4.1; see Appendix B for more discussion of signal saturation).

For most samples, D_e distributions were normally distributed around a central value, although show broad scatters and overdispersions which range between 21 and 65%, as well as an overdispersion of 83% for the low D_e sample OM20/10/3 (Table 4.1). Previous studies (e.g. Blechschmidt et al., 2009; Parton et al., 2015a) have speculated that the very broad, gaussian-like D_e scatters observed in Hajar alluvial sediments may be the result of beta heterogeneity. Heterogeneity in beta dose rate is more likely to be present where sediments have low radionuclide concentrations, are subject to post-depositional carbonate growth, have coarse grain sizes and low K-feldspar contents (Nathan

et al., 2003; Mayya et al., 2006; Guérin et al., 2015), as is the case with alluvial material from the Hajar (e.g. Blechschmidt et al., 2009; Parton et al., 2015a; Hoffmann et al., 2015; Woor et al., 2022b). Based on the approach taken by previous studies dating Hajar alluvium (e.g. Parton et al., 2015; Mueller et al., 2022; Beuzen-Waller et al., 2022) as well as other dryland fluvial contexts where broad, gaussian-like D_e distributions are often observed (e.g. Kenworthy et al., 2014; Durcan et al., 2019), the CAM is judged to be an appropriate means for final D_e calculation (Table 4.1).

Five out of the twenty samples presented here had visibly skewed D_e distributions with tails of larger D_e values outside of 2σ of the mean D_e (e.g. Fig.4.4d). Similar distributions have been previously reported from Hajar alluvial sediments (e.g. Hoffmann et al., 2015; Mueller et al., 2022), although are less common than the gaussian-like distributions described above. These were interpreted as being indicative of partial bleaching which is common in fluvial sediments (Rittenour, 2008), particularly from dryland contexts (Walsh et al., 2022b). Final D_es for these samples were calculated using the MAM (Galbraith et al., 1999). A MAM was also used for sample OM20/6/3 due to it producing a bi-modal dose distribution confirmed statistically by comparing with the finite mixture model (FMM; see Appendix B for discussion).

Ages show good chrono-stratigraphic agreement with a considerable range across the sites sampled, spanning the historical period (OM20/10/3) to 299 ± 33 ka (OM20/6/3; Table 4.1). Relative age uncertainties range from 6 % (OM20/8/1) to 18% (OM20/5/3), with the very young age of OM20/10/3 giving an outlying relative uncertainty of 24%. Ages from Wadi Sahtan and the Rustaq fan fall primarily between 65-30 ka, although the lower unit of site OM20/5 was older at 85 ± 16 ka (Table 4.1). For the Ibri and Dhank fans, resulting ages are more spread across sites at ~300 ka, 150 ka, 130 ka, 90 ka and 8-1 ka (Table 4.1).

Table 4.1. Luminescence age results, including: the sampling depth, grain size, soil radionuclide concentrations (measured using ICP-MS), total environmental dose rate and its components, number of aliquots accepted out of total measured, relative overdispersion (OD), the age model applied for De calculation, final De and resulting age reported with 1σ errors. CAM: central age model (Galbraith et al. 1999), MAM: minimum age model (Galbraith and Laslett, 1993). Values are reported to 2 decimal places, with calculations made prior to rounding. For the two samples considered saturated, the minimum De and age are reported to the nearest integer.

Sample	Depth (m)	Grain size (µm)	K (%)	U (ppm)	Th (ppm)	Beta dose rate (Gy ka^{-1})	Gamma dose rate (Gy ka^{-1})	Cosmic dose rate (Gy ka^{-1})	Environmental dose rate (Gy ka^{-1})	n	OD (%)	Age model	D_e (Gy)	Age (ka)
OM20/3/1	10.30	90-150	1.22±0.12	1.38±0.14	5.44±0.54	1.16±0.10	0.70±0.04	0.07±0.01	1.92±0.11	34/96	28	MAM	60.96±5.27	31.75±3.29
OM20/3/2	10.80	90-210	1.14±0.11	1.31±0.13	3.53±0.35	1.03±0.09	0.57±0.04[a]	0.07±0.01	1.67±0.10	27/48	21	CAM	70.91±4.43	42.44±3.62
OM20/3/3	12.30	150-210	1.19±0.12	1.12±0.11	8.05±0.81	1.13±0.09	0.77±0.05[a]	0.06±0.01	1.95±0.11	27/70	43	CAM	120.19±8.64	61.51±5.53
OM20/4/1	8.50	150-210	0.70±0.07	1.40±0.14	2.74±0.27	0.71±0.06	0.34±0.02	0.08±0.01	1.13±0.06	9/48	64	CAM	>116	>103
OM20/4/2	8.75	150-210	0.93±0.09	1.37±0.14	3.65±0.37	0.89±0.07	0.53±0.03[a]	0.07±0.01	1.49±0.08	17/48	23	CAM	90.55±5.76	60.77±5.07
OM20/4/4	9.60	90-250	0.87±0.09	1.37±0.14	3.04±0.30	0.84±0.07	0.49±0.03[a]	0.07±0.01	1.40±0.08	55/95	23	MAM	84.45±5.46	60.32±5.21
OM20/4/5	10.40	150-210	0.70±0.07	1.32±0.13	2.63±0.26	0.70±0.06	0.68±0.04	0.08±0.01	1.45±0.07	22/52	22	CAM	94.91±5.48	65.46±4.92
OM20/5/1	0.35	150-210	0.29±0.03	0.45±0.05	0.81±0.08	0.27±0.02	0.26±0.02	0.22±0.02	0.76±0.03	43/113	65	CAM	40.71±4.13	53.85±6.00
OM20/5/2	2.60	150-210	0.40±0.04	0.73±0.07	1.60±0.16	0.40±0.03	0.31±0.02	0.15±0.02	0.86±0.04	23/48	23	CAM	>94	>109
OM20/5/3	4.50	150-210	0.19±0.02	0.65±0.07	0.62±0.06	0.22±0.02	0.29±0.02	0.12±0.01	0.63±0.03	15/40	62	CAM	53.63±9.48	85.13±15.58
OM20/6/1	1.50	180-210	0.27±0.03	0.41±0.04	1.13±0.11	0.26±0.02	0.18±0.01	0.17±0.01	0.61±0.03	16/32	23	CAM	179.05±12.42	294.01±23.99
OM20/6/3	4.80	125-180	0.36±0.04	0.50±0.05	1.23±0.12	0.34±0.03	0.20±0.01	0.12±0.01	0.66±0.03	19/34	20	MAM	197.84±20.15	299.76±33.43
OM20/8/1	0.50	150-210	0.37±0.04	1.05±0.11	0.06±0.01	0.38±0.03	0.44±0.03	0.18±0.02	1.00±0.05	33/48	21	CAM	91.15±3.82	91.06±5.77
OM20/8/2	0.90	150-250	0.16±0.02	0.46±0.05	0.03±0.00	0.17±0.01	0.27±0.02	0.16±0.02	0.59±0.03	27/48	28	CAM	79.06±4.59	133.10±10.22
OM20/10/3	1.80	150-180	0.81±0.08	0.83±0.08	1.30±0.13	0.70±0.06	0.34±0.02[a]	0.22±0.02	1.26±0.07	13/48	83	CAM	0.90±0.21	0.71±0.17
OM20/11/1	0.30	150-180	1.21±0.12	0.45±0.05	0.91±0.09	0.93±0.09	0.38±0.03[a]	0.19±0.02	1.50±0.10	28/48	24	MAM	4.63±0.35	3.09±0.31
OM20/11/2	0.75	150-180	0.62±0.06	0.78±0.08	1.20±0.12	0.55±0.05	0.29±0.02[a]	0.17±0.02	1.01±0.05	36/48	63	MAM	4.09±0.50	4.05±0.53
OM20/11/3	1.40	150-180	0.34±0.03	0.51±0.05	0.38±0.04	0.31±0.03	0.15±0.01[a]	0.22±0.02	0.68±0.03	41/48	56	MAM	5.12±0.51	7.53±0.82
OM20/12/1	0.30	150-180	0.34±0.03	1.07±0.11	0.70±0.07	0.38±0.03	0.30±0.02	0.15±0.02	0.83±0.04	44/48	42	CAM	21.34±1.34	25.71±2.07
OM20/12/2	2.60	90-150	0.16±0.02	0.38±0.04	0.15±0.02	0.16±0.01	0.38±0.02	0.15±0.02	0.69±0.03	25/32	29	CAM	102.93±6.51	149.17±11.45

[a] The gamma dose rates of these samples were calculated based on ICP-MS measurements of radionuclides and not in-situ gamma spectrometry.

4.5.2 Sedimentary descriptions and chronostratigraphic relationships

The samples taken for luminescence dating have modal grain sizes that range from very fine sand (63-125 µm) to coarse sand (0.5-1 mm; Table 4.2). Some samples had up to 50% silt and clay content (e.g. OM20/6/3, OM20/12/1); others where predominantly (over 90%) sand-sized (e.g. OM20/11/1, OM20/11/3; Table 4.2). All samples except OM20/10/3 and OM20/11/1 which are moderately sorted display poor or very poor sorting and distributions are typically either symmetrical or very fine-skewed.

Table 4.2. Grain size data from the <2 mm fractions of the samples taken for luminescence dating, calculated using the GRADISTAT software (version 9.1; Blott and Pye, 2001).

Sample	Silts and clays (%)	Sands (%)	Modal grain size (µm)	Description	Sorting (σ)	Description	Skewness (*Sk*)	Description
OM20/3/1	44.3	55.7	84.5	Very fine sand	2.9	Poorly sorted	-0.2	Fine-skewed
OM20/3/2	31.7	68.3	106.4	Very fine sand	2.4	Poorly sorted	-0.1	Fine-skewed
OM20/3/3	38.0	62.0	119.3	Very fine sand	4.4	Very poorly sorted	-0.2	Fine-skewed
OM20/4/2	27.3	72.7	94.8	Very fine sand	2.5	Poorly sorted	0.0	Symmetrical
OM20/4/4	47.1	52.9	84.5	Very fine sand	3.1	Poorly sorted	-0.1	Fine-skewed
OM20/4/5	27.4	72.6	94.8	Very fine sand	2.7	Poorly sorted	0.0	Symmetrical
OM20/5/1	23.6	76.4	238.1	Fine sand	3.6	Poorly sorted	-0.5	Very fine-skewed
OM20/5/2	34.8	65.2	94.8	Very fine sand	6.6	Very poorly sorted	-0.1	Fine-skewed
OM20/5/3	23.1	76.9	150.2	Fine sand	4.1	Very poorly sorted	-0.1	Fine-skewed
OM20/6/1	44.3	55.7	475.1	Medium sand	5.1	Very poorly sorted	0.0	Symmetrical
OM20/6/3	50.0	50.0	212.2	Medium sand	5.2	Very poorly sorted	0.0	Symmetrical
OM20/8/1	35.0	65.0	475.1	Medium sand	5.3	Very poorly sorted	-0.4	Very fine-skewed
OM20/8/2	22.6	77.4	752.9	Coarse sand	4.0	Very poorly sorted	-0.3	Very fine-skewed
OM20/10/3	12.7	87.3	119.3	Very fine sand	1.8	Moderately sorted	-0.3	Very fine-skewed
OM20/11/1	5.9	94.1	189.1	Fine sand	2.0	Moderately sorted	0.1	Symmetrical
OM20/11/2	26.5	73.5	133.9	Fine sand	2.5	Poorly sorted	-0.3	Fine-skewed
OM20/11/3	3.7	96.3	189.1	Fine sand	2.1	Poorly sorted	0.2	Coarse-skewed
OM20/12/1	50.3	49.7	119.3	Very fine sand	7.2	Very poorly sorted	0.1	Symmetrical
OM20/12/2	48.8	51.2	106.4	Very fine sand	4.7	Very poorly sorted	0.0	Symmetrical

The eight exposures both west and east of the Hajar watershed divide were composed of fluvial deposits ranging from silty-sand units to matrix supported conglomerates (Figs.4.5, 4.6). The stratigraphic interpretations and associations for each section are as follows:

OM20/3: The base of the section intersects with the modern channel floor where there is an exposure of ~1 m of conglomerate material (Fig.4.5). Above is a sharp contact with 5.75 m of very fine palustrine silt-sands dated to 61.5 ± 5.5 ka (sample OM20/3/3; Table 4.1, 4.2) which display fine lamination and are highly cemented, becoming less friable with depth, yet lack evidence of palaeosol development so could indicate deposition in a low-energy, ponded environment (Miall, 1977). These sediments are overlain by a coarser unit of low-angle (<15°), planar-bedded fluvial sands which fine upwards dated to 42.4 ± 3.6 and 31.8 ± 3.3 ka (OM20/3/2, -/1). Above is a sharp contact with channel infills of gravel and coarse sands which coarsen upwards into larger, poorly sorted gravels and cobbles which are semi-rounded comprising the upper clast-supported conglomerate unit. The basal 1.5 m of this unit displays weak planar cross bedding indicative of low-velocity streamflow (Bowman, 2019).

OM20/4: The basal unit above the modern channel is comprised of 0.8 m of poorly sorted, very fine fluvial sand dated to 65.5 ± 4.9 ka (OM20/4/5; Fig.4.5) with occasional gravel inclusions. These sands coarsen upwards into a thin layer (<0.1 m) of sands and fine gravels. This is overlain by a thin unit (0.2 m) of very fine fluvial sand dated to 60.3 ± 5.2 ka (OM20/4/4;). Above is a series of thin gravel lenses interrupting the deposition of very fine sands and coarse silts with gravel inclusions which are 1.5 m thick, with sample OM20/4/2 taken from the penultimate sand unit dated to 60.8 ± 5.1 ka (Table 4.1). The sharp contacts between these gravel lenses and over- and underlying sands as well as their horizontal bedding suggest they are the result of sheetfloods under a flashy flow regime (Miall, 1977). Overlying this are a series of bedded channel lag deposits comprising gravels and small pebbles which coarsen upwards into semi-rounded to angular gravels and well-rounded pebbles and cobbles displaying imbrication downstream. These grade upwards again into a clast-supported conglomerate of larger pebbles and cobbles with no apparent bedding, comprising the upper 4 m of the section.

OM20/5: This section extends to a height of 5.75 m above the modern channel. The basal unit is comprised of highly indurated pebbles within a calcareous matrix of silt-sands. This is overlain by a unit of weakly laminated fine sands which is 2 m thick (Fig.4.5), the base of which yielded an age of 85.1 ± 15.6 ka (OM20/5/3). This unit is highly cemented by carbonates and preserves pinprick root voids throughout, indicative of deposition overbank of the main channel and of incipient palaeosol development (Parton et al., 2015a). Above is a sharp contact with a channel infill of gravels and small, imbricated pebbles in a sandy matrix with planar bedding typical of shallow, avulsing alluvial channels (Miall, 1977). This unit coarsens upwards into a conglomerate of larger pebbles and cobbles in a gravelly matrix. Viewing the exposure laterally, multiple channel scour and fill sequences are apparent in this unit, reaffirming the interpretation of a dynamic system of braided channels on the fan surface. Deposition is interrupted at 0.5 m by a lens of finer fluvial sands which was dated to 53.9 ± 6 ka (OM20/5/1). The top of the sequence is a thin (0.1 m) unit of pebbles and cobbles forming a desert pavement of varnished clasts on the relict fan surface above the sequence.

OM20/6: The base of this section consists of 1 m of highly calcareous, weakly laminated and well-cemented sands deposited in an overbank setting dated to 300 ± 33 ka (OM20/6/3; Fig.4.6). The presence of root voids dispersed throughout the unit and evidence of staining suggests palaeosol development (Parton et al., 2015a). Above this is a sharp contact with a conglomerate unit of gravels and semi-rounded pebbles and cobbles (1.5 m thick). Channel fill sequences are evident, fining upwards into planar bedded gravels and sands which indicate channel avulsion across the fan surface (Bowman, 2019). Again, this conglomerate unit is overlain by a sharp contact with a palaeosol unit comprised of sands with root voids and weak lamination suggesting its gradual accumulation in an overbank setting dated to 294 ± 24 ka (OM20/6/1). The section is topped with another conglomerate unit of channel lag deposits which forms the overlying desert pavement.

OM20/8: The basal 0.3 m consists of highly cemented, coarse sand dated to 133 ± 10 ka (OM20/8/2; Fig.4.6) with occasional small clasts indicative of low, overbank flow regimes. Deposition is

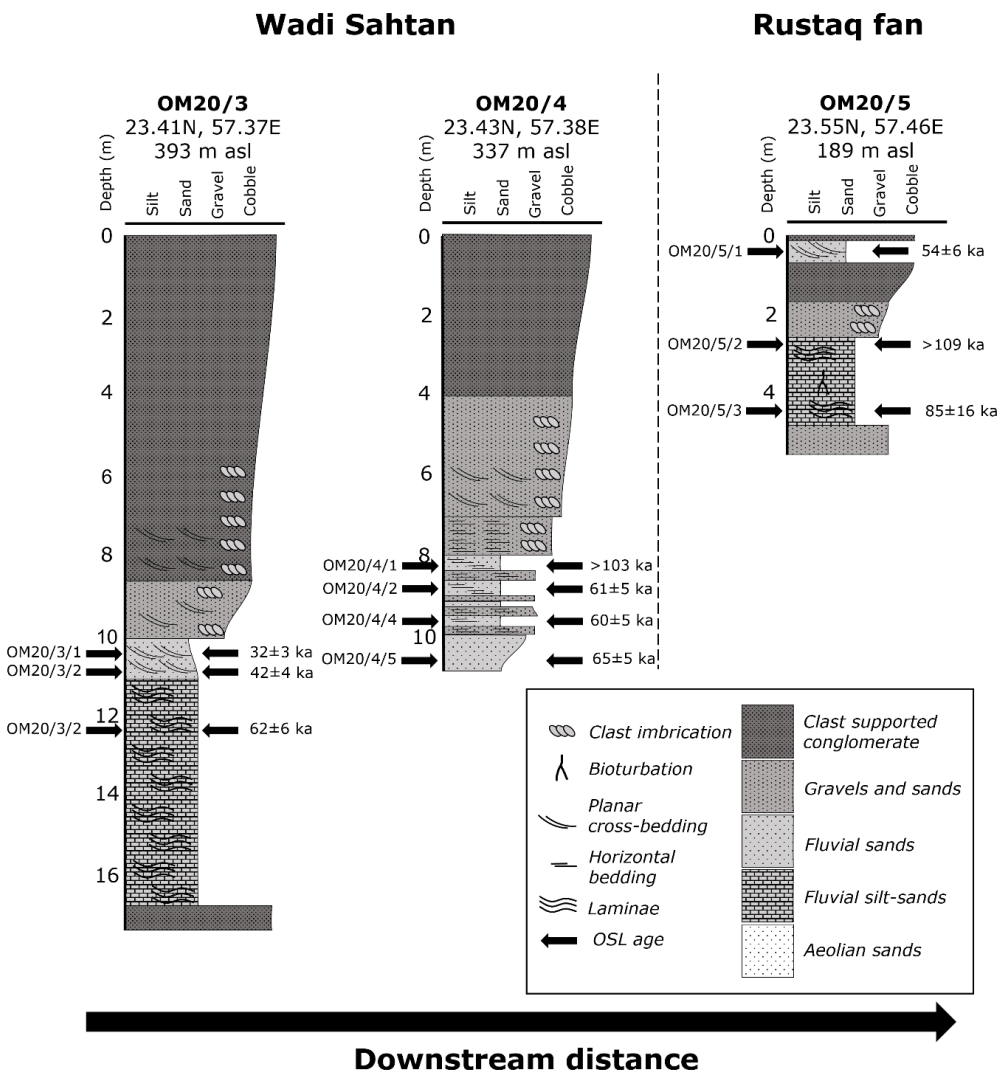

Figure 4.5. Stratigraphic logs of sites from the eastern Hajar (OM20/3-5). See Fig.4.2 for site locations.

interrupted by a lens of gravels (0.1 m thick) deposited by sheetflooding, before recommencing as a unit of sands with angular gravel inclusions and no discernible bedding architecture dated to 91.1 ± 5.8 ka (OM20/8/1), likely deposited under flashy flows.

OM20/10: The base of this sequence is the upper 0.5 m of the underlying playa sediments composed of very fine, laminated sands dated to 0.7 ± 0.2 ka (OM20/10/3; Fig.4.6). These playa sands are interpreted as being derived from runoff from surrounding dunes and direct aeolian input into the basin because they show moderate sorting in comparison to typically poorly sorted

sediments of fluvial origin (Table 4.2). This is overlain by 1.5 m of modern aeolian dune sands from the flanks of a large star dune.

OM20/11: The basal 0.8 m of this section is comprised of fluvial sands and gravels which fine upwards into coarse sands dated to 7.5 ± 0.8 ka (OM20/11/3; Fig.4.6). Above, there is a sharp contact with 0.4 m of bedded channel lags of gravel and coarse sands, interspersed with occasional lenses of coarse, semi-rounded gravels. This unit terminates with another sharp contact into a bed of very fine fluvial sands dated to 4.1 ± 0.5 ka (OM20/11/2) topped with a thin lens (<0.1 m) of gravels. The uppermost fluvial unit of fine sand is moderately sorted, whereas the underlying units are poorly sorted and date to 3.1 ± 0.3 ka (OM20/11/1). This could indicate the reworking of aeolian material on fan surfaces by flashy flows. The section is overlain by a veneer of modern aeolian sands <0.1 m thick.

OM20/12: The base consists of 1.45 m of gravels and pebbles cemented within a calcareous matrix of silt-sands (Fig.4.6). Above is a thin (0.25 m) unit of very fine, weakly-bedded and highly cemented fluvial sand with occasional inclusions of small clasts deposited in an overbank context dated to 149 ± 11 ka (OM20/12/2). Overlying are poorly sorted fluvial sands and gravels and a conglomerate unit of imbricated pebbles (1.3 m). A second unit of silt-sands with small gravel inclusions indicating proximal floodplain deposition 1.2 m thick then fines upwards and is dated to 25.7 ± 2.1 ka (OM20/12/1). The section is capped by 0.1 m of conglomerate material forming an overlying desert pavement.

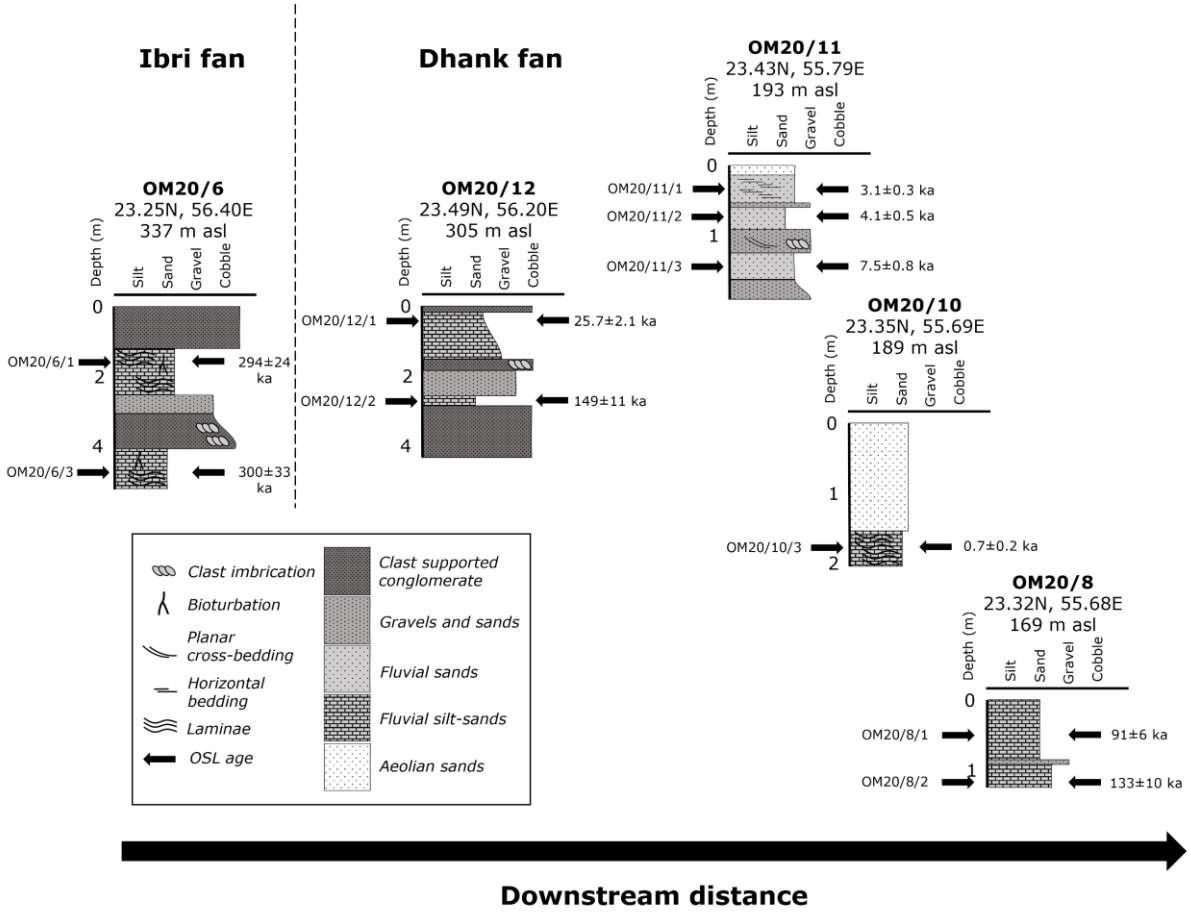

Figure 4.6. Stratigraphic logs of sites from the western Hajar (OM20/6-12). Note the change of scale for sites OM20/11, -/10 and -/8. See Fig.4.3 for sampling site locations.

4.6 Discussion

4.6.1 Palaeoenvironmental interpretation

Together, the chronologies and sedimentary interpretations of the alluvial records in the central Hajar represent aggradation under varying flow regimes, extending back to 300 ka (Fig.4.7; Table 4.3). Site OM20/6 is comprised of silty palaeosol units with laminae indicating gradual accumulation, likely as the result of seasonal flooding onto a stabilised floodplain, dated to ~300 ka (Table 4.3). These periods of floodplain accumulation are punctuated by the aggradation of fluvial conglomerates and sands, indicating an environment characterised by channel avulsion and the development of braided streams and point bars on fan surfaces. Aggradation phases from the southern megafans of the interior bajada have been previously dated within uncertainties of the

ages presented from OM20/6 (Blechschmidt et al., 2009), although large dating uncertainties mean that attributing them to increased IOSM rainfall with a 23 ka periodicity is impossible. However, these ages correspond with terminal Northern Hemisphere interglacial conditions at the end of MIS 9 (Lisiecki and Raymo, 2005).

The lower unit of OM20/12 records fan aggradation at 149 ± 11 ka. The conglomerate unit surrounding the sandy layer of OM20/12 shows increased channel activity which may be attributable to this period (Fig.4.6). Again, this coincides with increased precipitation interpreted from biological and geochemical proxies from marine sediments and dated to ~150 ka during MIS 6 (e.g. Clemens and Prell, 2003). Whilst there is no growth in the Hoti Cave speleothem at this time (Fleitmann and Matter, 2009), numerous alluvial fan records show increased drainage activity (e.g. Parton et al., 2015; Moraetis et al., 2020; Mueller et al., 2022).

The next phase of aggradation across the sites is recorded at 133.1 ± 10.2 ka in the basal unit of OM20/8, comprised of coarse, overbank sands and small gravels. This coincides with precessional maxima at ~130 ka at the transition from MIS 6 to 5e (Fig.4.7). MIS 5e ages are reported from other alluvial sediments from across south-east Arabia, with aggradation of the distal part of the Dhank fan occurring synchronously with that of alluvial fan aggradation at Remah to the north (Farrant et al., 2012) and alluvial sediment deposition underlying more recent aeolian deposits in the Wahiba Sands to the south (Preusser et al., 2002). Palaeolake Saiwan, also located at the distal extremity of the southern megafans, similarly records intensified hydrological conditions from 132-104 ka (Rosenberg et al., 2012). Increased monsoon rainfall is evidenced by palaeo-productivity proxies such as bromine concentrations from the Arabian Sea (Ziegler et al., 2010; Caley et al., 2011b), as well as the Hoti Cave speleothem record in the central Hajar which shows very low $\delta^{18}O$ values at this time (Fleitmann and Matter, 2009). The low gradient of the fan and the finer grain sizes, relative to more proximal locations, suggests that these down-fan reaches would have been characterised by low-energy seasonal flows (Table 4.3). This is consistent with an environment comprised of

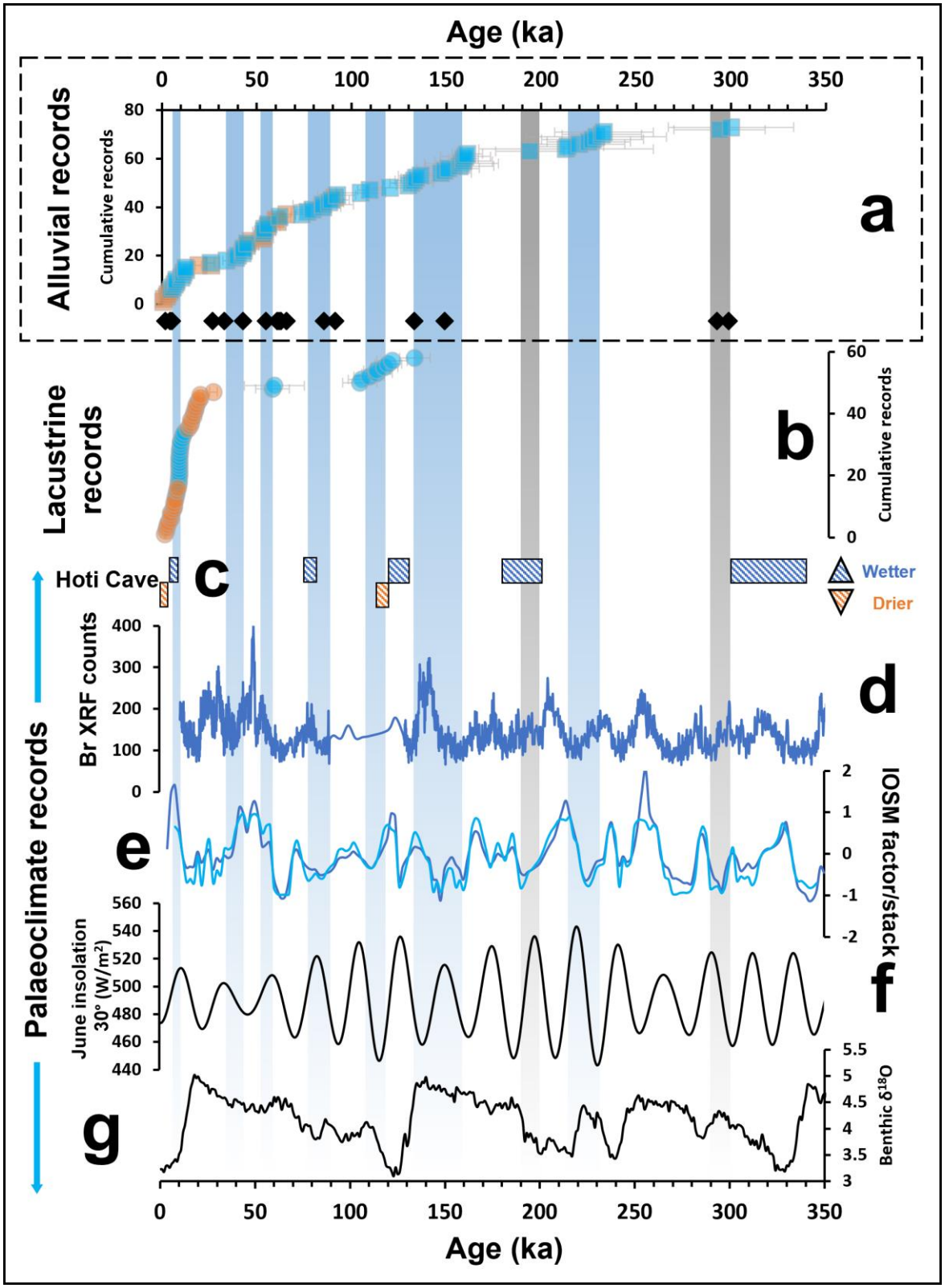

Figure 4.7. Palaeoenvironmental records from the Hajar Mountains. For alluvial and lacustrine records, blue symbols denote wetter conditions than present and orange symbols denote similar or drier conditions to present, based on the interpretations of original authors. **a:** Alluvial records: Dalongeville (1999); Blechschmidt et al. (2009); Farrant et al. (2012); Atkinson et al. (2013); Parton et al. (2015a); Hoffmann et al. (2015); Purdue et al. (2019); Moraetis et al. (2020);

Mueller et al. (2022); Beuzen-Waller et al. (2022); this study. **b:** Lacustrine records: Aqabah (Parton et al., 2013); Maqta (Fuchs and Buerkert, 2008); Wahala (Preston et al., 2015); Awafi (Parker et al., 2006); Saiwan (Rosenberg et al., 2012). Ages from this study are marked by black diamonds. **c:** The Hoti Cave speleothem record (Fleitmann et al., 2011). Marine proxy records from the Arabian Sea: **d:** bromine XRF counts (Ziegler et al., 2010) and **e:** the IOSM factor and stack (Clemens and Prell, 2003). **f:** June insolation at 30°N (Berger and Loutre, 1991). **g:** Global δ18O data from the LR04 benthic stack (Lisiecki and Raymo, 2005). The vertical blue bars denote periods of fan and lake aggradation, identified by a hierarchical cluster analysis conducted on age data from alluvial and lacustrine settings interpreted as being indicative of wetter conditions (see Appendix B for further details). The width of each bar is the interquartile range of each resulting age group. Grey bars denote periods of fan aggradation which are more speculative due to few data points.

Table 4.3. Summaries of site location, luminescence age results and sedimentary interpretations for units discussed in the text.

Site	Location within system	Age (ka)	Sedimentary interpretation of flow conditions
Wadi Sahtan and the Rustaq fan			
OM20/3	Catchment	Lower unit: 61.5 ± 5.5 (MIS 4/3 transition)	Shallow, ponded environment, likely the result of local damming in channel. Seasonal deposition of fine sand.
		Upper unit: 42.4 ± 3.6 - 31.8 ± 3.3 ka (MIS 3)	More sustained seasonal flow within channel than at present.
OM20/4	Catchment	Lower units: 65.6 ± 4.8 – 60.8 ± 5.1 (MIS4/3 transition)	Flashy flow regime within channel, similar to today.
		Upper units: <60 (MIS 3)	More sustained flow regime than today with higher transport competence. Likely coeval with upper units of OM20/3.
OM20/5	Proximal fan	Lower unit: 85.13 ± 15.58 (MIS 5a)	More sustained seasonal flow than today, resulting in periodic deposition onto stabilised floodplain.
		Upper unit: 53.9 ± 6.0 (MIS 3)	More sustained seasonal flow than today within channel.
Ibri and Rustaq fans			
OM20/6	Proximal fan	Lower and upper units: 300 ka (MIS 8/9 transition)	Greater seasonal flow than at present, resulting in deposition onto floodplains.
OM20/8	Medial-distal fan	Lower unit: 133.1 ± 10.2 (MIS 6/5e transition)	More sustained flow regime than today. Aggradation in lower energy environment of low-gradient distal fan.
		Upper unit: 91.1 ± 5.8 (MIS 5b/a transition)	Perhaps similarly intermittent or slightly greater flow regime than present.
OM20/10	Medial-distal fan	Lower unit: 0.7±0.2 (MIS 1)	Similar to present conditions: localised reworking of material during occasional flow events.
OM20/11	Medial-distal fan	Lower unit: 7.5 ± 0.8 (MIS 1)	More sustained flow than present in channel, resulting in development of gravel and sand bars.
		Middle unit: 4.1 ± 0.5 (MIS 1)	Potentially indicative of waning flow regimes following the southwards retreat of the IOSM rain-belt in the Mid-Late Holocene.
		Upper unit: 3.1 ± 0.3 (MIS 1)	Flashy flow regime resulting in local reworking of material, similar to present.
OM20/12	Proximal fan	Lower unit: 149 ± 11 (MIS 6)	More sustained seasonal flow within channel than today, resulting in deposition of thick conglomerate units.
		Upper unit: 25.7 ± 2.1 (MIS 2)	More sustained flow regime on fan relative to present.

*Ages and errors are averaged due to multiple ages from the same unit.

shallow wetlands and low-gradient plains typical for large fluvial fans (e.g. Moscariello, 2018).

The upper unit at site OM20/8 shows the aggradation of the distal end of the Dhank fan at 91.1 ± 5.8 ka (Fig.4.6). Similarly, fan activation is recorded further north in the UAE during early MIS 5a (90-76 ka) where the deposition of silts and gravels has been observed closer to the mountain front (Atkinson et al., 2013) (Fig.4.6). The upper deposit of OM20/8 suggests that the site was characterised by flashy flow regimes at this time, indicating drainage connections with feeder catchments were likely intermittent and perhaps similar to today. Evidence for speleothem growth during MIS 5a at Hoti Cave is absent until 82 ka (Fleitmann et al., 2003). Therefore, the earlier ages recorded at this site and from previously dated fan deposits in the UAE may be evidence of increasing fluvial activity in early MIS 5a, preceding a sufficient groundwater/throughflow threshold for speleothem growth. Site OM20/5 on the Rustaq fan records slightly later aggradation during this period at 85.13 ± 15.58 ka, with evidence of floodplain stabilisation as part of a braided channel network on the fan surface (Table 4.3). This age is coeval with periods of aggradation under more sustained streamflow conditions relative to today from the northern Hajar (Atkinson et al., 2013; Parton et al., 2015).

The next phase of aggradation is during late MIS 4-3, with age results from Wadi Sahtan and the Rustaq fan between ~65-40 ka (Fig.4.5). The basal, interstratified sands and gravels of OM20/4 suggest a flashy flow regime from 65-60 ka, indicating deposition under arid conditions with low flow competency. MIS 4 (75-60 ka) is often inferred to be very arid in southeast Arabia, due to the absence of speleothem growth recorded in Hoti Cave and the presence of dated dune sediments that have been interpreted to reflect increased dune mobility (Parker, 2010). Recording fluvial aggradation during this period is, therefore, unexpected under the IOSM model of alluvial aggradation but requires an understanding of site location and fan flow behaviour. The location of site OM20/4 in the upper part of the eastern fan-catchment system potentially means that it is more sensitive to changes in precipitation, preserving a signal of aggradation during arid MIS 4

because of the higher flow competency of wadis in their mountainous reaches, compared to downstream fans (Table 4.3). Significantly, the wadis which drain to the southern Batinah Coast frequently flow in their upper reaches under present climate conditions (some perennially), fed predominately by winter rainfall from the north-west. However only the largest, rare, flood events reach their distal fans (Shahin, 2007).

Site OM20/3 shows aggradation during MIS 3, with the basal section dated to 61.5 ± 5.5 ka (Fig.4.5). The finely laminated sediments of this unit suggest the channel was dammed downstream, creating a barrier to transport and creating a shallow lacustrine environment in which sediments slowing settled during deposition. Being situated at a confluence and in the steep, mountainous setting of the lower catchment feeding the Rustaq fan, it is reasonable to suggest that this could have been caused by a landslide, as recorded coevally in the nearby catchment of Wadi Mistal (Hoffmann et al., 2015). The sharp contact with the overlying unit of coarser fluvial sands shows an eventual catastrophic breaching of the dam and an increase in flow competency by 42 ka (Fig.4.5), with sediments continuing to coarsen upwards into overlying larger gravels and conglomerate material. Similar coarsening up sequences are observed downstream at site OM20/4 which are younger than 60 ka and can be observed along the exposed valley-fill between the two sites (Fig.4.5). An MIS 3 age of 53.9 ± 6 ka is also recorded in the upper unit of bedded sands at OM20/5 (Fig.4.5), indicating the wider and sustained drainage connection between mountain catchments and more distal fan settings. Multiple alluvial records from the western Hajar fans also indicate increased flow during this time (e.g. Parton et al., 2013; 2015a; Mueller et al., 2022; Fig.4.7). Marine proxies from the Arabian Sea similarly suggest enhanced monsoon precipitation, in line with precessional maxima (e.g. Clemens and Prell, 2003; Fig.4.7), as do palaeoclimate model simulations (Jennings et al., 2015). However, in the nearby Wadi Mistal catchment, Hoffmann et al. (2015) interpret alluvial sedimentation rates during MIS 3 to be similar to today's, conflicting with our record from Wadi Sahtan. The Hoti Cave speleothem also does not record growth during this period (Fleitmann et al.,

2003). Ultimately, enhanced precipitation in the Hajar during MIS 3 remains debated, although our data support this theory.

The upper sand unit of OM20/12 near the apex of the Dhank fan yielded an age of 25.7 ± 2.1 ka (Fig.4.6). Whilst the sedimentary interpretation for this unit is that it represents proximal floodplain deposition, this age dates to MIS 2 during precessional minima. Whilst there are other fan sediments from the region dating to this period (e.g. Mueller et al., 2022; Beuzen-Waller et al., 2022), they show sedimentary evidence for being deposited by flashy floods under more arid climate regimes. The unit fines upwards, indicating waning streamflow. Therefore, given potential dating uncertainties, this unit may represent reducing rainfall at the termination of the wetter period during MIS 3 (~30 ka).

Sites OM20/10 and -/11 record aggradation in western Hajar fan systems during the Holocene (Fig.4.6). An age of 7.5 ± 0.8 ka from the basal unit of OM20/11 shows the sustained flow of drainage systems at this time. This is in agreement with numerous palaeoenvironmental records from across the region which show intensified hydrological systems during the Arabian Holocene Humid Period (AHHP), ~10-6 ka, such as lakes and rivers (e.g. Woor et al., 2022a), as well as speleothem and marine core records evidencing the northwards incursion of the IOSM (e.g. Sirocko et al., 1993; Clemens and Prell, 2003; Fleitmann et al., 2007; Fig.4.7). The distal setting of OM20/11 suggests that flows reached the fringes of the interior Rub' al Khali, although with reduced competency and were likely still highly seasonal. It is unlikely that intensified IOSM precipitation directly penetrated as far inland as the distal extent of the Ibri and Dhank fans. While dune records suggest that northern and more coastal Rub' al Khali landscapes may have been stabilised (Thomas and Bailey, 2019), lacustrine records from the interior of southern Oman suggest that increased freshwater availability was the result of drainage connections with more coastal catchments and higher groundwater tables rather than direct meteoric inputs (e.g. Matter et al., 2015; Woor et al., 2022a).

The age of 4.1 ± 0.5 ka from sample OM20/11/2 indicates that flows reached the medial-distal parts of the Dhank fan later than the termination of the AHHP at ~6 ka. Other fan deposits in the region have been dated to the Mid-Late Holocene, such as at Mleiha (Dalongeville, 1999) and in the Emirate of Sharjah where luminescence ages from episodic flood deposits directly correspond with OM20/11/2 (Mueller et al., 2022).

The later Holocene ages of 3.1 ± 0.3 ka and 0.7 ± 0.2 ka from the upper unit of OM20/11 and OM20/10 (Fig.4.6), respectively, have greater grain size sorting coefficients relative to those from the other fluvial deposits reported (Table 4.2). This could be the result of lower discharge depositing a more narrow range of grain sizes as has been observed for other dryland fluvial systems which have undergone transitions from relatively wetter to drier climates (e.g. Walsh et al., 2022a), or the local reworking of aeolian sediments which typically display a higher degree of grain size sorting than fluvial sediments (e.g. Nottebaum et al., 2014; Kapui et al., 2018). Both scenarios suggest the reduced and more localised nature of flows in the medial-distal reaches of the Dhank fan during the Late Holocene, consistent with a more arid climate depicted in regional palaeoclimate records (e.g. Clemens and Prell, 2003; Fleitmann et al., 2011; Fig.4.7). The medial distal units of western fans, therefore, indicate a switch from a more connected sediment routing system between catchments and fans to a disconnected one during the Mid-Late Holocene. At this time, sediment transport on the distal, interior bajada became dominated by aeolian processes and only occasionally moved by fluvial processes during localised rainfall events or large flash floods.

4.6.2 Hajar alluvial fans as sensitive records of IOSM rainfall

This study aims to test whether the timing of aggradation of alluvial systems in the central Hajar are paced by IOSM rainfall variability over the Late Quaternary. The periods of aggradation reported from our sites which preserve sedimentary evidence of higher streamflow conditions relative to present support this model. Taken together with other data from regional alluvial and lacustrine systems, periods of greater hydrological activity occur clustered at 9, 38, 57, 84, 112, 147, 224 and

297 ka (mean ages from hierarchical clustering analysis; see Appendix B). This periodicity broadly aligns with proxy records that indicate higher rainfall in the Arabian Sea and Hoti Cave region, driven by insolation increases (Berger and Loutre, 1991; Ziegler et al., 2010; Caley et al., 2011b). These periods of alluvial and lacustrine deposition tend to align with precessional maxima, especially over the last 100 ka (Fig.4.7).

Whilst long-term variability in IOSM precipitation is driven by precessional cycles (e.g. Caley et al., 2011), larger scale drivers may also be important for determining rainfall and environmental conditions in south-east Arabia. Hoti Cave speleothem growth only occurs during interglacial periods at eccentricity timescales (~100 ka periodicity; Fleitmann et al., 2003; Lisiecki and Raymo, 2005; Fig.4.7). Burns et al. (2001) suggest that warmer sea surface temperatures during interglacials would result in increased water vapour transport in Indian Ocean air masses, leading to increased precipitation. Higher IOSM rainfall during precessional maxima coinciding with Northern Hemisphere interglacial periods potentially amplified hydrological activity in alluvial systems as a result, when compared to precessional maxima that occurred during glacials (e.g. MIS 3). This may explain why fan and lacustrine ages indicative of more sustained drainage activity do not produce discrete mean age clusters confined to precessional peaks from 150-100 ka (Fig.4.7), whereas during glacials they do. Therefore, interglacial conditions may have dampened the influence of precessional minima on regional rainfall during this time. The continued growth of the Hoti Cave speleothem from 120-110 ka (Fleitmann et al., 2003), following the transition from wetter MIS 5e to drier 5d, as well as evidence of more sustained flow conditions in fan and lake systems support this hypothesis.

This hypothesis of south-east Arabian rainfall being driven by the complex overprinting of precessional and eccentricity signals may explain the discrepancies between some periods of fan aggradation and the $\delta^{18}O$ record from the Hoti Cave speleothem. Fan aggradation during MIS 6 and 3 occurs during periods when the Hoti Cave speleothem ceased to grow (Fleitmann et al., 2003)

(Fig.4.7). Previous authors have suggested that this discrepancy could be because fluvial systems in the Hajar have a lower threshold for activation. The Hoti Cave speleothem requires >300-350 mm of rainfall for stalagmites to form (Vaks et al., 2006; Fleitmann et al., 2011; Parton et al., 2015a; Nicholson et al., 2020). Modern observations of wadi flow in the mountainous catchments of the Hajar support the idea that streamflow occurrence has a lower precipitation threshold, with seasonal flows occurring under present mean annual rainfall levels of 142.6 mm yr^{-1} for the Hajar Mountains (Shahin, 2007; Kwarteng et al., 2009), half of the >300-350 mm threshold required for speleothem growth. Therefore, even small increases in regional rainfall are more likely to result in alluvial aggradation, as occur with precessional peaks during glacials, relative to the larger increases in rainfall when precessional peaks coincide with interglacials and rainfall becomes sufficient for speleothem growth to occur.

The sensitivity of regional drainage networks to small increases of rainfall is further evidenced by an increasing number of fan and valley-fill deposits dated to periods when the IOSM model predicts rainfall intensity would have been lower in south-east Arabia, such as the sediments from Wadi Sahtan dating to MIS 4 (Fig.4.5). Fluvial deposits from drier periods have also recently been dated to ~20 ka and the Late Holocene (0-3 ka) in the UAE (Mueller et al., 2022). However, the sedimentary interpretations of both Mueller et al. (2022) and in this study suggest that these sediments were deposited by more intermittent flows than the bedded, coarser materials typically observed in association with periods of more intense IOSM rainfall. These deposits possibly represent similar low-frequency, high-magnitude events to those which occur across the Hajar region today (Kwarteng et al., 2009), with flows only periodically having sufficient energy to transmit sediment out of mountainous catchments to distal fan systems. As such, careful interpretation must be made of these deposits in terms of the hydrological signal they preserve.

The sites sampled in Wadi Sahtan are also all located within the mountainous setting of a fan-feeding catchment. Numerous ages assembled in the Synthesising Chronologies of Arabian

PalaeoEnvironments (SCAPE) database from catchment settings in the Hajar show similarly 'anomalous' hydrological activity, relative to established periods of greater regional precipitation, in fluvial systems (Woor et al., 2022a). For example, the Maqta basin in the southern-central Hajar records deposition almost continually over the last 20 ka, except for a hiatus from ~12-10.5 ka (Fuchs and Buerkert, 2008), as well as Wadi Dishshah in the southern Hajar recording sedimentation at ~26 ka (Beuzen-Waller et al., 2022). However, these ages at odds with the IOSM model are to be expected in mountainous settings due to the higher likelihood of flow occurrence in the steeper, elevated uplands of the Hajar. These are unlikely to transmit sediment further downstream in the system under periods of regionally more arid climate such as today (Shahin, 2007).

This could account for periods of fan aggradation mainly occurring during periods of increased IOSM intensity, whilst records from valley-fill sediments in the upper parts of fan-catchment systems are seemingly more continuous. This is because flows only have the sustained competence to contribute significant sediment loads downstream beyond mountain fronts during the wettest regional conditions. Burial ages recorded for deposits situated on fans which do not fit the IOSM model similarly seem to be the result of the localised reworking of material in response to intermittent flow activity under a more arid climate.

Finally, this chapter has already commented on the limited spatial coverage of previously published records from alluvial settings in the Hajar. Sampling is also biased by the inherent spatial heterogeneity of large fan systems where active channels tend to incise through relict, inactive surfaces and avulse across the fan over time (Bryant et al., 1995). As such, the temporal signals preserved by fans will be spatially heterogeneous. This is evidenced in this study: for example, this study records no deposition at the sites sampled from ~220-230 ka which other studies have shown to be a key period of Hajar fan aggradation (e.g. Parton et al., 2015a; Mueller et al., 2022). Contrastingly, the al Sibetah fan (Parton et al., 2015a) records no Early-Mid Holocene aggradation and the deposits in the eastern UAE dated by Mueller et al. (2022) record no aggradation from 135-

120 ka, both of which have also been established as key periods of regional fan aggradation. This does not necessarily mean that these systems did not respond to these periods of increased intensity and northwards displacement of the IOSM, but rather building a complete picture of Late Quaternary responses is difficult with spatially complex deposits. Taking a multi-site approach to sampling fan deposits, as adopted in this study, as well as amalgamating data from similar depositional settings is potentially means for resolving this issue.

In addition to spatial resolution, considering temporal resolution with regards to this discussion is also important. The precision of OSL dating is usually ~±10% (Mejdahl and Christiansen, 1994; excluding the very young age of OM20/10/3 the mean uncertainty of ages in this study is ±10.2%; Table 4.1). Therefore, environmental changes at ~23 ka periodicity can only be clearly distinguished over approximately the last 100-120 ka, beyond which the precision limits on OSL dating make drawing conclusions between cause and effect more difficult. Similarly, more rapid environmental and climatic changes at sub-orbital timescales are also difficult to resolve within current precision limits, yet rapid drying associated with the 8.2 ka and 4.2 ka events are resolved by radiocarbon dating in lacustrine records from the north-western Hajar (Parker et al., 2016). Despite these challenges, the OSL dating and stratigraphic interpretations of alluvial sediments in the Hajar provide an important long-term environmental record for a region where other proxies are limited.

4.7 Conclusions

The alluvial fans of the Hajar Mountains, south-east Arabia, are the most extensive and continuous terrestrial records of the region's palaeoenvironmental and palaeohydrological variability over the last 300 ka. Through the wide spatial sampling of alluvial sediments both east and west of the Hajar Mountains, this study identifies periods of sustained flow and fan aggradation occurring during MIS 9/8, MIS 6, MIS 5e, 5a, 3 and the Holocene. These main aggradation phases are driven by the northwards displacement of the IOSM and, when considered alongside findings from other fan systems in the region, build an increasingly comprehensive picture of precessionally-paced fan

aggradation throughout the Late Quaternary. Whilst the interpretation of some periods, such as MIS 3, remain debated due to conflictions within the regional palaeoenvironmental and palaeoclimate proxies, it is suggested that the sensitivity of drainage systems in the Hajar is such that signals of higher rainfall and subsequent streamflow are more readily preserved than other records.

Additionally, this study also finds evidence of palaeohydrological activity and deposition not being limited to these periods of increased rainfall, relative to the present. Fluvial deposits dating to the Late Holocene and MIS 4 represent apparent anomalies in this framework of the IOSM model of fan aggradation, occurring during more arid periods in south-east Arabia. Present aridity does not entirely preclude the region's wadi systems from flowing, with episodic flooding or seasonal flows in response to winter rainfall being commonplace, especially in catchment settings. Therefore, these seemingly anomalous ages are attributed to similar types of activity in the past: it does rain in deserts during arid periods and sediment does move through fluvial systems when this occurs.

The resulting interpretation is one of mountain catchments which retain a certain degree of flow activity throughout periods of broad regional aridity, with occasional high-magnitude, low-frequency events connecting fans and catchments or causing the localised reworking of sediments. Overprinted on this are signals preserved from periods of precessionally-paced increases in the intensity of the IOSM and its northwards displacement, resulting in more sustained periods of flow, higher stream competency and significant fan aggradation, which are amplified during eccentricity-paced interglacial periods.

There is a growing awareness of the nuances of the palaeoenvironmental signals preserved in a variety of geomorphological, isotopic and biological proxies across south-east Arabia that move beyond an overly simplistic narrative of the region being either 'wet' or 'dry' (Petraglia et al., 2020; Woor et al., 2022a; Mueller et al., 2022). The alluvial sediments of the Hajar Mountains paint an increasingly complex picture of landscape responses to Late Quaternary climate variability, as well

as having important implications for an increasingly complex archaeological record of hominin occupation in the region (e.g. Bretzke et al., 2022).

5 | Morphology and controls of the mountain front fan systems of the Hajar Mountains, south-east Arabia (Paper 2)

Authorship: Sam Woor, David Thomas, Ash Parton, Anya Leenman

This chapter is based on a research paper of the same name, published in the journal Earth-Science Reviews, January 2023. A number of changes have been made to the version in this chapter to ensure continuity of text and avoid over-duplication of background material in the thesis. This chapter meets Research Objective 2 (Section 1.2).

5.1 Paper abstract

Mountain-front fans are an important part of the global sediment system, acting as buffers and stores of sediment between upland sources and down-system sinks. Fans emanate from the Hajar Mountains in the eastern UAE and northern Oman which have developed from morphologically and geologically variable catchments and in a range of depositional settings, as well as spanning a wide range of shapes and sizes. There has been little prior research into the drivers of regional fan evolution and morphology at the landform scale, considering specific factors such as source-area morphology and geology and distal settings. Remotely-sensed data is used to map 438 fans and catchments along mountain fronts in Oman and the UAE. These data provide, for the first time, a regional overview of fan morphology using key morphometric parameters and demonstrate the utility of a remote sensing approach to understanding regional landform morphology of features at a range of spatial scales (10^{-3}-10^{4} km^2).

Comparing this large dataset to studies of dryland fans globally, the data show that Hajar fan morphology spans almost every order of magnitude previously recorded elsewhere. It shows statistically the importance of diverse catchment and depositional setting controls on alluvial fan morphology. Across the different mountain fronts of the Hajar range, fan morphology is controlled by 1) catchment morphology and geology, 2) changes in base level and 3) long-term climatic changes and tectonic processes, although the importance of these factors relative to one another is highly spatially variable. The fans of the Musandam Peninsula drain more recently uplifted rocks, are situated in an area of subsidence and have experienced foreshortening due to Quaternary sea-

level variability, hence produce the smallest, steepest fans. Similarly, many of the fans of the Batinah Coast are influenced by distal foreshortening by sea-level rise and demonstrate weak regression relationships with their catchment morphologies. By contrast, the large fans of the Rub' al Khali are mostly distally unconfined and drain large catchments formed during earlier phases of uplift, thus producing large fans and megafans with the strongest fan-catchment morphometric relationships. The Wahiba Sands fans are similar to those of the Rub' al Khali but are limited in their extent by erosion from an axial river system. As such, the fans of the Hajar are an important natural laboratory for investigating alluvial fan morphology, processes and long-term evolution in response to a range of controls. This includes potentially acting as analogues to extra-terrestrial fan systems due to their large scales in some areas and their dryland context. For example, the largest megafans of the Hajar display morphometric similarities to large fluvial fans reported on Saturn's moon, Titan, perhaps suggesting comparable long-term controls.

5.2 Introduction

Fan systems are conical splays of sediment which form where there is a sudden reduction in the confinement of sediment transport (Harvey, 2011). This commonly occurs where confined, often relatively steep, upland valleys transfer sediment into zones of less confinement and reduced gradients, such as along mountain fronts or at tributary junctions (Blair and McPherson, 2009). The form of mountain-front fans typically exhibits strong relationships with the morphological, lithological and other characteristics of their feeding catchments (e.g. Bull, 1968; Lecce, 1991; Densmore et al., 2007), since these control the rates and processes of sediment production and down-system sediment transport which result in fan formation. However, fan morphology and long-term evolution are also influenced by extrinsic factors such as tectonic activity (e.g. Goswami et al., 2009), base level changes (e.g. Harvey, 2002) and climatic change (e.g. D'Arcy et al., 2017).

5.2.1 Alluvial fan morphometry

Power-law regressions describe fan-catchment relationships determined from field and remote sensing measurements (Equations 2.1, 2.2), whereby fan morphometric parameters are the dependant variables of catchment morphometric parameters (Fig.5.1). Typically, the strongest power-law regressions tend to be between catchment area and either fan area or gradient (Harvey, 2011).

The directionality of these steady state relationships is the result of fundamental processes occurring in the sediment cascade (Hooke, 1968). In the case of Equation 2.1, a positive power-law relationship would be expected because as catchment area increases so too does the volume of sediment discharged (Allen and Hovius, 1998). Conversely, a negative power-law relationship is expected from Equation 2.2 because as catchment size increases the concentration of sediment in flow downstream decreases due to their higher water discharge. This increases the water-sediment ratio and as a result fan gradient decreases (Harvey, 2011). Put simply, one should expect larger, less steep fans from larger catchments (Bull, 1977; Blair and McPherson, 2009; Bowman, 2019).

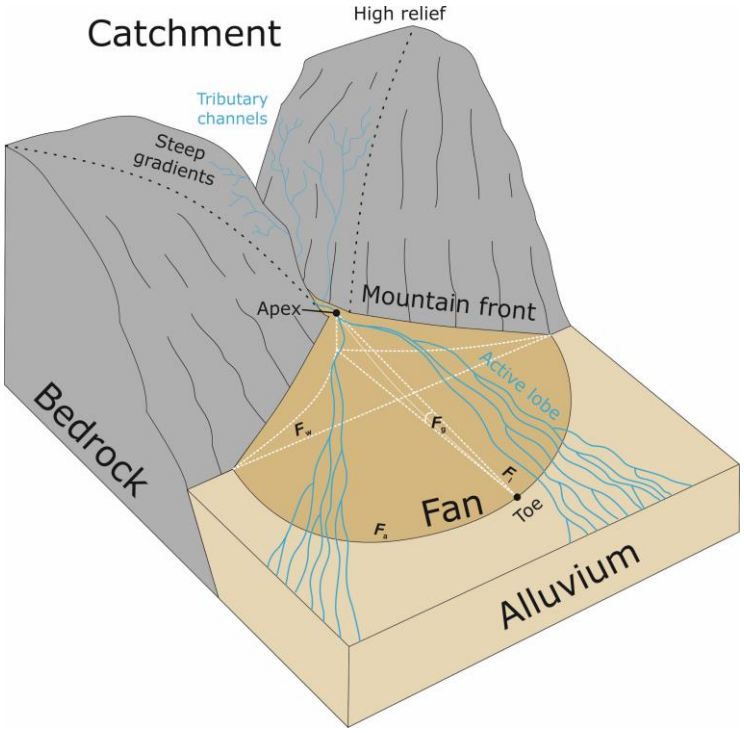

Figure 5.1. Schematic diagram showing the morphology of a typical unconfined fan in a mountain front setting and key morphometric parameters utilised in previous studies such as fan area (F_a), width (F_w), length (F_l) and gradient (F_g) and typical catchment characteristics.

Correlation coefficients (R^2 values) describe the strength of these regression relationships, i.e. the proportion of the scatter in the dependent variable (e.g. F_a in Equation 2.1) which can be explained by the independent variable (e.g. C_a in Equation 2.1). The R^2 statistics of fan-catchment morphometric regressions therefore statistically represent the coupling of fan morphology to that of their catchments. Regressions of fans in unconfined settings with fewer other controls on their morphology (e.g. erosional processes at their toes), such as those found in many mountain front settings (e.g. Viseras et al., 2003), may be expected to have stronger R^2 statistics closer to 1. This is opposed to fans in more complex depositional settings such as along coasts or at tributary junctions which typically have weaker morphometric relationships with their catchments (e.g. Stokes and Mather, 2015; Stokes and Gomes, 2020).

Previous studies have shown the utility of plotting the residuals of the F_a v. C_a and F_g v. C_a regression relationships as a means of examining how fan morphometry responds to non-quantifiable

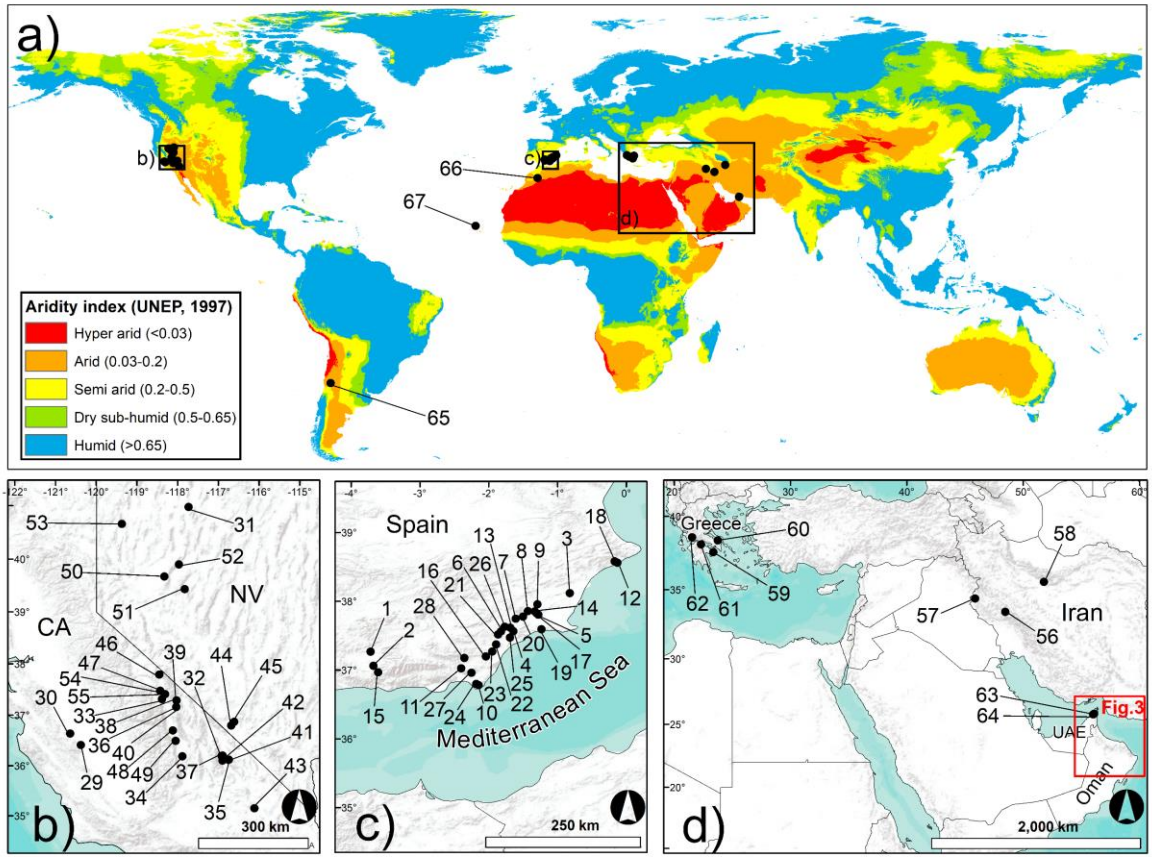

Figure 5.2. (a) The global distribution of dryland fan morphometric studies (see Appendix C for references and locations). The Global Aridity Index (UNEP, 1997) is a function of annual precipitation, temperature and evapotranspiration (data from Trabucco and Zomer, 2018). Fan morphometric studies in **(b)** the SW USA in California (CA) and Nevada (NV), **(c)** southern Spain, **(d)** Greece and SW Asia. The red box denotes the Hajar Mountain region of the UAE and northern Oman, detailed in Figure 5.3.

variables such as fan setting and catchment lithology (e.g. Silva et al., 1992; Harvey, 2002; Tomczyk, 2021). As such, these morphometric analyses provide an important tool for inferring the controls on fan morphology and allow comparisons between landform evolution in different geological and geomorphic settings. Figure 5.2 shows the locations of previous dryland fan morphometric studies.

5.2.2 Hajar Mountain fans and previous morphometric work

This analysis builds on previous work carried out on the extensive fan systems of the Hajar Mountains of Oman and the United Arab Emirates (UAE) to provide a regional overview of fan systems and their controls.

Generally, fans dominated by fluvial processes, primarily braided streamflow and sheetflooding (Weissmann et al., 2010), display greater planform areas and lower axial gradients than debris flow- or colluvial-dominated fans (Ventra and Clarke, 2018). Whilst contemporary channel activation is highly episodic under the arid climate of the region (Al-Rawas and Valeo, 2010), major phases of Hajar Mountain fan aggradation occurred throughout the Mid-Late Pleistocene and Early Holocene (e.g. Blechschmidt et al., 2009; Parton et al., 2013; 2015a), as discussed in Chapter 4. These coincided with periods of increased Indian Ocean Monsoon rainfall intensifying hydrological activity in mountain catchments, shown in speleothem (e.g. Burns et al., 2001; Fleitmann and Matter, 2009; Nicholson et al., 2020) and marine core records (e.g. Clemens and Prell, 2003; Caley et al., 2011b).

The large diversity in fan morphologies, their depositional settings and catchment characteristics along the Hajar range offers a natural laboratory to explore controls on fan evolution. However, relatively little work has been carried out on fan-catchment morphometric relationships in the region. The only previous morphometric survey was conducted by Al-Farraj and Harvey (2005) and focused on the morphology of debris-cones, tributary-junction and mountain-front fans in the Wadi Al-Bih region of northern UAE. They found that regional fan morphology was strongly controlled by variable accommodation space between unconfined mountain-front and confined tributary-junction settings. The controls on mountain-front fan morphology for the Hajar Mountains more broadly, however, remain a significant unknown.

This study aims to address these knowledge gaps for the Hajar mountain-front fans to better understand the evolution of the region's landscapes, first identifying and then comparing the non-climatic controls on fan morphology in different regions of the Hajar. Specifically, the non-climatic controls investigated through the remote sensing methodology are: catchment morphology, geology and fan setting. The longer-term controls of tectonics and climate variability on regional fan morphology will also be discussed. However, the scope of this study extends beyond just the Hajar as a large dataset of fan morphometric characteristics is generated for fans with diverse

controls. The utility of these analyses is demonstrated by drawing together the most comprehensive summary of dryland fan morphometric data so far published, including for fans from extra-terrestrial contexts.

5.3 Regional setting

5.3.1 Geological setting

The arcuate Hajar Mountains are oriented south-east to north-west, running 700 km from central Oman to north-eastern UAE, reaching approximately 3000 m asl at their highest point (Fig.5.3a, b). Situated along the north-eastern margin of the Arabian Plate, the position of the Hajar Mountains is in part the result of the rifting axes of the Gulf of Aden and the Red Sea to the south and west of the Arabian Peninsula, respectively, with a resulting collisional boundary to the north-east with the Eurasian Plate forming the Zagros and Makran fold and thrust belts (Glennie et al., 1990; Kusky et al., 2005). The zone of this active collision between the Arabian and Eurasian Plates is denoted by the Makran Subduction Zone, located off the coast of Oman in the Arabian Sea (Hoffmann et al., 2020; Fig.5.3a, b).

The Hajar is divided into four main geological groups. The principle lithological group of the Hajar is the exposed ancient oceanic crust comprising the primarily basaltic Semail ophiolite (Fig.5.3a). Along with the slope and basin units of the Hawasina nappes, this is the product of Late Cretaceous obduction commencing at approximately 104 ma as a result of the closing of the Tethys Ocean (Guilmette et al., 2018; Moraetis et al., 2018). The poste-nappe package is comprised of Late-Cretaceous to Eocene carbonates (Corradetti et al., 2020). Uplift continued at variable rates until the Oligocene and Neogene (Ninkabou et al., 2021) and it is during this time that the Hawasina Window, Jabal Akdhar and Saih Hatat domes of the Pre-Cambrian and Permian carbonates comprising the Arabian Proximal Domain were upwarped (Searle, 1988; Moraetis et al., 2018).

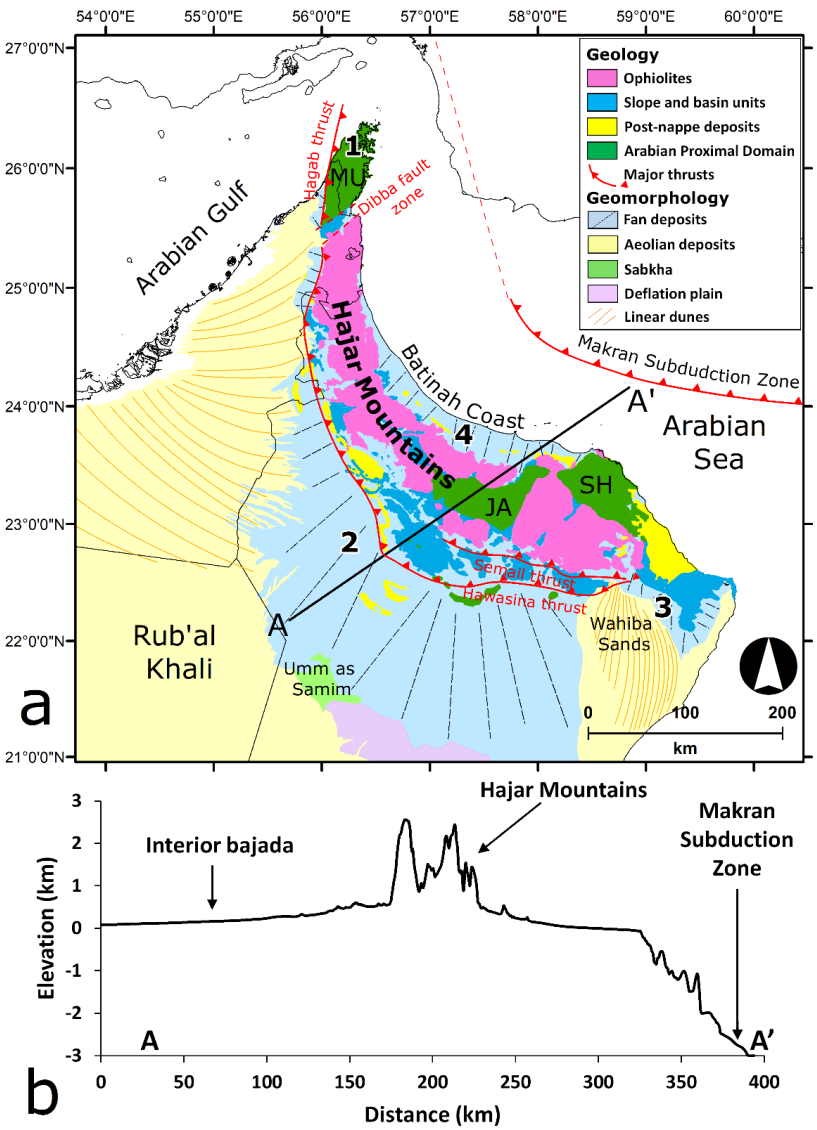

Figure 5.3. (a) Regional geology and geomorphology of the Hajar Mountains, south-east Arabia, showing major thrusts zones, lithological groups and principle landform types (geology redrawn from Corradetti et al., 2020). The exhumed domes of the Arabian Proximal Domain are as follows: Hawasina Window (Musandam; MU), Jabal Akdhar (JA) and Saih Hatat (SH). Four key areas of the mountain front were studied: 1) the Musandam Peninsula (MP), 2) the Rub' al Khali (RK), 3) the Wahiba Sands (WS) and 4) the Batinah Coast (BC). **(b)** Cross sectional elevation profile from the interior bajada to the Makran Subduction Zone in the Arabian Sea.

Throughout the Quaternary Period, the Hajar Mountains are generally considered to have been tectonically relatively quiescent; however, uplift is still active in the region (Abrams and Chadwick, 1994; Kusky et al., 2005; Yuan et al., 2016; Moraetis et al., 2018), although it is poorly locally constrained in many places. For example, Hoffmann et al. (2020) showed that raised marine

terraces in the south-eastern Hajar Mountains revealed a variable uplift rate of 0.1-0.89 mm/a throughout the Mid Quaternary. The highest marine terraces in the south-eastern Hajar along the Arabian Sea Coast suggest uplift in excess of 100 m throughout the Pliocene and Quaternary (Kusky et al., 2005). This is in contrast to the Musandam Peninsula, which has been subsiding since the initiation of subduction of the Arabian Plate under the Eurasian Plate at approximately 22 ma (Ali et al., 2018), resulting in a tilting of the Hajar Mountains which continues to the present. Kusky et al. (2005) provided a regional map of identified faults which are extensive across the Hajar Mountains, however data on specific slip rates are scarce in the literature. Therefore, it is difficult to comment on the specific relationships between local faulting and fan morphology in many of the areas covered in this study, thus this analysis relies on the regional-scale patterns of uplift and subsidence previously outlined.

5.3.2 Geomorphological and climatological setting

Bajadas occur in two main areas, extending 1) north- and eastwards from the Hajar to the Arabian Sea, forming the Batinah Coast, and 2) south- and westwards from the Hajar into the interior Rub' al Khali Desert and Arabian Gulf coastline, following the Hawasina thrust (Fig.5.3; Fig.5.4a, b). The bajada narrows northwards on the interior, western, side of the Hajar Mountains as the geometry of south-east Arabia narrows into the Musandam Peninsula in the Gulf of Oman, and follows the arcuate shape of the mountains on the Batinah Coast (Fig.5.3). A smaller bajada is located between the northern extent of the Wahiba Sands and the southern Hajar mountains (Fig.5.3a). Smaller mountain-front fans are found in coastal settings around the rugged Musandam Peninsula, north of the Dibba fault zone (Fig.5.3a). The Musandam Peninsula (MP), Rub' al Khali (RK), Wahiba Sands (WS) and Batinah Coast (BC) fans form the four key focus areas for this study (1-4 Fig.5.3a, respectively).

The fans primarily form low-gradient gravel plains which extend up to 125 km at their widest point south of the Hajar Mountains. These deposits exhibit varying degrees of desert pavement

formation; darker surfaces being relatively older than brighter ones as a result of ongoing weathering and rock varnish accretion on clast surfaces (e.g. Abrams and Chadwick, 1994; Al-Farraj and Harvey, 2000; Al-Farsi and Cookson, 2002; Fig.5.4d). Older surfaces are extensively incised by younger, ephemeral stream networks (Fig.5.4c), however the southern-most fans also preserve inverted paleochannel features (e.g. Maizels, 1987; 1990; Maizels and McBean, 1990). Internal fan architecture typically displays inter-stratified coarse gravel-supported channel-fill and overbank deposits and aeolian sands (e.g. Parton et al., 2015a; Fig.5.4c). Luminescence dating studies have shown that periods of fan deposition predominately relate to periods of increased rainfall in the region throughout the Late Quaternary (e.g. Blechschmidt et al., 2009; Parton et al., 2015; Mueller et al., 2022; Chapter 4), with more recent overlying aeolian deposition during the Terminal Pleistocene and Late Holocene (e.g. Atkinson et al., 2011; Leighton et al., 2013).

Whilst exoreic coastal fans terminate in the Arabian Gulf and Arabian Sea, the distal extremities of inland-draining, endoreic systems terminate in contemporary sabkha such as the Umm as Samim basin in central Oman (Fig.5.4a), the relicts of former lakes and wetlands (e.g. Parker et al., 2006; Rosenberg et al., 2012). South-east of the Umm as Samim is a large deflation plain that covers much of the south-western interior of Oman (Glennie and Singhvi, 2002; Fig.5.4a). The aeolian dunes of the Rub' al Khali are also a characteristic feature of the region (Fig.5.4a), extending from coastal sources over much of the alluvial plain in the northern UAE (Farrant et al., 2019), as well as the distal ends of fans in the central interior bajada (Fig.5.4e). Other significant areas of aeolian-alluvial interaction include the fans in the southern interior adjacent to the Wahiba Sands dunefield (Blechschmidt et al., 2009; Fig.5.4a) and smaller areas of linear dunes deposited in the inter-fan regions of the Batinah Coast.

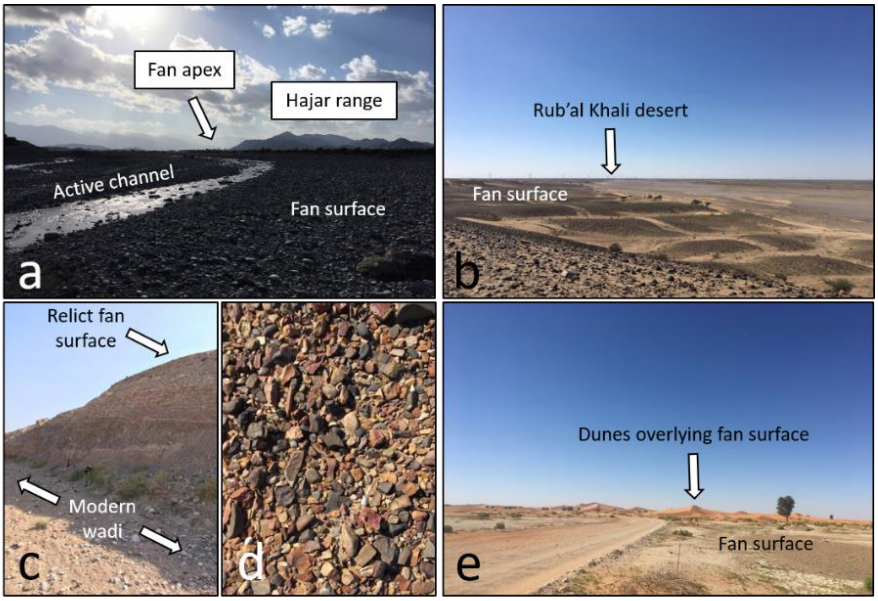

Figure 5.4. Hajar mountain front fans in Oman (January 2020). Landscape views of fan surfaces highlight their very low gradient, with **(a)** and **(b)** showing fan surfaces near Rustaq on the Batinah Coast and near Ibri on the interior bajada, respectively. **(a)** Shows the activation of a shallow surface channel in response to recent rainfall. **(c)** Older fan material has been incised by more recent streamflow, revealing internal architecture. **(d)** Fan surfaces are mantled by desert pavements showing varying degrees of clast varnishing. **(e)** At their medial-distal extents, interior-draining fans are overtopped by Rub' al Khali dune systems (shown by the view of the fan surface, foreground, over-topped by large linear dunes, background).

5.4 Methods

5.4.1 Mapping

Fan delineation

The Hajar mountain fans are difficult to delineate for two reasons. 1) They form coalesced bajadas, making it difficult to distinguish one fan from its neighbours where they merge. 2) For interior-draining systems, overtopping by dunes from the Rub' al Khali and Wahiba Sands adds a potential uncertainty to the ultimate extent of systems. As such, a range of satellite remote sensing products was utilised to map them in an attempt to maximise the discrimination of individual features.

An initial survey used high resolution satellite imagery in Google Earth (see Table 5.1 for details of the remote sensing products used in this study). However, the similar colouring of bajada surfaces still made identifying individual systems difficult in some instances. Cloud-free Landsat 8 scenes acquired from 01/06/2021-06/08/2021 were therefore downloaded and assembled into a combined raster of the study area in ArcMap 10.8 (Table 5.1). Various false-colour composite images were generated where red, green and blue (RGB) channels (Landsat 8 bands 4, 3 and 2, respectively) are replaced with bands of other spectral wavelengths. These images enhance the contrast between surfaces (Figs.5.5a, 5b), as has been applied in other studies of dryland alluvial fans to delineate different surfaces (e.g. Abrams and Chadwick, 1994; Singh et al., 2007; D'Arcy et al., 2018).

Synthetic aperture radar (SAR) data were further used to delineate fans. SAR is sensitive to surface textures, so that the radar back-scatter 'brightness' responds to variations in grain size and soil moisture (Paillou, 2017). L-band SAR (with a frequency of 1.25 GHz) can penetrate through several meters of dry soils, making it ideal for mapping palaeodrainage features that are obscured in optical imagery by shallow veneers of dry aeolian sand (e.g. Paillou et al., 2010; 2020; Abdelkareem et al., 2020). Terrain-corrected scenes with a 12.5 m resolution from the Advanced Land Orbiting Satellite

1 Phased Array L-band Synthetic Aperture Radar (ALOS PALSAR) instrument, acquired in 2010, were compiled in the same way as the Landsat 8 imagery (Table 5.1; Fig.5.5c, d). Whilst uncertainty remains where dunes are thick and impenetrable to SAR, sub-surface fan morphology is identifiable in some areas (Figs.5.5e, 5f).

Historical satellite imagery was also accessed via Google Earth Engine's time-lapse tool, extending observations back to 1984 (Table 5.1). This was useful in places where recent urbanisation has obscured the morphology of underlying fan surfaces.

Table 5.1. The free data sources employed in this study with product type, acquisition period, resolution and a link to where they were sourced from.

Data source	Product type	Acquisition period (year)	Spatial resolution (m)	Source URL
Google Earth	Visible imagery	2015-2022	0.15-15	https://www.google.com/earth/index.html
Landsat 8	Multispectral imagery	2021	30	https://earthexplorer.usgs.gov/
ALOS PALSAR	L-band synthetic aperture radar	2010	12.5	https://asf.alaska.edu/
Google Earth Engine Timelapse	Historical visible imagery	1984-2020	15	https://earthengine.google.com/timelapse/
ALOS World 3D-30m	Digital elevation model (terrestrial)	2006-2011	30	https://www.eorc.jaxa.jp/ALOS/en/dataset/aw3d30/aw3d30_e.htm
GEBCO 2021	Digital elevation model (bathymetric)	Before 2021	450	https://www.gebco.net/data_and_products/gridded_bathymetry_data/

Catchment delineation

To inform hydrological analysis, the ALOS World 3D-30m (AW3D30) digital elevation model (DEM) was used (Table 5.1). This product was selected as it produces the most realistic representation of fluvial geomorphology in mountainous settings when compared to similar products (Boulton and Stokes, 2018). Catchments and stream networks were delineated from the apexes of identified fans mapped onto the DEM using ArcMap's Hydrology Toolkit.

Topographic and bathymetric profiles

Fan long-profile morphology was characterised from the AW3D30 DEM. However, multiple studies have shown that fans in coastal settings have been subject to foreshortening as a result of sea level variability (e.g. Hayward, 1985; Robustelli et al., 2005; Adamson et al., 2017). As such, bathymetric data from the GEneral Bathymetric Chart of the Oceans' (GEBCO) 2021 grid was downloaded covering the Hajar Mountains, Batinah and Arabian Gulf coastlines and their associated continental

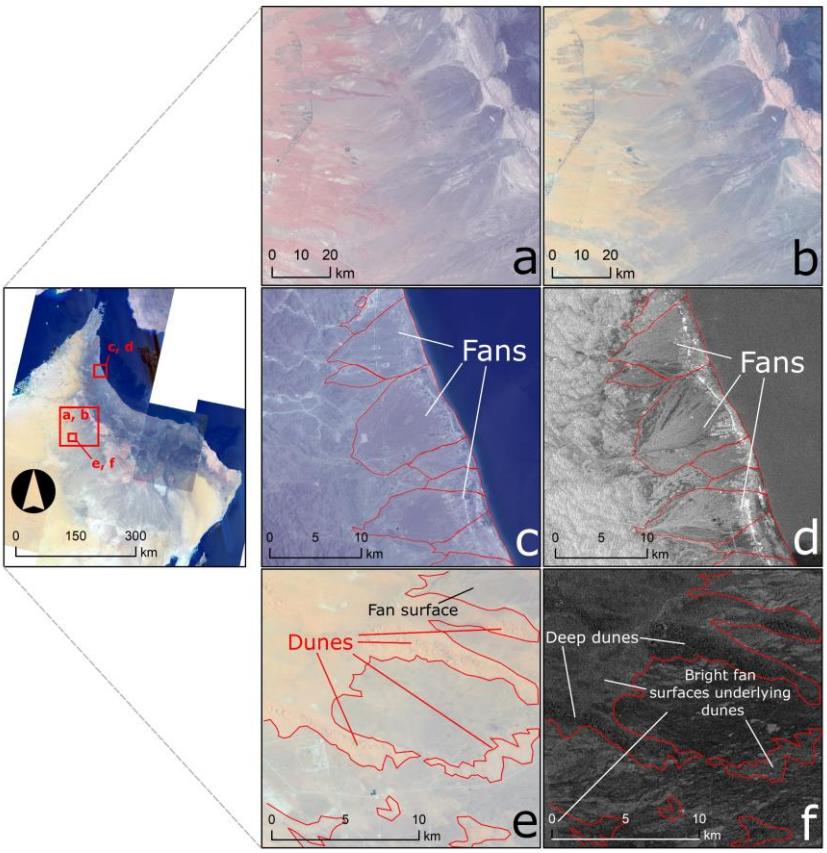

Figure 5.5. **(a)** Fan systems along the interior mountain front of the Hajar Mountains depicted in Landsat 8 true-colour imagery (bands 432) and **(b)** false-colour imagery (bands 642). Landsat false-colour imagery **(c)** is compared with L-band PALSAR **(d)** for radar-bright fans along the northern Batinah Coast. Landsat false-colour imagery of fan surfaces **(e)** is obscured by overtopping dunes, however L-band PALSAR imagery **(f)** is able to penetrate shallow sand veneers, although areas of radar-dark deep dunes remain.

shelves with a resolution of 450 m (Table 5.1). This was used to construct sub-marine long-profiles following coastal fan apexes to the edges of continental shelves. Whilst these long-profiles do not permit identification of the extent of fan deposits, they are useful for identifying the potential role of Quaternary sea-level variability in fan morphology, as has been applied in other studies of fan morphometry (e.g. Stokes and Gomes, 2020).

5.4.2 Fan and catchment morphometric variables

Morphometric variables were measured from the delineated fans and catchments (Table 5.2). For coastal fans, fan area denotes only the visible, subaerial surfaces of fans, not submerged surfaces. Mean fan gradient is calculated along the fan length from the elevation of the fan apex and fan toe. This method does not account for the concavity of fan long-profiles as two fans of the same relief and length but different concavities will still give the same overall gradient, however it serves as a practical means for characterising the gradients of numerous very large fans using GIS as has been applied elsewhere (e.g. Hartley et al., 2010; Tomczyk, 2021). Whilst it is unlikely that two fans would have exactly the same relief and length, comparisons with field-based studies (in which portions of the fan surface are measured to calculate gradient) must be done cautiously (e.g. Harvey et al., 1999). Qualitative variables were also recorded, such as catchment lithological group and distal setting (Table 5.2). Regression analyses was conducted between the quantitative fan and catchment morphometric variables to evaluate the strength of the relationships controlling fan morphology (e.g. Harvey, 2011; Stokes and Mather, 2015; Stokes and Gomes, 2020; e.g. Equations 2.1 and 2.2). The residuals of the F_a v. C_a and F_g v. C_a regressions were then plotted by fan location, depositional setting and catchment geology to examine how these variables influence morphology.

5.5 Results

5.5.1 Summary of fan and catchment mapping and general characteristics

438 mountain-front fans were identified in total (Fig.5.6). 109 are located in the Musandam Peninsula (Figs.5.6b, 5.6c), 43 in the Wahiba Sands (Fig.5.6e), 89 along the Batinah Coast (Fig.5.6d) and 197 in the Rub' al Khali (Figs.5.6f, 5.6g) (Table 5.3). This is unlikely to be an exhaustive survey due to the constraints of image resolution; there may be additional, small fans that have not been captured in the analysis.

Table 5.2. Fan and catchment morphometric variables (e.g. area) and qualitative characteristics (e.g. lithology).

Parameter	Abbreviation	Units	Description
Fan variables			
Area	F_a	km^2	Total planimetric area of fan
Gradient	F_g	-	Axial gradient from apex to toe
Length	F_l	km	Axial length from apex to toe
Apex elevation	F_{ae}	m	Elevation of fan apex above sea level
Toe elevation	F_{te}	m	Elevation of fan toe above sea level
Relief	F_r	m	Difference in fan elevation from the apex to the toe: $F_r = F_{ae} - F_{te}$
Relief-area ratio	F_{ra}		Ratio of fan relief to area: $F_{ra} = F_r / F_a$
Fan location (qualitative)	-	-	Location of fan: 1) Musandam Peninsula, 2) Rub' al Khali, 3) Wahiba Sands or 4) Batinah Coast
Depositional setting (qualitative)	-	-	Distally confined by erosive processes: coastal or fluvial, or topographic barriers (e.g. bedrock), or distally unconfined
Catchment variables			
Area	C_a	km^2	Total planimetric area of the catchment above the fan apex
Gradient	C_g	-	Mean gradient of the catchment
Maximum elevation	C_e	m	Elevation above sea level of the highest point within a catchment
Relief	C_r	m	Vertical difference between maximum catchment elevation and fan apex elevation: $C_r = C_e - F_{ae}$
Melton's ruggedness index	C_{mr}	-	Change in catchment relief across space: $C_{mr} = C_r C_a^{-0.5}$ (Melton, 1965)
Lithology (qualitative)	-	-	Predominate lithological group of each catchment

The smallest fans are in the Musandam Peninsula (mean F_a= 1.35 km^2) whereas the largest are located along the Rub' al Khali mountain front (mean F_a= 220.69 km^2) (Fig.5.6); see Table 5.3 for a full summary of key morphometric variables. The steepest fans are also found in the Musandam Peninsula (mean F_g = 0.09), with the other three areas having much lower mean fan gradients by comparison (Table 5.3). The greatest fan relief is located in the Rub' al Khali (max F_r = 333 m); however, the Batinah Coast has the greatest mean fan relief (mean F_r = 104 m) whereas the other

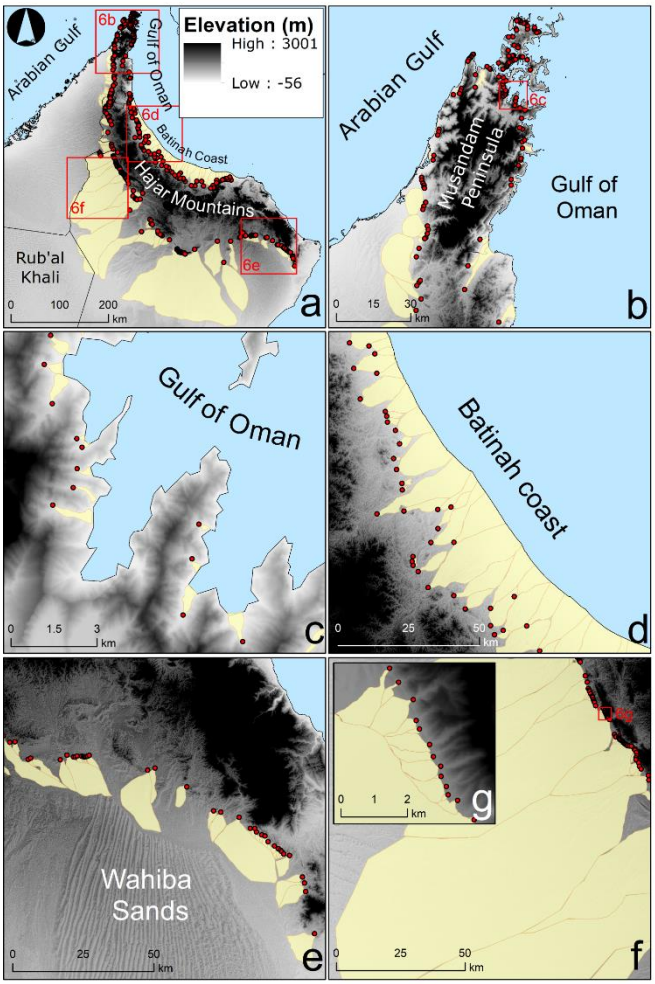

Figure 5.6. (a) Overview of fans mapped in this study, with their apex points shown (red dots). **(b)** Smaller fans were observed in the Musandam Peninsula, with the smallest **(c)** located around the rugged northern coastline. **(d)** Coastal fans also drain to the Batinah Coast. **(e)** The Wahiba Sands fans. **(f, g)** Examples of the large range of scales of Rub' al Khali fans.

three regions have lower and more similar mean fan reliefs (mean F_r = 42-55 m).

The largest catchments are found along the Rub' al Khali and Batinah Coast bajadas (in the order of >10^3 km^2) and unsurprisingly they produce the largest fans (Table 5.3). By contrast, the Musandam Peninsula is characterised by smaller, steeper catchments with the smallest catchment area and highest mean catchment gradient recorded in the dataset (Table 5.3). Catchment relief is similar across all regions, with minimum and maximum values ranging from 10^{-1}-10^3 m in all cases and mean values ranging from 430 m in the Rub' al Khali to 840 m for the Batinah Coast.

5.5.2 Fan morphology

Fan planform morphology

Laterally unconfined features displaying the radial morphology typical of fan systems (e.g. Fig.5.1) are rare along the Hajar Mountain fronts. Only very few of these typically lobate features were identified along the Arabian Gulf coast (e.g. Fig.5.7a). Hajar fans often have elongated morphologies as a result of lateral confinement by neighbouring fans (Fig.5.7b). These features are demarcated by inter-fan channels and coalesce into bajadas along the Rub' al Khali, Batinah Coast and Wahiba Sands mountain fronts (Figs.5.7b, 5.7c, 5.7d). These fans commonly display a telescopic style whereby subsequent phases of deposition prograde distally beyond an intersection point at which younger channels incise through older deposits (Fig.5.7d; Al-Farraj and Harvey, 2005). By contrast, the majority of fans in the Musandam Peninsula do not coalesce to form bajadas. This is due to their situation in rocky coves, restricting them laterally, as well as their distal extremes being coastal which limits accommodation space (Fig.5.7e). Where fan apexes are located in wide valleys along the Rub' al Khali and Batinah Coast mountain fronts, fans back-fill into the lower reaches of catchments (Fig.5.7f).

Distal confinement is clearly an important control on planform morphology. Smaller fans along bajadas are 'pinched-out' where their larger neighbours coalesce, limiting accommodation space (Figs.5.7b, 5.7d). Fluvial and coastal processes acting at fan toes present an erosive control which results in fans being abruptly cut-off at their toes, following the morphologies of the coastline and axial channels, e.g. along the Batinah and Musandam Peninsula coastlines and Wadi Batha north of the Wahiba Sands dunefield, respectively (Figs.5.7c, 5.7d, 5.7e).

Table 5.3. Summary statistics of fan and catchment morphometric parameters.

		Fan variable			Catchment variable		
Area	**Statistic**	**F_a (km^2)**	**F_g**	**F_r (m)**	**C_a ($km^{2)}$**	**C_g (°)**	**C_r (m)**
All fans	Minimum	0.002	0.001	2	0.002	1.61	10
	Maximum	17595	0.37	333	4777	41.40	2760
	Mean	114.11	0.04	61	76.58	19.59	560
	σ (±)	918.23	0.05	59	327.50	8.94	470
	n	**438**					
Musandam Peninsula	Minimum	0.002	0.004	2	0.002	8.90	20
	Maximum	51.03	0.37	193	474.37	41.40	2010
	Mean	1.35	0.09	42	8.46	27.43	620
	σ (±)	6.81	0.08	33	46.47	8.92	380
	n	**109**					
Rub' al Khali	Minimum	0.007	0.001	5	0.003	1.89	10
	Maximum	17595	0.10	333	4777	35.63	2710
	Mean	220.69	0.02	55	94.96	18.16	430
	σ (±)	1360	0.02	60	450.70	7.37	350
	n	**197**					
Wahiba Sands	Minimum	0.04	0.004	6	0.03	1.61	40
	Maximum	233.17	0.02	165	708.84	22.96	1880
	Mean	20.71	0.01	50	45.37	13.19	440
	σ (±)	44.23	0.004	38	128.04	5.17	450
	n	**43**					
Batinah Coast	Minimum	0.38	0.004	11	0.21	2.70	40
	Maximum	425.23	0.03	265	1665.93	29.51	2760
	Mean	61.44	0.01	104	134.39	16.21	840
	σ (±)	81.58	0.005	67	239.63	7.18	630
	n	**89**					

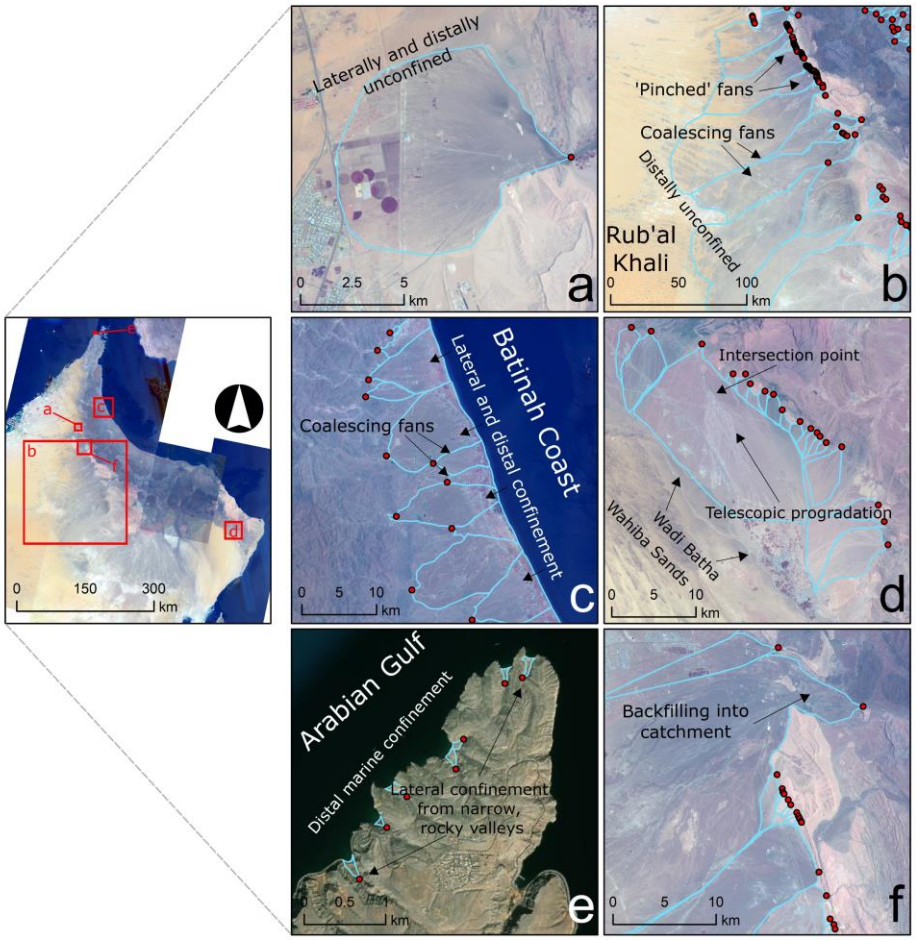

Figure 5.7. (a) Very few fans surveyed displayed 'typical' planform morphology (Fig.5.1). Fans are laterally confined by each other, coalescing into elongated bajadas, principally along **(b)** the Rub' al Khali mountain front, **(c)** Batinah Coast and **(d)** Wahiba region in the southern Hajar. **(e)** The fans of the Musandam Peninsula do not form bajadas, being confined laterally by bedrock. **(f)** Larger fans display backfilling into catchment areas along the Rub' al Khali and Batinah Coast mountain fronts.

Fan long-profile morphology

Inland-draining, distally unconfined fans have a stable base level and typically have concave long profiles (Fig.5.8a). These profiles also show that the mean gradients of smaller fans are steeper than those of larger fans. Where fans drain into active dunefields, dunes produce a secondary topography imposed upon that of inactive fan surfaces (Fig.5.8a). Some fans are distally confined by erosion from ephemeral streams with their toes exhibiting steep basal gradients as a result of axial channels cutting into the fan (Fig.5.8b).

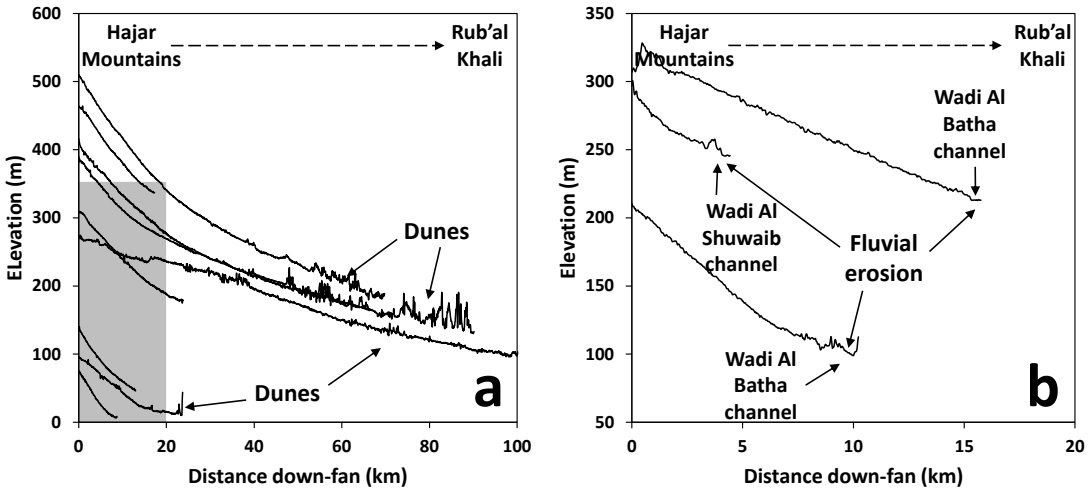

Figure 5.8. Example long profiles are shown for distally **(a)** unconfined and **(b)** fluvially confined fans along the Rub' al Khali and Wahiba Sands bajadas. Smaller fans show steeper profiles than larger fans. Dune encroachment on fans produces a superimposed topography, whilst erosion by axial channels results in sharp, erosive profiles at fan toes. The shaded area in **(a)** denotes the scale of **(b).**

Coastal fans along the Batinah Coast and around the Musandam Peninsula have steep toes. Their concave long-profiles extend beneath current sea level across the continental shelf (Fig.5.9). Abrupt, steep gradients where fans enter the littoral zone (relative to modern sea level) indicate steepening and foreshortening by marine processes (Figs.5.9c, 5.9d).

5.5.3 Interactions with distal environments

Hajar fans interacted with the linear dunes of the Rub' al Khali by reworking aeolian sediments and trimming their extent during periods of increased hydrological activity throughout the Quaternary, thereby imposing a limit on dune extent which scales with catchment size (Al Farraj and Harvey, 2004). Similarly, the northwards extent of the Wahiba Sands linear dunes is limited by the periodic activation of Wadi Al Batha, which in turn interacts with fan toes, steepening their distal profiles (Fig.5.8b). By contrast, on coastal fans along the Batinah Coast, channels appear to have become drowned at the fan toes due to marine incursion, forming small rias (Fig.5.10). These features show varying degrees of evolution into closed and semi-open lagoons as long-shore drift has formed spits, reworking fan material. The stratigraphy of the littoral zone on the Batinah Coast likewise

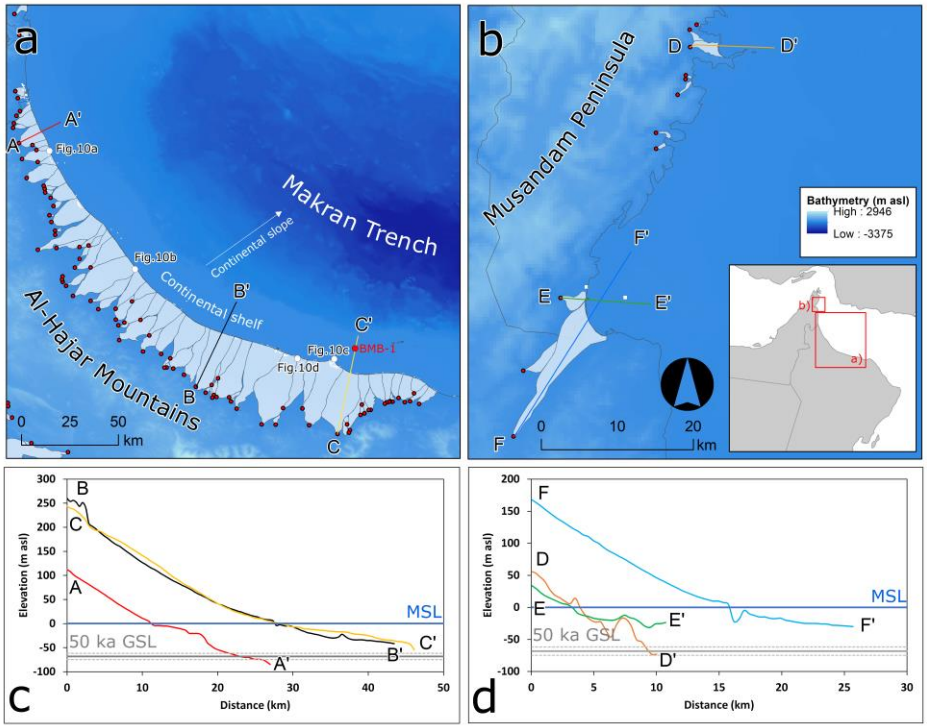

Figure 5.9. The offshore bathymetry of **(a)** the Batinah Coast and **(b)** south-western Musandam Peninsula. **(a)** Also shown: examples of small rias and an onshore (Fig.5.10) and offshore sediment core BMB-1 (referred to in the discussion). **(c, d)** Longprofiles for selected fans, including the continental shelf, show low distal gradients are not achieved until below modern sea level (MSL). Toe steepening is observed where fans intersect with the coastal zone. Global mean sea level (GSL) estimates at 50 ka are also marked with standard deviations (Spratt and Lisiecki, 2016).

reveals long-term interactions between fan and marine processes. For example, fluvial conglomerates indicative of higher energy transport regimes and past fan progradation are overlain by more recent sands and silts in the coastal zone (Fig.5.10).

SAR imagery reveals the extent of relict channel systems and fan surfaces under aeolian dunes and sand sheets along the Rub' al Khali bajada. Landforms suggest Quaternary interactions with interior sabkha basins, such as the Umm as Samim (Figs.5.11a, 5.11b). At the distal extents of these largest fan systems in the south-western Hajar, lacustrine features were identified including palaeoshorelines (Fig.5.11c). Lobes located around the edges of palaeoshorelines were deposited as fan deltas (Figs. 5.11c, 5.11d) where channels disgorged into standing water. These are indicative

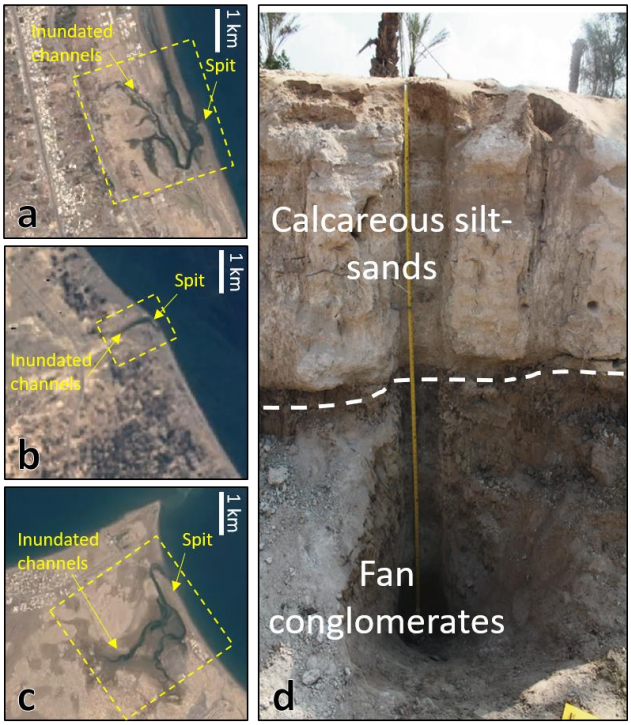

Figure 5.10. (a-c) Historical Google Earth Engine imagery reveals numerous drowned channel systems or rias at fan toes, which have been modified by marine processes forming semi-open and closed lagoons behind spits along the distal extents of Batinah Coast fans. **(d)** An exposed pit section from the coastal zone showing highly calcareous silt/sand deposits overlying fan conglomerates and gravels, indicating previous fan extent (Image credit: A. Parton). Locations marked in Fig.5.9.

of low-energy hydrological environments and increased base level during periods of greater fluvial activity on fan surfaces.

5.5.4 Fan-catchment morphometric relationships

Table 5.4 summarises selected morphometric regressions between all fans and catchments measured, as well as the F_g v. F_a relationship (see Table 5.2 for abbreviations). These relationships are displayed graphically in Figure 5.12. Tables 5.5 and 5.6 display the same summary statistics but for the F_a v. C_a and F_g v. C_a regressions grouped by individual focus areas to examine the diversity in these two key relationships in different geomorphic and geological settings (e.g. Silva et al., 1992).

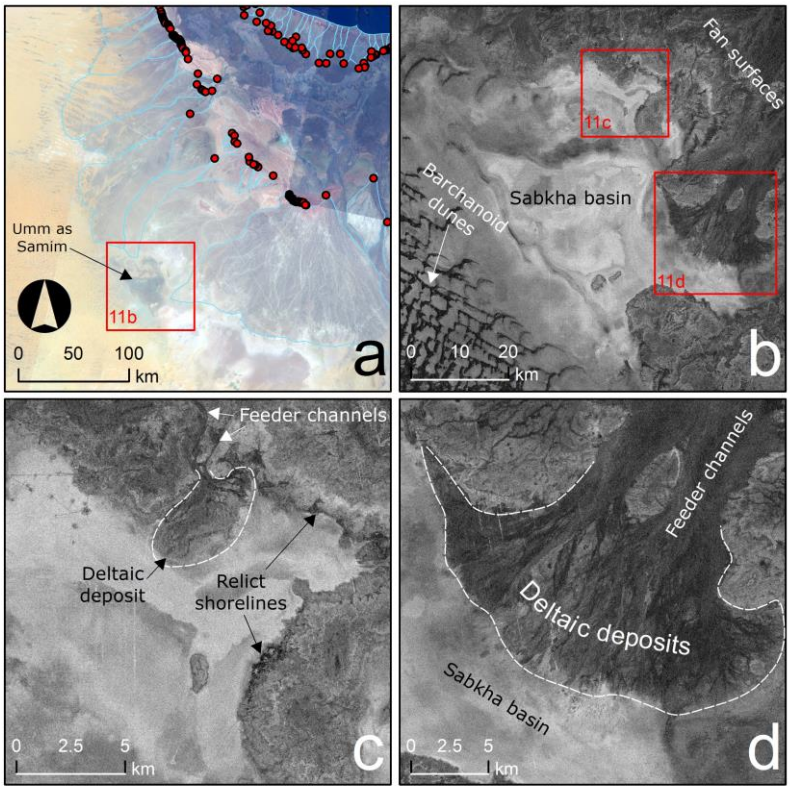

Figure 5.11. (a) The Umm as Samim is a large interior drainage basin fed by fan drainage networks. **(b)** L-band PALSAR imagery reveals that the basin and fan toes are geomorphologically diverse. **(c)** Lobate structures contrasting with the sabkha floor are interpreted as shallow shoreline features. **(d)** Large fan systems form fan deltas where they disgorge into the basin, indicating a low energy environment under periods of wetter climate.

When considering relationships between all fans in the dataset and their catchment characteristics, the strongest correlations were observed for F_a v. C_a ($R^2 = 0.77$), F_a v. C_{mr} ($R^2 = 0.66$) and F_g v. C_{mr} ($R^2 = 0.65$; Table 5.4; Fig.5.12). R^2 values of medium strength were observed for F_g v. C_a ($R^2 = 0.51$) and F_r v. C_a ($R^2 = 0.47$), whilst the weakest fan-catchment relationships were F_g v. C_g ($R^2 = 0.32$) and F_a v. C_r ($R^2 = 0.25$) but are still significant at the 95% level. Of these regressions, only two are negative (F_g v. C_a and F_a v. C_{mr}). These relationships show that as catchments become larger, there are corresponding increases in fan size and relief, reflecting an increase in overall sediment volume, along with a reduction in fan gradient. The topographic characteristics of catchments (C_{mr}, C_g and C_r) are also important, despite in most cases displaying lower R^2 values than C_a, showing that as catchments become steeper and more rugged, fans become smaller and steeper, while increasing

catchment relief is positively correlated with increasing fan area (Fig.5.12). These broad trends are consistent with the findings of previous fan morphometric studies (e.g. Karymbalis et al., 2018; Tomczyk, 2021), including the observations that F_a usually displays the strongest relationship with C_a (Harvey, 2011). The second strongest relationship observed was a negative correlation for F_g v. F_a (R^2 = 0.68); larger fans are flatter, reflecting both the water-sediment ratio of their depositional processes and the progressive flattening of fans with elongation (e.g. Harvey, 1987).

Significant and often highly variable relationships were also observed between the individual study areas. Whilst these differences are apparent for all the selected regressions (Fig.5.12), they are exemplified by the most widely used morphometric relationships: F_a v. C_a and F_g v. C_a (Tables 5.5 and 5.6, respectively). In both cases, the fan-catchment systems of the Rub' al Khali and Wahiba Sands display the strongest correlations, with R^2 values greater than those reported for all fans in the case of F_a v. C_a (R^2 = 0.89 and 0.82, respectively; Table 5.5). The Rub' al Khali is also the only area to display a higher R^2 value than that for the all fans case in the F_g v. C_a regression (R^2 = 0.78). The Musandam Peninsula, Batinah Coast and Wahiba Sands fans (the latter in the case of the F_g v. C_a regression) consistently return R^2 values weaker than the all fans case. The F_g v. C_a relationship is especially weak for the Batinah Coast fans (R^2 = 0.23). These regional relationship disparities are,

therefore, likely the result of differences in the geomorphic and geological settings of fans, in turn influencing fan histories along different fronts of the Hajar. The strong relationships observed for the Rub' al Khali likely reflect fans which are more strongly controlled by their catchment characteristics as opposed to the influence of factors extrinsic to the fan-catchment system such as base-level alterations and confinement, although differences in catchment lithology also likely play a role in the diversity of these regional relationships (e.g. Silva et al., 1992).

The regression coefficients and exponents suggest a wide variety of controls on fan morphology across the Hajar. For the F_a v. C_a regression, coefficient x ranges from 0.09 in the Musandam Peninsula to 2.21 along the Batinah Coast, suggested to be the result of specific catchment lithology

Table 5.4. Summary of selected regressions between morphometric variables for all fans in the dataset (displayed in Fig.5.12). Bold p-values denote statistically significant relationships at the 95% confidence level.

Relationship (dependent v. independent)	Coefficient x	Exponent y	R^2	Standard error	p-value
F_a vs. C_a	0.46	1.02	0.77	1.54	**0.00**
F_g vs. C_a	0.03	-0.28	0.51	0.76	**0.00**
F_r vs. C_a	31.27	0.24	0.47	0.69	**0.00**
F_g vs. C_g	0.001	1.09	0.32	0.89	**0.00**
F_g vs. C_{mr}	0.04	0.63	0.65	0.64	**0.00**
F_a vs. C_{mr}	0.18	-1.87	0.66	1.86	**0.00**
F_a vs. C_r	0.000	1.70	0.25	2.76	**0.00**
F_g vs. F_a	0.02	-0.28	0.68	0.61	**0.00**

Table 5.5. Summary of F_a v. C_a regression relationships for each study area (displayed in Fig.5.12). Bold p-values denote statistically significant relationships at the 95% confidence level.

Area	Coefficient x	Exponent y	R^2	Standard error	p-value
Musandam Peninsula	0.09	0.86	0.56	1.43	**0.00**
Rub' al Khali	0.83	1.02	0.89	1.04	**0.00**
Wahiba Sands	1.36	0.80	0.82	0.91	**0.00**
Batinah Coast	2.21	0.66	0.60	1.06	**0.00**

Table 5.6. Summary of F_g v. C_a regression relationships for each study area (displayed in Fig.5.12). Bold p-values denote statistically significant relationships at the 95% confidence level.

Area	Coefficient x	Exponent y	R^2	Standard error	p-value
Musandam Peninsula	0.06	-0.37	0.42	0.81	**0.00**
Rub' al Khali	0.02	-0.27	0.78	0.42	**0.00**
Wahiba Sands	0.01	-0.12	0.48	0.30	**0.00**
Batinah Coast	0.01	-0.10	0.23	0.37	**0.00**

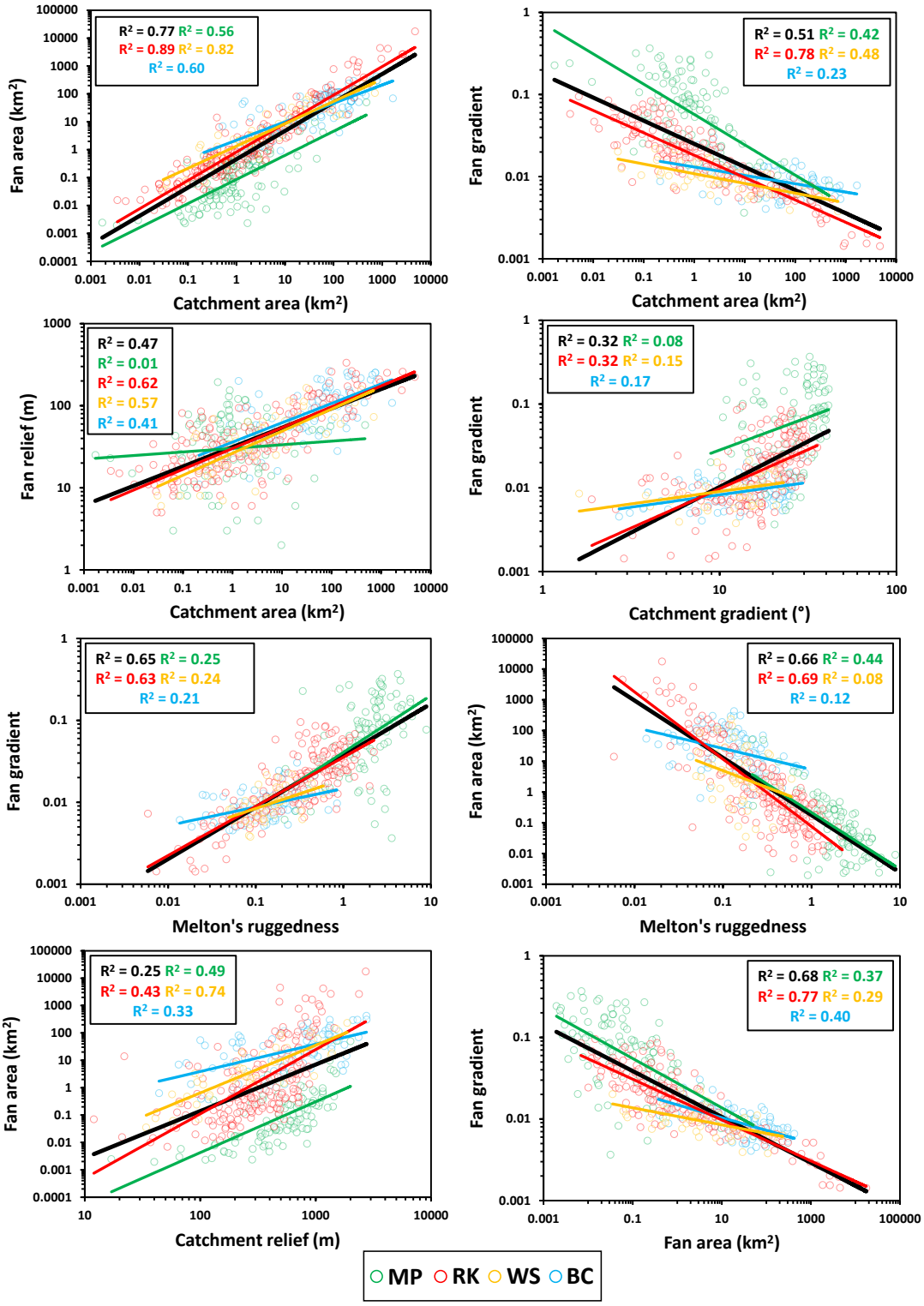

Figure 5.12. Selected morphometric regressions for the mapped fans and their catchments discussed in the text. Colours in the key respond to the four study areas: Musandam Peninsula (MP), Rub' al Khali (RK), Wahiba Sands (WS) and Batinah Coast (BC). The black regression line in each plot reflects the relationship for all studied fans. R^2 values are shown corresponding to each study area as well as the all fans case. See Tables 5.4-5.6 for summary statistics from the regression relationships. See Appendix C for statistical data by individual study areas for the regressions in Table 5.4.

and fan history, such as toe trimming by an axial stream (e.g. Hooke and Rohrer, 1977), which will be discussed in more detail in Section 5.5. This means that, for a given catchment area, fans in the Musandam Peninsula are generally smaller than those on the Batinah Coast. Exponent y ranges from 0.66 for the Batinah Coast to 1.02 for the Rub' al Khali fans (Table 5.5), showing that Rub' al Khali fan area becomes more sensitive to catchment area for larger catchments. This exponent range broadly fits with the whole range of values observed for dryland fans suggested elsewhere (~0.7-1.1; e.g. Al-Farraj and Harvey, 2005).

The F_g v. C_a regression results tend to be more variable than F_a v. C_a parameters between different studies globally (Al-Farraj and Harvey, 2005). Exponent y varies from -0.10 for the Batinah Coast to -0.37 along the Musandam Peninsula (Table 5.6), showing that Musandam Peninsula fan gradients are more sensitive to catchment areas than in other areas. Coefficient x ranges from 0.01-0.06 which is suggestive of differences in catchment lithology, depositional processes (e.g. deposition by fluvial or debris flow processes) as well as factors affecting fan base level (Harvey et al., 1999).

Residuals of morphometric relationships

The residuals of key regression relationships reveal the variability in fan area and gradient, relative to what is expected based on their catchment areas. Figure 5.13 shows the standardised residuals of the fan area vs. catchment area regression relationships (all fans) plotted against the standardised residuals of the fan gradient vs. catchment area regression relationships (all fans; Table 5.4). As such, the four corners of these plots show tendencies towards smaller and steeper fans (-x, +y), larger and steeper fans (+x, +y), larger and less steep fans (+x, -y) and smaller and steeper fans (-x, +y). Fan residuals are plotted according to fan location (Fig.5.13a), catchment lithological group (Fig.5.13b) and distal confinement (Fig.5.13c). Residuals primarily plot in the top left and bottom right of Figure 5.13, indicating that fans are either steeper and smaller or flatter and larger than expected.

Fans differ in their morphology depending on their location along the four studied mountain fronts (Fig.5.13a). Rub' al Khali and Wahiba Sands fans primarily plot as larger and less steep than the overall regressions predict, whilst the Musandam Peninsula and Batinah Coast fans are steeper but smaller than expected. Rock type is an important control on fan morphology (Fig.5.13b); fans draining APD catchments are smaller and steeper, whereas the other lithological groups produce fans which are generally larger and flatter. Fans from SB catchments cluster most tightly around the regression relationships, while the largest and least steep fans are produced by OPH and PN catchments.

Distal confinement also produces clear clusters of fan morphology (Fig.5.13c). Coastal fans influenced by marine processes at their toes are mostly smaller and steeper than expected, albeit with some outliers. Conversely, unconfined fans are larger and flatter than expected. Topographically confined fans (distally confined by outcropping geology) and fluvially trimmed fans are spread across all four quadrants but still mainly give rise to larger and less steep features. This finding is surprising as fan area may be expected to be restricted in these settings, either due to toe trimming by an axial channel or limited accommodation space (e.g. Stokes and Mather, 2015). However, fluvially confined fans do not plot far into the larger/flatter quadrant, indicating that they are still more restricted than the largest and flattest unconfined fans. Fan extent is, therefore, more limited in these settings although not as limited as coastal settings.

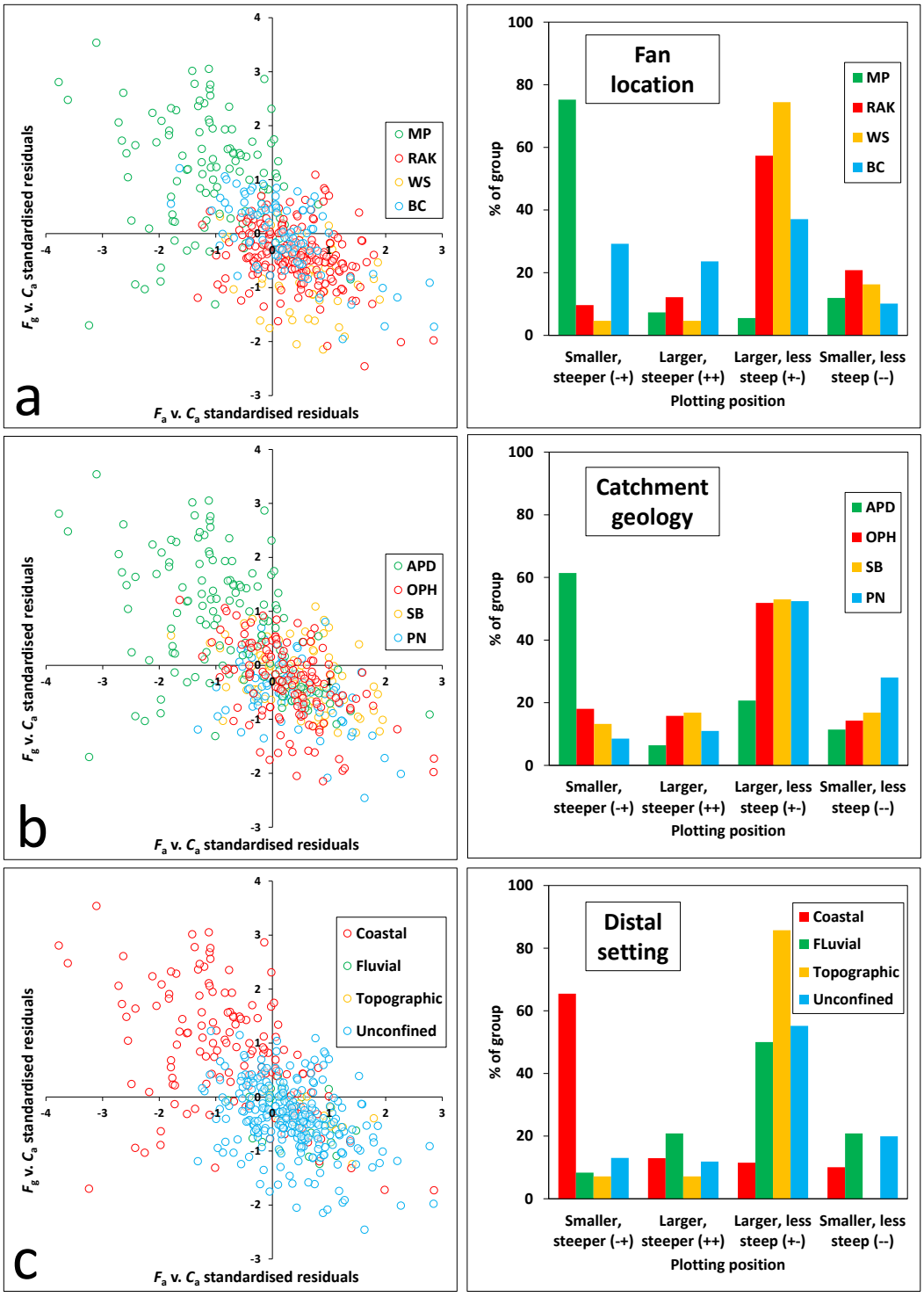

Figure 5.13. Standardised residual plots of the fan area vs. catchment area and fan gradient vs. catchment area relationships by **(a)** fan location, **(b)** catchment lithological group; Arabian Proximal Domain (APD), ophiolite (OPH), slope and basin (SB) or post nappe units (PN) (see Fig.5.3a for geological map), and **(c)** distal confinement either by coastal and fluvial processes or topographic barrier, or fans which are unconfined. Bar charts on the right show the percentage of fans by each classification group for each of the four plotting positions on the residual plots.

5.6 Discussion

The key controls on Hajar fan morphology are catchment morphology, base level variability and climatic change and tectonics. Each are discussed here in the context of the data from the Hajar mountain fan analysis, followed by a comparison of their morphology to other dryland fans on Earth and extra-terrestrial contexts.

5.6.1 Catchment controls

Catchment morphometry is a fundamental control on sediment transport and supply to mountain-front alluvial fans. Larger catchments supply more sediment to their fans and they also generate higher flows so the water-sediment ratio is higher. Consequently, larger catchments generate larger, less steep fans (Table 5.5; Fig.5.12) as their higher discharges can transport the supplied sediment at lower gradients. Therefore, strong relationships are observed between both fan area (positive) and fan gradient (negative) and catchment area, respectively (Table 5.5; Fig.5.12). The relationships between fan and catchment properties show some differences from those described in previous work in the region by Al-Farraj and Harvey (2005), although coefficient x of their F_a v. C_a regression for mountain front fans in the Wadi Bih region of the northern Hajar is very similar to that derived by this study for the all fans case (0.45 and 0.46, respectively).

On the other hand, their F_g v. C_a regression of $F_g = 0.09C_a^{-0.23}$ deviates from the coefficient x value derived in this study for all fans ($F_g = 0.03C_a^{-0.28}$). Al-Farraj and Harvey (2005) utilised a field-based methodology for measuring F_g, whereby a portion of the medial-distal surfaces of large fans were sampled to derive fan gradient, whereas the remote sensing approach utilised here measures axial gradient between the apex and the toe. Therefore, the difference in regression statistics between these two studies may be explained by this methodological discrepancy. However, the Wadi Bih fans are located in the Musandam Peninsula study area, which derived a similar coefficient x to that which was previously measured by Al-Farraj and Harvey (2005; $F_g = 0.06C_a^{-0.37}$, Table 5.6) and thus indicates that the results from our approach may be comparable to field-based studies. The close

correspondence of these regression statistics for the Musandam Peninsula and the previous work from Wadi Bih may reflect similarities in catchment lithology across what is a broadly geologically homogeneous region dominated by rocks and structures of the Arabian Proximal Domain.

Catchment topography, measured through catchment relief, gradient and Melton's ruggedness index, is another key control on Hajar mountain-front fan morphology and their depositional processes. In this data, steeper and more rugged catchments produce steeper and smaller fans. This is because topography modulates the rates of runoff and erosivity controlling sediment transport from catchments onto fans, with steeper and more rugged catchments generating high discharge and rapid decreases in gradient at the fan apex (Melton, 1965). However, catchment relief and gradient seem to be more variable controls on fan morphology than Melton's ruggedness index which produced stronger relationships (Fig.5.12; Table 5.4). Numerous studies have commented on the utility of Melton's ruggedness as a measure of topography as it incorporates changing relief over space to provide a better characterisation of the gradient down which sediment moves to the fan, as opposed to the more generalised measures of absolute relief and mean gradient (Church and Mark, 1980; Kostaschuk et al., 1986; Karymbalis et al., 2022). The F_g v. C_{mr} regression is often expected to be roughly linear, with an exponent of 1.0 (Church and Mark, 1980). However, this is not the case for Hajar fans for which an exponent of 0.63 is derived (Table 5.4), meaning that mean fan gradients generally do not seem to increase as rapidly as catchment ruggedness for the Hajar. More rugged catchments and steeper fans are indicative of debris flow processes, as opposed to less rugged catchments and less steep fans which tend to be dominated by fluvial deposition (Valkanou et al., 2013; Karymbalis et al., 2018). Previous studies have utilised these morphometric parameters to suggest thresholds which divide debris flow- from fluvial-dominated fans. For example, Karymbalis et al. (2018) suggested that for coastal fans along the Gulf of Corinth, Greece, thresholds of F_g = 0.03 and C_{mr} = 0.15-0.24 defined the boundary between fans dominated by fluvial processes and those formed through combined fluvial and debris flow activity. However, these threshold values are globally variable (e.g. Harvey, 1992; De Scally and Owens, 2004; Scheidl and

Rickenmann, 2010), not least of all because of different approaches to measuring fan gradients (field measurements of mid-fan gradient or remote sensing-based measurements of apex-toe gradient). For the Hajar fans, defining these thresholds will require more field surveying of individual fan morphologies to categorise them into explicit groups of process dominance. Nevertheless, there appears to be a divide between the steeper fans and more rugged catchments located in the Musandam Peninsula and the flatter fans and less rugged catchments generally observed for the other three areas at around $F_g = 0.08$ and $C_{mr} = 1$ (Fig.5.12). It is therefore more likely that the fans and catchments of the Musandam Peninsula are dominated by debris flow processes.

Older catchments, based on the relative uplift of their predominate lithological group, generally produce larger, flatter fans because longer weathering histories have produced more sediment for fan building. Previous studies show that catchment lithology plays a key role in controlling fan morphology as it is a fundamental control on the erodibility of sediment and the rate at which it is produced (e.g. Bull, 1962; Harvey, 1987; Al-Farraj and Harvey, 2005). For example, Stokes and Mather (2015) found in the High Atlas Mountains of Morocco, tributary-junction fans were produced by catchments with weaker bedrock whereas catchments of less erodible lithologies did not generate fans. Therefore, sediment supply is critical for generating fans. The exposure time to sub-aerial weathering and structural strength of rocks are important determinants of erodibility. Catchments which have longer weathering histories (i.e. older) due to earlier exposure may have relatively less resistant lithologies, resulting in greater overall sediment production for fan building. Whilst there are no data on rock strength currently available for the Hajar Mountains, catchments draining older lithological groups (ophiolites, slope and basin and post nappe groups) produce the largest, flattest fans (Fig.5.13b), such as the large megafans of the southern Rub' al Khali bajada which drain primarily ophiolite catchments. These groups date from Late Cretaceous uplift (e.g. Guilmette et al., 2018; Moraetis et al., 2018; Corradetti et al., 2020), thus giving them the longest potential exposure times for weathering to take place. Fans draining catchments composed

primarily of rock types within the Arabian Proximal Domain are by contrast smaller and steeper (Fig.5.13b), likely in part due to the relatively shorter exposure times of these rocks since the Oligocene (Ninkabou et al., 2021). Within this general trend, the ophiolite group does display variability around both the fan area vs. catchment area and fan gradient vs. catchment area relationships (Fig.5.13b). This scatter is likely because of many of the ophiolite catchments are along the Batinah Coast so the morphology of many of these fans is also influenced by distal marine processes. Also, it is unlikely that erodibility scales linearly with exposure age; catchment structural and lithological characteristics will also impact erodibility and thus the rate of sediment production for fan building (e.g. Zondervan et al., 2020).

5.6.2 Base level controls

Changes in the basal level of fans' depositional settings can have a significant impact on their morphology, usually by either falling, and increasing accommodation space, or rising and limiting the extent of distal areas as well as creating steeper forms by drowning the concave long-profiles of fans (e.g. Harvey, 2002). Coastal fans display almost ubiquitously smaller and steeper forms, relative to the fan area vs. catchment area and fan gradient vs. catchment area relationships derived for the Hajar (Fig.5.13c). There are multiple strands of evidence to suggest that Quaternary sea-level variability has led to variability in the base level of Hajar fans, with Holocene sea-level rise resulting in the foreshortening and steepening observed in this study.

First, fan long profiles along the Batinah Coast and Musandam Peninsula which incorporate the submarine continental shelf indicate that low distal gradients are not reached until beneath contemporary sea level. Steep erosive features are also observed at many fan toes because of coastal dissection (Fig.5.9). During sea level low stands the accommodation space for fan aggradation and progradation on the continental shelf would have been much greater, such as during MIS 3 (c.50 ka) when mean global sea levels were an estimated 68.30 ± 4.49 m lower than present (Spratt and Lisiecki, 2019; Fig.5.9). This period coincides with a significant period of

sediment production and fan aggradation recorded across the Hajar fans more broadly and on the Batinah Coast fans (Chapter 4; e.g. sites OM20/3 and OM20/5). It is therefore likely that increased sediment supply and greater accommodation space would have resulted in progradation onto the exposed continental shelf.

Second, channel inundation is apparent at the toes of fluvial fans along the Batinah Coast (e.g. Al-Hatrushi, 2013; Kwarteng et al., 2016). This inundation shows that Holocene sea level rise and subsequent spit formation have resulted in a switch between fan-process dominance in these channels to marine dominated environments. Third, both onshore and offshore sedimentological evidence suggests the extension of coastal fans during times of lower base level. Sediment logs from the coastal zone on the Batinah Coast demonstrate the extension of fan conglomerates underlying the more recent deposition of coastal sediments (Fig.5.10). Similar stratigraphic relations have also been reported from the coastal zone of the south-western Musandam Peninsula where fan sediments underly marine and aeolian sediments (e.g. Macklin et al., 2012; Pain and Abdelfattah, 2015). Offshore, geological surveys in the Arabian Sea have reported Plio-Pleistocene conglomerate units underlying calcareous marine deposits, such as core BMB-1 which lies approximately 14 km off the Batinah Coast (Ravaut et al., 1998; Mount et al., 1998; Al-Lazki et al., 2002; Ninkabou et al., 2021) (Fig.5.9).

Numerous studies of fans in coastal settings also report foreshortening and steepening as a result of marine transgression (e.g. Hayward, 1985; Nemec and Postma, 1993; Harvey et al., 1999; Robustelli et al., 2005; Stokes and Gomes, 2020). Coastal processes are therefore key to explaining the variability in fan morphology along the Hajar Mountains and modulating the relationship between fans and their catchments. This gives rise to the generally weaker fan-catchment relationships derived for fans in primarily coastal settings such as the Musandam Peninsula and Batinah Coast as opposed to fans along the inland Rub' al Khali and Wahiba Sands mountain fronts (Fig.5.12; Tables 5.4, 5.5), as well as modulating catchment lithological controls (Fig.5.13b, 5.c).

By contrast, fan trimming by axial wadis does not appear to produce the dramatic foreshortening and steepening observed for coastal fans (Fig.5.13c), although it is a dominant control on fan morphology elsewhere (e.g. Leeder and Mack, 2001; Al-Farraj and Harvey, 2005; Stokes and Mather, 2015; Leenman and Tunnicliffe, 2020). Whilst evidence of erosion by axial channels at fan toes is evident where they intersect with wadis (Fig.5.8), the overall influence of fluvial erosion on fan area and gradient is insufficient to systematically alter the regression relationships. This weak influence of axial streams is likely due to the size of these mountain front fans, relative to small and only sporadically active wadi systems at their toes which do not exert a continuous erosive control under the presently arid climate. This is in contrast to the findings of Al-Farraj and Harvey (2005) for tributary-junction fans along Wadi al Bih in the north-west of the Hajar, however these fans are generally much smaller than their mountain-front counterparts and thus even ephemerally active trimming at their toes is likely to make a proportionally greater difference in terms of fan area and gradient. By contrast, fans where toes are not confined by coastal or fluvial processes and are not inhibited by topographic barriers have much greater accommodation space within sedimentary basins, such as the large megafans of the southern Rub' al Khali mountain front.

5.6.3 Long-term controls: climate change and tectonics

Quaternary climatic change is the principal pacer of periods of fan aggradation in south-east Arabia. This variability has created the distinct relict morphologies indicative of wetter environments evident in the landscape today. Geochronological records established over the last 20 years have constrained the timings of these aggradation periods.

Luminescence and radiocarbon dating of alluvial sediments from fans and their catchments, as well as the distal lakes in the Arabian interior into which they drain, indicate that the Hajar fans have aggraded periodically throughout the Mid-Late Quaternary. Periodic drainage activation has been related to intensifications in the IOSM, driven by precessional insolation variability (Chapter 4). This mechanism is supported by the timing of speleothem growth due to higher precipitation levels from

Hoti Cave in the central Hajar Mountains, as well as Mukalla Cave on the southern coast of the Arabian Peninsula (Fleitmann and Matter, 2009) and marine core proxies from the Arabian Sea (e.g. Caley et al., 2011). Key periods for fan activation throughout the Mid-Late Quaternary include the Early-Mid Holocene (c.12-5 ka Parker et al., 2006; Atkinson et al., 2013; Preston et al., 2015; Woor et al., 2022a), ~100-130 ka (Rosenberg et al., 2012; Parton et al., 2015a), ~150 ka (Parton et al., 2015a; Moraetis et al., 2020), ~220 ka (Blechschmidt et al., 2009) and ~300 ka (Chapter 4). Data also suggest aggradation in line with lower-amplitude peaks in insolation, such as at ~60-30 ka (Parton et al., 2013; Chapter 4), as well as older periods during the Mid Quaternary (Blechschmidt et al., 2009) although larger uncertainties associated with older ages make it difficult to identify precise depositional timings.

These periodic phases of increased rainfall throughout the Quaternary resulted in the aggradation of sinuous palaeochannel networks on the large megafans of the Rub' al Khali, subsequently exhumed through incision and deflation during regional aridity to create inverted relief (e.g. Maizels, 1987), as well as abandoned terraces of desert-varnish stained pavements which have been observed on fans from around the Hajar region (e.g. Abrams and Chadwick, 1994; Al-Farraj and Harvey, 2000; Fig.5.4d). For the largest inland fans, periods of greater discharge into distal areas generated low-energy lacustrine and wetland environments at fan toes. Lake formation has resulted in the erosion of lake-margin shoreline features into fan sediments and the development of fan deltas where channels disgorged into basins (e.g. Harvey, 2010). Whilst only three Quaternary terminal lake basins from the region have been subject to palaeoenvironmental reconstructions thus far (the Awafi, Wahala and Saiwan basins; Parker et al., 2004; 2006; Rosenberg et al., 2012; Preston et al., 2015), SAR imagery suggests that there are other shallow lacustrine basins which follow the distal extremities of the inland Rub' al Khali bajada. The largest of these is the Umm as Samim basin (Fig.5.11) which has been observed to flood as a result of fan activation during contemporary high magnitude, low frequency rainfall events (e.g. Fookes et al., 2019).

In contrast with these previous periods of fan building, incision dominates contemporary fan surfaces, although some localised aggradation is still recorded under flashier flow conditions (Chapter 4). Reduced rainfall under the arid-hyper arid climate limits sediment supply to fans leading to dissection by more recent flow events. These events may be the result of localised convective rainfall over the larger fans; thus flows may only infrequently be connected to source catchments. This model for climatically-paced aggradation interspersed with periods of dissection resulting from increased aridity was previously proposed for the fans of the Wadi Bih region of the northern Hajar based on observations of terrace sequences (Harvey, 2011). However, periods of dominant aggradation and dissection likely apply more broadly to Rub' al Khali fans based on the available chronological data as well as being suggested as a model of dryland fan evolution in numerous settings (e.g. Harvey, 2002; Harvey, 2011; Stokes and Gomes, 2020). Regional aridity has also led to the encroachment of aeolian dunes onto inland fan toes, most recently during the Mid-Late Holocene from approximately 6 ka (e.g. Atkinson et al., 2011a). This encroachment reflects the climatic dependency of sediment transport to the distal reaches of these fans with its source shifting from mountain catchments during more humid periods to aeolian transport from the Rub' al Khali sand sea during more arid periods (Al Farraj and Harvey, 2004).

Much less work has been carried out on the relationship between fan morphology and ongoing tectonic processes along the Hajar. Although generally thought of as being tectonically quiescent during the Quaternary, there is evidence of ongoing uplift from various sites during this period with faulting observed in fan conglomerates and alluvial terraces uplifted above eustatic sea level (e.g. Kusky et al., 2005; Moraetis et al., 2018; Hoffmann et al., 2020). This uplift is as much as >100 m in some areas of the south-eastern Hajar (Kusky et al., 2005). Whilst spatially variable, uplift is occurring in the Batinah Coast, Wahiba Sands and Rub' al Khali catchments, whilst the Musandam Peninsula is subsiding. This tectonic context is interesting with respect to the residual plots shown in Figure 5.13 in which the Musandam Peninsula fans are notably smaller than the other regions of the Hajar. Ongoing subsidence has likely reduced fan area due to submerging fans whilst relative

sea-level rises. Subsidence has also been noted elsewhere as a key control on fan morphometric variability (e.g. Whipple and Trayler, 1996). The large, unconfined fans of the Rub' al Khali bajada which are larger than expected from the overall F_a v. C_a regression (Fig.5.13) are, by contrast, situated within the interior foreland basin generated by the forebulge axis of the central Hajar Mountains (Rodgers and Gunatilaka, 2003). Therefore, tectonics play an important role in determining the accommodation space available for fan formation along the Hajar range.

At the smaller scale, however, it is difficult to ascertain the role of particular active faults in modulating the relationship between fan morphology and their catchment and other extrinsic controls. The region is extensively faulted by features which are smaller than the major thrusts outlined in Figure 5.3, some of which occur at mountain fronts (Kusky et al., 2005). However, there is little available data on specific slip-rates and the relative movements of fans relative to their feeder catchments where smaller faults intersect the mountain front. The presence of active faults has been shown in other contexts to be an important control on the development and morphology of Quaternary alluvial fans in drylands, such as in southern Mongolia (Owen et al., 1997) and the south-west USA (Owen et al., 2014). More detailed studies of slip rates are therefore warranted to constrain the role of localised faulting in the Hajar on fan morphological development.

Abrams and Chadwick (1994) previously concluded that, for the fans along the Batinah Coast, there was no evidence for tectonic activity being the driver of fan aggradation periods relative to a Quaternary climatic driver of sediment transport from catchments. Whilst more recently available chronology for Hajar fan aggradation supports this argument (Chapter 4), ongoing tectonic processes have likely played a role in modulating fan morphology, either through altering older deposits or by influencing hydrological processes during periods of higher rainfall. For example, for fans in intra-montane settings of the southern Hajar, Scharf et al. (2019) attribute wadi incision into fan material to uplift although they also acknowledge the role of climatically induced base-level changes, i.e. through the more sustained activation of axial drainage. Ultimately, the relative

importance of climatic and tectonic influences on Hajar mountain-front fans remains an avenue for future research.

5.6.4 Summary of the controls on mountain front fan morphology along the Hajar

The evolution of Hajar mountain-front fans is principally controlled by climate. In unconfined areas, the morphologies of mountain-front fans have strong relationships to the morphologies of their catchments. However, these relationships are weaker where tectonic and base-level controls are important. Figure 5.14 illustrates fans in each of the four key Hajar Mountain fronts, thereby summarising the key controls on their morphology for their specific settings:

(a) Musandam Peninsula: small, steep fans fed from small, rugged and less erodible catchments which are likely to generate debris flows. These fans are laterally confined by steep, narrow valleys and are distally foreshortened as a result of Late Quaternary sea-level rise and ongoing subsidence may also exacerbate this.

(b) Rub' al Kahli: the planform area of fans spans eight orders of magnitude (10^{-3}-10^{4} km^2), with smaller fans located to the north where catchments are smaller as well as within inter-megafan settings. Large, low gradient megafans result from distal unconfinement, deeply weathered catchments and greater accommodation space. Low-energy forms such as sinuous channels, fan deltas and distal lacustrine basins are present.

(c) Wahiba Sands: similar fan-catchment regression relationships to Rub' al Khali fans, although long profiles often display steep toes where the axial Wadi al Batha incises fan material. Trimming limits fan progradation during periods of higher fluvial activity

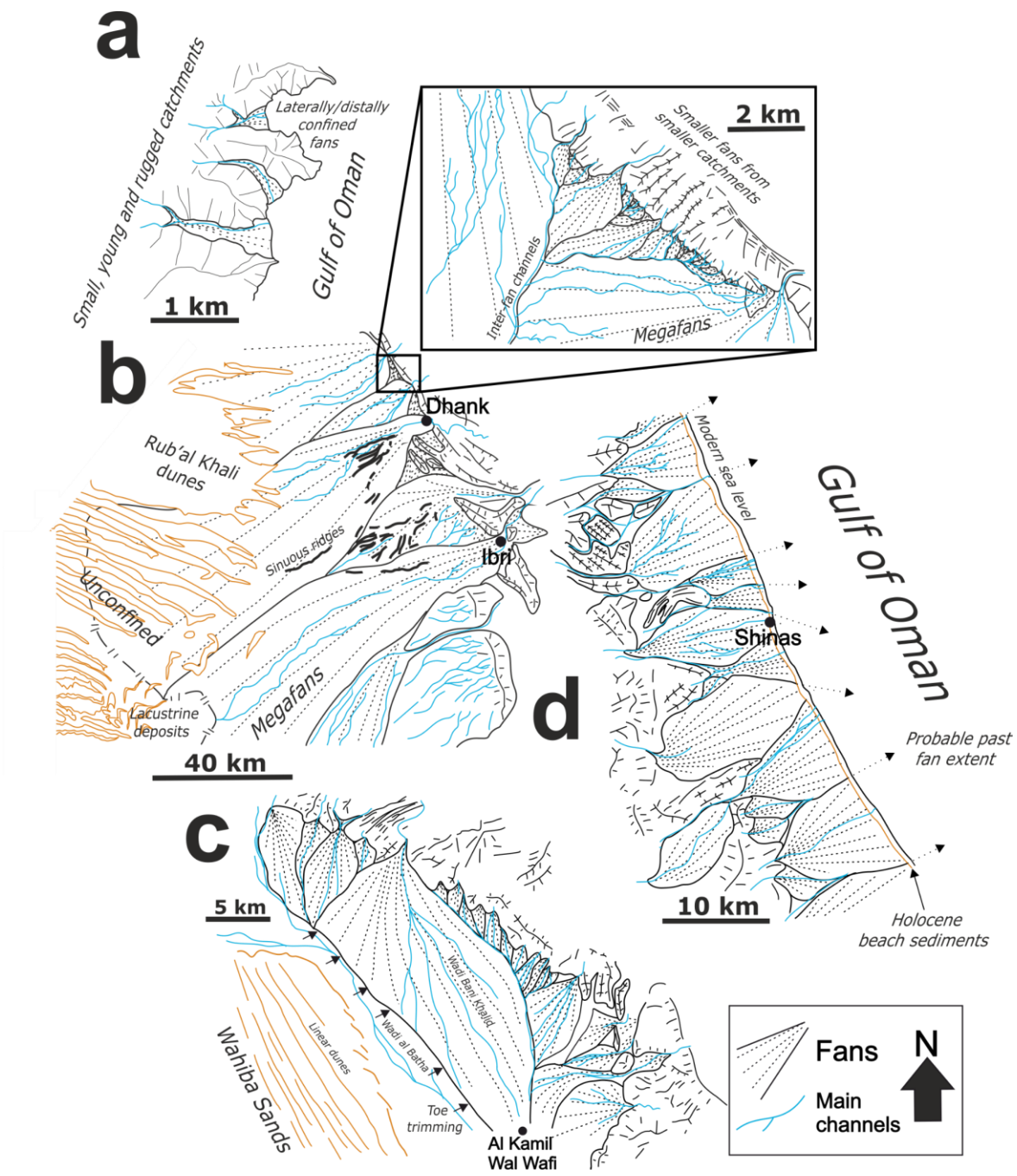

Figure 5.14. Fans typical of each study area along Hajar Mountain fronts and their key controls. **(a)** Musandam Peninsula, **(b)** Rub' al Khali, **(c)** Wahiba Sands, **(d)** Batinah Coast.

throughout the Quaternary while the Wahiba Sands dunefield also limits distal accommodation space, creating smaller fans relative to the Rub'al Kahli.

(d) Batinah Coast: fans in coastal settings also display foreshortening and steepening as a result of Late Quaternary sea-level rise. However, they are orders of magnitude larger than Musandam Peninsula fans owing to greater catchment areas and longer rock weathering histories. Fan conglomerate material extends offshore under more recent marine sediments as fans previously extended past their currently confined distal extremities.

5.6.5 Implications at the global and planetary scale: comparisons with other fans

The magnitude of the mountain front fans of the Hajar relative to other studied terrestrial fans means that the research here plugs an important gap in the literature. No previous study has examined fan morphometry in a dryland context over such a broad range of scales: eight orders of magnitude in terms of fan area (Fig.5.15a). This breadth of magnitude, alongside the variability in fan settings and long weathering histories, makes the Hajar a unique natural laboratory for studies of fan morphology and processes.

Fan morphometric regression coefficients reported in the literature vary due to differences in local conditions, such as lithology and depositional settings (Tomczyk, 2021). For dryland fans, the exponent (y; Equation 2.1) of the fan area vs. catchment area regression usually shows little variability between ~0.7 and ~1.1, whereas the constant (x; Equation 2.1) varies considerably from ~0.1 to ~2.1 (Harvey, 2011; Appendix C). This means that, while fans in most settings are similarly sensitive to increases in catchment area, there is a wide range in the average fan area for a given catchment area. For the fan gradient vs. catchment area regression, the exponent (y; Equation 2.2) ranges between ~-0.15 to ~-0.35 whilst the constant (x; Equation 2.2) ranges from ~0.03 to ~0.17 (Appendix C). This similarly suggests that whilst fan gradient is comparably sensitive to increasing catchment area, the gradients of fans are variable for catchments of the same size. Gradients are typically less sensitive to increasing catchment area than fan area (Fig.5.15). Broadly, the

relationships derived for the Hajar fans fit these ranges (Table 5.4), although when divided into study areas there is a wide range of exponents and constants. However, it is worth again noting that the methods used to derive fan gradient may differ, with many studies in the literature deriving a mean gradient along the whole of a fan's axis (e.g. Kostaschuk et al., 1986; Hartley et al., 2010; Tomczyk, 2021), whilst field-based studies often measure a sample gradient from a segment of the medial-distal part of fans (e.g. Al-Farraj and Harvey, 2005; Harvey, 2005).

The regions studied along Hajar Mountain fronts span the expected range of regression coefficients and exponents from the literature. For example, the constant of the F_a v. C_a relationships ranges from 0.09 for the Musandam Peninsula to 2.21 for the Batinah Coast whilst exponents range from 0.66 for the Batinah Coast to 1.02 for the Rub' al Khali (Appendix C). Hajar fans in confined settings, such as the Musandam Peninsula and Batinah Coast fall in the extreme ends of the range of coefficient values, or slightly outside them, as well as displaying weaker R^2 values relative to the Rub' al Khali and Wahiba Sands fans (Appendix C). This discrepancy likely reflects the fact that morphometric regression values reported in the literature are usually derived for unconfined mountain front fans with typically stronger regression relationships (Stokes and Gomes, 2020). Contrastingly, fans in confined settings or settings where base level changes are frequent, such as tributary junctions where toe processes have a strong influence on morphology, do not fall conformably into these expected coefficient and exponent ranges (e.g. Milana and Ruzycki, 1999; Al-Farraj and Harvey, 2005; Stokes and Mather, 2015; Table 7). The values for constant x measured for fans in coastal settings, for example, seem to mostly lie on the periphery of the range suggested by Harvey (2011) for the F_a v. C_a relationship, with fans such as those along the North Evoikos Gulf and Gulf of Corinth in Greece giving values of 0.12 and 0.17, respectively (Valkanou et al., 2013; Karymbalis et al., 2018). Coastal fans globally are reported to have been influenced by variable Quaternary sea levels (Hayward, 1985; Nemec and Postma, 1993; Harvey et al., 1999; Stokes and Gomes, 2020). They have, therefore, experienced significant base level changes which act as external controls on their morphology, as is also evidenced by this study in the case of the Batinah

Coast and Musandam Peninsula. In complex settings such as in this study, the relative importance of catchment properties as a control on resulting fan morphology could be expected to be less than that of unconfined mountain-front settings. However, there are still relatively few quantitative morphometric datasets available for fans and their feeder catchments from these complex settings, not only from drylands, but globally.

The Hajar fans display considerably lower gradients for the size of their catchments than other previously studied fans in dryland contexts (Fig.5.15b). Even though higher water-sediment ratios produced by larger, less rugged catchments would lead us to expect that fluvial fans have lower gradients than debris-flow fans (Harvey, 1990), fan gradients for the Rub' al Khali, Batinah Coast and Wahiba Sands are in some cases two orders of magnitude lower than previously studied fluvial fans. For example, the fluvial megafans of the Kohrud Mountains, Iran, have planform areas of the order 10^2 km^2 and gradients of the order 10^{-2} (Arzani, 2012), whereas the Hajar fans with comparable planform areas have consistently lower gradients of the order 10^{-3}. Perhaps, the location of the Hajar Mountains at lower latitudes than the distribution of most other dryland fan morphometry studies explains these low gradients (Fig.5.2). The region's location in the low latitudes and various palaeoclimate archives show that it has experienced substantial rainfall variability throughout the Quaternary, with periodic incursions of monsoon rainfall likely to have significantly increased the resulting water-sediment ratios of flows onto fans (Blechschmidt et al., 2009). Comparatively, other dryland fans, such as those in the southwest USA (e.g. Harvey, 2002; 2005) and Iran (Arzani, 2005; 2012; Arzani and Jones, 2018), produced primarily through climatically-paced aggradation periods throughout the Quaternary may not have experienced such dramatic increases in rainfall as they are located outside of the sub-tropical monsoon belt. The low-gradients of the Hajar fans, by contrast, are theorised to be the result of higher water-sediment ratios produced during periods of precessionally paced Indian Ocean Summer Monsoon incursion into the Arabian landmass, meaning that depositional processes in all regions but the Musandam Peninsula fall further towards

the fluvial end of the fluvial-debris flow spectrum than other studied regions. However, this remains speculative, and these differences could relate to more localised factors, such as tectonics.

Hartley et al. (2010) compiled a database of fluvial megafans from across different climate zones on Earth, for which mean gradients from apex to toe range from 0.00004-0.026. The gradients of the largest Rub' al Khali fans sit within this global range, although the lowest gradient recorded in this study (0.0014) is two orders of magnitude greater than the lowest recorded by Hartley et al. (2010; Table 5.3). Typically, megafans in dryland climatic contexts have relatively higher gradients than those in more temperate climates due to having greater transport limitations resulting from ephemeral flows but higher sediment supply (Hartley et al., 2010). The largest megafans of the arid Hajar region therefore fit this global pattern.

The potential utility of Hajar fan morphometry could also extend to extra-terrestrial contexts. Advances in remote sensing have permitted fans to be observed on extra-terrestrial bodies over the last few decades, namely in Martian craters (e.g. Moore and Howard, 2005; Kraal et al., 2008; Morgan et al., 2014) and on Saturn's moon, Titan (e.g. Birch et al., 2016; Radebaugh et al., 2018), with fans shown to be generally larger than expected from comparably-sized catchments on Earth (Fig.5.15a). This raises questions about the ubiquity of sediment transport and buffering thereof, despite differences in both bedload composition and the nature of its entrainment by fluids under different atmospheric and gravity conditions.

Having terrestrial analogues which are comparable in scale to extra-terrestrial features is important when trying to infer formative processes. Fan systems on Titan are at similar scales to the large megafans of the southern Rub' al Khali (Radebaugh et al., 2018). Many fans on Titan also terminate in equatorial dune fields, similar to the Rub' al Khali fans (Fig.5.14b). The results of this study could therefore offer useful hypotheses about the formation of large fans on Titan. For example, the Hajar may serve as an analogue when considering the importance of tectonically generated accommodation space, long-term climatic variability as a driver of aggradation periods or the role

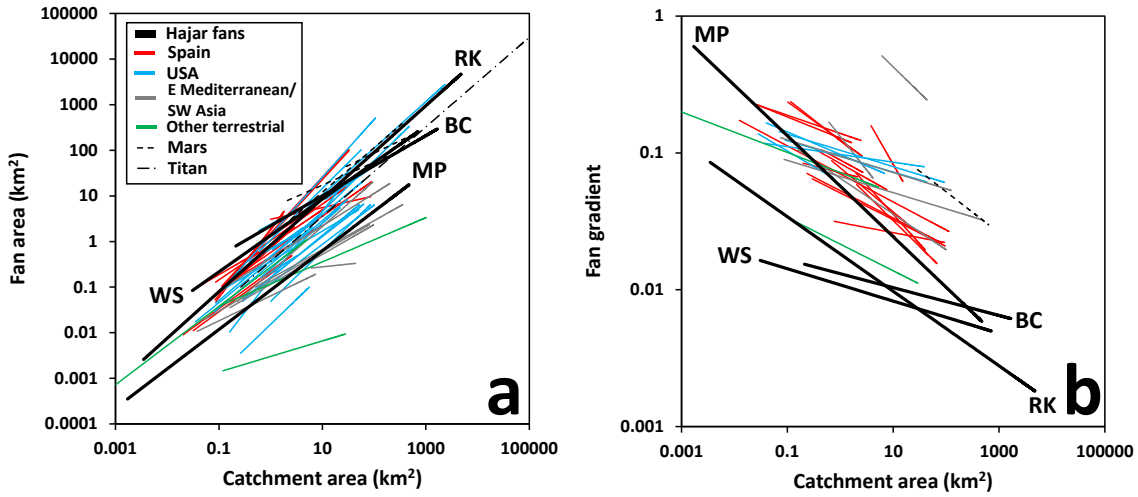

Figure 5.15. (a) Comparison of the fan area vs. catchment area and **(b)** fan gradient vs. catchment area relationships derived in this study for Hajar Mountain front fans, with studies from other terrestrial dryland and extra-terrestrial contexts. Note: the gradients in **(b)** reproduced from the literature have been derived by the original authors using different methodologies. See Appendix C for regression coefficients, R^2 values, locations and references. MP: Musandam Peninsula, RK: Rub' al Khali, BC: Batinah Coast, WS: Wahiba Sands.

of distal confinement. When compared with available data for Titanian fans, the F_a v. C_a regression for Rub' al Khali fans displays similar coefficient and exponent values (Appendix C; Fig.5.15a). These similarities suggest that they potentially have similar settings and fan histories, although this remains speculative. Given the low resolution of present Titan imagery which makes precise catchment delineation difficult, these data must be treated with caution (Birch et al., 2016). Nonetheless, the Hajar Mountains could provide a useful test site for detailed analogue studies to better understand Titan's surface processes and evolution.

5.7 Conclusions

This analysis summarises the morphology of mountain front fans along the Hajar Mountains in south-eastern Arabia. This region has some of the most prominent terrestrial dryland fans on Earth and yet their morphology and controls have not been explored across the whole range. Quaternary climate variability and long-term tectonic processes set the scene pacing periods of fan aggradation

and forming accommodation space. Catchment morphology and lithology, as well as variable distal settings, also play important roles in controlling fan shape and size.

Our multi-product remote sensing approach was useful for mapping fan systems in complex depositional settings where fans merge into bajadas or are partially obscured by dunes. 438 fan systems were identified at Hajar mountain fronts, ranging in planform area across eight orders of magnitude from 10^{-3}-10^{4} km^2. The strength and nature of fan-catchment relationships is variable

across the Hajar range due to different fan depositional settings, catchment lithologies and depositional processes. Late Quaternary sea-level rise is an important control on fans along the Batinah Coast and Musandam Peninsula, which display foreshortening and steepening at fan toes, with bathymetric data revealing that distal low gradients are achieved below present sea level. The fans of the Wahiba Sands are also controlled, in part, by base-level changes through the erosive influence of axial drainage. By contrast, the large fans of the interior Rub' al Khali bajada are distally unconfined and so have much more accommodation space, resulting from long-term tectonic processes. The long weathering histories of their large catchments is hypothesised to be another important factor in their large size, likely having produced larger overall sediment volumes.

The investigated fans span almost every order of magnitude in terms of their size and gradient previously recorded for terrestrial dryland fans. Also, the coefficients of their morphometric regressions reflect the full range typical of dryland mountain-front fans. This morphometric diversity is because of the variability of catchment and fan depositional contexts present around the Hajar range, making it an excellent place to carry out future research on dryland fan processes and controls. Not only is Hajar fan morphology useful for understanding these landforms in a terrestrial context, but the larger fans of the Rub' al Khali have potential similarities to extra-terrestrial fans. In particular, they may be fruitful test-beds for understanding large fans on Titan. Whilst future work is needed to test more specific hypotheses, they may be a useful analogue for inferring the nature and significance of controls on fan morphology in other planetary contexts.

Overall, this study shows that the mountain-front fans of the Hajar represent highly significant landforms for understanding the controls on alluvial fan morphology in other contexts, owing to their variable controls and, as a result, their diverse morphologies. The dataset for Hajar mountain-front fans represents the largest sample of alluvial fan and catchment morphometry produced to date from a terrestrial dryland context, which will hopefully be useful in exploring the controls on fans in increasingly diverse settings.

6 | Assessing the robustness of geochronological records from the Arabian Peninsula: A new synthesis of the last 20 ka (Paper 3)

Authorship: Sam Woor, Catherine Buckland, Ash Parton, David S.G. Thomas

This chapter is based on a research paper of the same name, published in the journal Global and Planetary Change, January 2022. A number of changes have been made to the version in this chapter to ensure continuity of text and avoid over-duplication of background material in the thesis. This chapter meets Research Objective 3 (Section 1.2).

6.1 Paper abstract

The timing and extent of Late Quaternary climate and environmental changes in the Arabian Peninsula were critical for human demographic changes. High resolution palaeoclimate archives suggest that monsoon variability was a key driver of change, but these records obscure environmental heterogeneity at finer spatial scales. Recent decades have seen the production of new, chronometrically controlled records from a range of new sites, with a greater spatial coverage. However, records often appear contradictory vis a vis the hydro-climatic state of the environment and so synthesising them can be challenging.

To enhance collation and interpretation of records, a new database has been compiled consisting of terrestrial and coastal environmental chronologies for the Arabian Peninsula over the last 20 ka, a key period of marked hydrological change. The **SCAPE** (**S**ynthesising **C**hronologies for **A**rabian **P**alaeo**E**nvironments) database contains records that include >700 luminescence and radiocarbon ages. Robustness criteria are applied to identify the utility of each data source in regional hydroclimate reconstruction. The most robust data provide a unique synthesis of 20 ka of palaeoenvironmental change at sub-regional scales. This synthesis shows that Arabian environmental change does not necessarily follow broad narratives of 'wet' or 'dry' states but rather the climatic signal is a mosaic of substantial landscape heterogeneity. SCAPE also highlights regions in which more high-quality geochronological investigation is warranted to refine both temporal and spatial records, signifying important avenues for future research.

6.2 Introduction

Late Quaternary rainfall variability in the Arabian Peninsula has been documented from a variety of high resolution palaeoclimatic archives, including speleothems (e.g. Burns et al., 1998; Burns et al., 2001; Fleitmann et al., 2003a; Fleitmann et al., 2011; Nicholson et al., 2020) and marine cores (e.g. Sirocko et al., 1993; Clemens and Prell, 2003; Ziegler et al., 2010; Böll et al., 2015). These provide records of long-term climatic variability across the Saharo-Arabian desert belt, regarded as a key region for Late Quaternary hominin demographic changes and dispersals in and out of Africa (e.g. Armitage et al., 2011; Drake et al., 2011; Parton et al., 2015b; Breeze et al., 2015; Tierney et al., 2017). Despite this, the landscape-scale responses of terrestrial environments to these regional-scale climatic changes, which are critical for framing early human dynamics in Arabia, remain unclear and cannot be determined with spatial precision from the primary sources of palaeoclimatic data.

Increasing terrestrial palaeoenvironmental archives from landforms across the Arabian Peninsula are now available. These permit the construction of more detailed datasets of landscape change, which can be challenging in drylands that often lack the high-resolution biological, isotopic and geochemical proxies of higher-latitude temperate climates (Thomas, 2013). Geoproxies, such as aeolian dunes (e.g. Preusser et al., 2002; Atkinson et al., 2011; Leighton et al., 2013), alluvial deposits (e.g. McLaren et al., 2009; Berger et al., 2012; Matter et al., 2016) and palaeolakes and wetlands (e.g. McClure, 1976; Parker et al., 2004; Parton et al., 2018) have given new insight into hydro-climate dynamics and their site-scale controls on geomorphic processes. The application of luminescence dating in Arabia since the early 2000s, as well as continued use of radiocarbon dating where practicable, provide chronometric control to these geoproxies.

Terrestrial landscapes, environments and individual landforms do not respond to regional-scale climatic changes in a linear way. Landscape responses are the result of the complex interplay of geomorphic and geological and regional climatic drivers and feedbacks, with the relative

importance of these factors being temporally and spatially variable. As the volume of site-scale data has increased, the potential for apparently conflicting records has emerged when local and regional records are compared. For instance, it has been suggested that there is significant regional diversity in the timing of palaeohydrological activity during the Holocene, shown by fluvial and lacustrine records, which is not necessarily synchronous with variability in monsoon rainfall evidenced from speleothem and marine core data (e.g. Parker et al., 2016; Petraglia et al., 2020). Whilst integrating and resolving seemingly conflicting terrestrial proxy data as well as regional palaeoclimate records may be complex, heterogeneity should be expected and embraced in any synthesis (Leighton et al., 2014b) since it reflects variability in both local-regional landscape dynamics, which can be observed in the environment today, and site-specific sediment preservation processes. A landscape-scale approach is therefore more appropriate for integrating the smaller-scale drivers of palaeoenvironmental changes.

Whilst previous syntheses (e.g. Glennie and Singhvi, 2002; Parker, 2010; Preston and Parker, 2013; Lézine et al., 2014) have acknowledged environmental heterogeneity where apparent, there has been a significant increase in the number and variety of published records from the region over recent years. Previous syntheses have also not assessed the robustness of the geochronology which underpins interpretation of the palaeoenvironmental data. However, studies from other regions have shown this to be an important step in removing the potential for conclusions to be drawn as a result of geochronological imprecision, rather than from 'true' signals of palaeoenvironmental change (e.g. Thomas and Burrough, 2016; Small et al., 2017). These factors provide an opportunity for reappraisal of environmental changes and their drivers at finer spatial (sub-Peninsula) and temporal (sub-Marine Isotope Stage) scales. To date, there has been no systematic review of Arabian palaeoenvironmental changes and their spatial and temporal dynamics throughout the Terminal Pleistocene and Holocene, based on a quality assurance assessment of data.

This analysis compiles a new database of geoproxy chronologies for the Terminal Pleistocene and Holocene (20-0 ka) from across Arabia: **SCAPE** (**S**ynthesising **C**hronologies for **A**rabian **P**aleao**E**nvironments). Data were then screened using quality assurance criteria to assess the robustness of their chronologies. Following this, sub-regional palaeoenvironmental syntheses are constructed based on records with the most robust chronologies. Finally, sub-regional palaeoenvironmental controls are examined with respect to regional-scale climate dynamics and smaller-scale drivers of landscape change.

6.3 Arabian climate variability

The main climate systems of south-east Arabia were detailed in Section 2.2.1. This section frames these climate systems at a larger spatial scale across Arabia, as well as introduces the African Summer Monsoon (ASM).

The geographical position of the Arabian Peninsula within the broader mid-low latitude monsoon belt results in a complex configuration of meridional (north-south) and zonal (west-east) precipitation controls. Today, seasonal rainfall is largely limited to the margins of the predominately arid Peninsula, driven by three principal climate systems (Figure 6.1):

1. **IOSM:** a seasonally reversing system driven by the inter-annual variability of insolation and land-sea thermal contrast between the Indian Ocean and Tibetan Plateau (Molnar et al., 1993). This results in the northwards migration of IOSM rainfall to coastal Yemen and southern Oman during summer months (Scholte and De Geest, 2010).
2. **ASM:** a synoptic zonal feature extending eastwards from Africa, associated with the development of the low pressure Red Sea Trough (RST) and Red Sea Convergence zone (RSCZ), which is driven by converging winds from the Mediterranean to the north and Gulf of Aden to the south (Tsvieli and Zangvil, 2005; De Vries et al., 2013). The ASM provides rainfall to the Red Sea Coast and north-western Arabia (Athar, 2015; Almazroui et al., 2016).

3. **MLWs:** are a zonal system driving cyclonic depressions tracking south-eastwards from the Mediterranean, across northern Arabia and the Gulf as far as central Oman during winter months (Weyhenmeyer, 2000; Hasanean and Almazroui, 2015).

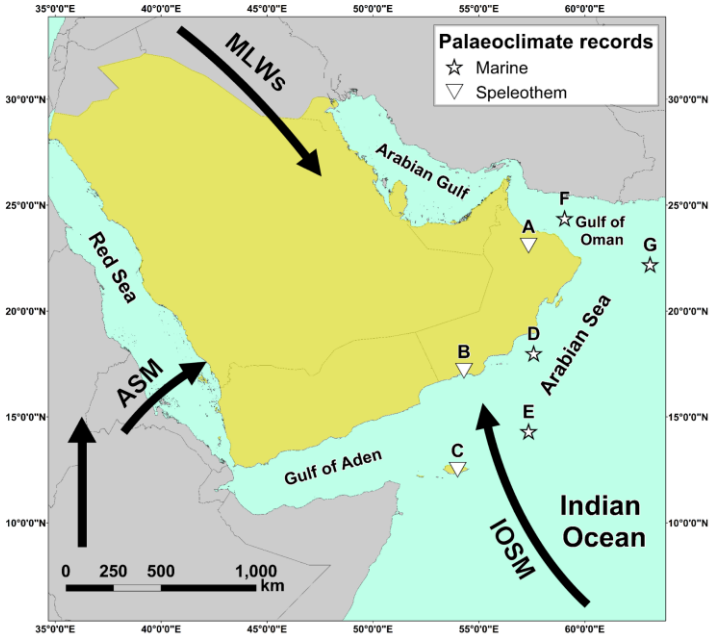

Figure 6.1. The principle modern climate circulations around Arabia: Indian Ocean Summer Monsoon (IOSM), African Monsoon (AM) and Mid-Latitude Westerlies (MLWs). Speleothem **(a-c)** and marine core **(d-g)** palaeoclimate archives of the IOSM in south-eastern Arabia and the Arabian Sea are also shown (see Appendix D for the names and references for **a-g**).

6.3.1 IOSM variability over the past 20 ka

Meridional variability has been the focus of much of the palaeoclimate research carried out around the Arabian Peninsula, with periodic intensifications and northwards migrations of the IOSM, followed by southern retreat and reductions in precipitation intensity, being recorded throughout the Late Quaternary (Parton et al., 2015b).

There is close coherence between palaeoclimate archives and precessionally-paced insolation variability over the last 20 ka (Berger and Loutre, 1991). Isotopic, sedimentological and geochemical

reconstructions from Arabian Sea cores show the gradual intensification of the IOSM between 20-9 ka (Sirocko et al., 1993; Overpeck et al., 1996; E, D, Fig.6.1). This is corroborated by a positive relationship between Arabian Sea biological productivity and insolation throughout the Terminal Pleistocene (Ziegler et al., 2010; G, Fig.6.1). Terrigenous dolomite and calcium carbonate input into the Gulf of Oman also show a decline from ~13 ka, indicating a shift towards relative humidity and continental landscape stabilisation (Cullen et al., 2000; F, Fig.6.1). Peak monsoon conditions in the Arabian Sea occur at ~9.5 ka, demonstrating a lag of ~3 ka with respect to June insolation maxima (Overpeck et al., 1996; D, Figure 6.1).

Early-Mid Holocene peak monsoon intensity is corroborated by speleothem data from Oman and Yemen (e.g. Burns et al., 1998; Fleitmann et al., 2003a; Fleitmann et al., 2011; A; Neff et al., 2001; Shakun et al., 2007; C; Fleitmann and Matter, 2009; B, Figure 6.1). The Qunf Cave (southern Oman; B) and Moomi Cave (Socotra; C) records indicate precipitation intensification occurred earlier at more southerly latitudes (Shakun et al., 2007; Fleitmann and Matter, 2009). Precipitation maxima at Hoti Cave, Oman (23°05'N; A) lagged behind the Qunf Cave (17°10'N) record by ~400 years, demonstrating the time-transgressive northwards displacement of the IOSM rain-belt (Fleitmann and Matter, 2009).

During the Mid Holocene, Hoti Cave records a rapid reduction in precipitation from 6.3 ka (Burns et al., 1998; Neff et al., 2001). This trend is observed in the Qunf Cave record, although the decrease is more gradual (Fleitmann and Matter, 2009). Hoq Cave (Soqotra) shows this drying trend from 6 ka, again indicating a latitudinal retreat of monsoon rainfall (Van Rampelbergh et al., 2013).

6.3.2 The 'wet' vs 'dry' narrative

This meridional framework describes an arid- to hyper-arid Late Pleistocene with rainfall gradually increasing into the Early Holocene from 20-10 ka. Peak monsoon conditions between 10-6 ka then resulted in climatic and environmental amelioration, before the southwards retreat of the IOSM caused the onset of present arid conditions from 6 ka. However, this framework is based on

palaeoclimate records exclusively from southern and south-eastern areas, so is unlikely to describe climatic conditions in western and north-western regions of the Peninsula (Enzel et al., 2015). The present climate of Arabia suggests that zonal circulations would have been important controls on past environments in western and north-western areas, however their long-term variability is also poorly constrained due to a lack of high-resolution, terrestrial palaeoclimate archives in Arabia outside of the IOSM rainfall zone (Nicholson et al., 2020).

High-resolution palaeoclimate archives are available for regions peripheral to Arabia that are influenced by the ASM and MLWs, including the Levant (e.g. Bar-Matthews et al., 1997, 1999, 2003; Verheyden et al., 2008; Litt et al., 2012) and NE Africa (e.g. Weldeab et al., 2014; El-Shenawy et al., 2018). A broad concept of the Arabian Holocene Humid Period (AHHP) from ~10-6 ka has prevailed in the palaeoenvironmental and geoarchaeological literature (e.g. Groucutt et al., 2020; Petraglia et al., 2015, 2020). Using proximal records to explain site-scale environmental changes in northern and western Arabia bears risks of spatial over-extrapolation. This framework also simplifies complex endogenic controls that are independent of regional climate, yet also drive environmental change. High quality environmental records are therefore important for understanding landscape changes at finer spatial and temporal scales outside of this broad climatic narrative.

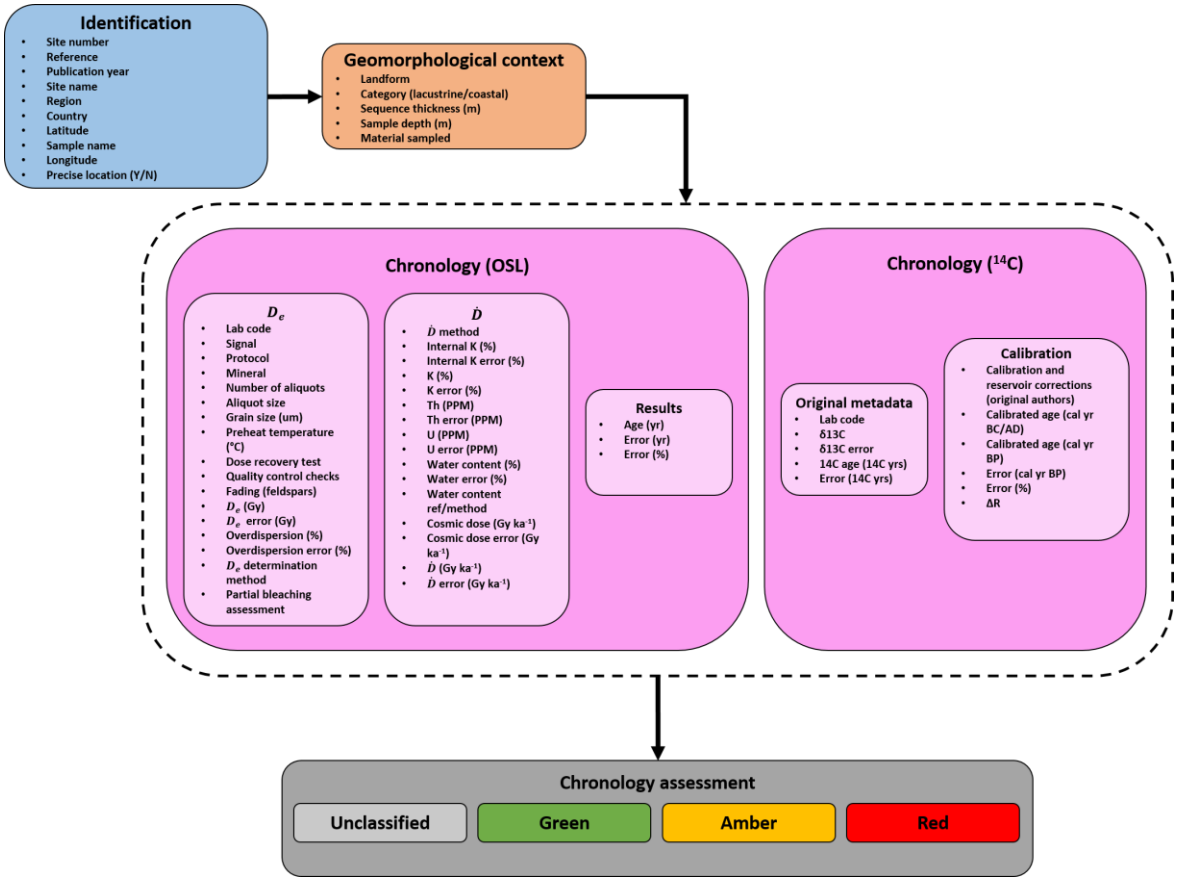

Figure 6.2. The structure of the database and the metadata it contains.

6.4 The SCAPE database

SCAPE is divided into four sections: 1) identification, 2) geomorphological context, 3) chronology and 4) chronological assessment:

1) Identification: includes publication reference, year and georeferenced site location. 'Precise location (Y/N)' denotes whether the original publication included site coordinates. If not, a best estimate of the site's location has been made using the publication and Google Earth.

2) Geomorphological context: contains information about the material, depositional setting of the dated sample and an interpretation of the type of environment represented.

3) Chronology (OSL/^{14}C): contains chronological metadata for both dating techniques (luminescence and radiocarbon).

4) Chronology assessment: process of chronological reliability assessment (see section 6.5).

6.4.1 Types of record

Interpreting geoproxies relies on identifying the geomorphic processes underpinning their formation, including climatic influences, environmental responses, scale issues and thresholds for dynamic behaviour. For example, Enzel et al. (2015) reassessed published 9-5 ka 'palaeolake' records from across Arabia, concluding that they were not lakes per se, but rather shallow wetlands due to their sedimentological, floral and faunal properties. Engel et al. (2017) postulate that some basins in Arabia do show evidence of hosting perennial lakes during the Early-Mid Holocene, pointing to evidence such as laminated marl sediments indicating undisturbed aqueous deposition in standing water in the Awafi (Parker et al., 2004), UAE, and Tayma (Dinies et al., 2015), northern Saudi Arabia, basins. Engel et al. (2017) also emphasise that the preservation of features such as shorelines, diagnostic of lakes as opposed to wetlands (Enzel et al., 2015), is unlikely in many Arabian environments due to post-depositional aeolian deflation under currently arid-hyper arid climate regimes. This does not mean individual lacustrine features need to be interpreted as a binary of either lakes or wetlands, but rather multiple records suggest spatio-temporal fluctuations between phases of higher and lower water abundance (e.g. Lézine et al., 1998, 2010; Fuchs and Buerkert, 2008; Parker et al., 2016; Parton et al., 2018). It is necessary therefore to draw on all available geomorphic information supplied by original authors, as well as other associated proxies such as micro- and macro-fauna, pollen and geochemical data, where available, to make nuanced interpretations of past environments.

Caution must also be exerted when extrapolating site-scale interpretations to regional-scale contexts. Leighton et al. (2014a) examined dune accumulation rates over the last 30 ka at individual sites in south-eastern Arabia, highlighting the spatio-temporal heterogeneity in aeolian sediment preservation based on chronological records at the time. This is the result of site-scale controls on erosion and deposition within the context of dynamic aeolian systems, that are not necessarily scalable to dunefield or regional contexts. Therefore, dune chronologies from individual sites should be treated cautiously as proxies themselves, with benefits accrued from the amalgamation

of site records, including age and sedimentation data, to the dunefield scale (i.e. Thomas and Bailey, 2019). This is not to say that ages should not be viewed as proxies, however it is imperative to recognise that they are signals resulting from site-scale controls on sediment accumulation and preservation. Any synthesis of chronological data from multiple sites must therefore a) be at an appropriate spatial scale based on specific geographical areas and, b) be caveated by understandings of endo- and exogenic controls at the site-scale.

Given these considerations, geochronological records are categorised into six landform types. 'Lacustrine' and 'Coastal' are subdivided into multiple record types, owing to the range of proxies within these groups. Whilst other groups could also be sub-divided, for instance there is abundant literature on different types of palaeosols (e.g. Retallack et al., 1988; Mack et al., 1993; Alonso-Zarza, 2003), it was more difficult to make post-hoc assessment of these often subtle differences in processes with the information provided in original publications. Groupings are detailed in Table 6.1. Where available, other proxies recorded within the context of these groups, such as pollen, have been considered when interpreting record types but, due to the scarcity of these biological proxies, geomorphological and sedimentological properties are the key focus for most records. Contextual geomorphic information is therefore recorded in Section 2 of the database (Fig.6.2).

6.4.2 Sub-regions, sites and individual records

To aid palaeoenvironmental syntheses, Arabia was divided into seven sub-regions based on physiographic and geomorphological characteristics (Fig.6.3): i) the Nefud, the sand sea situated in the topographic depression of interior northern Saudi Arabia; ii) the Arabian Gulf Coast/Northern Rub'al Khali, the coastal landscape from north-eastern Saudi Arabia to north-eastern UAE, incorporating the dunefields of the northern and north-eastern Rub'al Khali; iii) the Hajar Mountains, the mountain belt in northern Oman/UAE running parallel to the Arabian Sea coastline and its associated alluvial systems extending westwards; iv) the Arabian Sea Coast, the coastal lowlands of south-eastern Arabia, including the Wahiba Sands dunefield in central Oman; v) the

Table 6.1. Summary of the landform types recorded in the database from the published literature with a general description of the geomorphological, sedimentological and biological features they commonly exhibit.

Landform type		Description and key characteristics
Lacustrine	Palaeolakes	Basins, often with relatively large drainage areas, commonly preserving laminated marl/varve sediments, shorelines, deltas, species indicative of standing freshwater etc.
	Wetlands	Low elevation marsh environments with relatively small drainage areas, which commonly preserve unlaminated sediments, evaporites, evidence of relict vegetation (e.g. root voids), species indicative of shallow/brackish water etc.
Fluvial		Channel fill, overbank floodplain and sheetflood deposits resulting from the activation of water courses along drainage networks such as alluvial fans or rivers.
Coastal	Mangroves	Coastal forest-swamp ecosystems, often resulting in fine grain clay-silt sediment accumulation preserving root structures/rhizoliths and organic material.
	Shorelines	Beach deposits parallel to current coastline, often preserving marine sands and shells.
	Coastal sabkha	Intertidal mud flats in arid environments, commonly with overlying evaporite crusts.
	Lagoons	Intertidal water bodies partially open to marine incursion or closed by deposition, often preserving bioclastic sands and shells.
Aeolian		Well-sorted, medium-coarse grained aeolian sands constituting dunes and sand sheets.
Springs		Carbonate deposits from groundwater forming spring mounds; terraces, carbonate veins, incised channels and pools, laminations etc.
Palaeosols		Organic horizons indicating the development of soil in the past, often with evidence of bioturbation.

Rub'al Khali, the topographic depression of the Peninsula's interior occupied by an aeolian sand sea; vi) Western Arabia, the Asir Mountains running parallel to the Red Sea coast and associated piedmont landscapes of western Saudi Arabia and vii) Southern Arabia, the Yemen Highlands in the south-west and Hadramawt Plateau to the east, along with their associated drainage features in the interior Ramlat as'Sabatayn desert area.

Site-aggregation of age records was based on information provided by original authors, with multiple sections grouped together if they represent a continuation of the same depositional environment. For example, palaeolake Jubbah in the Nefud has age records from three separate sections but they are all located within the same basin constituting the palaeolake, with clearly related stratigraphic horizons (Parton et al., 2018). For many sites, the type of landform is

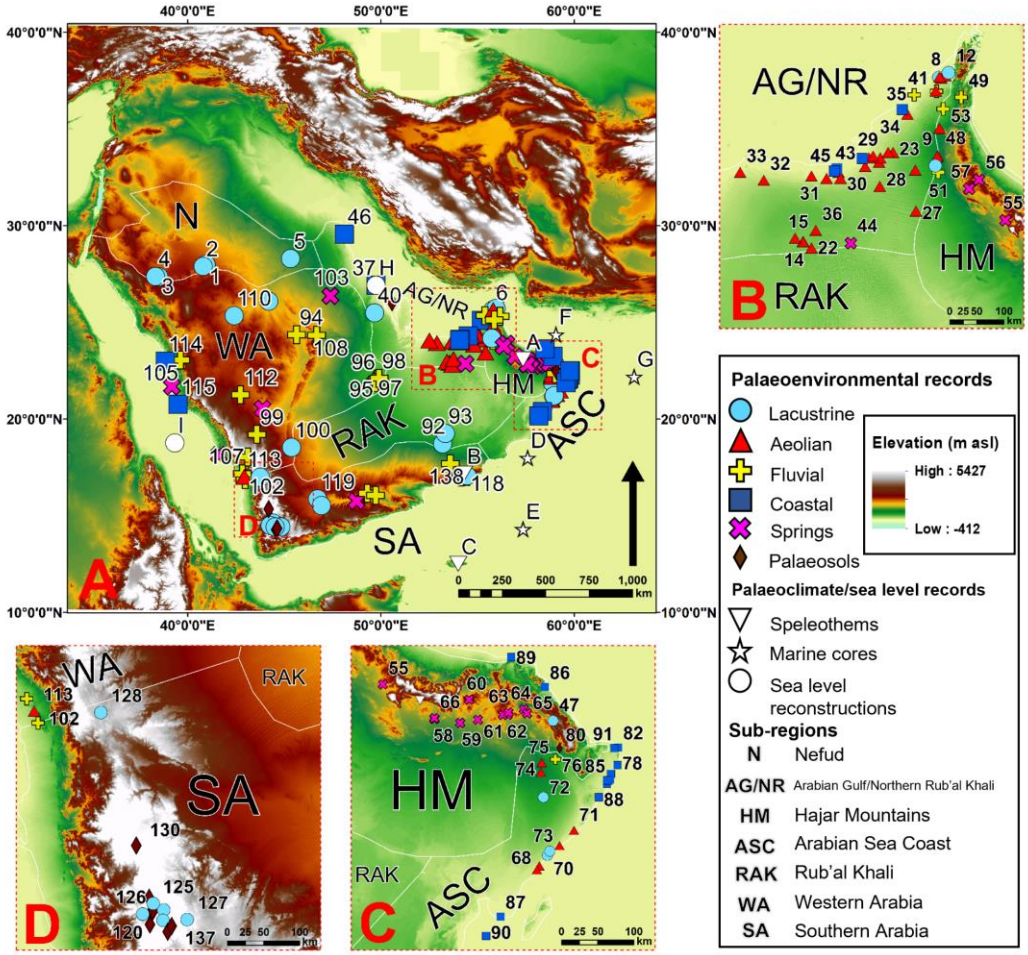

Figure 6.3. (a) All sites included in the database showing the predominate palaeoenvironmental interpretations of the age records they contain (1-138), as well as regional palaeoclimate and sea level archives (a-i). Sub-regional divisions of the Arabian Peninsula are shown. See Appendix D for a table listing the details of each numbered site. **(b)** The eastern portion of the Arabian Gulf/Northern Rub'al Khali sub-region. **(c)** The northern portion of the Arabian Sea Coast sub-region. d: The western portion of the Southern Arabia sub-region.

consistent throughout depositional sequences. Dune sequences from the Arabian Gulf/Northern Rub'al Khali, for example, are all composed of aeolian sand horizons with varying internal bedding architecture (Bray and Stokes, 2004). By contrast, some sites represent changes in dominant process regime through time and down-section, such as palaeolake Mundafan in the Rub'al Khali which reveals sections of aeolian sands overlain by lake marls, indicative of a successive switching to sub-aqueous deposition (Rosenberg et al., 2011). Table 6.2 summarises the number of sites, records and landform types available from the published literature for each sub-region.

Table 6.2. Sub-regional summary of sites and landform types of individual chronological records within the database.

Sub-region	Number of sites	Number of records										
		Lake	Wetland	Fluvial	Mangrove	Shoreline	Coastal sabkha	Lagoon	Aeolian	Spring	Palaeosol	Total
Nefud	5	32	7	0	0	0	0	0	0	0	0	39
Arabian Gulf /Northern Rub'al Khali	41	13	4	6	3	37	28	0	157	5	5	258
Hajar Mountains	20	0	46	5	0	0	0	0	20	61	1	133
Arabian Sea Coast	25	7	11	1	46	0	4	18	40	0	1	128
Rub'al Khali	2	0	9	0	0	0	0	0	0	0	0	9
Western Arabia	22	22	2	32	0	0	0	9	10	7	1	83
Southern Arabia	23	15	22	21	0	0	0	0	0	4	22	84
Total	138	89	101	65	49	37	32	27	227	77	30	734

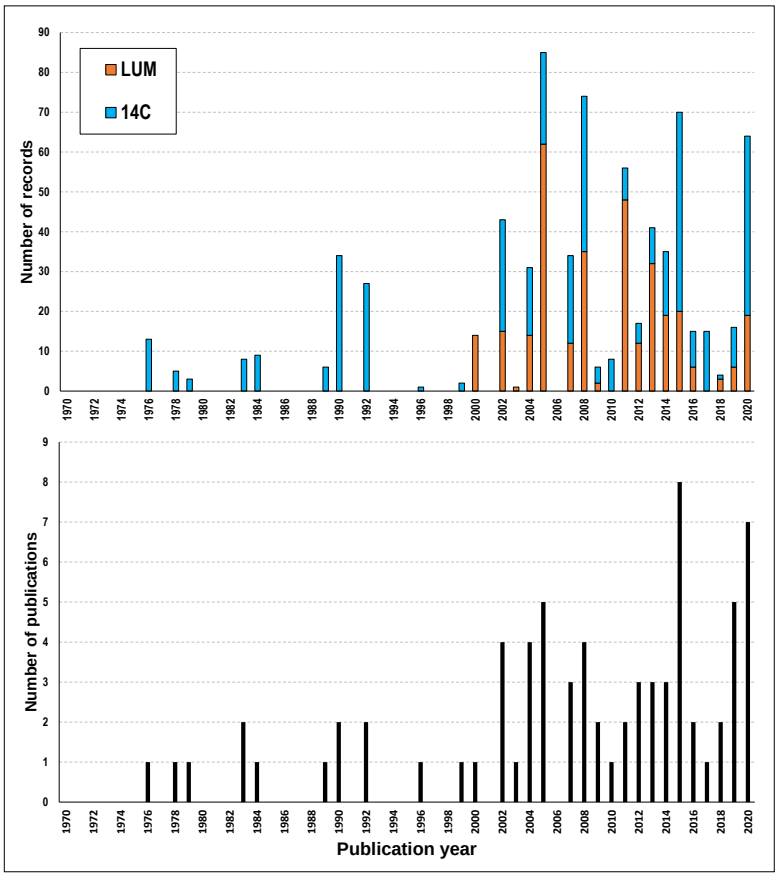

Figure 6.4. Temporal trends in published luminescence and radiocarbon dates from palaeoenvironmental sites from the Arabian Peninsula (1970-2020).

6.4.3 Geochronological metadata

Since the 1970s, the volume of geochronological data available for the Arabian Peninsula has greatly increased (Figure 6.4). SCAPE currently extends back to 20 ka and includes 328 OSL ages and 406 radiocarbon ^{14}C ages. This period encompasses the transition from colder, drier glacial-age conditions to the warmer and wetter Holocene. To assess the quality of ages and centralise data for future uses, metadata beyond published ages and associated uncertainty values were included.

OSL metadata

For background details of the OSL dating process, readers are referred back to Section 3.2.2. Whilst Duller (2008a) provides a comprehensive checklist of the metadata which should be included in publications with luminescence ages, reporting in the literature varies greatly. Following previous compilations of luminescence ages (e.g. Lancaster et al., 2016; Small et al., 2017), of particular importance for assessing ages are information such as the mineral dated, the aliquot size and grain size selected, the measurement protocol, the completion of a dose recovery test, the elemental dosimetry (K, U, Th), cosmic dose and estimated historical water content (for D_r; Figure 6.2). These considerations are commonly reported by authors. However, other information, such as the number of aliquots measured, the technique used to calculate dosimetry, measurement temperatures and references cited for choosing particular methods or parameters are also recorded where available to create a database that has a broad scope of potential utility for users.

Qualitative information is also important for assessing the potential for partial bleaching in luminescence samples. The trapped charge in mineral grains is assumed to have been fully ionised (or 'bleached') at the time of deposition, through exposure to sufficient sunlight. However, if grains are incompletely bleached it can result in an age overestimation (Rhodes, 2011). This is a common problem in aqueous depositional environments, such as fluvial settings (e.g. Smedley and Skirrow, 2019), where sediment deposited in murky water bodies or transported short distances may not be sufficiently exposed to sunlight for complete resetting of the luminescence signal. Hence, a

summary of the judgement of original authors on the potential for partial bleaching in their samples, based on the geomorphic context of material and D_e variability, has been included where available.

^{14}C metadata

Radiocarbon dating permits the estimate of time since the death of an organism, based on the radioactive decay of the ^{14}C isotope and laboratory measurement of the remaining ^{14}C in organic material (Arnold and Libby, 1949; see Bronk Ramsey, 2008 for a detailed introduction). Reporting is much more standardised for ^{14}C ages than OSL, with metadata included in publications usually limited to the material sampled (e.g. 'shell', and species, e.g. '*Terebralia palustris*'), an age estimate in ^{14}C years and a calibrated age in calendar years before present (or 'cal yr BP'; Figure 6.2), with 'present' defined as 1950 AD.

^{14}C ages in ^{14}C years need to be calibrated to yr BP using a calibration curve constructed by comparing measurements of ^{14}C years from high quality samples with independent chronologies in calendar yrs BP. For example, tree rings, speleothem laminations and lake varves can be accurately dated using independent methods (Reimer et al., 2020). ^{14}C ages in the database have been calibrated from the original publications using the latest IntCal20 and Marine20 calibration curves to ensure data comparability (Reimer et al., 2020; Figure 6.2; see Section 3.4 for an example).

However, ocean waters are depleted in ^{14}C concentrations relative to the atmosphere (Ascough et al., 2005). This marine reservoir effect (MRE) means organisms that fix carbon from ocean water will give erroneously 'old' ^{14}C ages (e.g. Lézine et al., 2002; Wood et al., 2012; Beuzen-Waller et al., 2019). Correction factors (ΔR values) are therefore also applied to ^{14}C age estimations during calibration where applicable, but vary regionally due to different ocean circulation patterns and by species (e.g. Lindauer et al., 2017). Again, to ensure comparability, ΔR values used for the calibration of coastal records have been re-calculated using the 14CHRONO Marine Reservoir Database which has been updated for the Marine20 calibration curve (http://calib.org/marine/; Figure 6.2).

6.5 Geochronological quality assurance

6.5.1 Sources of uncertainty in OSL and ^{14}C dating

Sources of uncertainty are inherent in all forms of laboratory-based dating techniques and should be adequately explored and reported in palaeoenvironmental studies. Numerous studies provide comprehensive overviews of these geochronological issues (see Wintle, 2008; Wallinga and Cunningham, 2015; Thomas and Burrough, 2016; Small et al., 2017). These uncertainties vary between samples and thus require assessment at the scale of individual sample metadata. Commonly reported sources of uncertainty in both dating techniques are outlined in Tables 6.3 and 6.4.

6.5.2 Quality assurance criteria

Based on the common sources of uncertainty outlined in Tables 6.3 and 6.4, other geochronological databases employ quality assessments to identify records with the highest likelihood of being robust (e.g. Graf, 2009; Seitsonen et al., 2012; Lancaster et al., 2016; Thomas and Burrough, 2016; Loftus et al., 2019). Following the approach used by Small et al. (2017), a green-amber-red classification (Table 6.5) is employed in SCAPE. All entries in the database are treated individually and assessed independently from existing 'wet vs. dry' narratives of regional climate variability.

It should be noted that quality control can only progress as far as the available data allow. It is not possible to identify all potential sources of uncertainty from post-hoc assessments of metadata, such as laboratory contamination of ^{14}C samples with modern carbon producing age underestimations (Small et al., 2017). Rather, the quality criteria should be viewed as a working framework for data reduction to test hypotheses of palaeoenvironmental change.

Table 6.3. Summary of the common sources of uncertainty in luminescence dating and examples from the database where these issues have been discussed.

Potential source of uncertainty	Description of uncertainty	Database example
D_e		
Partial bleaching	Incomplete resetting of the luminescence signal, resulting in age overestimation from residual trapped charge (Rhodes, 2011) Common in aqueous depositional contexts, less so in aeolian systems (e.g. Preusser et al., 2005; Leighton et al., 2013)	Maqta Oasis, Hajar Mountains (Fuchs and Buerkert, 2008)
Bioturbation	Mixing of sediments deposited at different times through biological processes, causing scatter in D_es as older/younger grains become incorporated (Bateman et al., 2007) Often the result of insect/animal burrowing	Palaeolake Mundafan, Western Arabia (Rosenberg et al., 2011)
Beta micro-dosimetry	Variable beta dosimetry throughout a horizon (Nathan et al., 2003) Asymmetry results from uneven concentrations of radionuclides emitting short-range beta radiation	Jubbah palaeolake, Nefud (Clark-Balzan et al., 2018)
D_r		
Disequilibrium in U/Th decay chains	D_r cannot be assumed to be a closed system and thus constant through time (Olley et al., 1996) Often a problem in environments which have experienced large fluxes in hydrological conditions, mobilising mobile radionuclides in and out of sediments (Clark-Balzan et al., 2018)	Dubai palaeoshorelines, Arabian Gulf Coast/Northern Rub'al Khali (Zander et al., 2007)
Cosmic dose estimation	Where sediment overburden has altered drastically through time the cosmic contribution to D_r is not necessarily time-dependent (Duller, 2008a) Problematic in low dose-rate and near-surface environments as the contribution of cosmic rays is proportionally larger (e.g. Blechschmidt et al., 2009)	No studies in the database make specific reference to this issue
Water content estimation	Within a sediment matrix water attenuates some of the radiation emitted by radionuclides (Nelson and Rittenour, 2015) In environments which have experienced dramatic changes in hydrological regime over time, estimating a realistic water content can be problematic (Thomas and Burrough, 2016)	Wahala aeolian dunes, Arabian Gulf Coast/Northern Rub'al Khali (Atkinson et al., 2011)

Geomorphic criteria

For an age to be categorised as green, it is essential that sufficient stratigraphic and sedimentological detail is available in the original publication to provide inference of the type of landform dated for correct palaeoenvironmental interpretation (Table 6.1). This includes the depths of individual samples and clear, annotated stratigraphic diagrams. The highest quality ages will also be supported by other ages from the section or site in chrono-stratigraphic agreement

Table 6.4. Summary of the common sources of uncertainty in radiocarbon dating relating to sample considerations and reservoir effects. Examples of studies where these issues have been discussed are included from the database.

Potential source of uncertainty	Description of uncertainty	Database example
Sample considerations		
Type of sample	Bulk samples, e.g. soil, do not represent one discreet event, but the temporally transgressive demise of possibly multiple organisms, with individually unknown lag times between death and deposition (Strunk et al., 2020) Macrofossil samples, e.g. a shell, representing singular events rather than a mean of unknown separate events are preferable for producing more reliable age estimates (e.g. Barnekow et al., 1998; Martin et al., 2019)	Sedd Adhra'ah palaeosols, Yemen (Wilkinson, 2005)
Laboratory contamination	Radiocarbon samples are often very small (<4mg) and have a low organic carbon content. Therefore, even small amounts of modern carbon contamination during laboratory analysis can produce an inaccurate age estimate (Lowe and Walker, 2000)	No studies in the database make specific reference to this issue
Reservoir effects		
Marine reservoir effects (MREs)	Organisms that fix carbon from ocean water give age overestimations as ocean water is depleted in 14C concentrations relative to the atmosphere (e.g. Lézine et al., 2002; Wood et al., 2012; Beuzen-Waller et al., 2019) MREs vary regionally due to different ocean circulation patterns and by species due to different food sources, habitats and climates (e.g. Lindauer et al., 2017). Correction factors (ΔR values) must be applied to ^{14}C age estimations	Dosariyah beach shells, Arabian Gulf Coast/Northern Rub'al Khali (Parker et al., 2020)
Hardwater effects	Result from the fixation of 'old' ^{14}C from terrestrial sources, such as the dissolution of carbon from carbonate geology, leading to age overestimation (Deevey et al., 1954)	Al Hawa basin, Yemen (Lézine et al., 2007)

Table 6.5. Descriptions of the quality assurance 'traffic-light' classifications devised by Small et al. (2017) and applied to SCAPE.

Quality assurance classification	Description
Green	Ages judged to be most reliable and should be considered in analysis. Conflicts with new data will require to be specifically addressed.
Amber	Ages are available to be included in analysis. Their reliability may be re-assessed based on new data.
Red	Ages should only be included in analysis with acknowledgement of important caveats or is dependent on new and supporting evidence.
Unclassified	Ages not considered in assessment due to insufficient information (e.g. original publications not accessible).

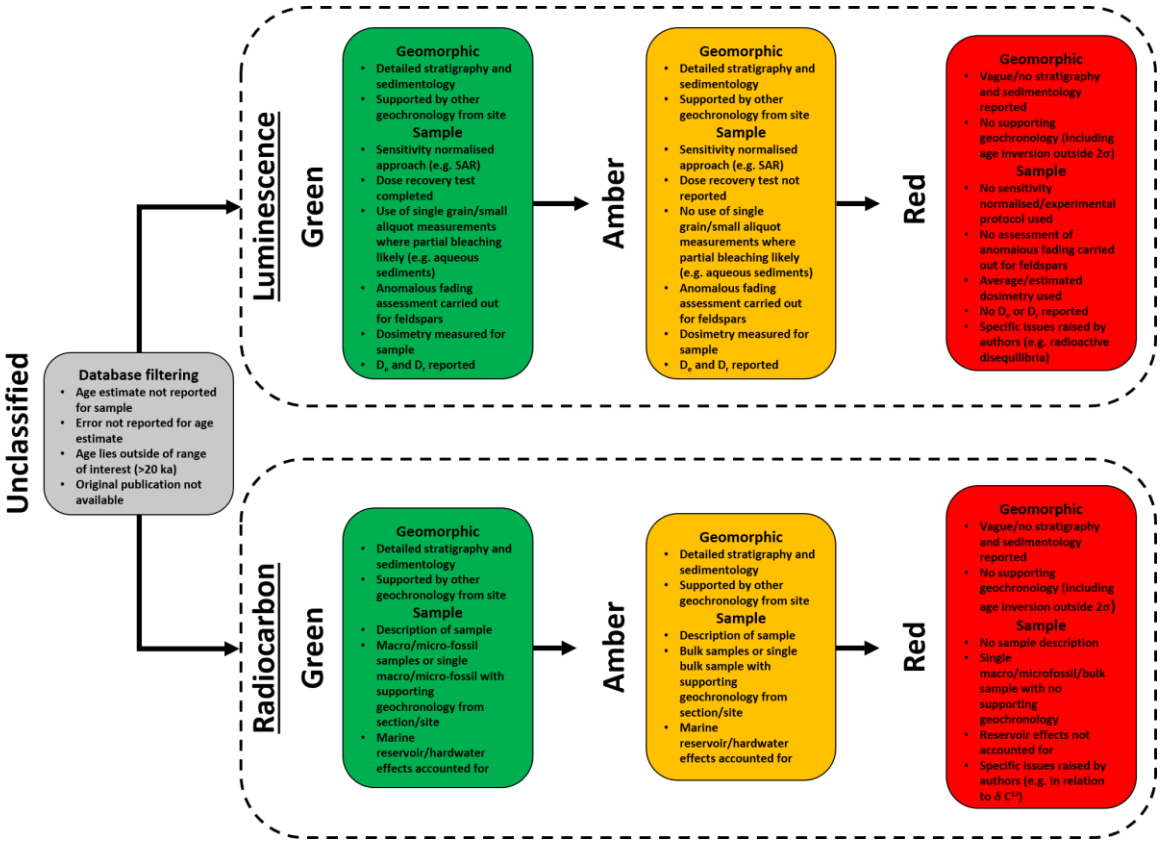

Figure 6.5. Geochronological quality assurance criteria for green, amber and red luminescence and radiocarbon dates with both 'Geomorphic' and 'Sample' considerations for each technique. After the approach of Small et al. (2017).

with each other, with age-reversals (ages outside of 2σ error) receiving red classifications. Supporting geochronology can be provided by ages generated using the same or different techniques or be older than the upper age limit of this study (>20 ka).

OSL dating criteria

These focus on the sources of uncertainty (Table 6.3; Figure 6.5) that are most readily appraisable from the metadata available in publications, following Small et al. (2017). Use of a sensitivity corrected protocol, such as the SAR protocol, for D_e measurement is an important criterion as it accounts for potential sensitivity changes which may be induced in samples as a result of heating and irradiation (Murray and Wintle, 2000; Murray and Wintle, 2003). The completion of a dose recovery test for at least one sample from a site is also important for a green classification as it can also reliably assess potential sensitivity changes in samples (Wintle and Murray, 2006). It is also

expected that D_e measurements from depositional settings likely to have experienced partial bleaching (e.g. fluvial and lacustrine sediments; Table 6.3) will have been made on small (1-2 mm) aliquots or single grains so as not to overly obscure variability (Duller, 2008b).

^{14}C dating criteria

Green ages are derived from macro- or micro-fossil samples with supporting geochronology (Table 6.4; Figure 6.5). Bulk samples, with supporting geochronology, can only achieve amber classifications due to the greater measurement uncertainties they pose (Strunk et al., 2020). This supporting geochronology can include other bulk ^{14}C ages in chrono-stratigraphic agreement, macro/micro-fossil samples or ages using a different technique. Important for determining the type of sample analysed is a clear description of samples taken from sites, with individual species identified where possible. Whilst terrestrial samples with suspected hardwater effects can only receive red classifications (e.g. Lézine et al., 2007), MREs have been accounted for using the 14CHRONO Marine Reservoir Database.

6.6 Arabia geochronology quality assessment

For the 734 database ages, 39.5% (n=290) attained green classifications, 22.8% (n=167) amber, 34.6% (n=254) red and 3.1% (n=23) remained unclassified (Table 6.6). The Arabian Gulf/N Rub'al Khali has the highest percentage of green records (57.8%, n=149), whilst the Rub'al Khali does not have any. By contrast, Western Arabia has the highest percentage of red records (62.7%, n=52). Based on this assessment and the recommendation of Small et al. (2017) that only green and amber records be utilised in subsequent analysis (Table 6.5), 62.3% (n=457) of ages remain available for inclusion in palaeoenvironmental syntheses.

Figure 6.6 compares geochronological data by landform type and temporally at 1 ka time-slices, both at the Peninsula (a) and sub-regional (b) scales. This shows the significant inter-regional variability in the quality of different proxies as well as the temporal coverage of records which is

Table 6.6. Number of records attaining each dating method quality level, by sub-region.

Sub-region	GREEN	AMBER	RED	UNCLASSIFIED	Total
Nefud	20	9	7	3	39
Arabian Gulf/Northern Rub'al Khali	149	58	36	15	258
Hajar Mountains	20	55	54	4	133
Arabian Sea Coast	51	6	71	0	128
Rub'al Khali	0	8	1	0	9
Western Arabia	28	2	52	1	83
Southern Arabia	22	29	33	0	84
Total	290	167	254	23	734
%	39.5	22.8	34.6	3.1	100

not apparent when aggregated at the Peninsula scale, reinforcing the need for palaeoenvironmental syntheses at smaller spatial scales to identify landscape heterogeneity and where robust data is lacking.

Regional variability in proxy diversity is partly due to physiographic differences affecting the formation of particular landforms. However, there are some sub-regions within which the lack of representation of particular landform types is surprising. There are no aeolian records from either the Rub 'al Khali or Nefud (Figure 6.6b). However, these regions both contain significant dunefields, highlighting the much greater potential for aeolian dune records across the Peninsula. Of 227 aeolian records in total, 157 (69.2%) are located in the Arabian Gulf/Northern Rub'al Khali sub-region. Of the remaining 70 records from other sub-regions, 60% (n=42) attain red classifications, emphasising the paucity of high-quality dune data from elsewhere. The Arabian Gulf/Northern Rub'al Khali is extremely accessible for field sampling, likely explaining this region as a focal point for aeolian research. However, extrapolation of these data beyond the scale of their sub-regional dunefield controls to infer the dynamics of other areas is problematic.

The suitability of materials sampled from specific landforms for dating also accentuates spatial differences in the database. For example, partial bleaching is a common problem in water-lain

deposits and is a key factor in the high proportion of red and amber luminescence ages reported from lacustrine sediments (94.3%). Similarly, uncertainties surrounding the precipitation of younger carbonates in the pore spaces of older deposits inhibits the robust ^{14}C dating of spring carbonates using bulk samples (Viles and Goudie, 1990). Consequently, there are no green spring records. Amber classifications were only given to spring records with independent chronology, such as U-Th dating (e.g. Mervine et al., 2015), or where organic material incorporated into carbonate deposits was targeted for ^{14}C dating (e.g. McCorriston et al., 2002).

As a result, some sub-regions with low proxy record diversity and few ages attaining green or amber quality levels have greater data reduction. For example, springs make up 45.9% (n=61) of total records for the Hajar Mountains (n=133), however only 15 of these are included in the final evaluation once quality criteria are applied. Conversely, 78.6% (n=114) of coastal records were classified as green. A large proportion of these were dated using ^{14}C (86%, n=98), with the abundance of macro-fossil samples in these settings aiding chronological robustness.

The lack of contextual information (e.g. sample depth) or any supporting chronology is a major reason for red classifications. In particular, palaeosol and lacustrine dates reported in older publications commonly provide very little stratigraphic detail or only reported a single age for a whole site (e.g. Whitney et al., 1983). While useful for constructing initial chronological frameworks at the time of publication, only limited confidence can be placed in post-hoc palaeoenvironmental interpretations relative to publications where more detailed metadata is available.

Figure 6.5a shows that the Holocene has better temporal resolution for all sub-regions compared to the Terminal Pleistocene. For most regions, there is a peak in the number of records between 10-6 ka (Fig.6.6b). This pattern is due to 1) sampling bias of younger, upper sediments and, 2) sediment preservation issues. As such, this trend in the amount of data increasing towards the present is observed in other databases aggregating Late Quaternary geochronological information (e.g. Thomas and Burrough, 2016).

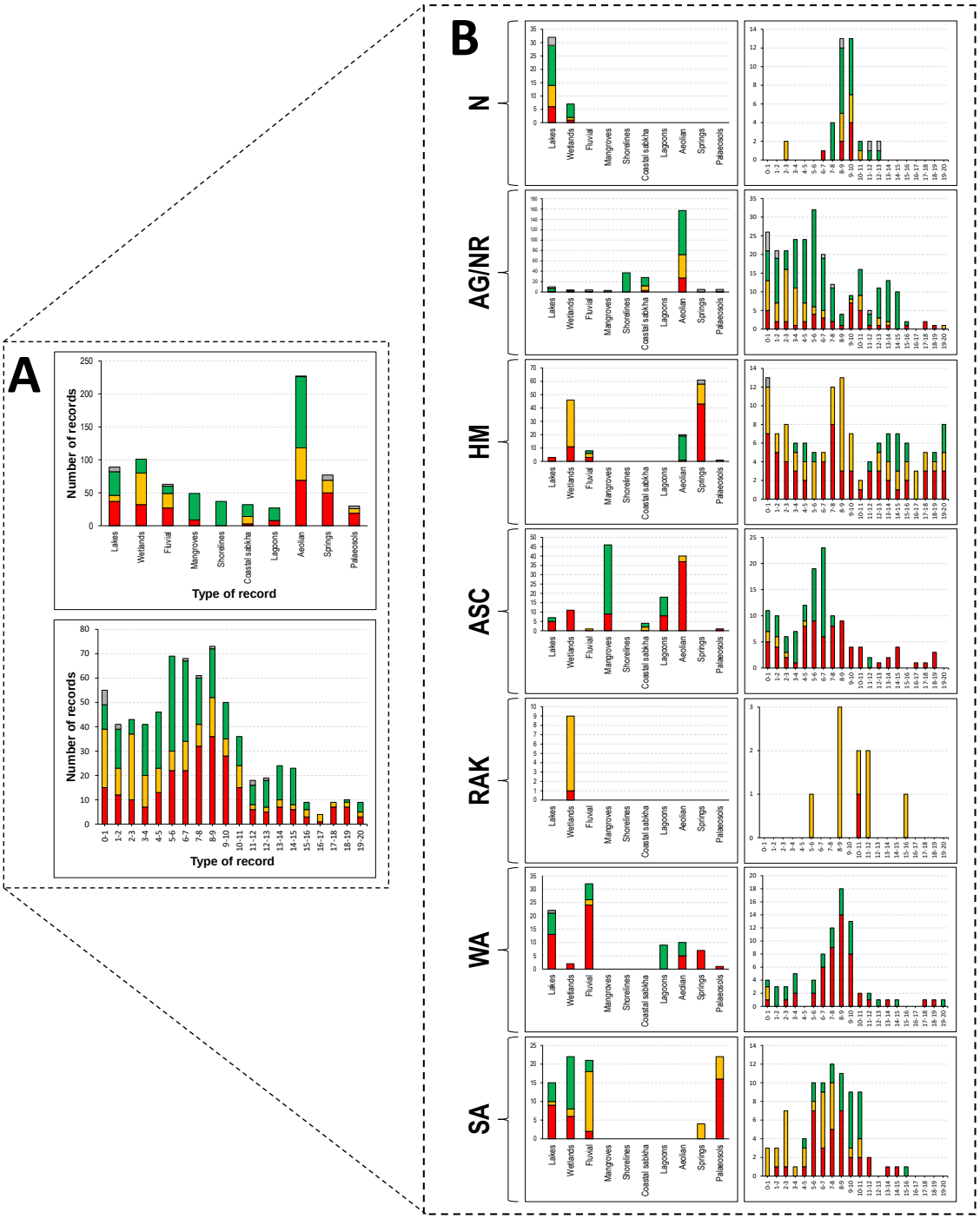

Figure 6.6. Classified records by landform type and 1 ka time-slice intervals at the Peninsula (A) and sub-regional (B) scales. Records have been placed into time-slices based on central age estimates.

Sediment preservation is an important control on temporal variability in the record. The Hajar Mountains have the highest proportion of records during the Terminal Pleistocene (26.3%, n=35). This potentially relates to the continuity of depositional environments such as wetlands in montane regions (e.g. Fuchs and Buerkert, 2008), relative to lowland regions where lacustrine basins may be subject to more intense aeolian deflation during periods of greater aridity (e.g. Engel et al., 2017). Temporal resolution is, therefore, a product of the controls on sediment deposition and preservation which vary by landform type and regional environmental setting.

6.7 Sub-regional palaeoenvironmental variability

Green and amber geoproxy records offer the most reliable data for assessing the drivers of sub-regional landscape change in Arabia throughout the Terminal Pleistocene/Holocene, and thus form the basis for the following syntheses of palaeoenvironmental change. Red records are not included due to being judged as relatively less robust. For the purpose of this review, green and amber ages are treated equally so as not to over-reduce the data available for analysis.

Sites with green and amber records are shown in Figure 6.7. Individual records from these sites are displayed in Figure 6.8 alongside records of monsoon variability and sea level change.

6.7.1 The Nefud

The dataset consists entirely of lacustrine records from three basins in the western Nefud: Jubbah, Jebel Oraf and Tayma (site numbers 1, 2 and 3, respectively; Figs.6.7, 6.8). The earliest sedimentation is recorded in Jubbah at 12.2 ± 1.1 ka (Hilbert et al., 2014). A high abundance of planktonic and tychoplanktonic species suggests a freshwater body was present during the Pleistocene/Holocene transition (Parton et al., 2018). However, water levels reduced during the Early Holocene, with higher ratios of eutrophic diatoms indicating a more saline, shallow wetland between 11.4 ± 0.8 - 6.6 ± 0.7 ka (Parton et al., 2018). The horizon dated to 6.6 ± 0.7 ka in the south of the basin contains a relatively high aeolian component, suggesting the encroachment of the

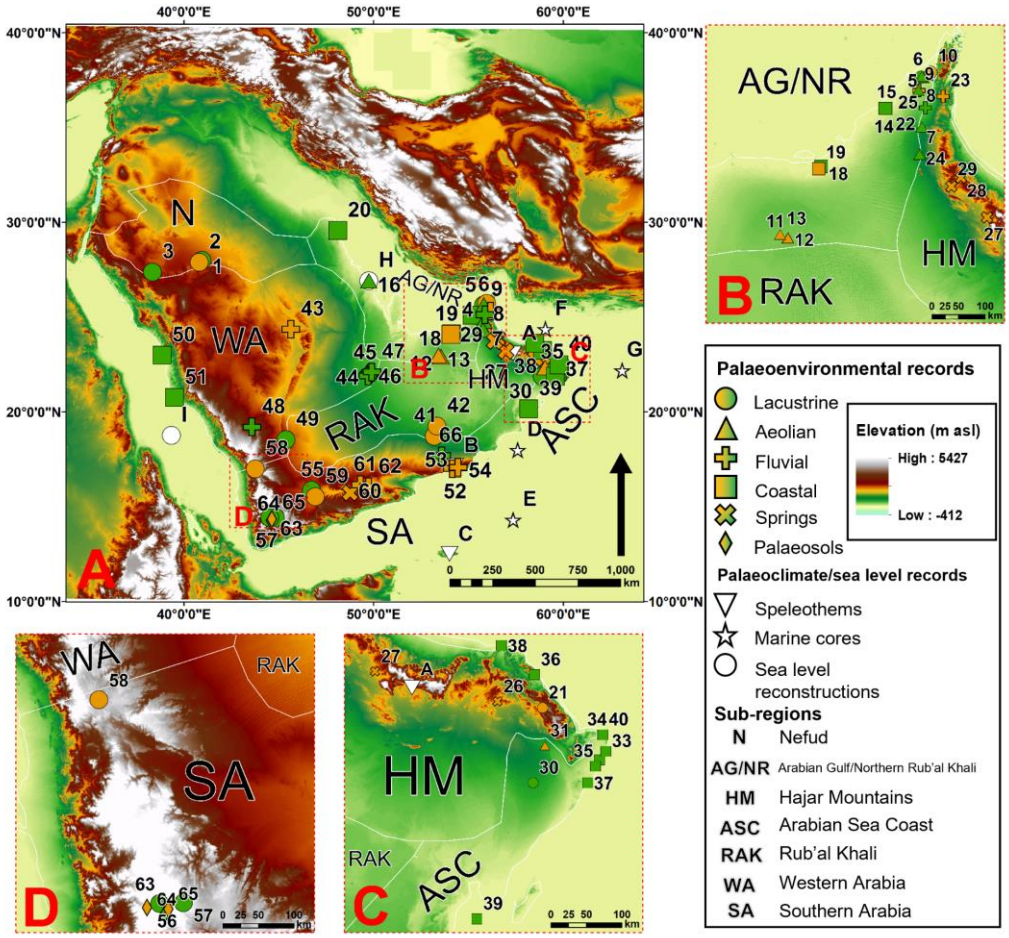

Figure 6.7. (a) Sites with records attaining GREEN and AMBER classifications referred to in the following sub-regional syntheses. Site numbers refer to 'Assessed site number' included as a table in Appendix D. **(b)** The eastern Arabian Gulf/Northern Rub'al Khali sub-region. **(c)** The northern portion of the Arabian Sea Coast and Hajar Mountains sub-regions. **(d)** The western portion of the Southern Arabia sub-region.

surrounding dunefield at this time (Hilbert et al., 2014). This is consistent with shallower, more erratic hydrological conditions. A second freshwater high-stand by 6.4 ± 0.4 ka is evident, with diatom assemblages indicative of a diverse palaeolake ecosystem (Clark-Balzan et al., 2018; Parton et al., 2018).

The Jebel Oraf basin lies approximately 10km south-west of Jubbah. An Early Holocene high-stand is recorded comparatively later, with marls dated to 8.6 ± 0.6 ka (Guagnin et al., 2020). However, Guagnin et al. (2020) report two Late Holocene ages from the basin. The first of these horizons is

composed of sand and organic material, suggesting an evaporitic, shallow wetland was present at 2.8 ± 0.2 ka. However, this is overlain by lake marls dated to 2.0 ± 0.2 ka, indicating a return to standing freshwater.

Early Holocene lacustrine conditions also lagged behind Jubbah at Tayma, with gastropod shells dated to 10.1 ± 0.08 cal kyr BP (Engel et al., 2012). However, the onset of lake formation remains disputed as Dinies et al. (2015) report the earliest Holocene hydrological activity commenced ~1 ka later based on radiocarbon ages obtained from pollen. However, both studies report lacustrine conditions in the basin between ~9.2 - 8.0 cal kyr BP. Initially, the basin was characterised by a shallow, permanent water body with high abundances of *Ruppia* and *Sparganium* type vegetation suggesting brackish conditions (Dinies et al., 2015). Peak lacustrine conditions are not apparent until ~0.6 cal kyr later with the development of the densest grasslands (Dinies et al., 2015). Palaeohydrological modelling suggests that precipitation during the Early Holocene lacustrine phase could have been 300% greater than today (Wellbrock et al., 2011; Engel et al., 2012). An abrupt shift towards drought-resistant shrub species and sediments no longer displaying lamination after 8.0 cal kyr BP, alongside the formation of evaporites (Ginau et al., 2012; Dinies et al., 2015), indicates deteriorating freshwater abundances by the Mid Holocene.

The Terminal Pleistocene/Early Holocene lacustrine phases in the Nefud coincide with increased northern-hemisphere insolation (Fig.6.8). It is unlikely that north-western Arabia was influenced by the northerly displacement of the IOSM, however intensified ASM rainfall has been suggested as a moisture source (Guagnin et al., 2016; Parton et al., 2018), as well as MLWs (Engel et al., 2012). However, Parton et al. (2018) note that lake basins in the Nefud occur in topographically shallow interdunal settings. As such, reduction in lake level throughout the Early Holocene could also be driven in part by a reduction in available accommodation space as basins infill over time, increasing evaporation from wider, shallower water bodies concurrently with reduced rainfall.

The geomorphology of these basins also controls lacustrine development. Parton et al. (2018)

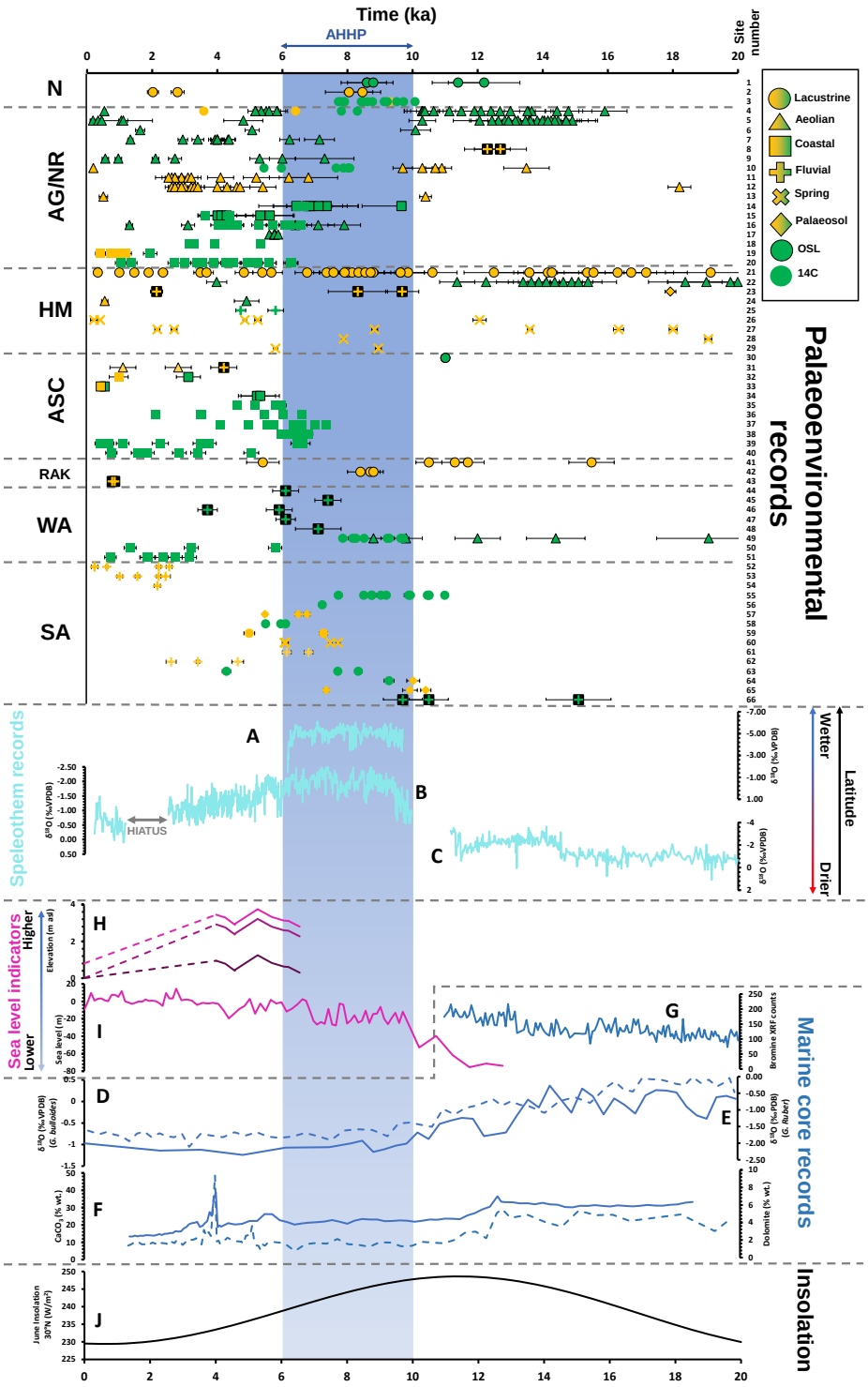

Figure 6.8. All GREEN and AMBER age records from the database displayed by landform type and included in the following sub-regional syntheses. Site numbers refer to sites listed in Appendix D. Sub-region abbreviations are as Figure 6.7. Palaeoclimate and sea level archives from around the Arabian Peninsula are shown (**a-i**; see Appedix D). **(j)** Summer insolation at 30°N (Berger and Loutre, 1991). The Arabian Holocene Humid Period (AHHP) is marked at ~10-6 ka (Petraglia et al., 2020).

suggest that Jubbah is sensitive to small increases in precipitation due to the position of the basin adjacent to a sandstone outcrop, maintaining accommodation space for standing water by inhibiting dune encroachment during periods of lower rainfall. It is also significantly influenced by groundwater recharge through the Saq Aquifer, facilitated by high infiltration rates into the surrounding dunefield (Parton et al., 2018). This is likely to be the reason that oasis conditions prevailed into the Mid Holocene at Jubbah, whereas both Jebel Oraf and Tayma indicate deteriorating water resources by the end of the Early Holocene.

Groundwater recharge has also been identified as a key control on Jebel Oraf's hydrology (Guagnin et al., 2020). The Late Holocene high-stand recorded at Jebel Oraf is anomalous with the wider geochronological record. However, historical evidence from Jubbah indicates the presence of near surface groundwater and oasis conditions (Parton et al., 2018). The development of shallow water bodies in the region's topographic depressions therefore occurs frequently despite coinciding with decreasing insolation (Fig.6.8).

6.7.2 The Arabian Gulf/N Rub'al Khali

Linear dunes in the UAE, including those at Awafi (Goudie et al., 2000; 10, Figs.6.7, 6.8), Wahala (Atkinson et al., 2011; 4, Figs.6.7, 6.8) and 'Emirates Highway' (Leighton et al., 2013; Leighton et al., 2014a; 5, Figs.6.7, 6.8) show extensive dune accumulation and preservation in the north-eastern Rub'al Khali from ~16 - 9 ka. The other phase of high dune activity and preservation is from ~7 - 0 ka at Liwa 1-3 (Bray and Stokes, 2004; Stokes and Bray, 2005; 11, 12, 13, Figs.6.7, 6.8), Al Ain (Atkinson et al., 2011b; 7, Figs.6.7, 6.8), Awafi (Goudie et al., 2000), Tawi Amar (Atkinson et al., 2013; 8, 9, Figs.6.7, 6.8) and around Wahala (Atkinson et al., 2011; Preston et al., 2015; 4, Figs.6.7, 6.8). However, the aggregation of data across multiple sites in a dunefield is not straightforward due to differences in sampling resolution between different sites and studies. As such, Thomas and Bailey (2019) present an Accumulation Intensity (AI) model for the northern Rub'al Khali, integrating

chronological data with stratigraphic information at the landscape scale. Their results broadly corroborate this pattern of aeolian sediment accumulation in the region.

Thomas and Bailey (2019) stress that high AI is not a direct indicator of aridity in the region. Other factors can control the formation and preservation of dunes, such as sediment supply and transport capacity (windiness; Goudie et al., 2000; Leighton et al., 2014b). There is almost complete paucity in dune accumulation (or preservation) between 10 - 7.5 ka, with the only sites recording activity during this period being Awafi (9.7±0.3 ka; Goudie et al., 2000) and Dosariyah (7.9±0.5 ka; Parker et al., 2020; 16, Figs.6.7, 6.8). This period corresponds with peak monsoon rainfall recorded by the Hoti Cave $\delta^{18}O$ isotope record, indicating regional IOSM rainfall increases in south-east Arabia (Fleitmann et al., 2003a; A, Figs.6.7, 6.8). While aeolian activity was reduced during this period, there was not a complete cessation in transport capacity. The coastal sites of Awafi and Dosariyah indicate aeolian activity was restricted to the Gulf coast during periods of regional landscape stabilisation, with inland sediment supply maintained by a large tidal range (Parker et al., 2020). Conversely, low AI from 20 - 16 ka is attributed to high transport capacity due to increased wind speeds during the hyper-arid LGM and resulting low preservation potential (Atkinson et al., 2011b; Thomas and Bailey, 2019). Aeolian sediment preservation is more likely under wetter conditions (Farrant et al., 2015), hence AI increases during the Terminal Pleistocene/Early Holocene and Mid Holocene.

Sediment availability is an important control on dunefield evolution, increasing during times of lower Arabian Gulf sea level (e.g. Goudie et al., 2000; Stokes and Bray, 2005; Leighton et al., 2014b). Multiple sites report a sea level high-stand in the Arabian Gulf during the Mid Holocene (e.g. Zander et al., 2007; Lokier and Steuber, 2008; 14, 15, 19, Figs.6.7, 6.8). For example, Parker et al. (2020) report inland marine transgression initiating prior to 6.6 ± 0.2 cal kyr BP at Dosariyah, eastern Saudi Arabia. A high-stand dated to 5.3 ± 0.2 cal kyr BP (1.25 - 3.22m asl greater than present) was followed by a rapid decline to present levels (H, Fig.6.8). This corresponds to the decline in sea level

observed from dated palaeoshorelines south-west of Abu Dhabi from 5.3 ± 0.2 cal kyr BP (Wood et al., 2012; 18, Figs.6.7, 6.8) and in north-eastern Kuwait Bay, which formed during a high-stand between ~5.0 - 3.5 cal kyr BP (Reinink-Smith, 2015; 20, Figs.6.7, 6.8). Declining sea levels from ~5 cal kyr BP corresponds to the rapid increase in dune AI (Thomas and Bailey, 2019). Increased sediment supply to the northern Rub'al Khali during the Late Holocene is also evidenced by the high $CaCO_3$ content of aeolian sediments, resulting from the incorporation of marine carbonates (White et al., 2001).

The palaeolakes of Awafi and Wahala (10, 4; Figs.6.7, 6.8), northern UAE, show that the Terminal Pleistocene/Early Holocene are characterised by dune accumulation until 9.7 ± 0.3 ka at Awafi (Goudie et al., 2000) and 10.3 ± 0.5 ka at Wahala (Atkinson et al., 2011). Stratified marls denote the formation of freshwater bodies from 8.3 ± 0.05 cal kyr BP (Preston et al., 2015), with pollen and phytolith records evidencing the development of a savannah grassland ecosystem (Parker et al., 2004). The nature of sedimentation, geochemistry and ecology of these records then proceeds to be variable from ~8.0 cal kyr BP until the final dated wetland development in the Awafi basin at 5.4 ± 0.1 cal kyr BP, and later at Wahala: 3.6 ± 0.05 cal kyr BP (Parker et al., 2004, 2006, 2016; Preston et al., 2015). However, the later phase of freshwater at Wahala may be a function of sampling. An upper-most phase of stratified marls has been reported at Awafi (0.45 - 0.30 m), yet no chronology is currently available (Parker et al., 2016).

Detrital sediment flux for both basins reveals phases of lake and, progressively, wetland development punctuated by periods of local aridity (Parker et al., 2016). After ~6.4 cal kyr BP, an abrupt increase in detrital sediment coincides with the rapid decrease in IOSM rainfall recorded at Hoti Cave (A, Fig.6.8; Fleitmann et al., 2003). However, the persistence of periodic wetland formation in the basins indicates they were still hydrologically active despite the southwards shift of the IOSM. Parker et al. (2016) explain this by noting the importance of winter rainfall in the Gulf region, driven by MLWs. Secondly, they suggest proximity to the Hajar Mountains results in the

basins benefitting from orographic rainfall. This indicates that hydrological processes are not only sensitive to regional synoptic systems but may also be amplified by localised geomorphic conditions.

Detrital sediment flux also indicates aridity between ~8.3 - 7.9 cal kyr BP, with marls interstratified with a phase of calcareous sand before the resumption of lacustrine conditions (Parker et al., 2016). A similar, abrupt increase in detrital sediments is recorded between ~4.3 - 3.9 cal kyr BP. The authors suggest that these increases in relative aridity were driven by coincident Bond Events in the North Atlantic (Bond, 1997). Whilst it is difficult to confirm this due to the coarse chronological resolutions and current lack of other lacustrine sites in the region, this suggests the telescopic sensitivity of Arabian Gulf hydrology to global climate drivers.

6.7.3 The Hajar Mountains

The highest-resolution lacustrine record in Arabia is from Maqta Oasis in the southern Hajar (21, Figs.6.7, 6.8). Sedimentation during the Terminal Pleistocene is characterised by gradual accumulation from 19.2 ± 1.4 ka, with molluscs scattered throughout a homogeneous sand-silt matrix indicating wetland activity under a broadly arid climate (Fuchs and Buerkert, 2008). Sedimentation rate increases in two steps during the Early Holocene. Firstly, at ~10.5 ka and again at ~9 ka, until reducing to similar levels experienced during the Terminal Pleistocene at ~8 ka. This abrupt increase in deposition coincides with increased organic content, mollusc remains and a reduced sand component. The most rapid deposition is synchronous with peak IOSM rainfall recorded by the Hoti Cave speleothem (Neff et al., 2001; A, Fig.6.7, 6.8).

Despite the reduction in sedimentation rate at Maqta due to the southwards migration of IOSM rainfall, consistent, albeit reduced, runoff into the basin remained persistent (Fuchs and Buerkert, 2008). This is in keeping with local oral histories of Maqta oasis use by pastoralists (Siebert et al., 2005). Nonetheless, this is anomalous with respect to other lacustrine records from south-east Arabia, which do not show continuity in hydrological activity over the last 20 ka. The seemingly

contradictory geoproxies recorded from the western alluvial fan systems of the Hajar Mountains during the Mid-Late Holocene also present evidence of local-scale environmental heterogeneity. The encroachment of Rub'al Khali dune systems over fan surfaces at Al Sibetah indicates intensified Shamal winds and increased aeolian activity at 4.9 ± 0.4 ka (Parton et al., 2015a; 24, Figs.6.7, 6.8). This occurred concurrently with fluvial deposition at Mleiha, approximately 50 km north of Al Sibetah, dated to 4.7 ± 0.2 cal kyr BP (Dalongeville, 1999; 25, Figs.6.7, 6.8). This suggests that, despite the reduction in regional precipitation during the Mid Holocene, sufficient rainfall over mountain catchments continued to provide limited freshwater to exterior drainage systems.

Continued deposition at Maqta throughout the Terminal Pleistocene also challenges the idea that the northwards displacement of monsoon rainfall is the predominant driver of hydrological activity in the Hajar. Alluvial deposition resulting from stream activity has also been dated to 17.9 ± 0.2 cal kyr BP at the Masafi oasis in the northern Hajar Mountains (Purdue et al., 2019; 23, Figures 7,8). Whilst interpreting regional environmental dynamics from two sites must be done cautiously, they pose important questions about the hydrological sensitivity of localised Hajar catchments to regional climate changes. Anomalous (relative to regional palaeoclimate archives) episodes of alluvial aggradation have also been detailed from the new sites presented in Chapter 4 and will be discussed in the context of this analysis in Section 7.4.2. It may be that during periods of regional aridity, local-scale factors such as topography were key for sustaining mountainous microclimates (Purdue et al., 2019).

Meteoric moisture is not the only driver of Hajar hydrology. ^{14}C ages from travertine deposits at four sites show that their formation has been continuous over last 20 ka (Mervine et al., 2014; 26-29, Figs.6.7, 6.8). Complementary U-series dating adds credence to the robustness of these ages as they show these travertines are isotopically closed systems, as well as providing independent age control for some samples (Mervine et al., 2015; Falk et al., 2016). Clark and Fontes (1990) reported that spring carbonate formation in the Hajar Mountains was driven predominately by regional

climate changes, with increased groundwater discharge from ~12.5 - 6.5 cal kyr BP, and hyperaridity from 16.3 - 13.0 cal kyr BP and from 6.5 - 0 cal kyr BP. Whilst this aligns with the prevailing theory of the timing of regional monsoon variability, the more reliable chronological data of Mervine et al. (2014) suggest that Hajar spring activity is decoupled from monsoon dynamics. However, it is reasonable to assume that increased IOSM precipitation during the early Holocene would have provided significant aquifer recharge.

6.7.4 The Arabian Sea Coast

Interdunal lacustrine deposits in the northern Wahiba Sand Sea indicate greater freshwater abundance during the Early Holocene (Radies et al., 2005; 30, Figs.6.7, 6.8). ^{14}C ages from the freshwater mollusc *Melanoides tuberculata* show wetter conditions from at least 11 ± 0.1 cal kyr BP, while associated fossils indicate greater vertebrate and invertebrate diversity than today (Radies et al., 2005).

Despite the speleothem record showing declining IOSM rainfall after 6 ka, fluvial activity is recorded at 4.2 ± 0.4 ka at Wadi Batha in the Wahiba Sands (Kocurek et al., 2020; 31, Figs.6.7, 6.8). Overlying horizons of fluvial clasts and muds interstratified with aeolian sediments indicate that the interdunal channel remained active for ~2 - 3 ka until being closed by dune migration by 1.8 ± 0.3 ka. Complex climatic drivers control contemporary flooding in Wadi Batha, such as seasonal contributions from winter MLWs and ASTCs along the Arabian Sea coastline (Fryberger et al., 2016), as well as contributions from Hajar fan systems (Robinson et al., 2007). This again highlights that enhanced IOSM precipitation is not necessary for local-scale hydrological activation in systems draining mountain catchments.

Numerous studies show established mangrove ecosystems from 7.3 ± 0.04 cal kyr BP at Suwayh (Lézine et al., 2002; Berger et al., 2013; 35, 37, Figs.6.7, 6.8). The presence of mangrove forests several kilometres inland of the present coastline is coeval with Mid Holocene sea level rise and marine transgression evident from multiple sites around the peninsula (Biagi and Nisbet, 1992;

Siddall et al., 2003; Beuzen-Waller et al., 2019; Parker et al., 2020; 38, I, 36, H, 16, Figs.6.7, 6.8). Their development is also attributed to increased IOSM rainfall, with the Suwayh, Filim and Kwar-al-Jaramah sites characterised by increased abundances of tropical species such as *Rhizophora*, the present distribution of which is limited to the very south-west of the peninsula (Lézine et al., 2002; Lézine et al., 2017; 35, 39, 40, Figs.6.7, 6.8).

The persistence of these ecosystems is variable. On the Ja'alan coastal plain, sedimentary horizons characteristic of mangrove forests are overlain by sediments indicative of brackish lagoons after 5.3 ± 0.6 ka (Richard et al., 2020; 32-34, Figs.6.7, 6.8), with increasing salinity attributed to a reduction in freshwater input (Lézine et al., 2002). This is linked to declining IOSM rainfall after ~6 ka. For example, Lézine et al. (2017) show that the more northerly site of Kwar-al-Jaramah (22.49°N) underwent a transition from a tropical mangrove to an arid-adapted ecosystem at ~4.5 cal kyr BP, earlier than the Filim site (20.61°N) at ~2.7 cal kyr BP (39, 40; Figs.6.7, 6.8). These trends are consistent with the latitudinally time-transgressive southwards displacement of IOSM rainfall (Fleitmann and Matter, 2009). However, on the Quriyat coastal plain (23.25°N), ^{14}C ages from mangrove wood show these ecosystems persisted until 2.1 ± 0.1 cal kyr BP, albeit their extent reduced from their local maxima at ~6 cal kyr BP (Beuzen-Waller et al., 2019; 36, Figs.6.7, 6.8). These coastal ecosystems are therefore not only controlled by regional climatic change, but also by local factors such as topography, sediment accumulation space on the coastal shelf and sediment availability (Berger et al., 2013).

By the Mid-Late Holocene, the coastline of eastern Oman was predominately characterised by sabkhas indicative of hyper-arid conditions. Sabkhas are established by 4.1 ± 0.1 cal kyr BP at Alashkara (Berger et al., 2013; 37) and by 3.1 ± 0.4 ka at Ruways and Daffah (Richard et al., 2020; 32, 33) on the Ja'alan coastal plain. This was the result of reduced meteoric rainfall causing more ephemeral freshwater input from channels draining the inland Hajar Mountains, as well as falling sea levels (Berger et al., 2013). Both factors may also explain the persistence of mangroves at

Quriyat (36) later than Ja'alan. With respect to the former, the proximity of Quriyat to the Hajar Mountains may have resulted in mangroves benefitting more frequently and directly from drainage activation due to orographic rainfall. As for the latter, regional tectonism has resulted in spatially heterogeneous changes in relative sea level (Beuzen-Waller et al., 2019). The Ja'alan coastal plain experienced sustained uplift throughout the Mid-Late Holocene (Moraetis et al., 2018), in contrast with the subsidence of the Quriyat coastline, resulting in stable relative sea levels since 6.6 ± 0.1 cal kyr BP (Beuzen-Waller et al., 2019).

6.7.5 The Rub'al Khali

The development of interdunal sabkhas in the south-eastern Rub'al Khali has been dated from 15.5 ± 0.7 - 5.4 ± 0.5 ka (Matter et al., 2015; 41, 42, Figs.6.7, 6.8). The mineralogy of gypsum in these deposits suggests that water body formation was primarily controlled by a rising groundwater table as opposed to direct meteoric rainfall in the Arabian interior. Isotopic and remote sensing investigations indicate that aquifer recharge across the south-eastern Rub'al Khali is predominately the result of precipitation over the Asir Mountains, western Saudi Arabia (Sultan et al., 2008; Sultan et al., 2019). The lack of fossil assemblages and laminated sediment deposition associated with Terminal Pleistocene/Early Holocene sabkha formations contrasts older lacustrine sediments in the region. This indicates greater freshwater input from meteoric rainfall during earlier periods of monsoon intensification, whereas these basins were predominately evaporitic, groundwater-driven systems during the Holocene. As such, Matter et al. (2015) hypothesise that IOSM rainfall did not significantly penetrate the Arabian interior during the AHHP.

6.7.6 Western Arabia

Early-Mid Holocene fluvial deposits from the trans-Arabian Wadi ad Dawasir system are also indicative of increased precipitation over Asir Mountain highlands, rather than the Rub'al Khali's interior (Matter et al., 2016; 44-48, Figs.6.7, 6.8). Sourced from tributaries draining the mountainous Red Sea coastline, sites throughout the catchment indicate an active fluvial plain

characterised by gravel-sand streams and lake systems from 7.4 ± 0.4 - 3.7 ± 0.3 ka. Faunal remains suggest that the system was flowing perennially during this period, sustaining floodplain habitats from the Asir to the Gulf. Whilst perennial flow declined during the Late Holocene, episodic flooding of tributary channels has been dated to the historical period (0.77±0.1 and 0.85±0.1 ka; McLaren et al., 2009; 43, Figs.6.7, 6.8). The persistence of perennial flow until at least 3.7 ± 0.3 ka is at odds with the termination of the AHHP at ~6 ka, potentially showing continued rainfall intensity over Asir Mountain catchments.

Asir drainage also feeds the Mundafan basin in the south-western Rub'al Khali. Dated lacustrine marls show that a lake developed at the site during the Early Holocene, by 9.7 ± 0.2 cal kyr BP (Rosenberg et al., 2011; 49, Figs.6.7, 6.8). However, aeolian horizons from the basin's periphery indicate that Early Holocene dune accumulation was concurrent with lake development (8.8 ± 0.4 ka). This suggests that dune systems in the Rub'al Khali's south-western interior were still active during the Early Holocene and perhaps not stabilised by increased monsoon intensity. Ostracode and diatom species indicate a freshwater, perennial lake persisted until at least 7.9 ± 0.1 cal kyr BP (Rosenberg et al., 2011).

Continuous terrigenous sediment influx into Red Sea coast lagoons until 5.8 ± 0.2 cal kyr BP further corroborates rainfall intensification over the Asir Mountains (Bantan et al., 2019; 50, Figs.6.7, 6.8). Mid Holocene sea level rise in the Red Sea then results in a transition towards higher lagoon levels and a dominance of marine deposition, however reduced rainfall intensity may have also reduced terrigenous influx (Siddall et al., 2003; Abu-Zied and Bantan, 2015; Bantan et al., 2019; 51, Figs.6.7, 6.8).

As Western Arabian geoproxies are predominately driven by Asir Mountain precipitation, it is likely that they are responding to intensified ASM rainfall during the Terminal Pleistocene and Early Holocene. Modern rainfall patterns and palaeoclimate modelling indicate that the region's dominant moisture source is the Red Sea as opposed to the Indian Ocean (e.g. Herold and Lohmann,

2009; Al-Ahmadi and Al-Ahmadi, 2014). The timing of hydrological activity in Western Arabia broadly corresponds with increased Early Holocene precipitation recorded by speleothems in the south and south-east of the Peninsula (e.g. Neff et al., 2001; Fleitmann et al., 2011). However, these archives are not directly comparable to geoproxies in Western Arabia as they record IOSM precipitation (Nicholson et al., 2020).

6.7.7 Southern Arabia

The al Hawa basin in the interior Ramlat as'Sabatayn received freshwater input during the Early Holocene due to the reactivation of channels draining the upland Yemen Highlands and Hadramawt Plateau to the south and south-east (Lézine et al., 1998; 55, Figs.6.7, 6.8). Water level fluctuations occurred from 11 ± 0.1 - 7.2 ± 0.1 cal kyr BP (Lézine et al., 2010; Lézine et al., 2007). However, pollen and sedimentological evidence indicate that the basin was characterised by arid-adapted vegetation and a shallow, evaporitic lake during the Early Holocene. Freshwater input increased at ~9.0 cal kyr BP, with a wetland ecosystem developing. This transition from arid to semi-arid flora coincides with peak Early Holocene IOSM rainfall recorded by the Qunf Cave speleothem, southern Oman (Fleitmann et al., 2007; B, Figs.6.7, 6.8). Desiccation of the wetland ecosystem began at ~8.5 cal kyr BP, however, the termination of relatively wet conditions in the basin was spatially heterogeneous. The southeastern Shabwa site shows shallow lacustrine conditions persisted until at least 7.2±0.1 cal kyr BP whereas the youngest lacustrine horizon at al Hawa was dated to 7.7±0.1 cal kyr BP (Lézine et al., 2010; 59).

The hydrological connection of al Hawa with upland watersheds and the basin's location on the periphery of the Rub'al Khali means that it likely did not receive significant rainfall directly from intensified IOSM precipitation. Quartz sand in the al Hawa sedimentary record is interpreted to be the result of aeolian transport into the basin from the Rub'al Khali (Lézine et al., 2007). Consistent levels of quartz in the site's sedimentary matrix suggests aeolian input occurred concurrently with

freshwater input. This corroborates interpretations from Mundafan that aeolian systems in the south-western Rub'al Khali remained active during the Early Holocene.

Lacustrine conditions persisted longer in the Yemen Highlands (Lézine et al., 2010). Lacustrine marls from Bayt Nahmi represent the youngest lake remains at 4.3 ± 0.1 cal kyr BP (Davies, 2006; 63, Figs.6.7, 6.8). Mid Holocene palaeosol development is also recorded in the Highlands, with organic material from horizons at Ghazwan dated to 5.5 ± 0.1 cal kyr BP (Wilkinson, 2005; 56, Figs.6.7, 6.8). Due to the southerly location of the Yemen coast and Highlands, it is likely that intensified IOSM rainfall persisted longer and declined more gradually than more northerly latitudes, as shown by the Qunf speleothem record (Fleitmann et al., 2007; B, Figs.6.7, 6.8). The Yemen Highlands also presently benefit from relatively high levels of rainfall driven by their relief (e.g. Wilby and Yu, 2013). This orographic effect may have also offset the waning of the AHHP.

Lacustrine development in Yemen between ~11 - 4 cal kyr BP closely corresponds with the timing of the northward displacement of IOSM rainfall recorded by speleothems (Fleitmann et al., 2007; Fleitmann and Matter, 2009). However, fluvial activity persisted from 6.8 ± 0.1 - 2.6 ± 0.2 cal kyr BP, based on organic horizons in terraces from the Hadramawt Plateau (Berger et al., 2012; 61, 62, Figs.6.7, 6.8). The authors suggest that this may have resulted from a shift in the dominance of IOSM rainfall to cyclonic winter rainfall driven by MLWs. However, detailed understandings of Holocene westerly rainfall variability remain elusive, especially in south-western Arabia which today receives minimal MLW precipitation (Weyhenmeyer et al., 2002).

Berger et al. (2012) also identify a fluctuating groundwater table as an important control on terrace soil development in the Hadramawt throughout the Mid-Late Holocene. Spring discharge has been recorded in the Hadramawt Plateau, dated to 7.7 ± 0.1 - 6.1 ± 0.1 cal kyr BP (McCorriston et al., 2002; 60, Figs.6.7, 6.8). As such, both Mediterranean rainfall and groundwater input from aquifers may represent significant controls on regional environmental heterogeneity following the retraction of the IOSM, however their relative contributions are poorly understood.

Fluvial deposits from the Salalah coastal plain also show continued freshwater input to coastal wetlands from the Gebel Qara uplands during the Late Holocene (Hoorn and Cremaschi, 2004; 52-54, Figs.6.7, 6.8). However, the nearby Gebel Qara flowstones and Qunf Cave speleothem records indicate relatively arid conditions (Fleitmann and Matter, 2009; Cremaschi et al., 2015). Further inland, flooding and gully erosion is recorded in Wadi Ghadun during the Terminal Pleistocene at 15.1 $\pm$ 1 ka (Rose et al., 2019; 66, Figs.6.7, 6.8). Hoorn and Cremaschi (2004) note the importance of upland springs in driving local fluvial system. Karstic geology results in perennial spring activity at the base of Gebel Qara today. Wider drainage networks are also activated in response to summer rainfall (Zerboni et al., 2020), with the region still receiving summer rainfall from the northern periphery of the IOSM. Relatively high precipitation (100 – 400 mm) is also driven by the orographic effect of Jebel Qara (Kwarteng et al., 2009; Zerboni et al., 2020). This highlights the present-day heterogeneity of the Arabian climate, the variability of which has likely persisted throughout both wet and arid phases.

Superimposed upon millennial-scale environmental changes in Yemen are centennial-scale arid periods. The al Hawa record shows three abrupt reductions in water levels centred at ~10.3, 8.8 and 7.9 cal kyr BP, with increases in aeolian deposition (Lézine et al., 2007; 55, Figs.6.7, 6.8). These broadly coincide with Bond Events in the North Atlantic (Bond, 1997), which have been linked to abrupt reductions in IOSM intensity (Gupta et al., 2003). The Qunf speleothem record also records $\delta^{18}O$ anomalies centred at 8.2 and 8.0 ka, indicating abrupt weakening of the IOSM (Fleitmann et al., 2007; B, Figs.6.7, 6.8). However, geochronological resolution remains an issue in relating the rapidity of sedimentation changes in lake basins to tele-connective links between the IOSM and North Atlantic.

6.8 Discussion

Applying quality assurance criteria to all available records has provided a framework of sub-regional palaeoenvironmental syntheses for the Arabian Peninsula based on what this analysis considers to

be the highest quality data available. Contrary to a linear relationship between regional-scale meridional climatic drivers and local-scale landscape responses, Arabian palaeoenvironmental changes over the last 20 ka are spatially and temporally heterogeneous. This highlights that complexity in palaeoenvironmental signals are not likely to be a product of geochronological uncertainties; rather signifying landscapes responding to diverse controls at a variety of scales.

6.8.1 The role of regional climatic factors in Arabian palaeoenvironmental change

Evidence for climatic heterogeneity during the AHHP is seen with the earliest lacustrine development recorded in the Nefud at the Terminal Pleistocene/Early Holocene transition at c. 12 ka. Similarly, high groundwater tables in the south-eastern Rub'al Khali also develop ~5 ka earlier than the classical onset of the AHHP at ~10 ka. Both these regions are linked to runoff and aquifer recharge from precipitation over the Asir Mountains so the earlier timing of their reactivation, relative to other lacustrine records, is potentially explained by an ASM rainfall source. Reconstructions of runoff levels in the Nile basin NE Africa, show that runoff peaked at ~10.1 ka in response to increased ASM rainfall (Revel et al., 2010; Weldeab et al., 2014). Therefore, the ASM may have reached peak intensity over the Asir Mountains earlier than IOSM rainfall in southern Oman. The timing of lacustrine development in Southern Arabia and the Arabian Gulf as well as mangrove establishment along the Arabian Sea Coast seems to be more closely aligned to the timing of intensified IOSM rainfall between ~10-6 ka than records from central and north-western Arabia. Caley et al. (2011a) showed that there are regional differences in the controls of the ASM and IOSM systems so they should not be assumed to have the same temporal progression. However, without high resolution palaeoclimate records from western Arabia it is difficult to interpret precipitation dynamics and provenance during the Terminal Pleistocene/Holocene.

MLWs provide a potential mechanism for the persistence of weaker lacustrine and fluvial activity in northern Arabia after the Mid Holocene decline in monsoon rainfall. Indeed, Mid-Late Holocene rainfall events attributed to MLW winter rainfall are recorded in Levantine speleothem records (e.g.

Bar-Matthews and Ayalon, 2011; Bar-Matthews et al., 2019). However, MLW rainfall sources are also attributed as drivers of fluvial activity during the Mid-Late Holocene in regions as far removed as Yemen and central Oman. Based on the minimal contribution of westerly systems to these parts of the Peninsula today (Weyhenmeyer et al., 2002), it seems less likely that they were the dominant control on hydrological activity but may have had a relatively greater contribution with declining IOSM rainfall. Again, this emphasises the need for high resolution palaeoclimate archives outside of just south-eastern Arabia.

AHHP precipitation did not appear to significantly penetrate the interior Rub'al Khali. Sedimentological and geochronological evidence for the continued activity of aeolian processes in the interior appear coevally with lacustrine phases in peripheral basins. This implies that increased precipitation during the AHHP was limited to the coastal margins of the Arabian Peninsula, primarily confined to the Red Sea, Yemen, Oman and the Arabian Gulf. The only evidence for perennial freshwater in the interior Rub'al Khali during the Early-Mid Holocene are from sites which are hydrologically connected with mountainous coastal regions. However, the dune systems of the Northern Rub'al Khali exhibit low sediment accumulation between 10 - 6 ka, indicating greater landscape stability (Leighton et al., 2013). The establishment of high-quality dune chronologies for interior regions of the Rub'al Khali and Nefud would help to test this hypothesis of intensified precipitation being a coastal phenomenon during the Early Holocene, as opposed to a Peninsula-wide panacea.

6.8.2 The role of wider environmental factors in Arabian palaeoenvironmental change

The key non-climatic controls highlighted across multiple sub-regional contexts are 1) groundwater, 2) topography and 3) relative sea level (RSL). These factors are significant drivers of environmental heterogeneity over the last 20 ka, particularly following the termination of the AHHP.

As in many dryland contexts where meteoric water availability is low or highly seasonal, groundwater plays a crucial role in habitat stability. There is a growing corpus of evidence that spring

activity in mountainous regions of Arabia continued throughout periods of low precipitation during the Terminal Pleistocene and Mid-Late Holocene. Indeed, spring discharge still occurs in the Hajar Mountains at present, recharging mountain oases (e.g. Siebert et al., 2005). Some low altitude lake basins also exhibit strong groundwater components, which result in their longer persistence following regional climatic deterioration. High water tables are particularly important in the endorheic basins of the western Nefud, such as Jubbah and Tayma, which are highly sensitive to aquifer recharge. Whilst there remain relatively few studies of palaeolakes in the Arabian interior, similarly rapid onset and slow termination of lacustrine phases in basins with high water tables have been recorded during the Holocene in African drylands (Lézine et al., 2011).

The most anomalous geoproxy records, relative to the timings of climatic change occur in high relief regions. Continuous sedimentation in oases in the Hajar Mountains over the last 20 ka is inconsistent with cessations in lacustrine deposition from all other sub-regions, as well as alluvial aggradation after the LGM, suggesting that significant hydrological activity was not limited to the AHHP. The distribution of uplands around the coastal margins of Arabia means that orography plays an important role in local climate. Relatively high precipitation is observed in weather data and model simulations for upland regions, such as the Hajar Mountains, Oman (e.g. Weyhenmeyer et al., 2002; Gunawardhana et al., 2018) and the Asir Mountains, Saudi Arabia (e.g. Al-Ahmadi and Al-Ahmadi, 2013; Hasanean and Almazroui, 2015; El Kenawy and McCabe, 2016).

Rainfall exhibits less inter-annual variability in uplands relative to adjacent lowlands (Hasanean and Almazroui, 2015). More stable precipitation results in less ecosystem variability than is experienced in inland or low-altitude regions. For example, the montane semi-arid microclimate of the western Hajar Mountains maintains one of the richest floral assemblages in Arabia (Patzelt, 2015), with the region being an important centre of endemism (e.g. Brinkmann et al., 2009; Carranza and Arnold, 2012; Monks et al., 2019). Despite regional aridity since the Mid-Holocene, the Hajar Mountains still experience frequent surface runoff events in response to localised rainfall (Purdue et al., 2021).

Climatic variability, driven partly by orography, results in significant contemporary environmental heterogeneity between high and low relief regions of the Arabian Peninsula. Therefore, chronologically robust palaeoenvironmental interpretations from mountainous regions which diverge from broader 'wet vs. dry' paradigms should be expected.

RSL changes throughout the Holocene also exhibited key environmental controls along Arabia's coastlines. RSL changes are driven by both global eustatic sea level fluctuations (e.g. Stevens et al., 2014) and variable rates of uplift and subsidence between and along coastlines (e.g. Wood et al., 2012; Moraetis et al., 2018). These factors control the timing, extent and duration of inland marine transgressions, with Holocene high stands in the Arabian Gulf and Arabian Sea coinciding with the development of mangrove ecosystems. Whilst Lézine et al. (2017) show that mangrove decline in Oman was concurrent with reductions in monsoon precipitation, it is also important to note that synchronous reductions in Arabian Sea level were also an important driver of coastal ecosystem change from ~5 ka. The heterogeneity of tectonic subsidence and uplift along the coastline of Oman influenced localised RSLs and the fragmented persistence of mangrove forests into the Late Holocene. Arabian Gulf high-stands also influenced northern Rub'al Khali landscape evolution, limiting sediment supply for dune aggradation during the Early-Mid Holocene (Preusser, 2009; Leighton et al., 2014a; Parker et al., 2020). Controls such as RSLs which influence sediment supply must also be considered when interpreting dune chronologies, rather than inferring a paucity of accumulation as the result of monsoon-driven landscape stability alone.

6.9 Conclusions

SCAPE highlights the growing wealth and diversity of data from a range of depositional contexts across Arabia. By reappraising this data at sub-regional scales relating to the specific uncertainties in dating methods, disparities in the quality of available data have emerged. There is a significant spatial bias towards sub-regions in the south-east, such as the Arabian Gulf/Northern Rub'al Khali, in terms of the amount of high-quality green and amber records. Areas in the centre, north and

west such as the Nefud, Western Arabia and the central Rub'al Khali desert remain important avenues for future research in terms of establishing both chronologically robust and geomorphologically diverse palaeoenvironmental archives. Robust dune chronologies outside of predominately just the north-eastern Rub'al Khali would test key hypotheses regarding the extent of landscape stabilisation during the AHHP. Moving towards sub-regional data syntheses is important for identifying these biases and not over-extrapolating palaeoenvironmental changes at the Peninsula-scale.

Chronological metadata is important for assessing the reliability of ages and should be reported in as much detail as possible to aid post-hoc analyses, as well as detailed stratigraphic and sedimentological descriptions to contextualise ages. SCAPE serves as an important first step to reduce the amount of data in a rational way for 1) ease of interpretation and 2) constructing what are considered based on these criteria to be the most robust palaeoenvironmental syntheses.

Arabian landscapes demonstrate greater environmental heterogeneity than can be assumed from palaeoclimatic data alone. Palaeoenvironmental data suggest that the AHHP was not synchronous due to the different forcing mechanisms of the individual climate systems influencing Arabia. However, intensified IOSM rainfall does not appear to have significantly penetrated the interior of the Rub'al Khali, although more data is needed to test this hypothesis. The relative contributions of ASM and MLW rainfall are also still poorly understood across the western and northern parts of the Peninsula, highlighting a need for high resolution palaeoclimate archives and more high quality geoproxy records in these areas.

Wider environmental controls on landforms such as groundwater, topography and RSL are important drivers of landscape heterogeneity. The relative influence of regional climatic and non-climatic controls also varies by proxy, with spring records, for example, seemingly decoupled from IOSM dynamics over the last 20 ka. As a result, some coastal, mountainous, and inland landscapes whose hydrology is in part driven by orography or groundwater are less sensitive to regional climatic

changes. It is hypothesised that uplands, such as the Hajar Mountains, have displayed greater hydrological and ecosystem stability throughout the Late Quaternary, relative to lowlands.

We should move beyond overly simplistic narratives of wet or dry climates at the Peninsula-scale to better capture the complexity of Arabian palaeoenvironments. This is also important for nuancing understandings of how environmental changes impacted Homo sapiens, with archaeological and genetic evidence increasingly suggesting the presence of habitable environmental refugia during arid periods (e.g. Fernandes et al., 2012; Gandini et al., 2016; Rose et al., 2019). Robust geochronological data from landforms supports these hypotheses in areas of Arabia which are relatively insensitive to regional-scale climate variability.

7 | Discussion and conclusions

7.1 Introduction

The aim of this thesis is to better understand the timing of aggradation and controls on alluvial fan systems in the Hajar Mountains and to compare palaeoenvironmental change in the Hajar to its adjacent regions. Three research objectives were set out in Chapter 1 (Section 1.2), each addressed through a specific research activity and relevant publication (Chapters 4-6). The purpose of this chapter is to assess the way each objective has been achieved, in the context of the wider literature, leading finally to some recommendations for potentially fruitful avenues for future research.

7.2 New records of fan aggradation from the central Hajar Mountains

The first thesis objective has been *to produce new records of alluvial fan aggradation for settings in the central interior and eastern bajadas of the Hajar Mountains, and test whether they align with the regional IOSM model of fan aggradation.*

7.2.1 Field sampling approach and determining the timing of fan aggradation

Addressing the first two sub-objectives, to integrate data from new field sites and to date periods of fan aggradation, has resulted in a significant body of new data on Late Quaternary fan development in the region. Chapter 4 presented new sites from the central interior and coast-wards draining alluvial fans of the Hajar Mountains, regions of the range which have not previously been investigated. These sites were dated using OSL, resulting in twenty new ages for Hajar alluvial sediments.

Smaller dryland fans often preserve surfaces of different relative ages which are readily identifiable through the weathering characteristics of their overlying desert pavements or topographic relationships between different generations of deposition, for example on telescopic forms. This can make targeting stratigraphic units for dating relatively simple as it is easier to identify at least most of the preserved aggradation phases. For the large fans of the Hajar, identifying these relative chrono-stratigraphic relationships can be more difficult. This is due to their large size and the complex nature of their braided channel morphology, with numerous channels on the fan surface.

Nonetheless, by targeting multiple sites located in different parts of these systems, Chapter 4 demonstrates that it is possible to generate a very long and detailed depositional record from Hajar fans, capturing deposition during the Holocene, MIS 3, 4, 5, 6 and 8/9. This highlights the spatio-temporal variability in the deposition of alluvial fan sediments which can make building a coherent record of aggradation difficult as none of these sites contains records of all identified phases of deposition. Reconstructing coherent, long-term records of Late Quaternary fan evolution requires a 3-dimensional approach of integrating multiple sites across space.

OSL provides an appropriate means for dating fan aggradation in the central and eastern Hajar, with the properties of quartz signals reported in this thesis very similar to those reported in other areas of the range (e.g. Blechschmidt et al., 2009; Atkinson et al., 2013; Parton et al., 2015a; Mueller et al., 2022). The OSL dating of fan sediments is often complicated by issues of broad D_e distributions, the necessary sampling of thin sand lenses within much coarser conglomeritic contexts and the partial resetting of luminescence signals (e.g. Porat et al., 1997; Kenworthy et al., 2014; Bartz et al., 2020). Despite these issues, the suite of new ages presented in Chapter 4 align well with ages previously published for periods of Hajar fan and lacustrine deposition in the region, as well as the regional-scale palaeoclimate record. Considerations outlined in Sections 3.2.2 and 4.3.1 based on the sampling contexts are more likely to mean that these ages are robust, such as the use of small aliquots for D_e measurement and the use of in-situ gamma spectrometry to calculate γ dose rates.

7.2.2 The IOSM as the driver of fan aggradation in the Hajar Mountains

To test the hypothesis that fan aggradation is paced by higher IOSM rainfall, age data along with the hydrological regime interpreted from fan sedimentary stratigraphy, were compared with data from regional marine and speleothem records of Late Quaternary IOSM rainfall. The results of Chapter 4 show that ages from sediment facies indicative of more sustained flow conditions, such as overbank floodplain deposits, channel sands and conglomerate units are related to periods of precessional maxima. By contrast, ages from deposits such as thin, structureless sand sheets, which suggest rapid

deposition under flashy flow conditions align with precessional minima. Similar conclusions have also been drawn from other alluvial systems across the wider Hajar, with an increasing number of studies reporting deposition during more arid periods (based on regional palaeoclimate archives) under ephemeral flow regimes (e.g. Mueller et al., 2022; Beuzen-Waller et al., 2022).

Chapter 4 utilises a hierarchical clustering approach to aggregate these data from fans and lakes across the wider Hajar, including the new sites presented in this thesis. This approach provides a useful means for objectively identifying clusters in this noisy and growing regional age dataset and could be applied to other regional geoproxy records. Whilst it has limitations, such as just being based on central age values and thus not incorporating uncertainties, it is less susceptible to issues of sampling size bias like probability density plotting. Crucial to the use of this approach is the palaeoenvironmental interpretation of the records as ages in themselves are not proxies, a theme which is developed in more detail in Chapter 6. These clusters align well with precessional peaks over the last 100 ka, supporting the IOSM model, and broadly well from 100-300 ka where ages are subject to greater uncertainty or are fewer in number.

Alluvial fans, therefore, provide the most detailed geoproxy record of Late Quaternary palaeoenvironmental and climatic change in south-east Arabia in terms of the number of periods of more sustained hydrological activity which they preserve. Other terrestrial records either have a lower preservation potential or have response thresholds which require higher levels of rainfall. Palaeolakes have a low preservation potential due to the high potential for aeolian erosion in south-east Arabia during more arid periods (Engel et al., 2015) and speleothem have a higher threshold of minimum rainfall to stimulate formation compared to alluvial systems, only forming during peak interglacial conditions (Fleitmann et al., 2003a).

These findings have interesting implications for understanding the nature of sediment routing through alluvial fan systems in south-east Arabia, as well as mountainous drylands more broadly, under long-term climatic variability. Mather et al. (2017) present a conceptual model for the

coupling status of alluvial fans and how they exist along a spectrum of buffering or connecting the sediment pathway between upland source areas and down-system transport and storage. This model could be applied to Hajar fans under wetter and more arid climate conditions. During periods of higher IOSM rainfall, transport capacity increases, increasing the sediment supply to fan. Hajar fans aggrade, storing sediment in channel bars and floodplains and are more likely to buffer the sediment cascade down-system. However, this buffering is only partial, evidenced by the fine-grained sedimentation in terminal lacustrine basins (e.g. Rosenberg et al., 2011). During more arid periods, sediment supply decreases and the Hajar fans become net-incisional. This means that they are more coupled to down-system sinks, although limited transport capacity due to lower stream competence means that sediment is only conveyed from catchments during the largest flash flood events.

7.3 Controls on Hajar fan aggradation outside of climate

The second thesis objective has been *to identify additional, non-climatic controls on Hajar Mountain alluvial fan morphology and evolution.*

7.3.1 Using remote sensing and GIS to build a database of fan and catchment morphometric variables for Hajar fans

Meeting the first sub-objective which was to use remote sensing to build a dataset of fan and catchment morphometric variables for the Hajar, a total of 438 fans and their catchments were mapped using a variety of different imagery products. This has provided the largest dryland fan morphometric dataset published to date. Taking a multi-method approach proved useful in the delineation of complex fans. For example, SAR imagery increased the contrast between fan surfaces where they merge on bajadas, often making the boundaries of individual fans clearer than they appear under false-colour Landsat 8 imagery. This approach is prudent where landforms are large, complex and field studies are not possible.

Using a remote sensing approach is appropriate for the scales of interest in this thesis, however there are potential issues of accuracy and reliability without accompanying field investigations. The only published morphometric data for fans and their catchments in the Hajar Mountains comes from Al Farraj and Harvey (2005) along the north-western mountain front in the UAE. The data gathered for the same fans in this thesis show generally good agreement with their aerial, topographic and field mapping approach. For example, they map the Wadi Al Bih fan as having a planform area of 48 km^2, a catchment area of 474 km^2 and a catchment relief of 2087 m. In this thesis, the Wadi Al Bih fan area was independently measured at 49.7 km^2, its catchment at 474.4 km^2 and its catchment's relief at 2006 m, demonstrating close correspondence.

On the other hand, their measurement of the Wadi Al Bih fan gradient does not correspond as closely with this study's at 0.07 and 0.01, respectively. This discrepancy is potentially attributable to the method used to measure fan gradient. Al Farraj and Harvey (2005) measured gradient for a portion of the fan's surface in the field, whereas in this thesis gradient was calculated by dividing the difference in elevation (m asl) between the fan apex and the toe by the total fan length (m). Due to the usually concave long profiles of alluvial fans, these methods could produce different results for gradient. However, both approaches are used in the literature (e.g. Harvey et al., 1999; Hartley et al., 2010; Tomczyk, 2021), supporting the choice made here. Furthermore, the similar fan gradient vs. catchment area regression results from Chapter 5 and Al-Farraj and Harvey (2005) for fans in the Musandam Peninsula suggest that these methods are comparable due to the consistency of results when considered relative to independent variables (e.g. catchment area).

7.3.2 The non-climatic controls on Hajar fan morphology

Chapter 5 compared the importance of controls on fan morphology between different areas of the Hajar Mountains through a methodology which integrated morphological measurements, regression and residual analyses. Variability in fan morphology around the Hajar is driven by differences in catchment morphology, geology, fan setting and tectonics.

The strongest F_a v. C_a and F_g v. C_a relationships are observed for the Rub' al Khali and Wahiba Sands fans because they are the most closely coupled to their catchments in terms of morphometric controls. The weaker F_a v. C_a and F_g v. C_a regression relationships observed for the Batinah Coast and Musandam Peninsula fans are typical for fans in more complex depositional settings where there is a stronger contribution external to catchments, not accounted for in regression relationships. Weak relationships are similarly observed for fans located at tributary junctions (e.g. Stokes and Mather, 2015) and along other coastal margins (e.g. Karymbalis et al., 2018). Residual analysis shows that fans in these coastal settings of the Hajar tend to be smaller and steeper than expected based on the size of their catchments due to foreshortening and steepening at their toes. Medium-strong (R^2 > 0.5) relationships were also observed between fan morphometry and catchment topography for the Rub' al Khali and Wahiba Sands fans but not for the coastal fans, again due to the greater role of external controls.

Residual analysis also suggests that catchment rock type is an important control on Hajar fan morphology. The relative ages of uplift of the four lithological groups compared may be the reason for this observation, with longer exposure histories resulting in greater rock erodibility, more sediment production and larger, flatter fans. However, there is no quantitative data on rock erodibility for the Hajar and collecting it was outside of the logistical scope of this thesis. Stokes and Gomes (2020) use mean catchment slope as a proxy for rock erodibility, after Goudie (2016), whereby steeper catchments are more likely to be comprised of less erodible rock types. Applying this assumption to the Hajar, a negative trend between mean catchment slope and mean fan area (Fig.7.1a) and a positive trend between mean catchment slope and mean fan gradient (Fig.7.1b) emerge for each lithological group. This supports the interpretation of the residual analysis presented in Chapter 5 but it is a somewhat surprising finding, as, typically, sedimentary rocks, such as the carbonates of the APD, may be expected to be more erodible than volcanic rocks like the basaltic Semail ophiolite (e.g. Maybeck, 1987; Zondervan et al., 2020). However, this remains only a very generalised assessment of the influence of geology on fan morphology.

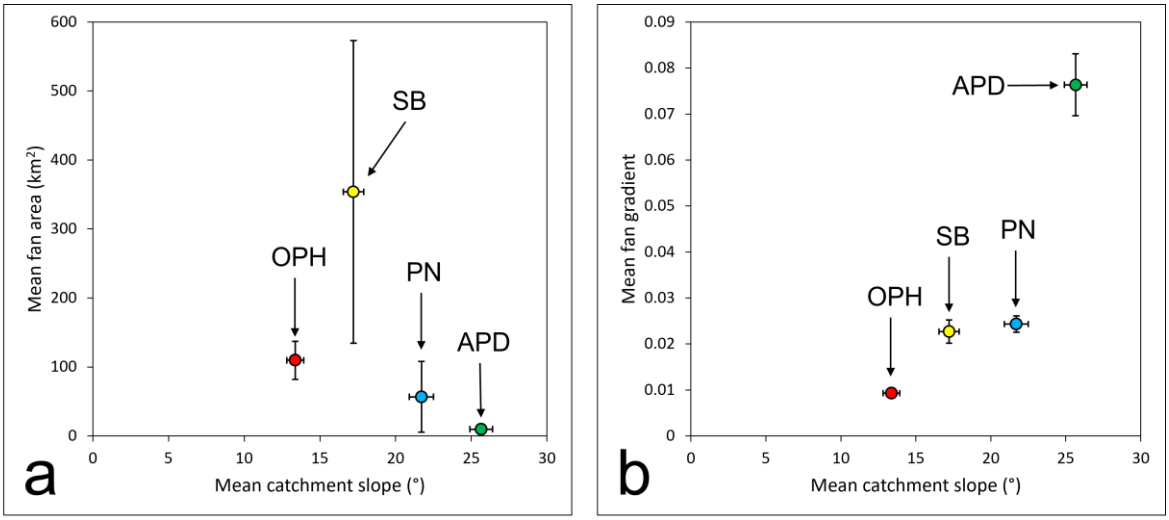

Figure 7.1. (a) Comparison between mean catchment slope and mean fan area by lithological group. **(b)** Comparison between mean catchment slope and mean fan gradient by lithological group. Error bars represent the standard errors of the means. Labels denote lithological groups: ophiolite (OPH), slope and basin deposits (SB), post-nappe deposits (PN) and the Arabian Proximal Domain (APD).

7.3.3 Comparing the Hajar fans with other dryland contexts

Chapter 5 concluded by comparing the F_a v. C_a and F_g v. C_a regression relationships calculated from the Hajar to dryland fans globally and in extra-terrestrial contexts. In terms of the magnitudes of fan areas and gradients measured, the Hajar fans span the full range previously measured in dryland settings. The large areal extents and low gradients of the largest Rub' al Khali megafans are also similar to Martian and Titanian fans. Of particular interest are the large fans observed on Titan, which bear morphological resemblance to those of Oman in terms of their scale, distributive channel systems and their termination in sand seas (Radebaugh et al., 2018; Fig.2.1g). Channelised flows on the surface of Titan are hypothesised to occur in response to highly seasonal 'methane monsoon' rainfall (Burr, 2010). Titan is also subject to periodic, long-term shifts in the latitudinal position of climate systems which have been likened to Croll-Milankovitch cycles on Earth (Hayes et al., 2018). The similarities in Hajar fan morphometry reported in Chapter 5, as well as their formation under periodic incursions of the IOSM throughout the Late Quaternary as shown in Chapter 4 could make these features useful analogues for understanding the evolution of the

Titanian surface in response to long-term climatic variability.

The regression coefficients (x) and exponents (y) of the $F_a = x\ C_a^y$ relationship for Rub' al Khali and Wahiba Sands fans fall within the expected range for dryland fans (Harvey, 2011), closely corresponding to unconfined mountain front fans in southern Spain, south-west USA and both Martian craters and Titanian features (Fig.7.2a). For the F_g v. C_a relationship, the Musandam Peninsula and Rub' al Khali fans sit very close to the range expected by Harvey (2011; Fig.7.2b).

For fans along the Batinah Coast and Musandam Peninsula, the regression parameters fall just outside the range expected for the F_a v. C_a relationship. Musandam Peninsula fans plot similarly to fans in other complex settings, likely due to their lateral and distal confinement by steep-sided coves and coastal setting, respectively, which is similar to tributary junction fans confined laterally by steep valley sides and distally by axial stream systems (e.g. Stokes and Mather, 2015). For the F_a v. C_a relationship in tributary junction settings, *x* ranges from ~0.003-0.1 and *y* from ~0.3-0.7, although only three data points are available from the literature (Fig.7.2a). Coefficient *x* for the Batinah Coast fans is much greater than this range (2.21), however exponent *y* falls within the range for confined tributary junction settings (0.66). Therefore, perhaps lower values of exponent y indicate a greater likelihood of fan-confining axial processes. This means that fan area is less sensitive to increases in catchment area due to the added influence of erosion at the fan toe.

There is a less clear trend in parameters *x* and *y* from the F_g v. C_a relationship (Fig.7.2b). Apart from the Musandam Peninsula, all fans in this study exhibit lower values of coefficient *x* than that expected by Harvey (2011). Harvey et al. (1999) suggests that coefficient *x* of the F_g v. C_a relationship is sensitive to differences in catchment lithology and depositional processes. The lower values of *x* could be indicative of the likely debris-flow dominance of the Musandam Peninsula fans as opposed to the fluvially-driven fans of the wider Hajar. Many of the fans and catchments previously studied

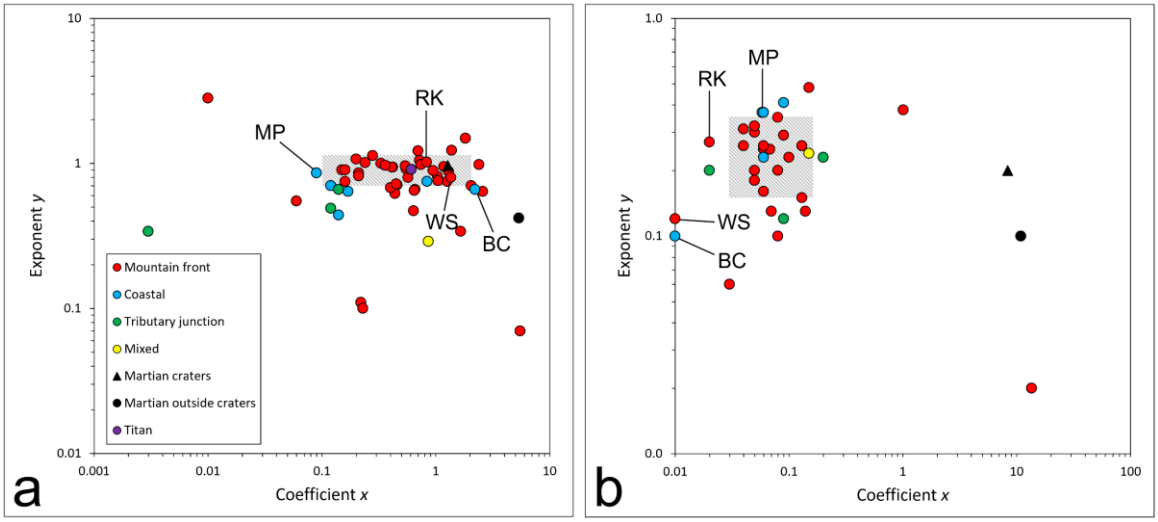

Figure 7.2. (a) Coefficient x and exponent y for the F_a v. C_a relationships from this study and the wider literature for dryland fans. **(b)** Coefficient x and exponent y for the F_g v. C_a relationships from this study and the wider literature for dryland fans. The grey shaded areas denote the expected range of values for mountain-front fans after Harvey (2011). Fans are categorised by location and setting. Fans from this study use the following abbreviation: Musandam Peninsula (MP); Rub' al Khali (RK); Wahiba Sands (WS); Batinah Coast (BC).

in other dryland contexts are orders of magnitude smaller than the Hajar fans along the Rub' al Khali, Batinah Coast and Wahiba Sands (e.g. Lecce, 1991; Harvey et al., 1999; Mather et al., 2000). Therefore, the cluster of data points in Fig.7.2b may be indicative of fans with higher sediment-water ratios than the predominately fluvial fans of the Hajar, except from the Musandam Peninsula.

Dryland fans typically exhibit stronger F_a v. C_a relationships than F_g v. C_a relationships, showing that catchment area is a stronger control over fan area than it is fan gradient (Fig.7.3). This trend is also observed for the Hajar fans. Regression relationships from Chapter 5 show that fan gradient is also strongly influenced by other catchment properties such as topography as a control on sediment-water ratios which in turn influence depositional processes. Fig.7.3 shows that fans in less-complex mountain-front settings, such as the Rub' al Khali, generally have the strongest F_a v. C_a and F_g v. C_a relationships, with R^2 values of >0.8 and >0.75, respectively. Fans in more complex settings like tributary junctions and along coastlines, such as the Batinah Coast and Musandam Peninsula, are likely to have lower R^2 values owing to the role of extrinsic controls on fan morphometry.

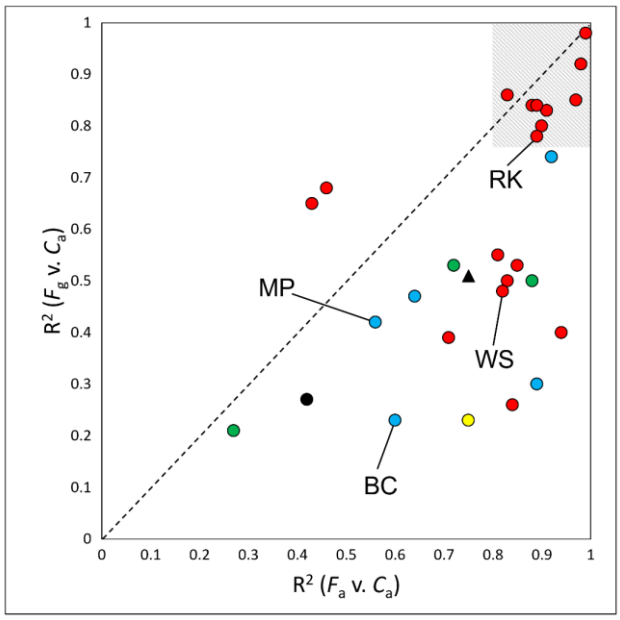

Figure 7.3. R^2 values from the F_a v. C_a and F_g v. C_a regression relationships reported in this study and the literature. The dashed black line shows unity. The grey shaded area denotes the group of strongest relationships reported for mountain-front fans. Figure legend the same as Fig.7.2.

7.4 Comparing Hajar geoproxy records to other regions of Arabia

The third thesis objective has been *to critically assess Hajar geoproxy records, improving interpretation of landscape responses to climatic and wider environmental controls during the Late Quaternary and compare with other regions of Arabia.*

7.4.1 The status of Arabian geochronology and geoproxy records for the last 20 ka

The focus of Chapter 6 was first constructing a database of geoproxy records with geochronological control over the last 20 ka for the entire Arabian Peninsula, critically assessing their robustness against a set of criteria based on sources of uncertainty in different geochronological techniques and using the records judged to be most robust to construct a new synthesis of Arabian palaeoenvironmental change. The SCAPE database brings together 734 luminescence and re-calibrated radiocarbon ages from different types of geoproxies. These records comprise data from 138 individual sites and are divided on geomorphological grounds into 7 sub-regions of Arabia. The analysis builds on the geochronology quality assurance criteria outlined by Small et al. (2017), based

on geomorphological and geochronological criteria.

It has been almost fifty years since McClure (1976) published the first geochronological constraints on an Arabian geoproxy: palaeolake Mundafan in southern Saudi Arabia. Lake marl sequences were redated by Rosenberg et al. (2011) using OSL, who used these older ages to infer that the earlier radiocarbon ages from McClure (1976) were likely contaminated with younger carbon, shifting the geochronological constraints on their formation back by ~80 ka. This example highlights the utility of the SCAPE database. Confidence in geochronological data is fundamental for making accurate interpretations of past environments. SCAPE is the first time that such an assessment has been carried out for geochronological records from the Arabian Peninsula, providing a timely reappraisal of almost fifty years of literature which is available to the community.

From this reassessment of legacy data, various temporal and spatial disparities emerge in the quantity and quality of records. The Arabian Gulf and the Northern Rub' al Khali sub-region has the highest number of palaeoenvironmental records, whilst the Nefud and the interior Rub' al Khali have the fewest. This is likely a factor of access to these more remote locations for field sampling. However, it means that geoproxy records are concentrated around the periphery of the Arabian Peninsula. In total, 34.6% of records were excluded from the resulting synthesis as they only achieved red quality assurance classifications, whilst 22.8% of records achieved amber and 39.5% achieved green.

7.4.2 Synthesising palaeoenvironmental data from across Arabia: how does the Hajar compare?

Using the green and amber records from the SCAPE database, Chapter 6 considers whether the AHHP was a spatially and temporally synchronous event across Arabia. Often, the dominant narrative in the literature is that Arabia, and the Arabo-Saharan desert belt more broadly, existed in states of either 'wet' ('green'; Petrgalia et al., 2015) or 'dry' based on either regional-scale palaeoclimate proxies or the extrapolation of site-scale geoproxy data. What the analysis of Chapter

6 reveals is that this narrative is not necessarily clear-cut: the geomorphological contexts of geoproxies are also important controls on past environmental changes at the site scale, as well as the proximity of sites to the main climate systems influencing rainfall over Arabia.

The highest quality data in the SCAPE database suggest that Arabian environments were more heterogeneous than this prevailing narrative. Indeed, there is a broad trend that between 10-6 ka the Arabian Peninsula was relatively wetter. However, the onset and termination of these wetter conditions seem to vary between sub-regions of the wider Peninsula, with the earliest records of hydrological amelioration recorded in the Nefud and southern Rub' al Khali. This spatial disparity likely results from the two main seasonal climate systems influencing different parts of Arabia, the ASM in the north-west and the IOSM in the south and south-east, which should not be viewed as one system in terms of their expansion in response to precessional maxima (Caley et al., 2011b). Evidence from fluvial sediments in north-western Africa suggest that the ASM reached peak rainfall earlier than the IOSM, at ~10.1 ka relative to ~8 ka (Waldeab et al., 2014).

The SCAPE data also suggest that some regions of the Arabian Peninsula did not experience significant hydrological change during the AHHP, with the central Rub' al Khali region likely remaining very arid. Whilst there are no geoproxy sites from the interior of the Rub' al Khali, those from the periphery suggest that aeolian sedimentation remained relatively constant throughout this period (e.g. Lezine et al., 2007; Rosenberg et al., 2011). Evidence for lake highstands and more sustained flow conditions in wadi networks is apparent from sites which are hydrologically linked to coastal uplands, such as the trans-Arabian Wadi ad Dawasir system (e.g. Matter et al., 2016) and the Hajar fans as discussed in Chapter 4. The Arabian Peninsula is fringed by mountains on all sides bar the Gulf region, therefore it is likely these topographic barriers would have had a rain-shadow effect limiting direct meteoric rainfall input into the interior. Instead, increased freshwater abundance would have been fed into the interior by rivers draining these uplands. Perhaps instead of a homogeneously 'green' Arabia during the AHHP, the narrative should be of an Arabia more

broadly characterised by green corridors through a still relatively arid landscape.

Crucially, not all regions of the Peninsula experienced aridity to the same extent during intervening drier periods coinciding with precessional minima. Mountainous areas which intensify precipitation through orographic uplift have more continuous records of freshwater availability over the last 20 ka than those from lowland areas. The Hajar Mountains show this trend very strongly due to the availability of data as well as the region receiving significant MLW rainfall during winter months (Kwarteng et al., 2009). At the time of publishing Chapter 6, the luminescence dating work included in Chapter 4 had not yet been completed. However, Chapter 4 supports these conclusions. These sites preserve records of flood sedimentation during the Late Holocene (~4-0 ka), MIS 4 (~65-60 ka) and MIS 5b (~91 ka), periods of precessional minima. Whilst the sedimentological interpretations of these deposits show that wadis were ephemeral, they show that the mountainous environment was still hydrologically active, just to a lesser extent relative to periods of precessional maxima. By contrast, lowland lake records show desiccation or the encroachment of Rub' al Khali dunes during these periods (e.g. Preston et al., 2015).

7.4.3 Implications for archaeology

The conclusions of Chapter 6 and the thesis more broadly have important implications for interpreting archaeological records in the Hajar. Over the last ten years, artefact and genetic data have increasingly postulated the presence of Late Quaternary hydro-climatic refugia in the Arabian Peninsula (e.g. Rose, 2010; Rose et al., 2013; 2019; Gandini et al., 2016; Petraglia et al., 2020). However, what these studies have lacked is the coherent and critical synthesis of palaeoenvironmental data from geoproxies which SCAPE provides for the last 20 ka.

A recent review published by Mateiciucová et al. (2023) assesses the biological evidence for the Hajar Mountains as a potential refugia for hominins during periods of wider regional aridity. They note characteristics of the environment such as the high numbers of endemic species, including freshwater fish and juniper woodlands. The findings of Chapters 4 and 6 support their argument,

with geoproxies suggesting that freshwater remained relatively abundant in the Hajar during precessional minima, albeit to a lesser extent than during maxima.

This emerging narrative of a Hajar refugia has implications for better understanding demographic shifts and dispersals of pre-historic populations out of Africa and across Arabia. Archaeological evidence of hominin occupation at the Jebel Faya rock shelter in the Hajar showing hominin presence throughout the last 200 ka has been dated to both insolation maxima *and* minima (Fig.2.5; Bretzke et al., 2022). South-east Arabia was not only habitable during the wettest climatic intervals as upland areas provided longer-term stability during drier periods. Having new geoproxy records, such as presented in Chapter 4, and a better understanding of heterogeneous landscape responses to climatic variability, as synthesised in Chapter 6, is fundamental for interpreting existing archaeological sites as well as new finds, such as the Palaeolithic hand-axe retrieved from the channel fill of site OM20/6 (Fig.3.3g).

It is naïve to become blinkered by a binary narrative of a 'wet' or 'dry' Arabia throughout the Late Quaternary. Evidence for the heterogeneous responses of landscapes to regional aridity is often staring us in the face as, today, these landscapes are a complex mosaic along a spectrum of hydro-climatic states. Take the contrasting experiences of the travellers quoted in Section 2.2.1 of this thesis. Thesiger (1950b) describes the 'waterless', 'barren' and 'featureless' landscape of the lowland Rub' al Khali, whereas Miles (1901) writes of the 'violent thunderstorms' and 'cascades' of water which occur frequently during the monsoon season in the central Hajar. The people and cultures who inhabit these landscapes also paint a picture of environmental heterogeneity. For example, Jebel Akhdar, one of the tallest peaks in the Hajar, translates as 'the Green Mountain'; named for its relatively humid, Mediterranean climate in contrast to a drier regional context (Melamid, 1992). Caution must be exercised when extrapolating past environmental and socio-cultural scenarios from the present, yet the environmental evidence presented in this thesis and the wider literature give an increasingly compelling case for long-term Hajar habitability.

7.5 Summary

As demonstrated above and in Chapters 4-6, the diverse array of results from these inter-weaving research objectives have yielded numerous discussion points with an equally diverse array of implications. Figure 7.4 summarises the key points of this discussion.

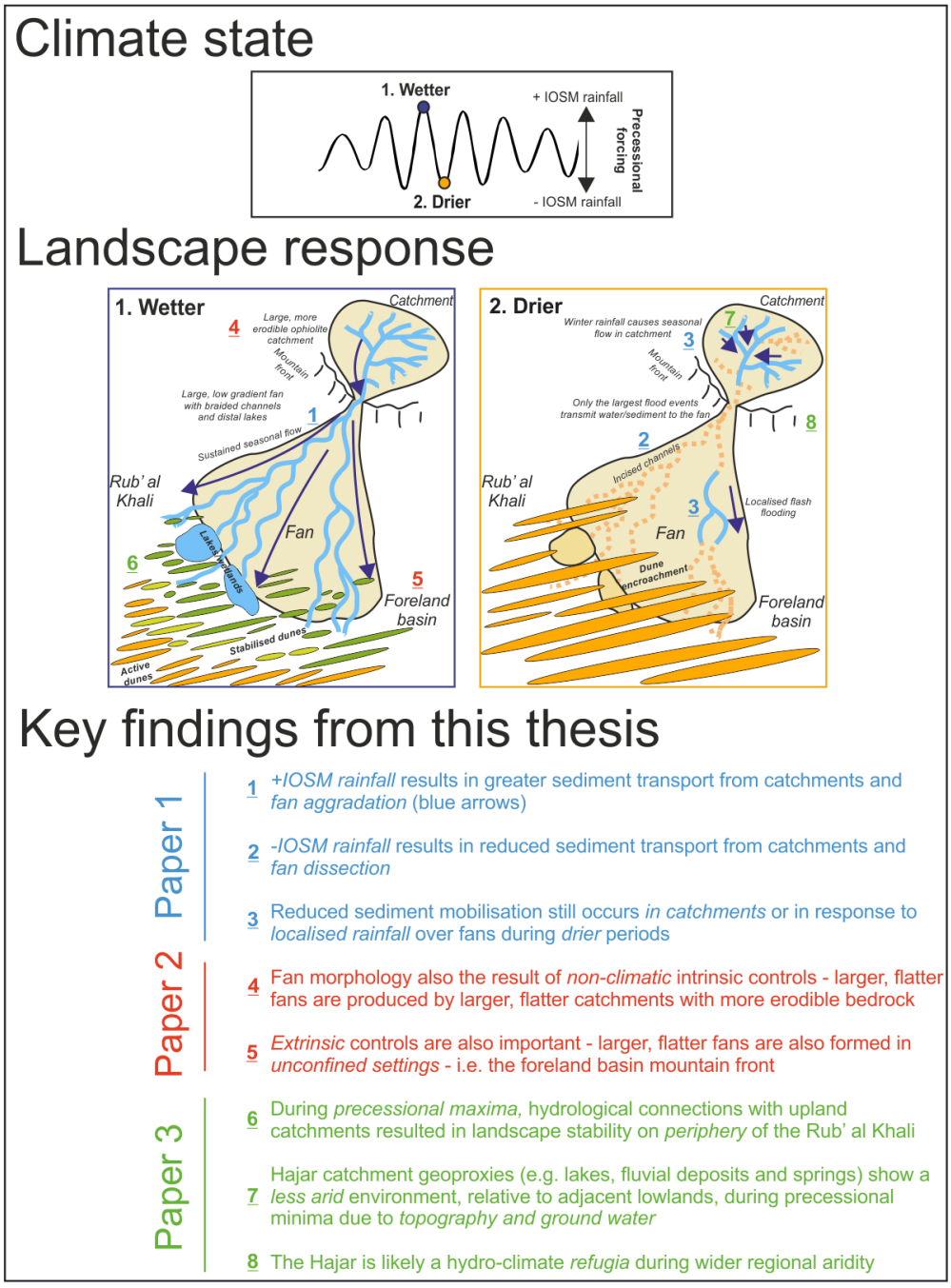

Figure 7.4. The key findings from Papers 1-3 (Chapters 4-6) discussed in Chapter 7, summarised relative to a refined model of Hajar landscape response to precessionally-paced climatic forcing ('Climate state').

7.6 Future research

Based on this thesis, multiple future research directions are suggested. These include: 1) further development of Hajar alluvial geoproxies, 2) quantifying the role of catchment geology in Hajar fan morphometry and the need for a global fan morphometric database, and 3) expanding the existing SCAPE database to test palaeoclimate models.

7.6.1 Further developing Hajar alluvial fan deposits as geoproxies

Alluvial fan sediments have now been described and dated extensively along the interior bajada of the Hajar, however these sediments are much more extensive than this. The Batinah Coast remains an important yet understudied area for future research into long-term fluvial dynamics in south-east Arabia, with Chapter 4 presenting only the first few sites from these systems.

There is also greater scope for applying more quantitative approaches to interpreting alluvial fan sediments in the region to complement the facies analysis approach taken in Chapter 4 and the regional literature more broadly. For example, palaeohydraulic modelling has been previously applied to preserved palaeochannels on Hajar fans to provide quantitative estimates of palaeodischarge (Maizels, 1987), although no absolute chronology was available for these sediments. An approach such as this would permit the comparison of streamflow conditions between different periods of time preserved in fan stratigraphy, providing a novel proxy of past hydrological conditions for the region.

The range of geochronological techniques applied to Hajar fans is currently limited to OSL dating and, in rare circumstances, radiocarbon dating. Whilst these techniques are very useful, they have limitations which could be compensated for using a broader spectrum of methods. This could include exploring other luminescence signals, such as thermally-transferred (TT-) OSL which has previously been used to date palaeolake deposits in central Oman (Rosenberg et al., 2012) and is useful where sediments are older than the typical range of quartz OSL (Porat et al., 2009), so may be useful for some of the issues of saturation reported in Section 4.4.1 and Appendix B. Rock-surface

luminescence dating is also a growing research frontier, with promising results from applications to fluvial cobbles (e.g. Sohbati et al., 2012; Jenkins et al., 2018; Ageby et al., 2023). This approach could facilitate the dating of conglomerate material directly, although it remains experimental. There has also been limited uptake of cosmogenic nuclide exposure dating in the Hajar, despite its successful application to fan surfaces in other arid environments (e.g. Nishiizumi et al., 2005). Widening the geochronological toolbox could help build more comprehensive records from these fans, as well as provide independent evaluation of OSL ages.

7.6.2 The role of geology in controlling Hajar fan morphology and a global fan morphometric database

Catchment geology appears to be a key control on Hajar fan morphology. Further work is needed to explain why differences in fan morphology result from geological variability. The hypothesis suggested here is that rock erodibility is key and this may be driven by different exposure histories. This warrants a more detailed field and laboratory analysis of rock erodibility for catchments of different geologies. Approaches such as Schmidt hammer rock resistivity measurements (e.g. Zondervan et al., 2020), or cosmogenic nuclide denudation rates measured from detrital wadi sediments (e.g. Starke et al., 2017) could be applied. These types of analyses were not within the scope of this thesis due to lack of field time but are important for understanding sediment production and fan morphology in arid landscapes.

Assembling the literature data used to compare with the data gathered in Chapter 5 made it apparent that there has been no global scale meta-analysis of alluvial fan morphometry, neither for drylands nor other climate zones. Numerous hypotheses exist about the influence of different variables such as climate, rock types and fan setting on resultant fan morphology and processes. For example, the parameters of fan-catchment power law regression relationships are often related to these variables (e.g. Harvey, 2011). Chapter 5 and the discussion of this thesis situate the findings for the Hajar within the broader context of dryland fans on Earth, yet these discussions remain

firmly focused on the Hajar. Quantitative analyses of these factors could go further to answer questions at larger scales, using the growing volume of data available.

7.6.3 Expanding the SCAPE database and testing palaeoclimate models

SCAPE is intended to be a useful resource for the academic community. However, these data only cover the last 20 ka. There is scope for SCAPE to be expanded to cover the whole Late Quaternary (300 ka). A practical application of this dataset could be a geoproxy data-palaeoclimate model comparison. Data-model comparisons enable the testing of variable palaeoclimate scenarios hypothesised by suites of different models and have been conducted at the regional scale for other low-latitude drylands (e.g. Singarayer and Burrough, 2015). The Palaeoclimate Model Intercomparison Project (PMIP) provides multi-model ensemble time-slice data for periods when geoproxy data suggests Arabia underwent significant palaeoenvironmental change, such as the Last Interglacial, the Last Glacial Maximum and the Mid-Holocene (e.g. Kageyama et al., 2021). Hypotheses could be related to the forcing mechanisms behind palaeoenvironmental changes evidenced in geoproxy records, such as the role played by different climate systems which influence the Arabian Peninsula. Whilst a similar study was conducted by Jennings et al. (2015), quality-filtered geoproxy data would be of great benefit for evaluating model performances relative to one another.

8 | References

ABDELKAREEM, M., GABER, A., ABDALLA, F. & EL-DIN, G. K. 2020. Use of optical and radar remote sensing satellites for identifying and monitoring active/inactive landforms in the driest desert in Saudi Arabia. Geomorphology, 362, 107197.

ABRAMS, M. & CHADWICK, O. 1994. Tectonic and climatic implications of alluvial fan sequences along the Batinah coast, Oman. Journal of the Geological Society, 151, 51-58.

ABU-ZIED, R. H. & BANTAN, R. A. 2015. Palaeoenvironment, palaeoclimate and sea-level changes in the Shuaiba Lagoon during the late Holocene (last 3.6 ka), eastern Red Sea coast, Saudi Arabia. The Holocene, 25, 1301-1312.

ADAMSON, K., WOODWARD, J., HUGHES, P., GIGLIO, F. & DEL BIANCO, F. 2017. Middle Pleistocene glaciation, alluvial fan development and sea-level changes in the Bay of Kotor, Montenegro. Geological Society, London, Special Publications, 433, 193-209.

AGEBY, L., BRILL, D., ANGELUCCI, D. E., BRÜCKNER, H. & KLASEN, N. 2023. Investigating optical dating of carbonate-rich cobbles from a river terrace: A pilot study from the Mula Valley, Spain. Radiation Measurements, 106962.

AITKEN, M. 1985. Thermoluminescence dating: past progress and future trends. Nuclear Tracks and Radiation Measurements (1982), 10, 3-6.

AL-AHMADI, K. & AL-AHMADI, S. 2014. Spatiotemporal variations in rainfall–topographic relationships in southwestern Saudi Arabia. Arabian Journal of Geosciences, 7, 3309-3324.

AL-FARRAJ, A. & HARVEY, A. M. 2000. Desert pavement characteristics on wadi terrace and alluvial fan surfaces: Wadi Al-Bih, UAE and Oman. Geomorphology, 35, 279-297.

AL-FARRAJ, A. & HARVEY, A. M. 2005. Morphometry and depositional style of Late Pleistocene alluvial fans: Wadi Al-Bih, northern UAE and Oman. Geological Society, London, Special Publications, 251, 85-94.

AL-FARSI, S. & COOKSON, P. Classifying arid soils near the edge of an alluvial fan in the Sultanate of Oman. Symposia of the 17th World Congress of Soil Science, Thailand, 2002. Citeseer.

AL-HATRUSHI, S. M. 2013. Monitoring of the shoreline change using remote sensing and GIS: a case study of Al Hawasnah tidal inlet, Al Batinah coast, Sultanate of Oman. Arabian Journal of Geosciences, 6, 1479-1484.

AL-HEMOUD, A., AL-DASHTI, H., AL-SALEH, A., PETROV, P., MALEK, M., ELHAMOUD, E., AL-KHAFAJI, S., LI, J., KOUTRAKIS, P. & DORONZO, D. 2022. Dust storm 'hot spots' and transport pathways affecting the Arabian Peninsula. Journal of Atmospheric and Solar-Terrestrial Physics, 238, 105932.

AL-LAZKI, A. I., SEBER, D., SANDVOL, E. & BARAZANGI, M. 2002. A crustal transect across the Oman Mountains on the eastern margin of Arabia. GeoArabia, 7, 47-78.

AL-RAWAS, G. A. & VALEO, C. 2010. Relationship between wadi drainage characteristics and peak-flood flows in arid northern Oman. Hydrological Sciences Journal–Journal des Sciences Hydrologiques, 55, 377-393.

AL-SAYARI, S. & ZOTL, J. 1978. Quaternary period in Saudi Arabia. Springer-Verlag, Wien, Germany. Quaternary period in Saudi Arabia. Springer-Verlag, Wien, Germany., -.

AL FARRAJ, A. & HARVEY, A. M. 2004. Late Quaternary interactions between aeolian and fluvial processes: a case study in the northern UAE. Journal of Arid Environments, 56, 235-248.

ALI, M., AIDARBAYEV, S., SEARLE, M. & WATTS, A. 2018. Subsidence history and seismic stratigraphy of the western Musandam Peninsula, Oman–United Arab Emirates mountains. Tectonics, 37, 154-181.

ALLEN, P. A. 2017. Sediment routing systems: The fate of sediment from source to sink, Cambridge University Press.

ALLEN, P. A. & HOVIUS, N. 1998. Sediment supply from landslide-dominated catchments: implications for basin-margin fans. Basin Research, 10, 19-35.

ALONSO-ZARZA, A. M. 2003. Palaeoenvironmental significance of palustrine carbonates and calcretes in the geological record. Earth-Science Reviews, 60, 261-298.

ALSHARHAN, A., GLENNIE, K. & WHITTLE, G. 2020. Quaternary deserts and climatic change, CRC Press.

ANDERSON, D. M. & PRELL, W. L. 1993. A 300 kyr record of upwelling off Oman during the late Quaternary: evidence of the Asian southwest monsoon. Paleoceanography, 8, 193-208.

ANTOHI-TRANDAFIR, O., TIMAR-GABOR, A., VULPOI, A., BĂLC, R., LONGMAN, J., VERES, D. & SIMON, S. 2018. Luminescence properties of natural muscovite relevant to optical dating of contaminated quartz samples. Radiation Measurements, 109, 1-7.

ARMITAGE, S. J., JASIM, S. A., MARKS, A. E., PARKER, A. G., USIK, V. I. & UERPMANN, H. P. 2011. The Southern Route "Out of Africa": Evidence for an Early Expansion of Modern Humans into Arabia. Science, 331, 453-456.

ARNOLD, J. R. & LIBBY, W. F. 1949. Age determinations by radiocarbon content: checks with samples of known age. Science, 110, 678-680.

ARNOLD, L. J., DUVAL, M., DEMURO, M., SPOONER, N. A., SANTONJA, M. & PÉREZ-GONZÁLEZ, A. 2016. OSL dating of individual quartz 'supergrains' from the Ancient Middle Palaeolithic site of Cuesta de la Bajada, Spain. Quaternary Geochronology, 36, 78-101.

ARZANI, N. 2005. The fluvial megafan of Abarkoh Basin (Central Iran): an example of flash-flood sedimentation in arid lands. Geological Society, London, Special Publications, 251, 41-59.

ARZANI, N. 2012. Catchment lithology as a major control on alluvial megafan development, Kohrud Mountain range, central Iran. Earth Surface Processes and Landforms, 37, 726-740.

ARZANI, N. & JONES, S. J. 2018. Upstream controls on evolution of dryland alluvial megafans: Quaternary examples from the Kohrud Mountain Range, central Iran. Geological Society, London, Special Publications, 440, 245-264.

ASCOUGH, P., COOK, G. & DUGMORE, A. 2005. Methodological approaches to determining the marine radiocarbon reservoir effect. Progress in Physical Geography, 29, 532-547.

ATHAR, H. 2015. Teleconnections and variability in observed rainfall over Saudi Arabia during 1978–2010. Atmospheric Science Letters, 16, 373-379.

ATKINSON, O. A., THOMAS, D. S., GOUDIE, A. S. & BAILEY, R. M. 2011. Late Quaternary chronology of major dune ridge development in the northeast Rub'al-Khali, United Arab Emirates. Quaternary Research, 76, 93-105.

ATKINSON, O. A., THOMAS, D. S., PARKER, A. G. & GOUDIE, A. S. 2013. Late Quaternary humidity and aridity dynamics in the northeast Rub'al-Khali, United Arab Emirates: implications for early human dispersal and occupation of eastern Arabia. Quaternary International, 300, 292-301.

BABIKIR, A. A. A. 1985. On the distribution of rainfall over the Sultanate of Oman. GeoJournal, 11, 165-172.

BAHRAMI, S. 2013. Tectonic controls on the morphometry of alluvial fans around Danehkhoshk anticline, Zagros, Iran. Geomorphology, 180, 217-230.

BAILEY, R., STOKES, S. & BRAY, H. 2003. Inductively-coupled plasma mass spectrometry (ICP-MS) for dose rate determination: some guidelines for sample preparation and analysis. Ancient TL, 21, 11-15.

BALLANTYNE, C. K. & WHITTINGTON, G. 1999. Late Holocene floodplain incision and alluvial fan formation in the central Grampian Highlands, Scotland: chronology, environment and implications. Journal of Quaternary Science, 14, 651-671.

BANTAN, R. A., ABU-ZIED, R. H. & AL-DUBAI, T. A. 2019. Late holocene environmental changes in a sediment core from Al-Kharrar Lagoon, eastern Red Sea Coast, Saudi Arabia. Arabian Journal for Science and Engineering, 44, 6557-6570.

BAR-MATTHEWS, M. & AYALON, A. 2011. Mid-Holocene climate variations revealed by high-resolution speleothem records from Soreq Cave, Israel and their correlation with cultural changes. The Holocene, 21, 163-171.

BAR-MATTHEWS, M., AYALON, A., GILMOUR, M., MATTHEWS, A. & HAWKESWORTH, C. J. 2003. Sea–land oxygen isotopic relationships from planktonic foraminifera and speleothems in the Eastern Mediterranean region and their implication for paleorainfall during interglacial intervals. Geochimica et cosmochimica acta, 67, 3181-3199.

BAR-MATTHEWS, M., AYALON, A. & KAUFMAN, A. 1997. Late Quaternary paleoclimate in the eastern Mediterranean region from stable isotope analysis of speleothems at Soreq Cave, Israel. Quaternary Research, 47, 155-168.

BAR-MATTHEWS, M., AYALON, A., KAUFMAN, A. & WASSERBURG, G. J. 1999. The Eastern Mediterranean paleoclimate as a reflection of regional events: Soreq cave, Israel. Earth and Planetary Science Letters, 166, 85-95.

BAR-MATTHEWS, M., KEINAN, J. & AYALON, A. 2019. Hydro-climate research of the late Quaternary of the Eastern Mediterranean-Levant region based on speleothems research–A review. Quaternary Science Reviews, 221, 105872.

BARNEKOW, L., POSSNERT, G. & SANDGREN, P. 1998. AMS 14C chronologies of Holocene lake sediments in the Abisko area, northern Sweden–a comparison between dated bulk sediment and macrofossil samples. Gff, 120, 59-67.

BARRE, M. & LAMOTHE, M. 2010. Luminescence dating of archaeosediments: a comparison of K-feldspar and plagioclase IRSL ages. Quaternary Geochronology, 5, 324-328.

BARTZ, M., DUVAL, M., BRILL, D., ZANDER, A., KING, G. E., RHEIN, A., WALK, J., STAUCH, G., LEHMKUHL, F. & BRÜCKNER, H. 2020a. Testing the potential of K-feldspar pIR-IRSL and quartz ESR for dating coastal alluvial fan complexes in arid environments. Quaternary International, 556, 124-143.

BARTZ, M., WALK, J., BINNIE, S. A., BRILL, D., STAUCH, G., LEHMKUHL, F., HOFFMEISTER, D. & BRÜCKNER, H. 2020b. Late Pleistocene alluvial fan evolution along the coastal Atacama Desert (N Chile). Global and Planetary Change, 190, 103091.

BATEMAN, M. D., BOULTER, C. H., CARR, A. S., FREDERICK, C. D., PETER, D. & WILDER, M. 2007. Detecting post-depositional sediment disturbance in sandy deposits using optical luminescence. Quaternary geochronology, 2, 57-64.

BEAUMONT, P. 1972. Alluvial fans along the foothills of the Elburz Mountains, Iran. Palaeogeography, Palaeoclimatology, Palaeoecology, 12, 251-273.

BELL, W. 1979. Attenuation factors for the absorbed radiation dose in quartz inclusions for thermoluminescence dating. Ancient TL, 8, 12.

BERGER, A. & LOUTRE, M.-F. 1991. Insolation values for the climate of the last 10 million years. Quaternary Science Reviews, 10, 297-317.

BERGER, J.-F., BRAVARD, J.-P., PURDUE, L., BENOIST, A., MOUTON, M. & BRAEMER, F. 2012. Rivers of the Hadramawt watershed (Yemen) during the Holocene: Clues of late functioning. Quaternary International, 266, 142-161.

BERGER, J. F., CHARPENTIER, V., CRASSARD, R., MARTIN, C., DAVTIAN, G. & LÓPEZ-SÁEZ, J. A. 2013. The dynamics of mangrove ecosystems, changes in sea level and the strategies of Neolithic settlements along the coast of Oman (6000–3000 cal. BC). Journal of Archaeological Science, 40, 3087-3104.

BEUZEN-WALLER, T., DESRUELLES, S., MARRAST, A., GIRAUD, J., GERNEZ, G., FORMAN, S., BESHKANI, A., BONILAURI, S., LEMÉE, M. & NACARRO, H. 2022. Late Pleistocene-Holocene fluvial records of the Wadi Dishshah: hydro-climatic and archaeological implications (Southern piedmont of the Hajar Mountains, Oman). Géomorphologie: relief, processus, environnement.

BEUZEN-WALLER, T., STÉPHAN, P., PAVLOPOULOS, K., DESRUELLES, S., MARRAST, A., PUAUD, S., GIRAUD, J. & FOUACHE, É. 2019. Geoarchaeological investigation of the Quriyat coastal plain (Oman). Quaternary International, 532, 98-115.

BIAGI, P. & NISBET, R. 1992. Environmental history and plant exploitation at the aceramic sites of RH5 and RH6 near the mangrove swamp of Qurm (Muscat—Oman). Bulletin de la Société Botanique de France. Actualités Botaniques, 139, 571-578.

BIRCH, S., HAYES, A., HOWARD, A., MOORE, J. & RADEBAUGH, J. 2016. Alluvial fan morphology, distribution and formation on Titan. Icarus, 270, 238-247.

BLAIR, T. C. & MCPHERSON, J. G. 1994. Alluvial fans and their natural distinction from rivers based on morphology, hydraulic processes, sedimentary processes, and facies assemblages. Journal of sedimentary research, 64, 450-489.

BLAIR, T. C. & MCPHERSON, J. G. 2009. Processes and forms of alluvial fans. Geomorphology of desert environments. Springer.

BLECHSCHMIDT, I., MATTER, A., PREUSSER, F. & RIEKE-ZAPP, D. 2009. Monsoon triggered formation of Quaternary alluvial megafans in the interior of Oman. Geomorphology, 110, 128-139.

BLOTT, S. J. & PYE, K. 2001. GRADISTAT: a grain size distribution and statistics package for the analysis of unconsolidated sediments. Earth surface processes and Landforms, 26, 1237-1248.

BÖLL, A., SCHULZ, H., MUNZ, P., RIXEN, T., GAYE, B. & EMEIS, K.-C. 2015. Contrasting sea surface temperature of summer and winter monsoon variability in the northern Arabian Sea over the last 25 ka. Palaeogeography, Palaeoclimatology, Palaeoecology, 426, 10-21.

BOND, G. 1997. A Pervasive Millennial-Scale Cycle in North Atlantic Holocene and Glacial Climates. Science, 278, 1257-1266.

BOSWORTH, W., HUCHON, P. & MCCLAY, K. 2005. The red sea and gulf of aden basins. Journal of African Earth Sciences, 43, 334-378.

BOUDIER, F., BARONNET, A. & MAINPRICE, D. 2010. Serpentine mineral replacements of natural olivine and their seismic implications: Oceanic lizardite versus subduction-related antigorite. Journal of Petrology, 51, 495-512.

BOULTON, S. J. & STOKES, M. 2018. Which DEM is best for analyzing fluvial landscape development in mountainous terrains? Geomorphology, 310, 168-187.

BOWMAN, D. 2019. Principles of alluvial fan morphology, Springer.

BRAY, H. E. & STOKES, S. 2004. Temporal patterns of arid-humid transitions in the south-eastern Arabian Peninsula based on optical dating. Geomorphology, 59, 271-280.

BREEZE, P. S., DRAKE, N. A., GROUCUTT, H. S., PARTON, A., JENNINGS, R. P., WHITE, T. S., CLARK-BALZAN, L., SHIPTON, C., SCERRI, E. M. & STIMPSON, C. M. 2015. Remote sensing and GIS techniques for reconstructing Arabian palaeohydrology and identifying archaeological sites. Quaternary International, 382, 98-119.

BRETZKE, K., PARTON, A., LINDAUER, S. & KENNET, D. 2018. Evidence of Neolithic settlement in the foothills of the Western al-Hajar Mountains. Arabian archaeology and epigraphy, 29, 103-114.

BRETZKE, K., PREUSSER, F., JASIM, S., MILLER, C., PRESTON, G., RAITH, K., UNDERDOWN, S., PARTON, A. & PARKER, A. 2022. Multiple phases of human occupation in Southeast Arabia between 210,000 and 120,000 years ago. Scientific reports, 12, 1-9.

BRINKMANN, K., PATZELT, A., DICKHOEFER, U., SCHLECHT, E. & BUERKERT, A. 2009. Vegetation patterns and diversity along an altitudinal and a grazing gradient in the Jabal al Akhdar mountain range of northern Oman. Journal of Arid Environments, 73, 1035-1045.

BRISTOW, C. & BEST, J. L. 1993. Braided rivers: perspectives and problems. Geological society, London, special publications, 75, 1-11.

BRONK RAMSEY, C. 2008. Radiocarbon dating: revolutions in understanding. Archaeometry, 50, 249-275.

BRYANT, M., FALK, P. & PAOLA, C. 1995. Experimental study of avulsion frequency and rate of deposition. Geology, 23, 365-368.

BULL, W. B. 1962. Relations of alluvial fan size and slope to drainage basin size and lithology in western Fresno County, California. US Geological Survey Professional Paper, 450, 51-53.

BULL, W. B. 1964. Geomorphology of segmented alluvial fans in western Fresno County, California, US Government Printing Office.

BULL, W. B. 1968. Alluvial fans. Journal of Geological Education, 16, 101-106.

BULL, W. B. 1977. The alluvial-fan environment. Progress in Physical geography, 1, 222-270.

BULL, W. B. 1991. Geomorphic responses to climatic change.

BURNS, S. J., FLEITMANN, D., MATTER, A., NEFF, U. & MANGINI, A. 2001. Speleothem evidence from Oman for continental pluvial events during interglacial periods. Geology, 29, 623-626.

BURR, D. M. 2010. Palaeoflood-generating mechanisms on Earth, Mars, and Titan. Global and Planetary Change, 70, 5-13.

BUYLAERT, J. P., JAIN, M., MURRAY, A. S., THOMSEN, K. J., THIEL, C. & SOHBATI, R. 2012. A robust feldspar luminescence dating method for Middle and Late P leistocene sediments. Boreas, 41, 435-451.

CABLE, S., CHRISTIANSEN, H. H., WESTERGAARD-NIELSEN, A., KROON, A. & ELBERLING, B. 2018. Geomorphological and cryostratigraphical analyses of the Zackenberg Valley, NE Greenland and significance of Holocene alluvial fans. Geomorphology, 303, 504-523.

CALEY, T., MALAIZÉ, B., REVEL, M., DUCASSOU, E., WAINER, K., IBRAHIM, M., SHOEAIB, D., MIGEON, S. & MARIEU, V. 2011a. Orbital timing of the Indian, East Asian and African boreal monsoons and the concept of a 'global monsoon'. Quaternary Science Reviews, 30, 3705-3715.

CALEY, T., MALAIZÉ, B., ZARAGOSI, S., ROSSIGNOL, L., BOURGET, J., EYNAUD, F., MARTINEZ, P., GIRAUDEAU, J., CHARLIER, K. & ELLOUZ-ZIMMERMANN, N. 2011b. New Arabian Sea records help decipher orbital timing of Indo-Asian monsoon. Earth and Planetary Science Letters, 308, 433-444.

CALVACHE, M. L., VISERAS, C. & FERNÓEZ, J. 1997. Controls on fan development—evidence from fan morphometry and sedimentology; Sierra Nevada, SE Spain. Geomorphology, 21, 69-84.

CARRANZA, S. & ARNOLD, E. N. 2012. A review of the geckos of the genus Hemidactylus (Squamata: Gekkonidae) from Oman based on morphology, mitochondrial and nuclear data, with descriptions of eight new species. Zootaxa, 3378, 1-95.

CHAKRABORTY, T., KAR, R., GHOSH, P. & BASU, S. 2010. Kosi megafan: Historical records, geomorphology and the recent avulsion of the Kosi River. Quaternary International, 227, 143-160.

CHAMBERLAIN, E. L., WALLINGA, J., REIMANN, T., GOODBRED JR, S. L., STECKLER, M. S., SHEN, Z. & SINCAVAGE, R. 2017. Luminescence dating of delta sediments: Novel approaches explored for the Ganges-Brahmaputra-Meghna Delta. Quaternary Geochronology, 41, 97-111.

CHAVAGNAC, V., CEULENEER, G., MONNIN, C., LANSAC, B., HOAREAU, G. & BOULART, C. 2013. Mineralogical assemblages forming at hyperalkaline warm springs hosted on ultramafic rocks: a case study of Oman and Ligurian ophiolites. Geochemistry, Geophysics, Geosystems, 14, 2474-2495.

CHURCH, M. & MARK, D. M. 1980. On size and scale in geomorphology. Progress in Physical Geography, 4, 342-390.

CLARK-BALZAN, L., PARTON, A., BREEZE, P. S., GROUCUTT, H. S. & PETRAGLIA, M. D. 2018. Resolving problematic luminescence chronologies for carbonate-and evaporite-rich sediments spanning multiple humid periods in the Jubbah Basin, Saudi Arabia. Quaternary Geochronology, 45, 50-73.

CLARK, I. D. & FONTES, J.-C. 1990. Paleoclimatic reconstruction in northern Oman based on carbonates from hyperalkaline groundwaters. Quaternary Research, 33, 320-336.

CLEMENS, S. C. & PRELL, W. L. 2003. A 350,000 year summer-monsoon multi-proxy stack from the Owen Ridge, Northern Arabian Sea. Marine Geology, 201, 35-51.

CORRADETTI, A., SPINA, V., TAVANI, S., RINGENBACH, J.-C., SABBATINO, M., RAZIN, P., LAURENT, O., BRICHAU, S. & MAZZOLI, S. 2020. Late-stage tectonic evolution of the Al-Hajar Mountains, Oman: new constraints from Palaeogene sedimentary units and low-temperature thermochronometry. Geological Magazine, 157, 1031-1044.

CREMASCHI, M., ZERBONI, A., CHARPENTIER, V., CRASSARD, R., ISOLA, I., REGATTIERI, E. & ZANCHETTA, G. 2015. Early–Middle Holocene environmental changes and pre-Neolithic human occupations as recorded in the cavities of Jebel Qara (Dhofar, southern Sultanate of Oman). Quaternary International, 382, 264-276.

CULLEN, H. M., DEMENOCAL, P. B., HEMMING, S., HEMMING, G., BROWN, F. H., GUILDERSON, T. & SIROCKO, F. 2000. Climate change and the collapse of the Akkadian empire: Evidence from the deep sea. Geology, 28, 379-382.

D'ARCY, M., MASON, P. J., RODA-BOLUDA, D. C., WHITTAKER, A. C., LEWIS, J. M. & NAJORKA, J. 2018. Alluvial fan surface ages recorded by Landsat-8 imagery in Owens Valley, California. Remote Sensing of Environment, 216, 401-414.

D'ARCY, M., RODA BOLUDA, D. C., WHITTAKER, A. C. & CARPINETI, A. 2015. Dating alluvial fan surfaces in Owens Valley, California, using weathering fractures in boulders. Earth Surface Processes and Landforms, 40, 487-501.

D'ARCY, M., WHITTAKER, A. C. & RODA-BOLUDA, D. C. 2017. Measuring alluvial fan sensitivity to past climate changes using a self-similarity approach to grain-size fining, Death Valley, California. Sedimentology, 64, 388-424.

DALONGEVILLE, R. 1999. Mleiha: étude physique et paléoenvironnement. MOM Éditions, 29, 33-54.

DAVIES, C. P. 2006. Holocene paleoclimates of southern Arabia from lacustrine deposits of the Dhamar highlands, Yemen. Quaternary Research, 66, 454-464.

DAVIS, J. M., GRINDROD, P. M., BANHAM, S. G., WARNER, N. H., CONWAY, S. J., BOAZMAN, S. J. & GUPTA, S. 2021. A record of syn-tectonic sedimentation revealed by perched alluvial fan deposits in Valles Marineris, Mars. Geology, 49, 1250-1254.

DAYEM, K. E., MOLNAR, P., BATTISTI, D. S. & ROE, G. H. 2010. Lessons learned from oxygen isotopes in modern precipitation applied to interpretation of speleothem records of paleoclimate from eastern Asia. Earth and Planetary Science Letters, 295, 219-230.

DE HAAS, T., KLEINHANS, M. G., CARBONNEAU, P. E., RUBENSDOTTER, L. & HAUBER, E. 2015. Surface morphology of fans in the high-Arctic periglacial environment of Svalbard: Controls and processes. Earth-Science Reviews, 146, 163-182.

DE SCALLY, F. A. & OWENS, I. F. 2004. Morphometric controls and geomorphic responses on fans in the Southern Alps, New Zealand. Earth Surface Processes and Landforms: The Journal of the British Geomorphological Research Group, 29, 311-322.

DE VRIES, A. J., TYRLIS, E., EDRY, D., KRICHAK, S., STEIL, B. & LELIEVELD, J. 2013. Extreme precipitation events in the Middle East: dynamics of the Active Red Sea Trough. Journal of Geophysical Research: Atmospheres, 118, 7087-7108.

DEER, W. A. Rock-forming minerals. 2011. Geological Society of London.

DEEVEY JR, E. S., GROSS, M. S., HUTCHINSON, G. E. & KRAYBILL, H. L. 1954. The natural C14 contents of materials from hard-water lakes. Proceedings of the National Academy of Sciences, 40, 285-288.

DEGERING, D. & DEGERING, A. 2020. Change is the only constant-time-dependent dose rates in luminescence dating. Quaternary Geochronology, 58, 101074.

DELONG, S. B. & ARNOLD, L. 2007. Dating alluvial deposits with optically stimulated luminescence, AMS 14C and cosmogenic techniques, western Transverse Ranges, California, USA. Quaternary Geochronology, 2, 129-136.

DEMENOCAL, P., ORTIZ, J., GUILDERSON, T., ADKINS, J., SARNTHEIN, M., BAKER, L. & YARUSINSKY, M. 2000. Abrupt onset and termination of the African Humid Period:: rapid climate responses to gradual insolation forcing. Quaternary science reviews, 19, 347-361.

DEMETS, C., GORDON, R. G., ARGUS, D. & STEIN, S. 1990. Current plate motions. Geophysical journal international, 101, 425-478.

DENNY, C. S. 1965. Alluvial fans in the Death Valley region, California and Nevada, US Government Printing Office.

DENSMORE, A. L., ALLEN, P. A. & SIMPSON, G. 2007. Development and response of a coupled catchment fan system under changing tectonic and climatic forcing. Journal of Geophysical Research: Earth Surface, 112.

DINIES, M., PLESSEN, B., NEEF, R. & KÜRSCHNER, H. 2015. When the desert was green: Grassland expansion during the early Holocene in northwestern Arabia. Quaternary International, 382, 293-302.

DORN, R. I. 1994. The role of climatic change in alluvial fan development. Geomorphology of desert environments, 593-615.

DRAKE, N. A., BLENCH, R. M., ARMITAGE, S. J., BRISTOW, C. S. & WHITE, K. H. 2011. Ancient watercourses and biogeography of the Sahara explain the peopling of the desert. Proceedings of the National Academy of Sciences, 108, 458-462.

DÜHNFORTH, M., DENSMORE, A. L., IVY-OCHS, S., ALLEN, P. & KUBIK, P. W. 2017. Early to Late Pleistocene history of debris-flow fan evolution in western Death Valley (California) using cosmogenic 10Be and 26Al. Geomorphology, 281, 53-65.

DULLER, G. 2003. Distinguishing quartz and feldspar in single grain luminescence measurements. Radiation measurements, 37, 161-165.

DULLER, G. A. 2008a. Luminescence Dating: guidelines on using luminescence dating in archaeology.

DULLER, G. A. T. 2008b. Single-grain optical dating of Quaternary sediments: why aliquot size matters in luminescence dating. Boreas, 37, 589-612.

DURCAN, J. A. & DULLER, G. A. 2011. The fast ratio: A rapid measure for testing the dominance of the fast component in the initial OSL signal from quartz. Radiation Measurements, 46, 1065-1072.

DURCAN, J. A., KING, G. E. & DULLER, G. A. 2015. DRAC: Dose Rate and Age Calculator for trapped charge dating. Quaternary Geochronology, 28, 54-61.

DURCAN, J. A., THOMAS, D. S., GUPTA, S., PAWAR, V., SINGH, R. N. & PETRIE, C. A. 2019. Holocene landscape dynamics in the Ghaggar-Hakra palaeochannel region at the northern edge of the Thar Desert, northwest India. Quaternary International, 501, 317-327.

EL-SHENAWY, M. I., KIM, S.-T., SCHWARCZ, H. P., ASMEROM, Y. & POLYAK, V. J. 2018. Speleothem evidence for the greening of the Sahara and its implications for the early human dispersal out of sub-Saharan Africa. Quaternary Science Reviews, 188, 67-76.

EL KENAWY, A. M. & MCCABE, M. F. 2016. A multi-decadal assessment of the performance of gauge- and model-based rainfall products over Saudi Arabia: climatology, anomalies and trends. International Journal of Climatology, 36, 656-674.

ENGEL, M., BRÜCKNER, H., PINT, A., WELLBROCK, K., GINAU, A., VOSS, P., GROTTKER, M., KLASEN, N. & FRENZEL, P. 2012. The early Holocene humid period in NW Saudi Arabia–Sediments, microfossils and palaeo-hydrological modelling. Quaternary International, 266, 131-141.

ENGEL, M., MATTER, A., PARKER, A. G., PARTON, A., PETRAGLIA, M. D., PRESTON, G. W. & PREUSSER, F. 2017. Lakes or wetlands? A comment on 'The middle Holocene climatic records from Arabia: Reassessing lacustrine environments, shift of ITCZ in Arabian Sea, and impacts of the southwest Indian and African monsoons' by Enzel et al. Global and Planetary Change, 148, 258-267.

ENZEL, Y., KUSHNIR, Y. & QUADE, J. 2015. The middle Holocene climatic records from Arabia: Reassessing lacustrine environments, shift of ITCZ in Arabian Sea, and impacts of the southwest Indian and African monsoons. Global and Planetary Change, 129, 69-91.

FALK, E. S., GUO, W., PAUKERT, A. N., MATTER, J. M., MERVINE, E. M. & KELEMEN, P. B. 2016. Controls on the stable isotope compositions of travertine from hyperalkaline springs in Oman: Insights from clumped isotope measurements. Geochimica et Cosmochimica Acta, 192, 1-28.

FARRANT, A., ELLISON, R., THOMAS, R., PHARAOH, T., NEWELL, A., GOODENOUGH, K., LEE, J. & KNOX, R. 2012. The Geology and Geophysics of the United Arab Emirates. Volume 6, Geology of the western and central United Arab Emirates, British Geological Survey.

FARRANT, A. R., DULLER, G. A., PARKER, A. G., ROBERTS, H. M., PARTON, A., KNOX, R. W. & BIDE, T. 2015. Developing a framework of Quaternary dune accumulation in the northern Rub'al-Khali, Arabia. Quaternary International, 382, 132-144.

FARRANT, A. R., MOUNTENEY, I., BURTON, A., THOMAS, R. J., ROBERTS, N. M., KNOX, R. W. & BIDE, T. 2019. Gone with the wind: dune provenance and sediment recycling in the northern Rub'al-Khali, United Arab Emirates. Journal of the Geological Society, 176, 269-283.

FERNANDES, V., ALSHAMALI, F., ALVES, M., MARTA, JOANA, NUNO, CHERNI, L., HARICH, N., CERNY, V., SOARES, P., MARTIN & PEREIRA, L. 2012. The Arabian Cradle: Mitochondrial Relicts of the First Steps along the Southern Route out of Africa. The American Journal of Human Genetics, 90, 347-355.

FERRILL, D. A., STAMATAKOS, J. A., JONES, S. M., RAHE, B., LAWRENCE MCKAGUE, H., MARTIN, R. H. & MORRIS, A. P. 1996. Quaternary slip history of the Bare Mountain fault (Nevada) from the morphology and distribution of alluvial fan deposits. Geology, 24, 559-562.

FICK, S. E. & HIJMANS, R. J. 2017. WorldClim 2: new 1-km spatial resolution climate surfaces for global land areas. International journal of climatology, 37, 4302-4315.

FIEBIG, M., PREUSSER, F., STEFFEN, D., THAMÓ-BOZSÓ, E., GRABNER, M., LAIR, G. J. & GERZABEK, M. H. 2009. Luminescence dating of historical fluvial deposits from the Danube and Ebro. Geoarchaeology: An International Journal, 24, 224-241.

FLEITMANN, D., BURNS, S., MATTER, A., CHENG, H. & AFFOLTER, S. 2022. Moisture and seasonality shifts recorded in Holocene and Pleistocene speleothems from southeastern Arabia. Geophysical Research Letters, 49, e2021GL097255.

FLEITMANN, D., BURNS, S. J., MANGINI, A., MUDELSEE, M., KRAMERS, J., VILLA, I., NEFF, U., AL-SUBBARY, A. A., BUETTNER, A. & HIPPLER, D. 2007. Holocene ITCZ and Indian monsoon dynamics recorded in stalagmites from Oman and Yemen (Socotra). Quaternary Science Reviews, 26, 170-188.

FLEITMANN, D., BURNS, S. J., MUDELSEE, M., NEFF, U., KRAMERS, J., MANGINI, A. & MATTER, A. 2003a. Holocene forcing of the Indian monsoon recorded in a stalagmite from southern Oman. science, 300, 1737-1739.

FLEITMANN, D., BURNS, S. J., NEFF, U., MANGINI, A. & MATTER, A. 2003b. Changing moisture sources over the last 330,000 years in Northern Oman from fluid-inclusion evidence in speleothems. Quaternary Research, 60, 223-232.

FLEITMANN, D., BURNS, S. J., PEKALA, M., MANGINI, A., AL-SUBBARY, A., AL-AOWAH, M., KRAMERS, J. & MATTER, A. 2011. Holocene and Pleistocene pluvial periods in Yemen, southern Arabia. Quaternary Science Reviews, 30, 783-787.

FLEITMANN, D. & MATTER, A. 2009. The speleothem record of climate variability in Southern Arabia. Comptes Rendus Geoscience, 341, 633-642.

FOOKES, P., WARING, D. & LEE, M. 2019. Wilfred Thesiger and the Umm as Samim, Oman. Geology Today, 35, 221-227.

FRYBERGER, S. G., HERN, C. Y. & GLENNIE, K. 2016. PSSedimentology of Reservoir-scale Aeolian-Fluvial Interactions, Wadi Batha, Northern Wahiba Sand Sea, Oman. American.

FUCHS, M. & BUERKERT, A. 2008. A 20 ka sediment record from the Hajar Mountain range in N-Oman, and its implication for detecting arid–humid periods on the southeastern Arabian Peninsula. Earth and Planetary Science Letters, 265, 546-558.

FUCHS, M. & OWEN, L. A. 2008. Luminescence dating of glacial and associated sediments: review, recommendations and future directions. Boreas, 37, 636-659.

FUCHS, M. C., BÖHLERT, R., KRBETSCHEK, M., PREUSSER, F. & EGLI, M. 2013. Exploring the potential of luminescence methods for dating Alpine rock glaciers. Quaternary Geochronology, 18, 17-33.

GALBRAITH, R. F. & ROBERTS, R. G. 2012. Statistical aspects of equivalent dose and error calculation and display in OSL dating: An overview and some recommendations. Quaternary Geochronology, 11, 1-27.

GALBRAITH, R. F., ROBERTS, R. G., LASLETT, G. M., YOSHIDA, H. & OLLEY, J. M. 1999. Optical dating of single and multiple grains of quartz from Jinmium rock shelter, northern Australia: Part I, experimental design and statistical models. Archaeometry, 41, 339-364.

GANDINI, F., ACHILLI, A., PALA, M., BODNER, M., BRANDINI, S., HUBER, G., EGYED, B., FERRETTI, L., GÓMEZ-CARBALLA, A., SALAS, A., SCOZZARI, R., CRUCIANI, F., COPPA, A., PARSON, W., SEMINO, O., SOARES, P., TORRONI, A., RICHARDS, M. B. & OLIVIERI, A. 2016. Mapping human dispersals into the Horn of Africa from Arabian Ice Age refugia using mitogenomes. Scientific Reports, 6, 25472.

GEBEL, H., HANSS, C., LIEBAU, A. & RAEHLE, W. 1989. The Late Quaternary environments of 'Ain al-Faidha/Al-'Ain, Abu Dhabi Emirate. Archaeology in the United Arab Emirates, 5, 9-48.

GHAZANFAR, S. A. 1992. Quantitative and biogeographic analysis of the flora of the Sultanate of Oman. Global ecology and biogeography letters, 189-195.

GILES, P. T. 2010. Investigating the use of alluvial fan volume to represent fan size in morphometric studies. Geomorphology, 121, 317-328.

GINAU, A., ENGEL, M. & BRÜCKNER, H. 2012. Holocene chemical precipitates in the continental sabkha of Tayma (NW Saudi Arabia). Journal of Arid Environments, 84, 26-37.

GLENNIE, K., BOEUF, M., CLARKE, M. H., MOODY-STUART, M., PILAAR, W. & REINHARDT, B. 1973. Late Cretaceous nappes in Oman Mountains and their geologic evolution. AAPG Bulletin, 57, 5-27.

GLENNIE, K., CLARKE, M. H., BOEUF, M., PILAAR, W. & REINHARDT, B. 1990. Inter-relationship of Makran-Oman Mountains belts of convergence. Geological Society, London, Special Publications, 49, 773-786.

GLENNIE, K. W. & SINGHVI, A. K. 2002. Event stratigraphy, paleoenvironment and chronology of SE Arabian deserts. Quaternary Science Reviews, 21, 853-869.

GODFREY-SMITH, D. I., HUNTLEY, D. J. & CHEN, W.-H. 1988. Optical dating studies of quartz and feldspar sediment extracts. Quaternary Science Reviews, 7, 373-380.

GOODBRED JR, S. L. 2003. Response of the Ganges dispersal system to climate change: a source-to-sink view since the last interstade. Sedimentary Geology, 162, 83-104.

GOSWAMI, P. K., PANT, C. C. & PANDEY, S. 2009. Tectonic controls on the geomorphic evolution of alluvial fans in the Piedmont Zone of Ganga Plain, Uttarakhand, India. Journal of Earth System Science, 118, 245-259.

GOUDIE, A. S., COLLS, A., STOKES, S., PARKER, A., WHITE, K. & AL-FARRAJ, A. 2000. Latest Pleistocene and Holocene dune construction at the north-eastern edge of the Rub Al Khali, United Arab Emirates. Sedimentology, 47, 1011-1021.

GRAF, K. E. 2009. "The Good, the Bad, and the Ugly": evaluating the radiocarbon chronology of the middle and late Upper Paleolithic in the Enisei River valley, south-central Siberia. Journal of Archaeological Science, 36, 694-707.

GROUCUTT, H. S., BREEZE, P. S., GUAGNIN, M., STEWART, M., DRAKE, N., SHIPTON, C., ZAHRANI, B., OMARFI, A. A., ALSHAREKH, A. M. & PETRAGLIA, M. D. 2020. Monumental landscapes of the Holocene humid period in Northern Arabia: The mustatil phenomenon. The Holocene, 30, 1767-1779.

GUAGNIN, M., BREEZE, P., SHIPTON, C., OTT, F., STEWART, M., BATEMAN, M., MARTIN, L., GRAHAM, L., EL-DOSSARY, S., KINGWELL-BANHAM, E., ZAHRANI, B., AL-OMARI, A., ALSHAREKH, A. M. & PETRAGLIA, M. 2020. The Holocene humid period in the Nefud Desert: Hunters and herders in the Jebel Oraf palaeolake basin, Saudi Arabia. Journal of Arid Environments, 178, 104146.

GUAGNIN, M., JENNINGS, R., EAGER, H., PARTON, A., STIMPSON, C., STEPANEK, C., PFEIFFER, M., GROUCUTT, H. S., DRAKE, N. A., ALSHAREKH, A. & PETRAGLIA, M. D. 2016. Rock art imagery as a proxy for Holocene environmental change: A view from Shuwaymis, NW Saudi Arabia. The Holocene, 26, 1822-1834.

GUÉRIN, G., JAIN, M., THOMSEN, K. J., MURRAY, A. S. & MERCIER, N. 2015. Modelling dose rate to single grains of quartz in well-sorted sand samples: the dispersion arising from the presence of potassium feldspars and implications for single grain OSL dating. Quaternary Geochronology, 27, 52-65.

GUÉRIN, G., MERCIER, N. & ADAMIEC, G. 2011. Dose-rate conversion factors: update. Ancient Tl, 29, 5-8.

GUÉRIN, G., MERCIER, N., NATHAN, R., ADAMIEC, G. & LEFRAIS, Y. 2012. On the use of the infinite matrix assumption and associated concepts: a critical review. Radiation Measurements, 47, 778-785.

GUILMETTE, C., SMIT, M. A., VAN HINSBERGEN, D. J., GÜRER, D., CORFU, F., CHARETTE, B., MAFFIONE, M., RABEAU, O. & SAVARD, D. 2018. Forced subduction initiation recorded in the sole and crust of the Semail Ophiolite of Oman. Nature Geoscience, 11, 688-695.

GUNAWARDHANA, L. N., AL-RAWAS, G. A. & AL-HADHRAMI, G. 2018. Quantification of the changes in intensity and frequency of hourly extreme rainfall attributed climate change in Oman. Natural Hazards, 92, 1649-1664.

GUPTA, A. K., ANDERSON, D. M. & OVERPECK, J. T. 2003. Abrupt changes in the Asian southwest monsoon during the Holocene and their links to the North Atlantic Ocean. Nature, 421, 354-357.

GUZZETTI, F., MARCHETTI, M. & REICHENBACH, P. 1997. Large alluvial fans in the north-central Po Plain (Northern Italy). Geomorphology, 18, 119-136.

HANSMAN, R. J., RING, U., THOMSON, S. N., DEN BROK, B. & STÜBNER, K. 2017. Late Eocene uplift of the Al Hajar Mountains, Oman, supported by stratigraphy and low-temperature thermochronology. Tectonics, 36, 3081-3109.

HARRIES, R. M., KIRSTEIN, L. A., WHITTAKER, A. C., ATTAL, M. & MAIN, I. 2019. Impact of recycling and lateral sediment input on grain size fining trends—Implications for reconstructing tectonic and climate forcings in ancient sedimentary systems. Basin Research, 31, 866-891.

HARTLEY, A. J., WEISSMANN, G. S., NICHOLS, G. J. & WARWICK, G. L. 2010. Large distributive fluvial systems: characteristics, distribution, and controls on development. Journal of Sedimentary Research, 80, 167-183.

HARVEY, A. 1984. Aggradation and dissection sequences on Spanish alluvial fans: influence on morphological development. Catena, 11, 289-304.

HARVEY, A. 1987. Alluvial fan dissection: relationships between morphology and sedimentation. Geological Society, London, Special Publications, 35, 87-103.

HARVEY, A. Factors influencing Quaternary alluvial fan development in southeast Spain. Alluvial fans. A field approach, 1990. 247-269.

HARVEY, A. 1996. The role of alluvial fans in the mountain fluvial systems of southeast Spain: implications of climatic change. Earth Surface Processes and Landforms, 21, 543-553.

HARVEY, A. 2002. The role of base-level change in the dissection of alluvial fans: case studies from southeast Spain and Nevada. Geomorphology, 45, 67-87.

HARVEY, A. 2004. The response of dry-region alluvial fans to late Quaternary climatic change. Desertification in the third millenium. Balkema, Rotterdam, 83-98.

HARVEY, A. 2011. Dryland alluvial fans. In: THOMAS, D. (ed.) Arid zone geomorphology: Process, form and change in drylands.

HARVEY, A. M. 2005. Differential effects of base-level, tectonic setting and climatic change on Quaternary alluvial fans in the northern Great Basin, Nevada, USA. Geological Society, London, Special Publications, 251, 117-131.

HARVEY, A. M. 2010. Local buffers to the sediment cascade: debris cones and alluvial fans. Sediment cascades: An integrated approach, 153-180.

HARVEY, A. M. 2012. The coupling status of alluvial fans and debris cones: a review and synthesis. Earth Surface Processes and Landforms, 37, 64-76.

HARVEY, A. M., SILVA, P. G., MATHER, A. E., GOY, J. L., STOKES, M. & ZAZO, C. 1999. The impact of Quaternary sea-level and climatic change on coastal alluvial fans in the Cabo de Gata ranges, southeast Spain. Geomorphology, 28, 1-22.

HASANEAN, H. & ALMAZROUI, M. 2015. Rainfall: features and variations over Saudi Arabia, a review. Climate, 3, 578-626.

HAWLEY, J. W. & WILSON, W. E. 1965. Quaternary geology of the Winnemucca area, Nevada, Desert Research Institute, University of Nevada.

HAYES, A. G., LORENZ, R. D. & LUNINE, J. I. 2018. A post-Cassini view of Titan's methane-based hydrologic cycle. Nature Geoscience, 11, 306-313.

HAYWARD, A. 1985. Coastal alluvial fans (fan deltas) of the Gulf of Aqaba (Gulf of Eilat), Red Sea. Sedimentary Geology, 43, 241-260.

HEIRI, O., LOTTER, A. F. & LEMCKE, G. 2001. Loss on ignition as a method for estimating organic and carbonate content in sediments: reproducibility and comparability of results. Journal of paleolimnology, 25, 101-110.

HEROLD, M. & LOHMANN, G. 2009. Eemian tropical and subtropical African moisture transport: an isotope modelling study. Climate Dynamics, 33, 1075-1088.

HILBERT, Y. H., WHITE, T. S., PARTON, A., CLARK-BALZAN, L., CRASSARD, R., GROUCUTT, H. S., JENNINGS, R. P., BREEZE, P., PARKER, A., SHIPTON, C., AL-OMARI, A., ALSHAREKH, A. M. & PETRAGLIA, M. D. 2014. Epipalaeolithic occupation and palaeoenvironments of the southern Nefud desert, Saudi Arabia, during the Terminal Pleistocene and Early Holocene. Journal of Archaeological Science, 50, 460-474.

HOFFMANN, G., RUPPRECHTER, M., RAHN, M. & PREUSSER, F. 2015. Fluvio-lacustrine deposits reveal precipitation pattern in SE Arabia during early MIS 3. Quaternary International, 382, 145-153.

HOFFMANN, G., SCHNEIDER, B., MECHERNICH, S., FALKENROTH, M., DUNAI, T. & PREUSSER, F. 2020. Quaternary uplift along a passive continental margin (Oman, Indian Ocean). Geomorphology, 350, 106870.

HOOKE, R. L. 1967. Processes on arid-region alluvial fans. The Journal of Geology, 75, 438-460.

HOOKE, R. L. 1968. Steady-state relationships on arid-region alluvial fans in closed basins. American Journal of Science, 266, 609-629.

HOOKE, R. L. & ROHRER, W. L. 1977. Relative erodibility of source-area rock types, as determined from second-order variations in alluvial-fan size. Geological Society of America Bulletin, 88, 1177-1182.

HOORN, C. & CREMASCHI, M. 2004. Late Holocene palaeoenvironmental history of Khawr Rawri and Khawr Al Balid (Dhofar, Sultanate of Oman). Palaeogeography, Palaeoclimatology, Palaeoecology, 213, 1-36.

HORNUNG, J., PFLANZ, D., HECHLER, A., BEER, A., HINDERER, M., MAISCH, M. & BIEG, U. 2010. 3-D architecture, depositional patterns and climate triggered sediment fluxes of an alpine alluvial fan (Samedan, Switzerland). Geomorphology, 115, 202-214.

HORTON, B. & DECELLES, P. 2001. Modern and ancient fluvial megafans in the foreland basin system of the central Andes, southern Bolivia: Implications for drainage network evolution in fold-thrust belts. Basin research, 13, 43-63.

HUNTLEY, D. J. & BARIL, M. 1997. The K content of the K-feldspars being measured in optical dating or in thermoluminescence dating. Ancient Tl, 15, 11-13.

HUNTLEY, D. J., GODFREY-SMITH, D. I. & THEWALT, M. L. 1985. Optical dating of sediments. Nature, 313, 105-107.

HUNTLEY, D. J. & LAMOTHE, M. 2001. Ubiquity of anomalous fading in K-feldspars and the measurement and correction for it in optical dating. Canadian Journal of Earth Sciences, 38, 1093-1106.

HUNTLEY, D. J. & LIAN, O. B. 2006. Some observations on tunnelling of trapped electrons in feldspars and their implications for optical dating. Quaternary Science Reviews, 25, 2503-2512.

HUOT, S. & LAMOTHE, M. 2012. The implication of sodium-rich plagioclase minerals contaminating K-rich feldspars aliquots in luminescence dating. Quaternary Geochronology, 10, 334-339.

ISHII, Y., TAKAHASHI, T. & ITO, K. 2022. Luminescence dating of cobbles from Pleistocene fluvial terrace deposits of the Ara River, Japan. Quaternary Geochronology, 67, 101228.

ITOH, N., STONEHAM, D. & STONEHAM, A. 2002. Ionic and electronic processes in quartz: mechanisms of thermoluminescence and optically stimulated luminescence. Journal of Applied Physics, 92, 5036-5044.

JACOBS, Z., MEYER, M. C., ROBERTS, R. G., ALDEIAS, V., DIBBLE, H. & EL HAJRAOUI, M. A. 2011. Single-grain OSL dating at La Grotte des Contrebandiers ('Smugglers' Cave'), Morocco: improved age constraints for the Middle Paleolithic levels. Journal of Archaeological Science, 38, 3631-3643.

JENKINS, G., DULLER, G., ROBERTS, H., CHIVERRELL, R. C. & GLASSER, N. 2018. A new approach for luminescence dating glaciofluvial deposits-High precision optical dating of cobbles. Quaternary Science Reviews, 192, 263-273.

JENNINGS, R. P., SINGARAYER, J., STONE, E. J., KREBS-KANZOW, U., KHON, V., NISANCIOGLU, K. H., PFEIFFER, M., ZHANG, X., PARKER, A. & PARTON, A. 2015. The greening of Arabia: Multiple opportunities for human occupation of the Arabian Peninsula during the Late Pleistocene inferred from an ensemble of climate model simulations. Quaternary International, 382, 181-199.

JEROLMACK, D. J. & PAOLA, C. 2010. Shredding of environmental signals by sediment transport. Geophysical Research Letters, 37.

JULL, A. T. & GEERTSEMA, M. 2006. Over 16,000 years of fire frequency determined from AMS radiocarbon dating of soil charcoal in an alluvial fan at Bear Flat, northeastern British Columbia. Radiocarbon, 48, 435-450.

KAGEYAMA, M., HARRISON, S. P., KAPSCH, M.-L., LOFVERSTROM, M., LORA, J. M., MIKOLAJEWICZ, U., SHERRIFF-TADANO, S., VADSARIA, T., ABE-OUCHI, A. & BOUTTES, N. 2021. The PMIP4 Last Glacial Maximum experiments: preliminary results and comparison with the PMIP3 simulations. Climate of the Past, 17, 1065-1089.

KALIŃSKA, E., WECKWERTH, P. & ALEXANDERSON, H. 2022. Recent advances in luminescence dating of the Late Quaternary sediments in the Baltic States, Northern Europe: A review. Earth-Science Reviews, 104272.

KAPUI, Z., KERESZTURI, A., KISS, K., SZALAI, Z., ÚJVÁRI, G., HICKMAN-LEWIS, K., FOUCHER, F. & WESTALL, F. 2018. Fluvial or aeolian grains? Separation of transport agents on Mars using earth analogue observations. Planetary and Space Science, 163, 56-76.

KARYMBALIS, E., FERENTINOU, M., FUBELLI, G., GILES, P., TSANAKAS, K., VALKANOU, K., BATZAKIS, D.-V. & KARALIS, S. 2022. Classification of Trichonis Lake graben (Western Greece) alluvial fans and catchments using geomorphometry and artificial intelligence. Zeitschrift für Geomorphologie, 295-312.

KARYMBALIS, E., FERENTINOU, M. & GILES, P. T. 2018. Use of morphometric variables and self-organizing maps to identify clusters of alluvial fans and catchments in the north Peloponnese, Greece. Geological Society, London, Special Publications, 440, 45-64.

KELEMEN, P. B. & MATTER, J. 2008. In situ carbonation of peridotite for CO2 storage. Proceedings of the National Academy of Sciences, 105, 17295-17300.

KENWORTHY, M., RITTENOUR, T. M., PIERCE, J. L., SUTFIN, N. A. & SHARP, W. D. 2014. Luminescence dating without sand lenses: An application of OSL to coarse-grained alluvial fan deposits of the Lost River Range, Idaho, USA. Quaternary Geochronology, 23, 9-25.

KOBER, F., ZEILINGER, G., IVY-OCHS, S., DOLATI, A., SMIT, J. & KUBIK, P. 2013. Climatic and tectonic control on fluvial and alluvial fan sequence formation in the Central Makran Range, SE-Iran. Global and planetary change, 111, 133-149.

KOCUREK, G., WESTERMAN, R., HERN, C., TATUM, D., RAJAPARA, H. & SINGHVI, A. K. 2020. Aeolian dune accommodation space for Holocene Wadi Channel Avulsion Strata, Wahiba Dune Field, Oman. Sedimentary Geology, 399, 105612.

KORTEKAAS, M. & MURRAY, A. S. 2005. A method for the removal of mica from quartz separates. Ancient TL, 23, 43-46.

KOSTASCHUK, R. 1987. Identification of debris flow hazard on alluvial fans in the Canadian Rocky Mountains. Debris flows/avalanches: process, recognition, and mitigation, 7, 115.

KOSTASCHUK, R., MACDONALD, G. & PUTNAM, P. 1986. Depositional process and alluvial fan-drainage basin morphometric relationships near Banff, Alberta, Canada. Earth Surface Processes and Landforms, 11, 471-484.

KRAAL, E. R., ASPHAUG, E., MOORE, J. M., HOWARD, A. & BREDT, A. 2008. Catalogue of large alluvial fans in martian impact craters. Icarus, 194, 101-110.

KRBETSCHEK, M., GÖTZE, J., DIETRICH, A. & TRAUTMANN, T. 1997. Spectral information from minerals relevant for luminescence dating. Radiation Measurements, 27, 695-748.

KREUTZER, S., BUROW, C., DIETZE, M., FUCHS, M. C., FISCHER, M. & SCHMIDT, C. 2017. Software in the context of luminescence dating: status, concepts and suggestions exemplified by the R package'Luminescence'. Ancient TL, 35, 1-11.

KUSKY, T., ROBINSON, C. & EL-BAZ, F. 2005. Tertiary–Quaternary faulting and uplift in the northern Oman Hajar Mountains. Journal of the Geological Society, 162, 871-888.

KWARTENG, A., AL-HATRUSHI, S., ILLENBERGER, W., MCLACHLAN, A., SANA, A., AL-BULOUSHI, A. & HAMED, K. 2016. Beach erosion along Al Batinah coast, Sultanate of Oman. Arabian Journal of Geosciences, 9, 1-20.

KWARTENG, A. Y., DORVLO, A. S. & VIJAYA KUMAR, G. T. 2009. Analysis of a 27-year rainfall data (1977–2003) in the Sultanate of Oman. International Journal of Climatology: A Journal of the Royal Meteorological Society, 29, 605-617.

LANCASTER, N., WOLFE, S., THOMAS, D., BRISTOW, C., BUBENZER, O., BURROUGH, S., DULLER, G., HALFEN, A., HESSE, P. & ROSKIN, J. 2016. The INQUA dunes atlas chronologic database. Quaternary International, 410, 3-10.

LECCE, S. A. 1990. The alluvial fan problem. Alluvial fans: A field approach, 3-24.

LEE, J.-S. 1981. Speckle analysis and smoothing of synthetic aperture radar images. Computer graphics and image processing, 17, 24-32.

LEEDER, M. & MACK, G. 2001. Lateral erosion (‘toe-cutting’) of alluvial fans by axial rivers: implications for basin analysis and architecture. Journal of the Geological Society, 158, 885-893.

LEENMAN, A., EATON, B. & MACKENZIE, L. G. 2021. Floods on alluvial fans: implications for reworking rates, morphology and fan hazards. Journal of Geophysical Research: Earth Surface, e2021JF006367.

LEENMAN, A. & TUNNICLIFFE, J. 2020. Tributary-junction fans as buffers in the sediment cascade: a multi-decadal study. Earth Surface Processes and Landforms, 45, 265-279.

LEGGET, R. F., BROWN, R. E. & JOHNSTON, G. 1966. Alluvial fan formation near Aklavik, Northwest Territories, Canada. Geological Society of America Bulletin, 77, 15-30.

LEIGHTON, C. L., BAILEY, R. M. & THOMAS, D. S. 2013. The utility of desert sand dunes as Quaternary chronostratigraphic archives: evidence from the northeast Rub'al Khali. Quaternary Science Reviews, 78, 303-318.

LEIGHTON, C. L., BAILEY, R. M. & THOMAS, D. S. 2014a. Interpreting and modelling late Quaternary dune accumulation in the southern Arabian Peninsula. Quaternary Science Reviews, 102, 1-13.

LEIGHTON, C. L., THOMAS, D. S. G. & BAILEY, R. M. 2014b. Reproducibility and utility of dune luminescence chronologies. Earth-Science Reviews, 129, 24-39.

LÉZINE, A.-M., BASSINOT, F. & PETERSCHMITT, J.-Y. 2014. Orbitally-induced changes of the Atlantic and Indian monsoons over the past 20,000 years: New insights based on the comparison of continental and marine records. Bulletin de la Société Géologique de France, 185, 3-12.

LÉZINE, A.-M., IVORY, S. J., BRACONNOT, P. & MARTI, O. 2017. Timing of the southward retreat of the ITCZ at the end of the Holocene Humid Period in Southern Arabia: Data-model comparison. Quaternary Science Reviews, 164, 68-76.

LÉZINE, A.-M., ROBERT, C., CLEUZIOU, S., INIZAN, M.-L., BRAEMER, F., SALIÈGE, J.-F., SYLVESTRE, F., TIERCELIN, J.-J., CRASSARD, R. & MÉRY, S. 2010. Climate change and human occupation in the Southern Arabian lowlands during the last deglaciation and the Holocene. Global and Planetary Change, 72, 412-428.

LÉZINE, A.-M., SALIÈGE, J.-F., MATHIEU, R., TAGLIATELA, T.-L., MERY, S., CHARPENTIER, V. & CLEUZIOU, S. 2002. Mangroves of Oman during the late Holocene; climatic implications and impact on human settlements. Vegetation History and Archaeobotany, 11, 221-232.

LÉZINE, A.-M., SALIEGE, J.-F., ROBERT, C., WERTZ, F. & INIZAN, M.-L. 1998. Holocene lakes from Ramlat as-Sab'atayn (Yemen) illustrate the impact of monsoon activity in southern Arabia. Quaternary Research, 50, 290-299.

LÉZINE, A.-M., TIERCELIN, J.-J., ROBERT, C., SALIÈGE, J.-F., CLEUZIOU, S., INIZAN, M.-L. & BRAEMER, F. 2007. Centennial to millennial-scale variability of the Indian monsoon during the early Holocene from a sediment, pollen and isotope record from the desert of Yemen. Palaeogeography, Palaeoclimatology, Palaeoecology, 243, 235-249.

LI, B. & LI, S.-H. 2012. Luminescence dating of Chinese loess beyond 130 ka using the non-fading signal from K-feldspar. Quaternary Geochronology, 10, 24-31.

LINDAUER, S., MARALI, S., SCHÖNE, B. R., UERPMANN, H.-P., KROMER, B. & HINDERER, M. 2017. Investigating the local reservoir age and stable isotopes of shells from southeast Arabia. Radiocarbon, 59, 355-372.

LISIECKI, L. E. & RAYMO, M. E. 2005. A Pliocene-Pleistocene stack of 57 globally distributed benthic δ18O records. Paleoceanography, 20.

LITT, T., OHLWEIN, C., NEUMANN, F. H., HENSE, A. & STEIN, M. 2012. Holocene climate variability in the Levant from the Dead Sea pollen record. Quaternary Science Reviews, 49, 95-105.

LOFTUS, E., MITCHELL, P. J. & RAMSEY, C. B. 2019. An archaeological radiocarbon database for southern Africa. Antiquity, 93, 870-885.

LOKIER, S. & STEUBER, T. 2008. Quantification of Carbonate-Ramp Sedimentation and Progradation Rates for the Late Holocene Abu Dhabi Shoreline. Journal of Sedimentary Research, 78, 423-431.

LOKIER, S. W., BATEMAN, M. D., LARKIN, N. R., RYE, P. & STEWART, J. R. 2015. Late Quaternary sea-level changes of the Persian Gulf. Quaternary Research, 84, 69-81.

LOWE, J. J. & WALKER, M. J. 2000. Radiocarbon Dating the Last Glacial-Interglacial Transition (Ca. 14–9 14C Ka Bp) in Terrestrial and Marine Records: The Need for New Quality Assurance Protocols1. Radiocarbon, 42, 53-68.

MACK, G. H., JAMES, W. C. & MONGER, H. C. 1993. Classification of paleosols. Geological society of America bulletin, 105, 129-136.

MACKLIN, S., ELLISON, R., MANNING, J., FARRANT, A. & LORENTI, L. 2012. Engineering geological characterisation of the Barzaman Formation, with reference to coastal Dubai, UAE. Bulletin of Engineering Geology and the Environment, 71, 1-19.

MAIZELS, J. 1987. Plio-Pleistocene raised channel systems of the western Sharqiya (Wahiba), Oman. Geological Society, London, Special Publications, 35, 31-50.

MAIZELS, J. 1990. Raised channel systems as indicators of palaeohydrologic change: a case study from Oman. Palaeogeography, Palaeoclimatology, Palaeoecology, 76, 241-277.

MAIZELS, J. & MCBEAN, C. 1990. Cenozoic alluvial fan systems of interior Oman: palaeoenvironmental reconstruction based on discrimination of palaeochannels using remotely sensed data. Geological Society, London, Special Publications, 49, 565-582.

MARCHI, B., PASUTO, A. & TECCA, P. R. 1993. Flow processes on alluvial fans in the Eastern Italian Alps. Zeitschrift fur Geomorphologie, 37, 447-447.

MARTIN, L., GOFF, J., JACOBSEN, G. & MOONEY, S. 2019. The radiocarbon ages of different organic components in the mires of eastern Australia. Radiocarbon, 61, 173-184.

MATEICIUCOVÁ, I., WILDING, M., OTAVA, J. & ŠINDELÁŘ, J. 2023. The Al-Hajar Mts as a prehistoric refugium? On the habitability of karst mountain places in Oman during arid climate periods. Journal of Arid Environments, 212, 104951.

MATHER, A., HARVEY, A. & STOKES, M. 2000. Quantifying long-term catchment changes of alluvial fan systems. Geological Society of America Bulletin, 112, 1825-1833.

MATHER, A., STOKES, M. & WHITFIELD, E. 2017. River terraces and alluvial fans: the case for an integrated Quaternary fluvial archive. Quaternary Science Reviews, 166, 74-90.

MATTER, A., MAHJOUB, A., NEUBERT, E., PREUSSER, F., SCHWALB, A., SZIDAT, S. & WULF, G. 2016. Reactivation of the Pleistocene trans-Arabian Wadi ad Dawasir fluvial system (Saudi Arabia) during the Holocene humid phase. Geomorphology, 270, 88-101.

MATTER, A., NEUBERT, E., PREUSSER, F., ROSENBERG, T. & AL-WAGDANI, K. 2015. Palaeo-environmental implications derived from lake and sabkha deposits of the southern Rub'al-Khali, Saudi Arabia and Oman. Quaternary International, 382, 120-131.

MATTHEWS, J. A. & WINKLER, S. 2022. Schmidt-hammer exposure-age dating: a review of principles and practice. Earth-Science Reviews, 230, 104038.

MAYYA, Y., MORTHEKAI, P., MURARI, M. K. & SINGHVI, A. 2006. Towards quantifying beta microdosimetric effects in single-grain quartz dose distribution. Radiation Measurements, 41, 1032-1039.

MCCLAIN, K. P., YıLDıRıM, C., ÇINER, A., SARıKAYA, M. A., ÖZCAN, O., GÖRÜM, T., KÖSE, O., ŞAHIN, S., KıYAK, N. G. & ÖZTÜRK, T. 2021. River, alluvial fan and landslide interactions in a tributary junction setting: Implications for tectonic controls on Quaternary fluvial landscape development (Central Anatolian Plateau northern margin, Turkey). Geomorphology, 376, 107567.

MCCLURE, H. 1976. Radiocarbon chronology of late Quaternary lakes in the Arabian Desert. Nature, 263, 755-756.

MCCORRISTON, J., WALTER, D., OCHES, E. & COLE, K. 2002. Holocene paleoecology and prehistory in highland southern Arabia. Paléorient, 61-88.

MCEWEN, L. J., MATTHEWS, J. A. & OWEN, G. 2020. Development of a Holocene glacier-fed composite alluvial fan based on surface exposure-age dating techniques: The Illåe fan, Jotunheimen, Norway. Geomorphology, 363, 107200.

MCFADDEN, L. D., WELLS, S. G. & JERCINOVICH, M. J. 1987. Influences of eolian and pedogenic processes on the origin and evolution of desert pavements. Geology, 15, 504-508.

MCKEEVER, S. W., CHEN, C. & HALLIBURTON, L. 1985. Point defects and the pre-dose effect in natural quartz. Nuclear Tracks and Radiation Measurements (1982), 10, 489-495.

MCLAREN, S. J., AL-JUAIDI, F., BATEMAN, M. D. & MILLINGTON, A. C. 2009. First evidence for episodic flooding events in the arid interior of central Saudi Arabia over the last 60 ka. Journal of Quaternary Science: Published for the Quaternary Research Association, 24, 198-207.

MEJDAHL, V. 1979. Thermoluminescence dating: beta-dose attenuation in quartz grains. Archaeometry, 21, 61-72.

MEJDAHL, V. 1988. Long-term stability of the TL signal in alkali feldspars. Quaternary Science Reviews, 7, 357-360.

MEJDAHL, V. & CHRISTIANSEN, H. H. 1994. Procedures used for luminescence dating of sediments. Quaternary Science Reviews, 13, 403-406.

MELAMID, A. 1992. The Jebel al-Akhdar (Oman). Geographical Review, 82, 470-472.

MELTON, M. A. 1965. The geomorphic and paleoclimatic significance of alluvial deposits in southern Arizona. The Journal of geology, 73, 1-38.

MERVINE, E. M., HUMPHRIS, S. E., SIMS, K. W. W., KELEMEN, P. B. & JENKINS, W. J. 2014. Carbonation rates of peridotite in the Samail Ophiolite, Sultanate of Oman, constrained through 14C dating and stable isotopes. Geochimica et Cosmochimica Acta, 126, 371-397.

MERVINE, E. M., SIMS, K. W. W., HUMPHRIS, S. E. & KELEMEN, P. B. 2015. Applications and limitations of U–Th disequilibria systematics for determining ages of carbonate alteration minerals in peridotite. Chemical Geology, 412, 151-166.

MEYBECK, M. 1987. Global chemical weathering of surficial rocks estimated from river dissolved loads. American journal of science, 287, 401-428.

MEYER, M. C., AUSTIN, P. & TROPPER, P. 2013. Quantitative evaluation of mineral grains using automated SEM–EDS analysis and its application potential in optically stimulated luminescence dating. Radiation measurements, 58, 1-11.

MIALL, A. D. 1977. Lithofacies types and vertical profile models in braided river deposits: a summary.

MILANA, J. P. & RUZYCKI, L. 1999. Alluvial-fan slope as a function of sediment transport efficiency. Journal of Sedimentary Research, 69, 553-562.

MILES, S. B. 1901. Across the Green Mountains of Oman. The Geographical Journal, 18, 465-498.

MILLS, H. H. 2000. Controls on form, process, and sedimentology of alluvial fans in the Central and Southern Appalachians, southeastern USA. Southeastern Geology, 39, 281-313.

MINELI, T., SAWAKUCHI, A., GURALNIK, B., LAMBERT, R., JAIN, M., PUPIM, F., DEL RIO, I., GUEDES, C. & NOGUEIRA, L. 2021. Variation of luminescence sensitivity, characteristic dose and trap parameters of quartz from rocks and sediments. Radiation Measurements, 144, 106583.

MOKARRAM, M., SEIF, A. & SATHYAMOORTHY, D. Use of morphometric analysis and self-organizing maps for alluvial fan classification: case study on Ostorankooh altitudes, Iran. IOP Conference Series: Earth and Environmental Science, 2014. IOP Publishing, 012003.

MOLLAEI, Z., DAVARY, K., HASHEMINIA, S. M., FARIDHOSSEINI, A. & POURMOHAMAD, Y. 2018. Enhancing flood hazard estimation methods on alluvial fans using an integrated hydraulic, geological and geomorphological approach. Natural Hazards and Earth System Sciences, 18, 1159-1171.

MOLNAR, P., ENGLAND, P. & MARTINOD, J. 1993. Mantle dynamics, uplift of the Tibetan Plateau, and the Indian monsoon. Reviews of Geophysics, 31, 357-396.

MONKS, J., ROSS, S., GEISER, M., DE PRINS, J., SHARAF, M., WYATT, N., AL RIJEIBI, S. & POLASZEK, A. 2019. A preliminary survey of the insect fauna of the Hajar Mountain Range, Oman. Journal of Natural History, 53, 939-963.

MOORE, J. M. & HOWARD, A. D. 2005. Large alluvial fans on Mars. Journal of Geophysical Research: Planets, 110.

MORAETIS, D., MATTERN, F., SCHARF, A., FRIJIA, G., KUSKY, T. M., YUAN, Y. & EL-HUSSAIN, I. 2018. Neogene to Quaternary uplift history along the passive margin of the northeastern Arabian Peninsula, eastern Al Hajar Mountains, Oman. Quaternary Research, 90, 418-434.

MORAETIS, D., SCHARF, A., MATTERN, F., PAVLOPOULOS, K. & FORMAN, S. 2020. Quaternary Thrusting in the central Oman Mountains—novel observations and causes: insights from optical stimulate luminescence dating and kinematic fault analyses. Geosciences, 10, 166.

MORENO, D., GUTIÉRREZ, F., DEL VAL, M., CARBONEL, D., JIMÉNEZ, F., ALONSO, M. J., MARTÍNEZ-PILLADO, V., GUZMÁN, O., LÓPEZ, G. I. & MARTÍNEZ, D. 2021. A multi-method dating approach to reassess the geochronology of faulted Quaternary deposits in the central sector of the Iberian Chain (NE Spain). Quaternary Geochronology, 65, 101185.

MORGAN, A., HOWARD, A., HOBLEY, D. E., MOORE, J. M., DIETRICH, W. E., WILLIAMS, R. M., BURR, D. M., GRANT, J. A., WILSON, S. A. & MATSUBARA, Y. 2014. Sedimentology and climatic environment of alluvial fans in the martian Saheki crater and a comparison with terrestrial fans in the Atacama Desert. Icarus, 229, 131-156.

MORGAN, A. M., WILSON, S. A. & HOWARD, A. D. 2022. The global distribution and morphologic characteristics of fan-shaped sedimentary landforms on Mars. Icarus, 115137.

MOSCARIELLO, A. 2018. Alluvial fans and fluvial fans at the margins of continental sedimentary basins: geomorphic and sedimentological distinction for geo-energy exploration and development. Geological Society, London, Special Publications, 440, 215-243.

MOUNT, V. S., CRAWFORD, R. I. & BERGMAN, S. C. 1998. Regional structural style of the central and southern Oman Mountains: Jebel Akhdar, Saih Hatat, and the northern Ghaba Basin. GeoArabia, 3, 475-490.

MOUSAVI, Z., FATTAHI, M., KHATIB, M., TALEBIAN, M., PATHIER, E., WALPERSDORF, A., SLOAN, R. A., THOMAS, A. L., RHODES, E. & CLIVE, F. 2021. Constant Slip Rate on the Doruneh Strike-Slip Fault, Iran, Averaged Over Late Pleistocene, Holocene, and Decadal Timescales. Tectonics, 40, e2020TC006256.

MUELLER, D., RAITH, K., BRETZKE, K., FÜLLING, A., PARKER, A. G., PARTON, A., PRESTON, G. W., JASIM, S., YOUSIF, E. & PREUSSER, F. 2022. Luminescence chronology of fluvial and aeolian deposits from the Emirate of Sharjah, UAE. Quaternary Research, 1-17.

MURRAY, A., ARNOLD, L. J., BUYLAERT, J.-P., GUÉRIN, G., QIN, J., SINGHVI, A. K., SMEDLEY, R. & THOMSEN, K. J. 2021. Optically stimulated luminescence dating using quartz. Nature Reviews Methods Primers, 1, 1-31.

MURRAY, A. S. & WINTLE, A. G. 2000. Luminescence dating of quartz using an improved single-aliquot regenerative-dose protocol. Radiation measurements, 32, 57-73.

MURRAY, A. S. & WINTLE, A. G. 2003. The single aliquot regenerative dose protocol: potential for improvements in reliability. Radiation measurements, 37, 377-381.

NANSON, G. C., PRICE, D. M. & SHORT, S. A. 1992. Wetting and drying of Australia over the past 300 ka. Geology, 20, 791-794.

NATHAN, R. & MAUZ, B. 2008. On the dose-rate estimate of carbonate-rich sediments for trapped charge dating. Radiation Measurements, 43, 14-25.

NATHAN, R. P., THOMAS, P. J., JAIN, M., MURRAY, A. S. & RHODES, E. J. 2003. Environmental dose rate heterogeneity of beta radiation and its implications for luminescence dating: Monte Carlo modelling and experimental validation. Radiation Measurements, 37, 305-313.

NEFF, U., BURNS, S. J., MANGINI, A., MUDELSEE, M., FLEITMANN, D. & MATTER, A. 2001. Strong coherence between solar variability and the monsoon in Oman between 9 and 6 kyr ago. Nature, 411, 290-293.

NEHLIG, P., GENNA, A., ASFIRANE, F., BRGM, F., GUERROT, C., EBERLÉ, J., KLUYVER, H., LASSERRE, J., LE GOFF, E. & NICOL, N. 2002. A review of the Pan-African evolution of the Arabian Shield. GeoArabia, 7, 103-124.

NELSON, M. S. & RITTENOUR, T. M. 2015. Using grain-size characteristics to model soil water content: application to dose-rate calculation for luminescence dating. Radiation Measurements, 81, 142-149.

NEMEC, W. & POSTMA, G. 1993. Quaternary alluvial fans in southwestern Crete: sedimentation processes and geomorphic evolution. Alluvial sedimentation. International Association of Sedimentologists Oxford.

NETTLETON, W. & CHADWICK, O. 1996. Late Quaternary, redeposited loess-soil developmental sequences, South Yemen. Geoderma, 70, 21-36.

NICHOLS, G. & FISHER, J. 2007. Processes, facies and architecture of fluvial distributary system deposits. Sedimentary geology, 195, 75-90.

NICHOLSON, S. E. 2018. The ITCZ and the seasonal cycle over equatorial Africa. Bulletin of the American Meteorological Society, 99, 337-348.

NICHOLSON, S. L., PIKE, A. W., HOSFIELD, R., ROBERTS, N., SAHY, D., WOODHEAD, J., CHENG, H., EDWARDS, R. L., AFFOLTER, S. & LEUENBERGER, M. 2020. Pluvial periods in Southern Arabia over the last 1.1 million-years. Quaternary Science Reviews, 229, 106112.

NINKABOU, D., AGARD, P., NIELSEN, C., SMIT, J., GORINI, C., RODRIGUEZ, M., HAQ, B., CHAMOT-ROOKE, N., WEIDLE, C. & DUCASSOU, C. 2021. Structure of the offshore obducted Oman margin:

emplacement of Semail ophiolite and role of tectonic inheritance. Journal of Geophysical Research: Solid Earth, 126, 2020JB020187.

NISHIIZUMI, K., CAFFEE, M., FINKEL, R., BRIMHALL, G. & MOTE, T. 2005. Remnants of a fossil alluvial fan landscape of Miocene age in the Atacama Desert of northern Chile using cosmogenic nuclide exposure age dating. Earth and Planetary Science Letters, 237, 499-507.

NOTTEBAUM, V., LEHMKUHL, F., STAUCH, G., HARTMANN, K., WÜNNEMANN, B., SCHIMPF, S. & LU, H. 2014. Regional grain size variations in aeolian sediments along the transition between Tibetan highlands and north-western Chinese deserts–the influence of geomorphological settings on aeolian transport pathways. Earth Surface Processes and Landforms, 39, 1960-1978.

O'GORMAN, K., TANNER, D., SONTAG-GONZÁLEZ, M., LI, B., BRINK, F., JONES, B. G., DOSSETO, A., JATMIKO, ROBERTS, R. G. & JACOBS, Z. 2021. Composite grains from volcanic terranes: Internal dose rates of supposed 'potassium-rich' feldspar grains used for optical dating at Liang Bua, Indonesia. Quaternary Geochronology, 64.

OLLEY, J. M., MURRAY, A. & ROBERTS, R. G. 1996. The effects of disequilibria in the uranium and thorium decay chains on burial dose rates in fluvial sediments. Quaternary Science Reviews, 15, 751-760.

OPALKA, C. E., EPPES, M. C., BOBYARCHICK, A. R. & SPATZ, A. A. 2022. Alluvial fan aggradation in low relief, humid-temperate landscapes, Uwharrie National Forest, North Carolina Piedmont. Earth Surface Processes and Landforms.

OU, X., ROBERTS, H. & DULLER, G. 2022. Rapid assessment of beta dose variation inside cobbles, and implications for rock luminescence dating. Quaternary Geochronology, 72, 101349.

OVERPECK, J., ANDERSON, D., TRUMBORE, S. & PRELL, W. 1996. The southwest Indian Monsoon over the last 18 000 years. Climate Dynamics, 12, 213-225.

OWEN, L., WINDLEY, B., CUNNINGHAM, W., BADAMGARAV, J. & DORJNAMJAA, D. 1997. Quaternary alluvial fans in the Gobi of southern Mongolia: evidence for neotectonics and climate change. Journal of Quaternary Science: Published for the Quaternary Research Association, 12, 239-252.

PAILLOU, P. 2017. Mapping palaeohydrography in deserts: contribution from space-borne imaging radar. Water, 9, 194.

PAILLOU, P., LOPEZ, S., FARR, T. & ROSENQVIST, A. 2010. Mapping subsurface geology in Sahara using L-Band SAR: first results from the ALOS/PALSAR imaging radar. IEEE Journal of Selected Topics in Applied Earth Observations and Remote Sensing, 3, 632-636.

PAILLOU, P., LOPEZ, S., MARAIS, E. & SCIPAL, K. 2020. Mapping Paleohydrology of the ephemeral Kuiseb River, Namibia, from radar remote sensing. Water, 12, 1441.

PAIN, C. F. & ABDELFATTAH, M. A. 2015. Landform evolution in the arid northern United Arab Emirates: Impacts of tectonics, sea level changes and climate. Catena, 134, 14-29.

PARKER, A. G. 2010. Pleistocene climate change in Arabia: developing a framework for hominin dispersal over the last 350 ka. The evolution of human populations in Arabia. Springer.

PARKER, A. G., ECKERSLEY, L., SMITH, M. M., GOUDIE, A. S., STOKES, S., WARD, S., WHITE, K. & HODSON, M. J. 2004. Holocene vegetation dynamics in the northeastern Rub' al-Khali desert, Arabian Peninsula: a phytolith, pollen and carbon isotope study. Journal of Quaternary Science, 19, 665-676.

PARKER, A. G. & GOUDIE, A. S. 2008. Geomorphological and palaeoenvironmental investigations in the southeastern Arabian Gulf region and the implication for the archaeology of the region. Geomorphology, 101, 458-470.

PARKER, A. G., GOUDIE, A. S., STOKES, S., WHITE, K., HODSON, M. J., MANNING, M. & KENNET, D. 2006. A record of Holocene climate change from lake geochemical analyses in southeastern Arabia. Quaternary Research, 66, 465-476.

PARKER, A. G., MORLEY, M. W., ARMITAGE, S. J., ENGEL, M., PARTON, A., PRESTON, G. W., RUSS, H. & DRECHSLER, P. 2020. Palaeoenvironmental and sea level changes during the Holocene in eastern Saudi Arabia and their implications for Neolithic populations. Quaternary Science Reviews, 249, 106618.

PARKER, A. G., PRESTON, G. W., PARTON, A., WALKINGTON, H., JARDINE, P. E., LENG, M. J. & HODSON, M. J. 2016. Low-latitude Holocene hydroclimate derived from lake sediment flux and geochemistry. Journal of Quaternary Science, 31, 286-299.

PARTON, A. & BRETZKE, K. 2020. The PalaeoEnvironments and ARchaeological Landscapes (PEARL) project: Recent findings from Neolithic sites in Northern Oman. Arabian Archaeology and Epigraphy, 31, 194-201.

PARTON, A., CLARK-BALZAN, L., PARKER, A. G., PRESTON, G. W., SUNG, W. W., BREEZE, P. S., LENG, M. J., GROUCUTT, H. S., WHITE, T. S., ALSHAREKH, A. & PETRAGLIA, M. D. 2018. Middle-late Quaternary palaeoclimate variability from lake and wetland deposits in the Nefud Desert, Northern Arabia. Quaternary Science Reviews, 202, 78-97.

PARTON, A., FARRANT, A. R., LENG, M. J., SCHWENNINGER, J.-L., ROSE, J. I., UERPMANN, H.-P. & PARKER, A. G. 2013. An early MIS 3 pluvial phase in Southeast Arabia: climatic and archaeological implications. Quaternary International, 300, 62-74.

PARTON, A., FARRANT, A. R., LENG, M. J., TELFER, M. W., GROUCUTT, H. S., PETRAGLIA, M. D. & PARKER, A. G. 2015a. Alluvial fan records from southeast Arabia reveal multiple windows for human dispersal. Geology, 43, 295-298.

PARTON, A., WHITE, T. S., PARKER, A. G., BREEZE, P. S., JENNINGS, R., GROUCUTT, H. S. & PETRAGLIA, M. D. 2015b. Orbital-scale climate variability in Arabia as a potential motor for human dispersals. Quaternary International, 382, 82-97.

PATZELT, A. 2015. Synopsis of the flora and vegetation of Oman, with special emphasis on patterns of plant endemism. Abhandlungen der Braunschweigischen Wissenschaftlichen Gesellschaft, 282, 317.

PATZELT, A., HARRISON, T., KNEES, S. & AL HARTHY, L. 2014. Studies in the flora of Arabia: XXXI. New records from the Sultanate of Oman. Edinburgh Journal of Botany, 71, 161-180.

PETRAGLIA, M. D., GROUCUTT, H. S., GUAGNIN, M., BREEZE, P. S. & BOIVIN, N. 2020. Human responses to climate and ecosystem change in ancient Arabia. Proceedings of the National Academy of Sciences, 117, 8263-8270.

PETRAGLIA, M. D., PARTON, A., GROUCUTT, H. S. & ALSHAREKH, A. 2015. Green Arabia: Human prehistory at the crossroads of continents. Quaternary International, 382, 1-7.

PORAT, N., AMIT, R., ZILBERMAN, E. & ENZEL, Y. 1997. Luminescence dating of fault-related alluvial fan sediments in the southern Arava Valley, Israel. Quaternary Science Reviews, 16, 397-402.

PORAT, N., DULLER, G., ROBERTS, H. & WINTLE, A. 2009. A simplified SAR protocol for TT-OSL. Radiation Measurements, 44, 538-542.

PORAT, N., FAERSTEIN, G., MEDIALDEA, A. & MURRAY, A. 2015. Re-examination of common extraction and purification methods of quartz and feldspar for luminescence dating. Ancient TL, 33, 22-30.

POWERS, R., RAMIREZ, L., REDMOND, C. & ELBERG, E. 1966. Geology of the Arabian Peninsula, United States Department of the Interior, Geological Survey.

PRASAD, S. 2000. HF treatment for the isolation of fine grain quartz for luminescence dating. Ancient TL, 18, 15-17.

PRESCOTT, J. R. & HUTTON, J. T. 1994. Cosmic ray contributions to dose rates for luminescence and ESR dating: large depths and long-term time variations. Radiation measurements, 23, 497-500.

PRESTON, G. W. & PARKER, A. G. 2013. Understanding the evolution of the Holocene Pluvial Phase and its impact on Neolithic populations in south-east Arabia. Arabian Archaeology and Epigraphy, 24, 87-94.

PREUSSER, F. 2009. Chronology of the impact of Quaternary climate change on continental environments in the Arabian Peninsula. Comptes Rendus Geoscience, 341, 621-632.

PREUSSER, F., RADIES, D., DRIEHORST, F. & MATTER, A. 2005. Late Quaternary history of the coastal Wahiba sands, Sultanate of Oman. Journal of Quaternary Science: Published for the Quaternary Research Association, 20, 395-405.

PREUSSER, F., RADIES, D. & MATTER, A. 2002. A 160,000-Year Record of Dune Development and Atmospheric Circulation in Southern Arabia. Science, 296, 2018-2020.

PURDUE, L., CHARBONNIER, J., REGAGNON, E., CALASTRENC, C., SAGORY, T., VIRMOUX, C., CRÉPY, M., COSTA, S. & BENOIST, A. 2019. Geoarchaeology of Holocene oasis formation, hydro-agricultural management and climate change in Masafi, southeast Arabia (UAE). Quaternary Research, 92, 109-132.

PURDUE, L., KENNET, D., GARNIER, A., PARTON, A., DJERBI, H., BOTAN, S., HERVEUX, L., DAVTIAN, G., CARRÉ, A. & MOGER, D. 2021. Ancient agriculture in Southeast Arabia: A three thousand year record of runoff farming from central Oman (Rustaq). Catena, 204, 105406.

RADEBAUGH, J., VENTRA, D., LORENZ, R. D., FARR, T., KIRK, R., HAYES, A., MALASKA, M. J., BIRCH, S., LIU, Z. Y.-C. & LUNINE, J. 2018. Alluvial and fluvial fans on Saturn's moon Titan reveal processes, materials and regional geology. Geological Society, London, Special Publications, 440, 281-305.

RADIES, D., HASIOTIS, S., PREUSSER, F., NEUBERT, E. & MATTER, A. 2005. Paleoclimatic significance of Early Holocene faunal assemblages in wet interdune deposits of the Wahiba Sand Sea, Sultanate of Oman. Journal of Arid Environments, 62, 109-125.

RATNAYAKA, K., HETZEL, R., HORNUNG, J., HAMPEL, A., HINDERER, M. & FRECHEN, M. 2019. Postglacial alluvial fan dynamics in the Cordillera Oriental, Peru, and palaeoclimatic implications. Quaternary Research, 91, 431-449.

RAVAUT, P., CARBON, D., RITZ, J.-F., BAYER, R. & PHILIP, H. 1998. The Sohar Basin, Western Gulf of Oman: description and mechanisms of formation from seismic and gravity data. Marine and Petroleum Geology, 15, 359-377.

REIMANN, T. & TSUKAMOTO, S. 2012. Dating the recent past (<500 years) by post-IR IRSL feldspar – Examples from the North Sea and Baltic Sea coast. Quaternary Geochronology, 10, 180-187.

REIMER, P. J., AUSTIN, W. E., BARD, E., BAYLISS, A., BLACKWELL, P. G., RAMSEY, C. B., BUTZIN, M., CHENG, H., EDWARDS, R. L. & FRIEDRICH, M. 2020. The IntCal20 Northern Hemisphere radiocarbon age calibration curve (0–55 cal kBP). Radiocarbon, 62, 725-757.

REININK-SMITH, L. M. 2015. AMS-dated mollusks in beach ridges and berms document Holocene sea-level and coastal changes in northeastern Kuwait Bay. Quaternary Research, 84, 200-213.

RETALLACK, G. J., REINHARDT, J. & SIGLEO, W. 1988. Field recognition of paleosols. Geological Society of America Special Paper, 216, 1-20.

REVEL, M., DUCASSOU, E., GROUSSET, F., BERNASCONI, S., MIGEON, S., RÉVILLON, S., MASCLE, J., MURAT, A., ZARAGOSI, S. & BOSCH, D. 2010. 100,000 Years of African monsoon variability recorded in sediments of the Nile margin. Quaternary Science Reviews, 29, 1342-1362.

RHODES, E. & SCHWENNINGER, J. 2007. Dose rates and radioisotope concentrations in the concrete calibration blocks at Oxford. Ancient TL, 25, 5-8.

RHODES, E. J. 2011. Optically stimulated luminescence dating of sediments over the past 200,000 years. Annual Review of Earth and Planetary Sciences, 39, 461-488.

RHODES, E. J. 2015. Dating sediments using potassium feldspar single-grain IRSL: Initial methodological considerations. Quaternary International, 362, 14-22.

RICHARD, M., MERCIER, N., CHARPENTIER, V. & BERGER, J.-F. 2020. OSL chronology of socio-ecological systems during the mid-Holocene in the eastern coast of the Sultanate of Oman (Arabian Peninsula). Journal of Archaeological Science: Reports, 33, 102465.

RITTENOUR, T. M. 2008. Luminescence dating of fluvial deposits: applications to geomorphic, palaeoseismic and archaeological research. Boreas, 37, 613-635.

RITTER, J. B., MILLER, J. R., ENZEL, Y. & WELLS, S. G. 1995. Reconciling the roles of tectonism and climate in Quaternary alluvial fan evolution. Geology, 23, 245-248.

RIZZA, M., ABDRAKHMATOV, K., WALKER, R., BRAUCHER, R., GUILLOU, V., CARR, A., CAMPBELL, G., MCKENZIE, D., JACKSON, J. & AUMAÎTRE, G. 2019. Rate of slip from multiple Quaternary dating methods and paleoseismic investigations along the Talas-Fergana Fault: Tectonic implications for the Tien Shan Range. Tectonics, 38, 2477-2505.

ROBERTS, H. M. 2007. Assessing the effectiveness of the double-SAR protocol in isolating a luminescence signal dominated by quartz. Radiation measurements, 42, 1627-1636.

ROBINSON, C., EL-BAZ, F., KUSKY, T., MAINGUET, M., DUMAY, F., AL SULEIMANI, Z. & AL MARJEBY, A. 2007. Role of fluvial and structural processes in the formation of the Wahiba Sands, Oman: A remote sensing perspective. Journal of arid environments, 69, 676-694.

ROBUSTELLI, G., MUTO, F., SCARCIGLIA, F., SPINA, V. & CRITELLI, S. 2005. Eustatic and tectonic control on Late Quaternary alluvial fans along the Tyrrhenian Sea coast of Calabria (South Italy). Quaternary Science Reviews, 24, 2101-2119.

RODGERS, D. W. & GUNATILAKA, A. 2003. Bajada formation by monsoonal erosion of a subaerial forebulge, Sultanate of Oman. Sedimentary Geology, 154, 127-146.

RODNIGHT, H., DULLER, G., WINTLE, A. & TOOTH, S. 2006. Assessing the reproducibility and accuracy of optical dating of fluvial deposits. Quaternary Geochronology, 1, 109-120.

ROSE, J. I. 2010. New light on human prehistory in the Arabo-Persian Gulf Oasis. Current Anthropology, 51, 849-883.

ROSE, J. I., ČERNÝ, V. & BAYOUMI, R. 2013. Tabula rasa or refugia? Using genetic data to assess the peopling of Arabia. Arabian Archaeology and Epigraphy, 24, 95-101.

ROSE, J. I., HILBERT, Y. H., USIK, V. I., MARKS, A. E., JABOOB, M. M. A., ČERNÝ, V., CRASSARD, R. & PREUSSER, F. 2019. 30,000-year-old geometric microliths reveal glacial refugium in Dhofar, Southern Oman. Journal of Paleolithic Archaeology, 2, 338-357.

ROSENBERG, T., PREUSSER, F., FLEITMANN, D., SCHWALB, A., PENKMAN, K., SCHMID, T., AL-SHANTI, M., KADI, K. & MATTER, A. 2011. Humid periods in southern Arabia: windows of opportunity for modern human dispersal. Geology, 39, 1115-1118.

ROSENBERG, T. M., PREUSSER, F., BLECHSCHMIDT, I., FLEITMANN, D., JAGHER, R. & MATTER, A. 2012. Late Pleistocene palaeolake in the interior of Oman: a potential key area for the dispersal of anatomically modern humans out-of-Africa? Journal of Quaternary Science, 27, 13-16.

SAEED, S. & ALMAZROUI, M. 2019. Impacts of mid-latitude circulation on winter precipitation over the Arabian Peninsula. Climate Dynamics, 53, 5253-5264.

SAEED, W., SHOUAKAR-STASH, O., WOOD, W., PARKER, B. & UNGER, A. 2020. Groundwater and solute budget (a case study from Sabkha Matti, Saudi Arabia). Hydrology, 7, 94.

SANLAVILLE, P. 1992. Changements climatiques dans la péninsule Arabique durant le Pléistocène supérieur et l'Holocène. Paléorient, 5-26.

SARıKAYA, M. A., YıLDıRıM, C. & ÇINER, A. 2015. Late Quaternary alluvial fans of Emli Valley in the Ecemiş Fault Zone, south central Turkey: Insights from cosmogenic nuclides. Geomorphology, 228, 512-525.

SCHAEFER, J. M., CODILEAN, A. T., WILLENBRING, J. K., LU, Z.-T., KEISLING, B., FÜLÖP, R.-H. & VAL, P. 2022. Cosmogenic nuclide techniques. Nature Reviews Methods Primers, 2, 18.

SCHARF, A., MATTERN, F., MORAETIS, D., CALLEGARI, I. & WEIDLE, C. 2019. Postobductional kinematic evolution and geomorphology of a major regional structure—The Semail Gap Fault Zone (Oman Mountains). Tectonics, 38, 2756-2778.

SCHEIDL, C. & RICKENMANN, D. 2010. Empirical prediction of debris-flow mobility and deposition on fans. Earth Surface Processes and Landforms: The Journal of the British Geomorphological Research Group, 35, 157-173.

SCHOLTE, P. & DE GEEST, P. 2010. The climate of Socotra Island (Yemen): A first-time assessment of the timing of the monsoon wind reversal and its influence on precipitation and vegetation patterns. Journal of Arid Environments, 74, 1507-1515.

SEARLE, M. 1988. Structure of the Musandam culmination (Sultanate of Oman and United Arab Emirates) and the Straits of Hormuz syntaxis. Journal of the Geological Society, 145, 831-845.

SEARLE, M. 2019. Geology of the Oman mountains, eastern Arabia, Springer.

SEARLE, M. & COX, J. 1999. Tectonic setting, origin, and obduction of the Oman ophiolite. Geological Society of America Bulletin, 111, 104-122.

SEITSONEN, O., NORDQVIST, K., GERASIMOV, D. V. & LISITSYN, S. N. 2012. “The good, the bad, the weird”: Stone Age and Early Metal Period radiocarbon dates and chronology from the Karelian Isthmus, North-West Russia. Geochronometria, 39, 101-121.

SHAHIN, M. 2007. Wadis and wadi flow. Water resources and hydrometeorology of the Arab region. Springer.

SHOSHTA, A. & MARH, B. S. 2021. Alluvial fans of Trans-Himalayan cold desert (Pin valley, India): quantitative morphology and controlling factors. Physical Geography, 1-26.

SIDDALL, M., ROHLING, E. J., ALMOGI-LABIN, A., HEMLEBEN, C., MEISCHNER, D., SCHMELZER, I. & SMEED, D. A. 2003. Sea-level fluctuations during the last glacial cycle. Nature, 423, 853-858.

SIEBERT, S., HÄSER, J., NAGIEB, M., KORN, L. & BUERKERT, A. 2005. Agricultural, architectural and archaeological evidence for the role and ecological adaptation of a scattered mountain oasis in Oman. Journal of Arid Environments, 62, 177-197.

SILVA, P., HARVEY, A., ZAZO, C. & GOY, J. 1992. Geomorphology, depositional style and morphometric relationships of Quaternary alluvial fans in the Guadalentin depression (Murcia, southeast Spain). Zeitschrift für Geomorphologie, 36, 325-341.

SINGARAYER, J. S. & BURROUGH, S. L. 2015. Interhemispheric dynamics of the African rainbelt during the late Quaternary. Quaternary Science Reviews, 124, 48-67.

SINGH, A. K., JAISWAL, M. K., PATTANAIK, J. K. & DEV, M. 2016. Luminescence chronology of alluvial fan in North Bengal, India: Implications to tectonics and climate. Geochronometria, 43, 102-112.

SINHA, R., AHMAD, J., GAURAV, K. & MORIN, G. 2014. Shallow subsurface stratigraphy and alluvial architecture of the Kosi and Gandak megafans in the Himalayan foreland basin, India. Sedimentary Geology, 301, 133-149.

SIROCKO, F., SARNTHEIN, M., ERLENKEUSER, H., LANGE, H., ARNOLD, M. & DUPLESSY, J. C. 1993. Century-scale events in monsoonal climate over the past 24,000 years. Nature, 364, 322-324.

SMALL, D., CLARK, C. D., CHIVERRELL, R. C., SMEDLEY, R. K., BATEMAN, M. D., DULLER, G. A., ELY, J. C., FABEL, D., MEDIALDEA, A. & MORETON, S. G. 2017. Devising quality assurance procedures for assessment of legacy geochronological data relating to deglaciation of the last British-Irish Ice Sheet. Earth-Science Reviews, 164, 232-250.

SMEDLEY, R., DULLER, G., PEARCE, N. & ROBERTS, H. 2012. Determining the K-content of single-grains of feldspar for luminescence dating. Radiation Measurements, 47, 790-796.

SMEDLEY, R. & PEARCE, N. 2016. Internal U, Th and Rb concentrations of alkali-feldspar grains: Implications for luminescence dating. Quaternary Geochronology, 35, 16-25.

SMEDLEY, R. K. & SKIRROW, G. K. 2019. Luminescence dating in fluvial settings: Overcoming the challenge of partial bleaching. Palaeohydrology: Traces, Tracks and Trails of Extreme Events. Springer.

SOHBATI, R., MURRAY, A. S., BUYLAERT, J. P., ALMEIDA, N. A. & CUNHA, P. P. 2012. Optically stimulated luminescence (OSL) dating of quartzite cobbles from the T apada do M ontinho archaeological site (east-central P ortugal). Boreas, 41, 452-462.

SOLTANPOUR, M., RANJI, Z., SHIBAYAMA, T. & GHADER, S. 2021. Tropical Cyclones in the Arabian Sea: overview and simulation of winds and storm-induced waves. Natural Hazards, 108, 711-732.

SORIN, L., ANTON, V., MIRYAM, B.-M., ROI, P. & AMOS, F. 2010. Late Pleistocene palaeoclimatic and palaeoenvironmental reconstruction of the Dead Sea area (Israel), based on speleothems and cave stromatolites. Quaternary Science Reviews, 29, 1201-1211.

SPOONER, N. 1992. Optical dating: preliminary results on the anomalous fading of luminescence from feldspars. Quaternary Science Reviews, 11, 139-145.

SPRATT, R. M. & LISIECKI, L. E. 2016. A Late Pleistocene sea level stack. Climate of the Past, 12, 1079-1092.

STANGER, G. 1986. The hydrogeology of the Oman Mountains. The Open University.

STARKE, J., EHLERS, T. & SCHALLER, M. Latitudinal variation (15°-23° S) in denudation along the western Andean margin (Peru and Chile): Insights from cosmogenic 10Be. EGU General Assembly Conference Abstracts, 2017. 6518.

STEVENS, T., JESTICO, M. J., EVANS, G. & KIRKHAM, A. 2014. Eustatic control of late Quaternary sea-level change in the Arabian/Persian Gulf. Quaternary Research, 82, 175-184.

STOKES, M. & GOMES, A. 2020. Alluvial fans on volcanic islands: A morphometric perspective (São Vicente, Cape Verde). Geomorphology, 368, 107356.

STOKES, M. & MATHER, A. E. 2015. Controls on modern tributary-junction alluvial fan occurrence and morphology: High Atlas Mountains, Morocco. Geomorphology, 248, 344-362.

STOKES, S. & BRAY, H. E. 2005. Late Pleistocene eolian history of the Liwa region, Arabian Peninsula. Geological Society of America Bulletin, 117, 1466-1480.

STRUNK, A., OLSEN, J., SANEI, H., RUDRA, A. & LARSEN, N. K. 2020. Improving the reliability of bulk sediment radiocarbon dating. Quaternary Science Reviews, 242, 106442.

SULTAN, M., STURCHIO, N., AL SEFRY, S., MILEWSKI, A., BECKER, R., NASR, I. & SAGINTAYEV, Z. 2008. Geochemical, isotopic, and remote sensing constraints on the origin and evolution of the Rub Al Khali aquifer system, Arabian Peninsula. Journal of hydrology, 356, 70-83.

SULTAN, M., STURCHIO, N. C., ALSEFRY, S., EMIL, M. K., AHMED, M., ABDELMOHSEN, K., ABUABDULLAH, M. M., YAN, E., SAVE, H. & ALHARBI, T. 2019. Assessment of age, origin, and sustainability of fossil aquifers: A geochemical and remote sensing-based approach. Journal of Hydrology, 576, 325-341.

SURESH, N., BAGATI, T. N., KUMAR, R. & THAKUR, V. C. 2007. Evolution of Quaternary alluvial fans and terraces in the intramontane Pinjaur Dun, Sub-Himalaya, NW India: interaction between tectonics and climate change. Sedimentology, 54, 809-833.

TELFER, M. & THOMAS, D. 2007. Late Quaternary linear dune accumulation and chronostratigraphy of the southwestern Kalahari: implications for aeolian palaeoclimatic reconstructions and predictions of future dynamics. Quaternary Science Reviews, 26, 2617-2630.

TERRIZZANO, C. M., MORABITO, E. G., CHRISTL, M., LIKERMAN, J., TOBAL, J., YAMIN, M. & ZECH, R. 2017. Climatic and Tectonic forcing on alluvial fans in the Southern Central Andes. Quaternary science reviews, 172, 131-141.

TERRY, J., AL RUHEILI, A., BOLDI, R., GIENKO, G. & STAHL, H. 2022. Cyclone Shaheen: the exceptional tropical cyclone of October 2021 in the Gulf of Oman. Weather, 77, 364-370.

THALMEIER, M. B., KRÖHLING, D. M. & BRUNETTO, E. 2021. The geomorphology and Late Quaternary sedimentary record of the Salado/Juramento fluvial megafan, Central Andes foreland basin (Chaco Plain, Argentina). Geomorphology, 373, 107495.

THAMÓ-BOZSÓ, E., MURRAY, A. S., NÁDOR, A., MAGYARI, Á. & BABINSZKI, E. 2007. Investigation of river network evolution using luminescence dating and heavy mineral analysis of Late-Quaternary fluvial sands from the Great Hungarian Plain. Quaternary Geochronology, 2, 168-173.

THESIGER, W. 1950a. Desert borderlands of Oman. The Geographical Journal, 116, 137-168.

THESIGER, W. P. 1950b. The badu of southern Arabia. Journal of the Royal Central Asian Society, 37, 53-61.

THOMAS, D. S. & BAILEY, R. M. 2019. Analysis of late Quaternary dunefield development in Asia using the accumulation intensity model. Aeolian Research, 39, 33-46.

THOMAS, D. S. & BURROUGH, S. L. 2012. Interpreting geoproxies of late Quaternary climate change in African drylands: Implications for understanding environmental change and early human behaviour. Quaternary International, 253, 5-17.

THOMAS, D. S. G. 2013. Reconstructing paleoenvironments and palaeoclimates in drylands: what can landform analysis contribute? Earth Surface Processes and Landforms, 38, 3-16.

THOMAS, D. S. G. & BURROUGH, S. L. 2016. Luminescence-based dune chronologies in southern Africa: Analysis and interpretation of dune database records across the subcontinent. Quaternary International, 410, 30-45.

THOMSEN, K. J., MURRAY, A. S., JAIN, M. & BØTTER-JENSEN, L. 2008. Laboratory fading rates of various luminescence signals from feldspar-rich sediment extracts. Radiation Measurements, 43, 1474-1486.

TIERNEY, J. E., DEMENOCAL, P. B. & ZANDER, P. D. 2017. A climatic context for the out-of-Africa migration. Geology, 45, 1023-1026.

TIMAR-GABOR, A., BUYLAERT, J.-P., GURALNIK, B., TRANDAFIR-ANTOHI, O., CONSTANTIN, D., ANECHITEI-DEACU, V., JAIN, M., MURRAY, A. S., PORAT, N. & HAO, Q. 2017. On the importance of grain size in luminescence dating using quartz. Radiation Measurements, 106, 464-471.

TOMCZYK, A. M. 2021. Morphometry and morphology of fan-shaped landforms in the high-Arctic settings of central Spitsbergen, Svalbard. Geomorphology, 392, 107899.

TSUKAMOTO, S., DULLER, G., WINTLE, A. & FRECHEN, M. 2010. Optical dating of a Japanese marker tephra using plagioclase. Quaternary Geochronology, 5, 274-278.

TSVIELI, Y. & ZANGVIL, A. 2005. Synoptic climatological analysis of 'wet'and 'dry'Red Sea troughs over Israel. International Journal of Climatology: A Journal of the Royal Meteorological Society, 25, 1997-2015.

URBAN, B. & BUERKERT, A. 2009. Palaeoecological analysis of a Late Quaternary sediment profile in northern Oman. Journal of arid environments, 73, 296-305.

VAKS, A., BAR-MATTHEWS, M., AYALON, A., MATTHEWS, A., FRUMKIN, A., DAYAN, U., HALICZ, L., ALMOGI-LABIN, A. & SCHILMAN, B. 2006. Paleoclimate and location of the border between Mediterranean climate region and the Saharo–Arabian Desert as revealed by speleothems from the northern Negev Desert, Israel. Earth and Planetary Science Letters, 249, 384-399.

VALKANOU, K., KARYMBALIS, E., PAPANASTASSIOU, D., GAKI-PAPANASTASSIOU, K. & GILES, P. 2013. Analysis of relationships among coastal alluvial fans and their contributing catchments in North Evoikos Gulf (Central Greece). Bulletin of the Geological Society of Greece, 47, 344-355.

VAN RAMPELBERGH, M., FLEITMANN, D., VERHEYDEN, S., CHENG, H., EDWARDS, L., DE GEEST, P., DE VLEESCHOUWER, D., BURNS, S. J., MATTER, A. & CLAEYS, P. 2013. Mid-to late Holocene Indian Ocean Monsoon variability recorded in four speleothems from Socotra Island, Yemen. Quaternary Science Reviews, 65, 129-142.

VENTRA, D. & CLARKE, L. E. 2018. Geology and geomorphology of alluvial and fluvial fans: current progress and research perspectives. Geological Society, London, Special Publications, 440, 1-21.

VERHEYDEN, S., NADER, F. H., CHENG, H. J., EDWARDS, L. R. & SWENNEN, R. 2008. Paleoclimate reconstruction in the Levant region from the geochemistry of a Holocene stalagmite from the Jeita cave, Lebanon. Quaternary Research, 70, 368-381.

VILES, H. A. & GOUDIE, A. S. 1990. Tufas, travertines and allied carbonate deposits. Progress in Physical Geography: Earth and Environment, 14, 19-41.

VISERAS, C., CALVACHE, M. A. L., SORIA, J. M. & FERNÁNDEZ, J. 2003. Differential features of alluvial fans controlled by tectonic or eustatic accommodation space. Examples from the Betic Cordillera, Spain. Geomorphology, 50, 181-202.

WALK, J., BARTZ, M., STAUCH, G., BINNIE, A., BRÜCKNER, H. & LEHMKUHL, F. 2022. Weathering under coastal hyperaridity–Late Quaternary development of spectral, textural, and gravelometric alluvial fan surface characteristics. Quaternary Science Reviews, 277, 107339.

WALLINGA, J. 2002. Optically stimulated luminescence dating of fluvial deposits: a review. Boreas, 31, 303-322.

WALLINGA, J. & CUNNINGHAM, A. C. 2015. Luminescence dating, uncertainties and age range. Encyclopedia of scientific dating methods. Springer Netherlands.

WALLINGA, J., MURRAY, A. S., DULLER, G. A. & TÖRNQVIST, T. 2001. Testing optically stimulated luminescence dating of sand-sized quartz and feldspar from fluvial deposits. Earth and Planetary Science Letters, 193, 617-630.

WALSH, E., CARACCIOLO, L., RAVIDÀ, D., BURROUGH, S. & THOMAS, D. 2022a. Holocene fluvial depositional regimes of the Huab River, Skeleton Coast, Namibia. Earth Surface Processes and Landforms, 47, 1820-1844.

WALSH, E. V., BURROUGH, S. L. & THOMAS, D. S. 2022b. A chronological database assessing the late Quaternary palaeoenvironmental record from fluvial sediments in southwestern Africa. Earth-Science Reviews, 104288.

WEISSMANN, G., HARTLEY, A., SCUDERI, L., NICHOLS, G., DAVIDSON, S., OWEN, A., ATCHLEY, S., BHATTACHARYYA, P., CHAKRABORTY, T. & GHOSH, P. 2013. Prograding distributive fluvial systems: geomorphic models and ancient examples. New Frontiers in Paleopedology and Terrestrial Paleoclimatology: SEPM, Special Publication, 104, 131-147.

WELDEAB, S., MENKE, V. & SCHMIEDL, G. 2014. The pace of East African monsoon evolution during the Holocene. Geophysical Research Letters, 41, 1724-1732.

WELLBROCK, K., VOSS, P. & GROTTKER, M. 2011. Reconstruction of mid-Holocene climate conditions for north-western Arabian oasis Tayma. International Journal of Water Resources and Arid Environments, 1, 200-09.

WELLS, S. G. & HARVEY, A. M. 1987. Sedimentologic and geomorphic variations in storm-generated alluvial fans, Howgill Fells, northwest England. Geological Society of America Bulletin, 98, 182-198.

WEYHENMEYER, C. E. 2000. Cool Glacial Temperatures and Changes in Moisture Source Recorded in Oman Groundwaters. Science, 287, 842-845.

WHIPPLE, K. X. & TRAYLER, C. R. 1996. Tectonic control of fan size: the importance of spatially variable subsidence rates. Basin Research, 8, 351-366.

WHITNEY, J. W., FAULKENDER, D. & RUBIN, M. 1983. The environmental history and present condition of Saudi Arabia's northern sand seas, US Department of the Interior, Geological Survey.

WILBY, R. & YU, D. 2013. Rainfall and temperature estimation for a data sparse region. Hydrology and Earth System Sciences, 17, 3937-3955.

WILKINSON, T. J. 2005. Soil erosion and valley fills in the Yemen highlands and southern Turkey: Integrating settlement, geoarchaeology, and climate change. Geoarchaeology: An International Journal, 20, 169-192.

WINSEMANN, J., HARTMANN, T., LANG, J., FÄLBER, R. & LAUER, T. 2022. Depositional architecture and aggradation rates of sand-rich, supercritical alluvial fans: Control by autogenic processes or high-frequency climatic oscillations? Sedimentary Geology, 440, 106238.

WINTLE, A. G. 1973. Anomalous Fading of Thermo-luminescence in Mineral Samples. Nature, 245, 143-144.

WINTLE, A. G. 1997. Luminescence dating: laboratory procedures and protocols. Radiation measurements, 27, 769-817.

WINTLE, A. G. 2008. Luminescence dating: where it has been and where it is going. Boreas, 37, 471-482.

WINTLE, A. G. & MURRAY, A. S. 2006. A review of quartz optically stimulated luminescence characteristics and their relevance in single-aliquot regeneration dating protocols. Radiation measurements, 41, 369-391.

WOOD, R. 2015. From revolution to convention: the past, present and future of radiocarbon dating. Journal of Archaeological Science, 56, 61-72.

WOOD, W. W., BAILEY, R. M., HAMPTON, B. A., KRAEMER, T. F., LU, Z., CLARK, D. W., JAMES, R. H. & AL RAMADAN, K. 2012. Rapid late Pleistocene/Holocene uplift and coastal evolution of the southern Arabian (Persian) Gulf. Quaternary Research, 77, 215-220.

WOOD, W. W., RIZK, Z. S. & ALSHARHAN, A. S. 2003. Timing of recharge, and the origin, evolution and distribution of solutes in a hyperarid aquifer system. Developments in water science. Elsevier.

WOODS, W. W. & IMES, J. L. 1995. How wet is wet? Precipitation constraints on late Quaternary climate in the southern Arabian Peninsula. Journal of Hydrology, 164, 263-268.

WOOR, S., BUCKLAND, C., PARTON, A. & THOMAS, D. S. 2022a. Assessing the robustness of geochronological records from the Arabian Peninsula: A new synthesis of the last 20 ka. Global and Planetary Change, 103748.

WOOR, S., DURCAN, J. A., BURROUGH, S. L., PARTON, A. & THOMAS, D. S. 2022b. Evaluating the effectiveness of heavy liquid density separation in isolating K-feldspar grains using alluvial sediments from the Hajar Mountains, Oman. Quaternary Geochronology, 72, 101368.

WOOR, S., THOMAS, D. S., PARTON, A. & LEENMAN, A. 2023. Morphology and controls of the mountain front fan systems of the Hajar Mountains, south-east Arabia. Earth-Science Reviews, 104316.

YUAN, Y., KUSKY, T. M. & RAJENDRAN, S. 2016. Tertiary and Quaternary marine terraces and planation surfaces of Northern Oman: interaction of flexural bulge migration associated with the Arabian-Eurasian collision and eustatic sea level changes. Journal of Earth Science, 27, 955-970.

ZANDER, A., DEGERING, D., PREUSSER, F., KASPER, H. U. & BRÜCKNER, H. 2007. Optically stimulated luminescence dating of sublittoral and intertidal sediments from Dubai, UAE: Radioactive disequilibria in the uranium decay series. Quaternary Geochronology, 2, 123-128.

ZARINS, J., IBRAHIM, M., POTTS, D. & EDENS, C. 1979. Saudi Arabian Archaeological Reconnaissance 1978. The Preliminary Report on the Third Phase of the Comprehensive Archaeological Survey Program. The Central Province. Atlal. The Journal of Saudi Arabian Archaeology Riyadk, 9-42.

ZEBARI, M., GRÜTZNER, C., NAVABPOUR, P. & USTASZEWSKI, K. 2019. Relative timing of uplift along the Zagros Mountain Front Flexure (Kurdistan Region of Iraq): Constrained by geomorphic indices and landscape evolution modeling. Solid Earth, 10, 663-682.

ZERBONI, A., PEREGO, A., MARIANI, G. S., BRANDOLINI, F., AL KINDI, M., REGATTIERI, E., ZANCHETTA, G., BORGI, F., CHARPENTIER, V. & CREMASCHI, M. 2020. Geomorphology of the Jebel

Qara and coastal plain of Salalah (Dhofar, southern Sultanate of Oman). Journal of Maps, 16, 187-198.

ZHANG, J. & LI, S.-H. 2019. Constructions of standardised growth curves (SGCs) for IRSL signals from K-feldspar, plagioclase and polymineral fractions. Quaternary Geochronology, 49, 8-15.

ZHAO, Z., GRANGER, D. E., CHEN, Y., SHU, Q., LIU, G., ZHANG, M., HU, X., WU, Q., HU, E. & LI, Y. 2017. Cosmogenic nuclide burial dating of an alluvial conglomerate sequence: An example from the Hexi Corridor, NE Tibetan Plateau. Quaternary Geochronology, 39, 68-78.

ZIEGLER, M., LOURENS, L. J., TUENTER, E., HILGEN, F., REICHART, G.-J. & WEBER, N. 2010. Precession phasing offset between Indian summer monsoon and Arabian Sea productivity linked to changes in Atlantic overturning circulation. Paleoceanography, 25, n/a-n/a.

ZIMMERMAN, D. W. 1971. Thermoluminescent dating using fine grains from pottery. Archaeometry, 13, 29-52.

ZONDERVAN, J. R., STOKES, M., BOULTON, S. J., TELFER, M. W. & MATHER, A. E. 2020. Rock strength and structural controls on fluvial erodibility: Implications for drainage divide mobility in a collisional mountain belt. Earth and Planetary Science Letters, 538, 116221.

ZÖTL, J. G. & JADO, A.-R. 1984. Sedimentological, hydrogeological, hydrochemical, geomorphological, geochronological and climatological investigations in western Saudi Arabia, Springer-Verlag.

ZWEMER, S. 1907. Oman and Eastern Arabia. Bulletin of the American Geographical Society, 39, 597-606.

9 | Appendix A: Evaluating the effectiveness of heavy liquid density separation in isolating K-feldspar grains using alluvial sediments from the Hajar Mountains, Oman (Paper 4)

Authorship: Sam Woor, Julie Durcan, Sallie Burrough, David Thomas, Ash Parton

This appendix is based on a research paper of the same name, published in the journal Quaternary Geochronology, August 2022.

9.1 Paper abstract

Heavy liquid density separation is commonly utilised in isolating specific minerals from bulk sediment for luminescence dating. K-feldspars are commonly separated from other minerals by isolating the <2.58 g cm^{-3} fraction which yields infrared stimulated luminescence (IRSL) signals conducive to dating. However, initial measurements of the IRSL and thermoluminescence (TL) signals from the <2.58 g cm^{-3} fraction of alluvial fan sediments from the Hajar Mountains, northern Oman, were atypical of K-feldspar luminescence signals reported in the literature. In this study, three different density separates (<2.58 g cm^{-3}, 2.58-2.54 g cm^{-3} and <2.565 g cm^{-3}) were trialled to attempt to isolate pure K-feldspar samples for dating, to measure K-feldspar IRSL signals which are not contaminated with inputs from other feldspar, quartz and/or heavy mineral signals. The mineralogy of these separates was explored using microscopy, X-ray diffraction and mass spectrometry. We found that despite more refined heavy liquid density separation, the proportions of K-feldspar in these separates had a maximum of 40% by weight, remaining significantly contaminated by other minerals. IRSL and TL signals were atypical of K-feldspar for all density separates and it is likely that there is a contribution of signal from IR-sensitive contaminants, such as muscovite. This highlights the importance of investigating the mineralogy of samples for luminescence dating, especially in regions where little prior work has been undertaken.

9.2 Introduction

Despite the problem of anomalous fading (e.g. Wintle, 1973), comparisons of quartz optically stimulated luminescence (OSL) signals with data from other independent geochronological techniques (e.g. Reimann and Tsukamoto, 2012) has shown that accurate ages can be derived from K-feldspar infrared stimulated luminescence (IRSL) signals. This is thanks to advances in measurement protocols over the last 15 years, focused principally on the post-infrared IRSL (pIRIR) signal (e.g. Thomsen et al., 2008). There are numerous advantages to dating K-feldspar over quartz in mountainous and alluvial contexts because deriving quartz equivalent doses (D_es) using OSL signals in these environments can be challenging. For example, the proximity of quartz grains to nearby source bedrock means they commonly display low luminescence sensitivity, resulting in OSL signals which are low in sensitivity (Murray et al., 2021). They may also be low-yielding, with very few grains emitting detectable signals upon stimulation (e.g. Arnold et al., 2016). K-feldspar also typically has a higher saturation point than quartz (e.g. Li and Li, 2012), offering the opportunity to date older sediments.

To isolate specific minerals for dating, a common method applied across laboratories is heavy liquid density separation. Heavy liquids such as sodium polytungstate (SPT), sodium metatungstate and tetrabromoethane can be diluted to the density of specific minerals using water to produce a matrix in which the desired mineral will either sink or float and can be easily separated by pouring. Other methods, such as magnetic separation, provide alternatives to density separation (e.g. Porat, 2006), however the expensive equipment makes their use less commonplace. For the majority of luminescence dating applications, sediments which have been sieved to a specific grain-size following treatment with a concentrated acid (e.g. HCl) to remove carbonates and H_2O_2 to remove organics are separated into the following fractions (Wintle, 1997): >2.70 g cm^{-3} (heavy minerals), 2.70-2.62 g cm^{-3} (quartz), 2.62-2.58 g cm^{-3} (Ca/Na-feldspar), <2.58 g cm^{-3} (K-feldspar).

Feldspars are highly heterogeneous in both composition and luminescence characteristics (Smedley and Pearce, 2016). It is important to separate K-feldspar from Ca/Na- dominated feldspar minerals (plagioclase) as there is a positive correlation between Ca content and anomalous fading (Huntley and Lian, 2006). The luminescence efficiency of Ca-feldspar has also been shown to be low in comparison to K-feldspar (Spooner, 1992). Whilst reliable D_es have been produced using the plagioclase fraction in comparison to K-feldspar IRSL and quartz OSL measurements (e.g. Barre and Lamothe, 2010; Tsukamoto et al., 2010; Zhang and Li, 2019), K-feldspars are preferable in most sedimentary contexts (Wintle, 2008), and the pIRIR protocol was developed and tested using K-feldspar signals (Thomsen et al., 2008).

Whilst contamination of quartz OSL signals can be monitored during a single aliquot regenerative dose (SAR) protocol, using signal checks such as the OSL IR depletion ratio (Duller, 2003), it is less common that the mineralogical purity of density separated K-feldspar is assessed. However, in some source regions, the <2.58 g cm^{-3} separate has been shown to contain variable amounts of K-feldspars. For example, O'Gorman et al. (2021) use X-ray diffraction (XRD) spectroscopy to show that fluvial and colluvial sediments from Liang Bua, Indonesia, remained heavily contaminated by quartz and plagioclase feldspars, despite density separation at <2.58 g cm^{-3}.

The potassium content of K-feldspars has also been shown to be variable in sediments, relative to the 14% which would be expected from a pure sample (Huntley and Baril, 1997). Smedley et al. (2012) found that for single K-feldspar grains which gave detectable IRSL signals, potassium content ranged from 6-13% and suggest that K-feldspars separated at <2.58 g cm^{-3} can be assumed to have an average K-content of 10±2%. Some studies have suggested that the grains with the highest K-contents which yield the brightest IRSL signals lie within more specific density ranges, such as 2.58-2.54 g cm^{-3} (e.g. Wintle, 1997). Even more refined density separation has also been suggested. For instance, following an etch using 10% HF for 10 minutes on the <2.565 g cm^{-3} fraction (or "Super-K"), Rhodes (2015) found that IRSL signal brightness increased by an order of magnitude for samples

in a variety of depositional settings relative to the <2.58 g cm^{-3} fraction due to the greater concentration of KF grains, as well as the removal of their outer surfaces.

Initial measurements on the <2.58 g cm^{-3} density separates of alluvial sediments from the Hajar Mountains, northern Oman, yielded dim IRSL signals and thermoluminescence (TL) signals atypical of K-feldspar, as well as failed to recover a test dose in the dose recovery tests conducted. In this study, we investigate the purity and K-content of <2.58 g cm^{-3} density separates from these samples, and evaluate density separation approaches suggested in the literature to better separate K-feldspar mineral grains from the mixed-mineral bulk sediment.

9.3 Methods

9.3.1 Field location and sample collection

Alluvial fan systems extend both eastwards and westwards from the Hajar Mountains of northeast Oman and the UAE. Fan sediments have been dated using luminescence methods with the majority of studies focused on material from the western fans. These ages have been used to infer that mountain catchment hydrology is sensitive to precessionally-paced transgressions of Indian Ocean monsoon rainfall into south-east Arabia over Late Quaternary timescales (Blechschmidt et al., 2009; Parton et al., 2013; Parton et al., 2015a). By contrast, little attention has been paid to eastern fan sediments which transmit sediment to the coastal plain, their suitability for luminescence dating or utility as palaeohydrological archives.

The ultra-mafic Semail ophiolite which comprises much of the central Hajar Mountains is not generally conducive to producing silicious minerals such as quartz. Despite this, Hoffmann et al. (2015) were able to extract enough quartz from samples to produce the first OSL ages of alluvial sediments east of the mountains. They note the low abundance of feldspars in their samples; however, their ages were well within the saturation limits of quartz and demonstrated sufficiently bright OSL signals. Some western fan sediments have been shown to be much older than the typical

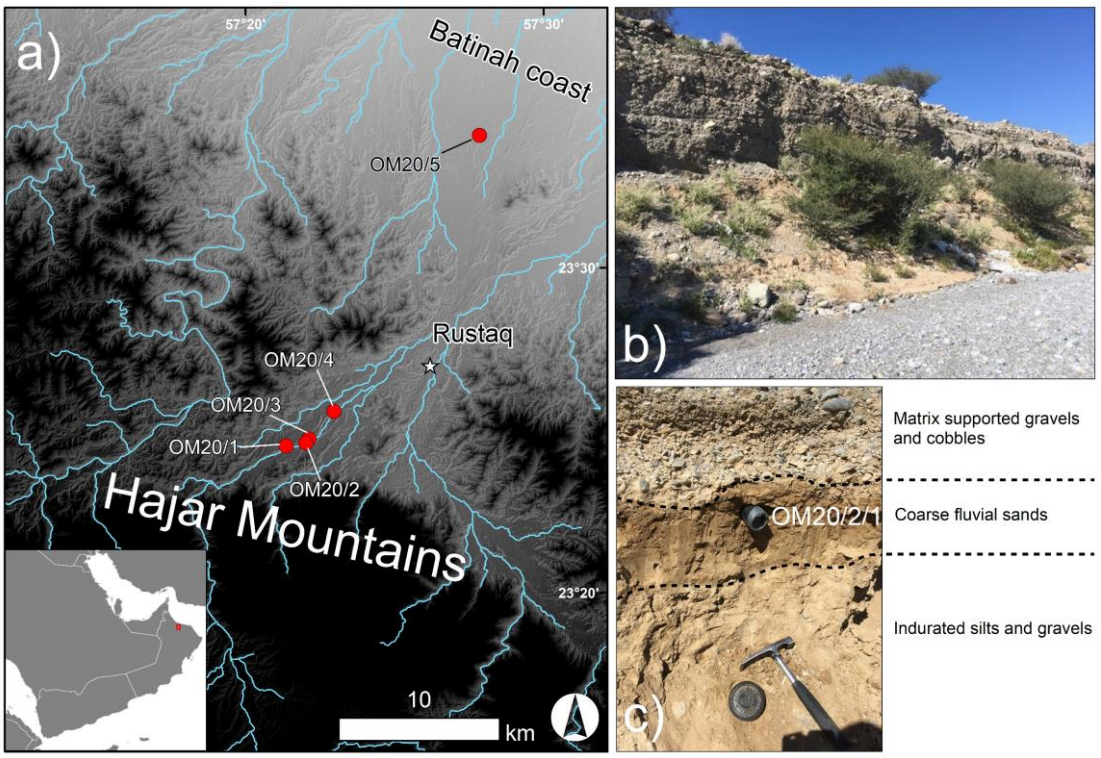

Figure 9.1. (a) The location of sample sites along an incised channel system near Rustaq, northern Oman. Shading shows relief in meters above sea level (darker = higher) and blue lines denote major drainage pathways. **(b)** Sediments exposed through incision at site OM20/2 (image taken from the contemporary channel bed). **(c)** Sample OM20/2/1 and a description of the sedimentary facies.

saturation point of quartz but low environmental dose rates facilitate older OSL age determinations (e.g. Blechschmidt et al., 2009). For the samples analysed by Hoffmann et al. (2015), dose rates from an eastern setting seem to be higher than those in the west, limiting the age range of quartz OSL. pIRIR ages from K-feldspars therefore offer a potentially viable chronometer that would enable comparable records of palaeohydrological change.

All samples were collected from sediments exposed by an incising channel at the apex of an alluvial fan near Rustaq, north-eastern Oman (Fig.9.1a). These sediments are characterised by their carbonate-dominated matrix, comprising medium-coarse grained sand from lenses interbedded with gravels, cobbles and boulders (Fig.9.1b, c). The close proximity of sample sites to source bedrock and their transportation by turbid streamflow and sheet-wash means they are likely to display variability in bleaching and luminescence sensitivity, as is common for both gravity- and

fluvial-driven fans (Rittenour, 2008). Samples were taken using both black plastic tubes hammered into cleaned stratigraphic sections as well as block samples chiselled out of exposures where sediments were highly cemented.

9.3.2 Sample preparation and density separation

The light exposed ends of tubes and outsides of block samples were prepared for analysis to maximise the volume of remaining sediments for actual age determinations. Samples were treated with HCl and H_2O_2 to remove carbonates and organic material respectively. They were then wet-sieved to 63-210 µm, this wide size range encompassing the grain sizes typically utilised for coarse-grained luminescence measurements. Density separation was carried out using SPT diluted to standard densities in order to isolate heavy mineral (>2.70 g cm^{-3}) and quartz mineral grains (2.70-2.62 g cm^{-3}). Density separation was carried out twice using small sample masses to ensure thorough separation and using newly mixed SPT. Three densities were chosen to test the mineralogical and IRSL characteristics of 'K-feldspars' in the samples and attempt to concentrate them in higher purities and increase signal brightness. The <2.58 g cm^{-3} fraction represents the standard K-feldspar isolation. However, samples were also separated at <2.565 g cm^{-3} after Rhodes (2015) reported that in some alluvial contexts, this density separation was able to isolate the most potassic K-feldspar (or 'Super-K'). Wintle (1997) also suggests that the most potassic K-feldspars yielding the brightest IRSL signals lie in the 2.58-2.54 g cm^{-3} range, so this range was isolated for comparison.

9.3.3 Mineralogy assessment

As an initial examination of the mineralogy of sediments, thin sections were prepared for the <2.58 g cm^{-3} separate of OM20/1/1 and OM20/3/3 to attempt to identify the results of standard K-feldspar density separation (Table 9.1). Thin section microscopy was constrained to these samples and separates due to limited amounts of available sample.

Table 9.1. Sediment samples in this study and the analytical methods used to assess the mineralogy of density separated fractions, including scanning electron microscopy (SEM), inductively-coupled plasma mass spectrometry (ICP-MS) and X-ray diffraction (XRD). A variety of IR luminescence signals were also measured, as well as TL up to 450°C.

Sample	Location		Density separate (g cm^{-3})	Thin section	SEM	ICP-MS	XRD	IR 50	pIRIR 150	pIRIR 225	TL 450
	Latitude (°N)	Longitude (°E)									
OM20/1/1	23.40	57.36	<2.58	X	X	X	X	X	X	X	X
			<2.565			X	X				
			2.58-2.54				X	X	X	X	X
OM20/3/3	23.41	57.37	<2.58	X	X	X		X	X	X	X
			<2.565			X		X	X	X	X
			2.58-2.54					X	X	X	X
OM20/4/1	23.43	57.38	<2.58			X	X	X	X	X	X
			<2.565			X	X	X	X	X	X
			2.58-2.54				X	X	X	X	X
OM20/4/5	23.43	57.38	<2.58			X	X	X	X	X	X
			<2.565			X	X	X	X	X	X
			2.58-2.54				X	X	X	X	X

A scanning electron microscope (SEM) was also used for a visual examination of mineralogy, based on characteristic features of mineral cleavage and morphology. The <2.58 g cm^{-3} separates of sample OM20/1/1 and OM20/3/3 were mounted on carbon stubs, gold coated and then imaged using a bench-top SEM to provide high-resolution images of individual grains (Table 9.1).

XRD provides a method for identifying contaminants in density separates for luminescence dating (e.g. Krbetschek et al., 1997; Prasad, 2000; O'Gorman et al., 2021). K-feldspar polymorphs, principally sanidine, orthoclase and microcline ($KAlSi_3O_8$), would be expected to be present in significant quantities for greater confidence in the origin of IRSL signals. All density separates from three samples were powdered and analysed (Table 9.1).

Inductively coupled plasma mass spectrometry (ICP-MS) was carried out to characterise the geochemistry of different density separates based on the three primary elements of both K-feldspar and Ca/Na-feldspar (Table 9.1). Both the <2.58 and <2.565 g cm^{-3} separates were analysed, with the expectation that the <2.565 g cm^{-3} should yield an increased K content relative to Na and Ca, due to

the isolation of 'Super-K' grains (Rhodes, 2015). Due to constraints on sample availability, the 2.58-2.54 g cm^{-3} fraction was not analysed.

9.3.4 Luminescence measurements

Very small (<50 grains) aliquots of sample were mounted on aluminium discs for each K-feldspar density separate. 6 aliquots of each density separate were measured per sample. IRSL and TL measurements were made using a Riso TL/OSL reader with a calibrated $^{90}Sr/^{90}Y$ beta source. IR-emitting diodes emitting at 870 nm were used to stimulate aliquots, with a combination of Schott BG39/Corning 7-59 filters to detect blue-violet signals.

Samples were measured using the pIRIR protocol (e.g Thomsen et al., 2008). As samples were potentially light-exposed, an initial SAR cycle was applied to remove the natural signal. Following this, a 20 Gy laboratory dose was administered and a SAR cycle was used to measure signal brightness. A pre-heat temperature of 250°C for 60 s was applied, followed by IRSL stimulation at 50, 150 and 225°C for 100 s. TL signals were also measured. Aliquots were given a 20 Gy laboratory dose and TL up to 450°C (heating rate of 5.00°C/s). This serves as another semi-quantitative assessment of mineralogical purity, because pure K-feldspar have been reported to yield TL peaks at specific temperatures, namely 150°C, 280°C and 330°C (Mejdahl, 1988; Wintle, 1997).

9.4 Results

9.4.1 Mineralogy

No grains typical of K-feldspar were identified under plain and cross-polarized light from a thin section of the <2.58 g cm^{-3} separate of OM20/1/1. Quartz and rock fragments with quartz inclusions were abundant and this was corroborated by SEM imagery of the <2.58 g cm^{-3} separates of OM20/1/1 and OM20/3/3 (Fig.9.2a). SEM imagery also revealed other mineral contaminants in samples (Fig.9.2b) and grains showing chemical pitting (Fig.9.2c), potentially the result of

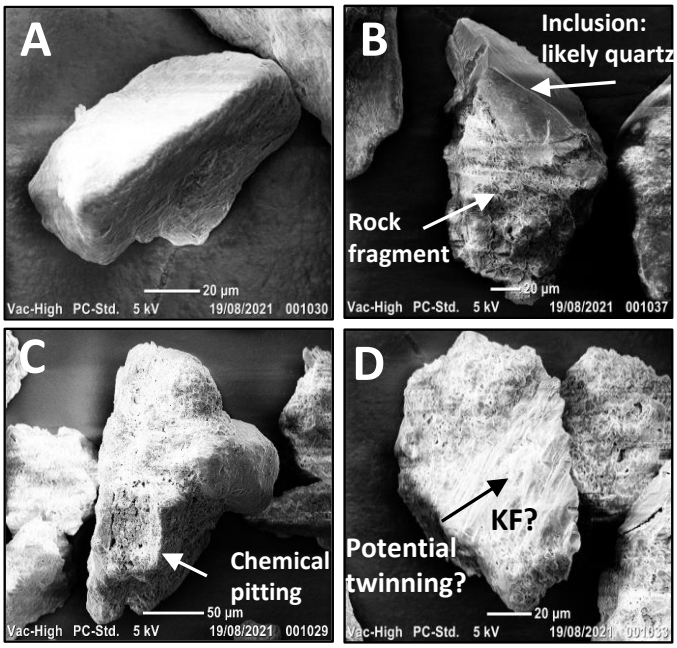

Figure 9.2. Bench-top SEM images of grains from the <2.58 g cm^{-3} separates of samples OM20/1/1 and OM20/3/3 showing the heterogeneity of grains. **(a)** A heavy mineral grain. **(b)** An example of a rock fragment with a quartz inclusion. **(c)** Unrecognisable grains with evidence of chemical attack on their surfaces, potentially from HCl. **(d)** A potential KF grain displaying twinning typical of feldspar morphology.

preparation with concentrated acid. Occasionally, grains with the twinning (i.e. striped appearance) typical of feldspars (Fig.9.2d) were observed, but these were few in number relative to the total number of grains.

XRD also detected low abundances of K-feldspars in the three samples analysed (Table 9.2), with no significant increase in purity between the refined, non-standard density separations (2.58-2.54 and <2.565 g cm^{-3}) relative to the standard <2.58 g cm^{-3} separate for most samples. OM20/4/1 displayed the highest percentages of K-feldspar by weight, increasing with subsequent density separation from 24% (<2.58 g cm^{-3}) to 27 and 40% at 2.58-2.54 and <2.565 g cm^{-3}, respectively. Across all three samples, the <2.565 g cm^{-3} separate yields the higher percentages of K-feldspar relative to <2.58 g cm^{-3}, although for samples OM20/1/1 and OM20/4/5 this is only 6 and 9%, respectively.

Table 9.2. Results of XRD and ICP-MS analysis showing the mineralogical and chemical composition of sample density separates by percentage weight.

	XRD									ICP-MS		
Sample	**Density separate (g cm^{-3})**	**K-feldspar**	**Na/Ca-Fe;dspar**	**Quartz**	**Lizardite**	**Calcite**	**Muscovite**	**Illite/smectite**	**Chlorite**	**K (%)**	**Ca (%)**	**Na (%)**
OM20/1/1	<2.58	4	5	43	-	-	43	-	5	2.1	0.2	1.3
	2.58-2.54	5	6	49	1	-	34	-	5	-	-	-
	<2.565	6	3	30	1	-	50	6	4	1.8	0.1	0.9
OM20/3/3	<2.58	-	-	-	-	-	-	-	-	1.4	0.2	1.1
	2.58-2.54	-	-	-	-	-	-	-	-	-	-	-
	<2.565	-	-	-	-	-	-	-	-	2.3	0.1	0.7
OM20/4/1	<2.58	24	31	34	4	1	5	-	-	2.4	0.1	0.8
	2.58-2.54	27	18	47	2	-	6	-	-	-	-	-
	<2.565	40	22	19	7	1	10	-	-	9.2	0.1	1.6
OM20/4/5	<2.58	5	9	23	12	-	41	6	4	5.2	0.2	1.6
	2.58-2.54	12	12	46	3	-	21	-	5	-	-	-
	<2.565	9	26	25	12	-	19	5	4	1.3	0.2	0.9

Quartz is a significant contaminant, comprising 19-49% of the density separated samples (Table 9.2) even after the density separation at 2.62 g cm^{-3} which should remove it. There does not seem to be a systematic decrease with separation beyond the standard <2.58 g cm^{-3}. For example, <2.565 g cm^{-3} separation reduces quartz from 43 to 30% in sample OM20/1/1 and from 34 to 19% in sample OM20/4/1 (relative to the <2.58 g cm^{-3} separate), but <2.565 g cm^{-3} separation shows an increased quartz percentage for sample OM20/4/5. Quartz abundances are consistently highest in the 2.58-2.54 g cm^{-3} fraction.

Other contaminants include Na/Ca-feldspar which is significantly higher in sample OM20/4/1 relative to the other samples (Table 9.2). Further density separation also gives mixed results with respect to reducing the percentage of plagioclase in samples, with sample OM20/4/1 being reduced from 31% at <2.58 g cm^{-3} to 22 and 18% at <2.565 and 2.58-2.54 g cm^{-3}, whereas OM20/4/5 increases from 9 to 26 and 12%, respectively. Muscovite also makes up a significant proportion of samples (up to 50%), with this proportion increasing with further separation in some cases, relative

to <2.58 g cm^{-3} (e.g. the <2.565 g cm^{-3} separates of samples OM20/1/1 and OM20/4/1). Lizardite also comprises small quantities of the separates of samples OM20/1/1 and OM20/4/1, although makes up 12% of the <2.58 and <2.565 g cm^{-3} separates of sample OM20/4/5.

The K-contents of samples ranges from 1.4-5.2% for the <2.58 g cm^{-3} separates and 1.3-9.2% for the <2.565 g cm^{-3} separates (Table 9.2). There is no systematic increase with additional separation at <2.565 g cm^{-3}, relative to <2.58 g cm^{-3} separates, except for sample OM20/4/1 (Table 9.2). Sample OM20/4/1 increases from 5.2 to 9.2%, with Na and Ca abundance remaining comparable at 1.6-1.6 and 0.2-0.2%, respectively.

9.4.2 Luminescence characteristics

Unsurprisingly, the brightness of IR50 and pIRIR225 signals do not systematically increase following density separation at <2.565 and 2.58-2.54 g cm^{-3}, relative to the standard <2.58 g cm^{-3} preparation (Fig.9.3), which would be expected if the relative proportion of K-feldspar increased with refinement of the density range. For example, the increase in the K-feldspar percentage and K-contents resulting from separation at <2.565 g cm^{-3} for sample OM20/4/1 has not had any impact on IR50 signal magnitude, with the brightest signal detected for the <2.58 g cm^{-3} separate (Table 9.2; Fig.9.3). IR50 signal magnitude is in fact lower for all <2.565 g cm^{-3} separates compared to <2.58 g cm^{-3}, however increases are seen for samples OM3/3 and OM20/4/5 at 2.58-2.54 g cm^{-3}.

Inter-aliquot signal brightness is also variable, ranging by an order of magnitude in some cases, such as the IR50 signals for the <2.58 g cm^{-3} separate of sample OM20/1/1 (Fig.9.3). The small aliquot size (<50 grains) and low K-feldspar abundance of the <2.58 g cm^{-3} separate of OM20/1/1 (4%; Table 9.2) means that some aliquots possibly contain no K-feldspar grains at all. The decay time of the IRSL signal in these samples is also slow for all density separates, taking up to 50 s to reduce to near-background levels for some IR50 and pIRIR225 signals (Fig.9.4).

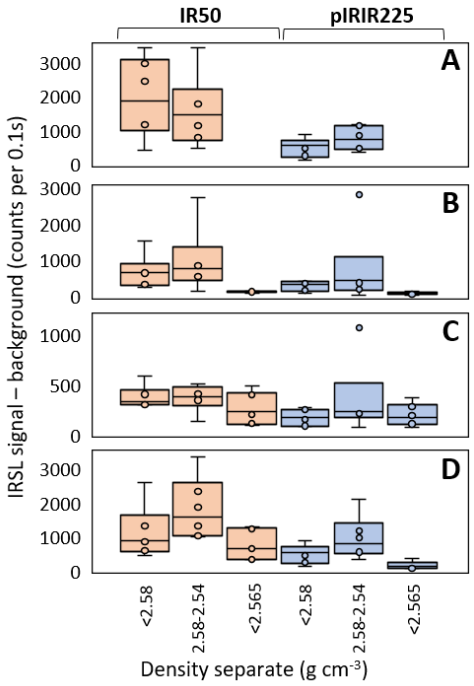

Figure 9.3. IRSL signal magnitude (signal-background) for the small aliquots (<50 grains) measured. Signal was taken as the first 10 s of stimulation and background was averaged over the final 50 s. Orange box plots represent IR50 signals and blue box plots represent pIRIR225 signals with individual aliquots (dots) plotted with mean and interquartile ranges for **(a)** OM20/1/1, **(b)** OM20/3/3, **(c)** OM20/4/1, **(d)** OM20/4/5.

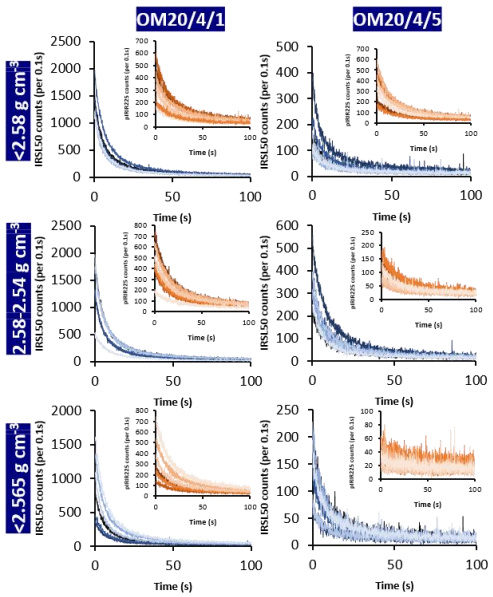

Figure 9.4. IR50/pIRIR225 curves for 6 small aliquots (<50 grains) of samples OM20/4/1 and OM20/4/5, separated at <2.58 g cm^{-3}, 2.58-2.54 g cm^{-3} and <2.565 g cm^{-3}.

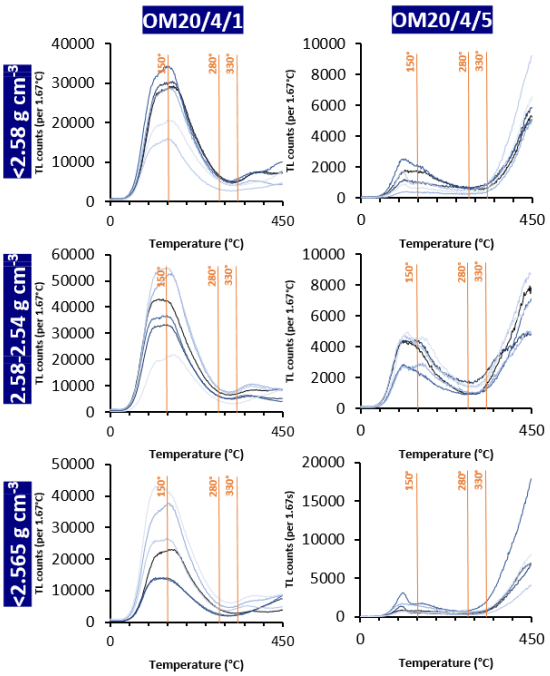

Figure 9.5. TL450 curves for 6 small aliquots (<50 grains) of samples OM20/4/1 and OM20/4/5, separated at <2.58 g cm^{-3}, 2.58-2.54 g cm^{-3} and <2.565 g cm^{-3}. Orange lines at 150, 280 and 330°C denote the typical TL peaks observed from pure K-feldspar (Wintle, 1997).

TL curves similarly show little variation between different density separates for all samples (Fig.9.5). However, they do display variability between samples. Sample OM20/4/1 is characterised by a principle broad peak centred at 150°C and a smaller but similarly broad peak centred at 375°C (Fig.9.5a). By comparison, sample OM20/4/5 also displays a broad peak around 150°C, however TL counts then steadily increase up to 450°C (Fig.9.5b). The magnitude of signals is also variable between aliquots, being an order of magnitude lower for the highest peaks of sample OM20/4/5 relative to OM20/4/1 (Fig.9.5). Crucially, there is little variability in the position of peaks with the refinement of the density separation, and the 150°C, 280°C and 330°C reported characteristic K-feldspar signals (e.g. Wintle, 1997) are not observed.

9.5 Discussion

More refined heavy liquid density separation did not achieve any significant increase in sample purity or luminescence brightness. Whilst the heavy liquid separations tested here have yielded

significant increases in both signal brightness and sample purity for alluvial sediments from other settings (e.g. Rhodes, 2015), IR50 and pIRIR225 signals from aliquots show no difference between density separates. TL curves also remained atypical of K-feldspar, not displaying characteristic large peaks at 280°C and 330°C (Wintle, 1997). XRD analysis confirms that for all samples, contamination by non-K-feldspar grains dominates, regardless of the range of densities considered.

The low abundance of K-feldspars in these samples is the result of the ultra-mafic geology of source catchment bedrock (Chavagnac et al., 2013), which is not generally conducive to the production of silicious minerals. The contaminants identified in samples are also a product of catchment geology. Lizardite results from the serpentinization of olivine in the Semail Ophiolite which comprises much of the central Hajar Mountains and the catchments which drain to the Batinah coastal fans (Boudier et al., 2010). Lizardite has a density of 2.55 g cm^{-3}, hence its presence in all but one of the samples examined (Deer, 2011).

Some contaminants with densities which we would expect to have been removed in density separation also persist, such as muscovite (2.77-2.88 g cm^{-3}) and quartz (2.65 g cm^{-3}; Deer, 2011). Muscovite and other micas are pervasive contaminants in some K-feldspar and quartz separates for luminescence dating, despite their higher density, due to their high surface energy (e.g. Kortekaas and Murray, 2005; Fiebig et al., 2009; Chamberlain et al., 2017; Antohi-Trandafir et al., 2018). It is possible that quartz is a significant contaminant as inclusions in less-dense rock-fragments which were identified in SEM imagery (Fig.2b; e.g. Meyer et al., 2013). In this setting, obtaining a pure (>99%) K-feldspar sample would likely require a more refined technique. Magnetic separation has been shown to effectively remove contaminants from K-feldspar and quartz luminescence samples (e.g. Porat, 2006; Porat et al., 2015). Likewise, statically charged surfaces and detergent solutions have been used to remove micas such as muscovite, with the former technique consisting of spreading grains over paper or plastic beakers causing mica grains to stick while other grains do not (e.g. Thamó-Bozsó et al., 2007; Fiebig et al., 2009; Antohi-Trandafir et al., 2018) and the latter

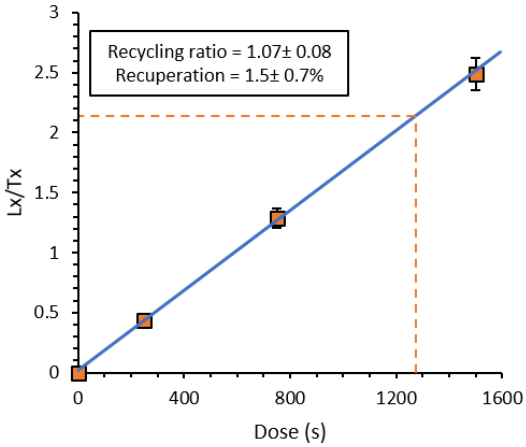

Figure 9.6. A dose response curve built from IRSL measurements on a non-light exposed small aliquot of sample OM20/1/1 using the SAR protocol. Regeneration doses were 0, 16.25, 48.75 and 97.5 Gy. The result was a D_e of 82.41 Gy, passing quality assurance checks for sensitivity changes included within the SAR protocol (recycling and recuperation).

removing them by pouring off the detergent solution (e.g. Kortekaas and Murray, 2005; Chamberlain et al., 2017). Irrespective of the separation technique used, it is important that the mineralogy of samples for luminescence dating is assessed more routinely.

Figure 9.6 shows an IRSL50 dose response curve resulting from applying the pIRIR protocol to a non-light exposed small aliquot (<50 grains) of the <2.58 g cm^{-3} fraction of sample OM20/1/1. This yields a D_e of 82.41 Gy and passes quality assurance checks for sensitivity changes intrinsic within the SAR protocol (recycling and recuperation; Wintle and Murray, 2006). However, this sample failed to recover within ±10% of a known laboratory dose during a dose recovery test, underestimating a given dose of 97.5 Gy by almost 50%. This may be particularly problematic for alluvial fan samples as they commonly display low luminescence sensitivity because of relatively short source-fan transport distances (Mineli et al., 2021), as well as other near-source sediments with similar luminescence characteristics such as glacial deposits (Fuchs and Owen, 2008). Therefore, dim signals from a very small number of K-feldspar grains potentially increases the proportional signal contribution of contaminants. This highlights the need for more thorough mineralogical investigations into sample composition and purity in certain settings, especially where few

luminescence dating studies have been carried out previously, as well as the importance of dose recovery testing to ensure measurement accuracy.

The contribution of these contaminants to IRSL signals prohibits the use of any of the density separates from this study as reliable felspar dosimeters for dating periods of fan aggradation in the eastern Hajar Mountains. Whilst IRSL and pIRIR signals are measured for the density separates from all samples, these are not characteristic of K-feldspar signals, and the XRD data show that K-feldspar is not the dominant component of the separates. This gives the possibility that other IR-responsive minerals are responsible for the luminescence signals observed. For instance, administering a dose to muscovite followed by IR stimulation has been shown to yield a luminescence signal with similar decay characteristics to K-feldspar (Antohi-Trandafir et al., 2018). Similarly, plagioclase contributes an IRSL signal but is more likely to suffer anomalous fading than K-feldspars, rendering them typically unsuitable for dating (Huntley and Lian, 2006; Huot and Lamothe, 2012; Fuchs et al., 2013). The relatively high proportions of these contaminants and relatively low (<50%) proportions of K-feldspar in the samples tested in this study means that the amount of signal originating from K-feldspar remains a significant unknown. In this case, such low K-feldspar percentages in samples made their atypical nature discernible. However, in samples with lower, but still significant, contaminant abundance unusual sample behaviour may be more difficult to identify based on IRSL signals and contamination may go un-noticed.

9.6 Conclusions

None of the three density separates tested in this study were able to isolate pure K-feldspar samples for dating. This limits the utility of K-feldspar as a dosimeter for dating Quaternary alluvial fan aggradation in the eastern Hajar Mountains. Whilst separation at <2.565 g cm^{-3} did increase the K-contents for one sample, no corresponding increase in IR50 or pIRIR225 signal brightness was observed. Contaminants remained pervasive despite narrower heavy liquid density ranges, with quartz, muscovite and plagioclase being the most common. Muscovite and plagioclase are

especially problematic as they are IR-sensitive and as such are likely contributing to the IRSL signals observed, especially in samples which have particularly low proportions of K-feldspar grains. These findings highlight that we must be cautious about the mineralogical content and purity of separates resulting from standard heavy liquid separation procedures. Regardless of the mineral in question, it is important to not simply assume the efficacy of laboratory procedures, but to test the robustness of these assumptions. This is of particular importance when working in environments where little geochronological or mineralogical research has been carried out previously, as well as working with dim samples where proportionally more signal may be contributed by contaminants.

10 | Appendix B: Supplementary material for Chapters 3 and 4 (Paper 1)

10.1. Luminescence dating

10.1.1. OSL measurements and D_e calculation

Single grain tests

To test whether measurement at the single grain scale would be appropriate for the samples in this thesis, a signal yield test was conducted. 200 grains from the 180-210 µm fraction of etched quartz for three samples (OM20/2/1, -3/3 and -4/5) first had their natural signals removed through a pre-heat at 220°C followed by stimulation with a blue laser for 1 s. Discs were then given a 50 Gy laboratory dose and the same measurement was undertaken. Results show that the yield, the overall proportion of grains responsible for 90% of the detected signal, was good at 10-20% (Fig.10.1). However, the resulting signals were dim relative to other studies of single grain quartz, with typically <5% of grains giving >100 OSL counts per 0.01 s (Fig.10.1). Out of 200 grains per sample, this represents only 10 grains before rejection criteria are considered which, based on the results showing in the following sections, could have significantly reduced the number of signals available for D_e calculations. Based on these considerations and many samples being finer grained than 180-210 µm, it was decided that small aliquots would be appropriate for this project.

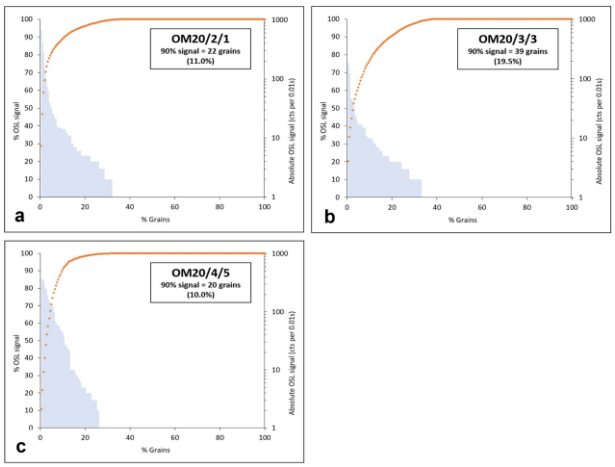

Figure 10.1. The results of single grain yield tests conducted on three samples: **(a)** OM20/2/1, **(b)** OM20/3/3 and **(c)** OM20/4/5. The dotted orange line shows the percentage of single grains contributing to the overall OSL signal. The shaded blue bars show the absolute OSL signal by percentage of individual grains.

Pre-heat plateau and dose recovery tests

Pre-heat plateau and dose recovery tests were conducted on aliquots of five samples. Across the tested samples, a pre-heat of 220°C was shown to consistently recover the administered laboratory dose within 1σ errors of $\pm$10% of unity (Fig.10.2a). Similarly, mean dose recovery ratios from tests conducted on the same samples at 220°C were all within $\pm$10% of unity (Fig.10.2b).

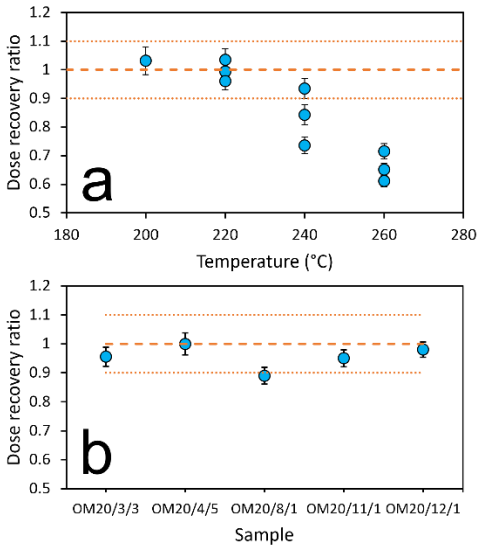

Figure 10.2. (a) Results of a preheat plateau test conducted on aliquots of sample OM20/3/3 using a given dose of 50 Gy. 3 aliquots each were tested at 200, 220, 240 and 260°C. **(b)** Mean dose recovery ratios conducted on up to 9 aliquots each per sample using the selected 220°C preheat for 10 s prior to optical stimulation. Samples OM20/3/3, OM20/4/5, OM20/8/1 and OM20/12/1 were given a known dose of 50 Gy and OM20/11/1 was given 5 Gy. The dashed orange lines represent unity ±10%. Only aliquots passing rejection criteria are shown.

Rejection criteria

Aliquots were rejected if the following criteria were not met: recycling ratio within uncertainties of $\pm$10% of unity and recuperation within uncertainties of $\leq$5% (Wintle and Murray, 2006); OSL-IR depletion ratio of within uncertainties of $\pm$10% of unity (Duller, 2003); T_n >3σ background (Jacobs et al., 2011) and a fast ratio $\geq$20 (Durcan and Duller, 2011). Table 10.1 shows the results of the different rejection criteria applied to measured aliquots for all samples. The most common cause of aliquots to be rejected was the presence of IR-sensitive minerals, although this issue was much

more prevalent for samples from the eastern Hajar rather than on the west of the drainage divide (Woor et al., 2022b). Signals were generally dominated by the fast component, although samples OM20/5/1 and OM20/10/3 showed larger proportions of aliquots being rejected due to a higher proportion of the signal originating from medium and slow components. A large proportion of aliquots from OM20/10/3 also failed the recuperation test due to the transfer of charge between measurements. A pre-heat plateau test was not conducted on this sample and dating results show that it is very young (<1 ka), therefore charge transfer may have occurred in these aliquots from the 220°C pre-heat. Otherwise, aliquots yielded bright, fast-dominated OSL signals.

Table 10.1. Summary of the number of aliquots rejected through the application of rejection criteria and the overall number of aliquots accepted for final D_e calculation for each sample. Note: some aliquots failed multiple criteria, hence the aliquots measured minus the total number of aliquots rejected for a sample does not necessarily equal the number of aliquots accepted.

Sample	n – aliquots rejected through application of rejection criteria					n (accepted/measured)
	IR depletion	Recycling	Recuperation	$T_n>3\sigma$ BG	Fast ratio	
OM20/3/1	47	17	1	0	0	40/96
OM20/3/2	14	8	1	0	0	28/48
OM20/3/3	30	5	2	0	10	33/70
OM20/4/1	34	1	0	0	9	11/48
OM20/4/2	23	10	2	0	5	18/48
OM20/4/4	28	6	4	0	4	61/95
OM20/4/5	22	6	4	0	0	26/52
OM20/5/1	37	30	6	1	28	46/113
OM20/5/2	0	15	3	0	1	29/48
OM20/5/3	15	11	3	0	5	15/40
OM20/6/1	4	6	1	0	10	16/32
OM20/6/3	3	12	7	0	0	20/34
OM20/8/1	5	3	1	0	3	36/48
OM20/8/2	5	12	0	0	0	32/48
OM20/10/3	1	9	19	0	26	13/48
OM20/11/1	3	13	2	0	2	28/48
OM20/11/2	2	8	1	1	2	36/48
OM20/11/3	1	3	0	2	3	41/48
OM20/12/1	0	4	0	0	0	44/48
OM20/12/2	4	0	0	0	0	28/32

Signal saturation

All OSL signals were checked for signal saturation during data processing and fifteen of the twenty samples contained saturated signals in the dose distributions which satisfied rejection criteria,

relative to the saturating exponential dose response curve fitted to regeneration points (Table 10.2). These D_es are separated into two groups. First, some aliquots yielded L_n/T_n values which did not intercept the dose response curve and so did not give numeric D_es, and therefore, they are omitted from De calculation. Second, some aliquots yielded L_n/T_n which did intercept the DRC but yielded D_e values in excess of double the characteristic dose ($2D_0$). $2D_0$ is a parameter which describes the point at which the dose response curve begins to curve towards an asymptote approaching saturation, which is approximately 85% of the maximum luminescence intensity). D_es interpolated from parts of the DRC above this point are associated with asymmetric errors and therefore may be less precise (e.g. Wintle and Murray, 2006).

For the most part, where signals were saturated but produced a finite D_e, D_es were with the range of $2D_0 – 3D_0$, with the exception of one one aliquot of sample OM20/12/2 where the calculated D_e was 3.5 times greater than D_0 (Table 10.2). Mean D_0 values for aliquots passing rejection criteria typically fall within the ~50-100 Gy range suggested by Wintle (2006) for multi-grain quartz aliquots (Table 10.2). However, these values are variable between aliquots, ranging between ~18-498 Gy for OM20/5/1. Factors such as specific catchment geology or grain size may play a control on D_0 (Timar-Gabor et al., 2017) but there is no trend between mean D_0 and mean grain size (Table 10.3). The heterogeneous catchment geology of the sites sampled perhaps relates to the spatial differences observed in mean D_0, with ~80-129 Gy, 126-189 Gy and 67-79 Gy calculated for samples taken from Wadi Sahtan and the Rustaq fan, the Ibri fan and the Dhank fan, respectively. This is only a hypothesis as complete saturation was not tested for by reaching a D_0 plateau and we only have a few data points for the Ibri and Dhank fans.

Central age model (CAM) values both including and excluding aliquots $>2D_0$ are within 1σ errors as there is no significant change to the shape of dose distributions with their inclusion (Table 10.2; Fig.10.2, 10.3). For all samples, CAM D_es including and excluding aliquots $>2D_0$ agree within 5%,

except OM20/5/2 and OM20/5/3 which are within 10%. Therefore, D_es > $2D_0$ are retained in final D_e calculations (Table 10.3).

Taking the numbers of discs which did not intercept DRCs and >$2D_0$, most samples had <25% of aliquots in or close to saturation (Table 10.2). However, two samples had >25% of aliquots in saturation as a proportion of those which passed rejection criteria: OM20/4/1 (27%) and OM20/5/2 (38%; Table 10.2). It was not possible to measure feldspars for these samples due to the low feldspar content of the sediment (Woor et al., 2022b), therefore we ascribe these samples minimum ages based on a CAM D_e (Table 10.3).

Table 10.2. The proportions of aliquots which passed the rejection criteria (Table 10.1) but produced D_es in or close to saturation.'Mean D_0' and 'D_0 range' are calculated from the D_0 values of all aliquots passing rejection criteria. Max. $2D_0$ factor' denotes the highest multiple of D_0 of an aliquot with a D_e > $2D_0$ for each sample. Central age model (CAM) values are shown for datasets excluding and including D_es > $2D_0$. 'n (final D_e)' is the number of aliquots included in final D_e calculations, excluding those in saturation beyond interception of the saturating exponential dose response curve.

Sample	No intercept with DRC	D_e > $2D_0$	Total no. saturated signals	% accepted aliquots considered saturated	Mean D_0 (Gy)	D_0 range (Gy)	Max. D_0 factor	CAM excluding >$2D_0$ (Gy)	CAM including $2D_0$ (Gy)	n (final D_e)
OM20/3/1	6	1	7	18	101.64±21.83	47.22-409.12	2.7	81.15±4.98	82.55±5.12	34
OM20/3/2	1	1	2	7	88.60±11.65	45.50-314.87	2.5	69.3±4.17	70.91±4.43	27
OM20/3/3	6	1	7	21	128.74±8.45	70.26-179.77	3.1	117.87±8.42	120.19±8.64	27
OM20/4/1	2	1	3	27	97.72±9.73	78.72-119.93	2.4	109.46±9.85	115.55±11.11	9
OM20/4/2	1	0	1	6	95.93±11.02	57.78-136.90	NA	NA	NA	17
OM20/4/4	6	4	10	16	84.52±5.91	50.70-158.51	3.1	103.88±3.41	106.19±3.48	55
OM20/4/5	4	1	5	19	85.31±7.87	39.31-137.36	2.5	95.12±5.27	94.91±5.48	22
OM20/5/1	3	1	4	9	105.27±40.14	17.66-498.30	2.9	39.5±3.92	40.71±4.13	43
OM20/5/2	6	5	11	38	79.38±5.33	46.33-130.19	3.2	90±5.52	97.14±5.12	23
OM20/5/3	0	1	1	7	111.62±12.93	76.59-166.95	2.8	49.27±8.24	53.63±9.48	15
OM20/6/1	0	2	2	13	126.14±6.68	90.95-200.44	3	170.97±11.88	179.05±12.42	16
OM20/6/3	1	2	3	15	189.43±15.80	97.13-216.34	3.2	235.75±12.55	242.51±12.91	19
OM20/8/1	3	3	6	17	71.11±6.74	43.06-134.07	2.7	89.08±3.83	91.15±3.82	33
OM20/8/2	5	2	7	22	66.98±4.52	42.26-137.03	2.7	75.94±4.15	79.06±4.59	27
OM20/12/2	3	1	4	14	78.62±6.87	50.56-132.33	3.5	102.94±6.52	105.36±6.96	25

D_e dose distributions and age model results

Two types of D_e distributions are observed (Figs.10.3, 10.4). The first type is gaussian-like, showing a typically broad spread of results. Previous authors working on Hajar fan sediments have attributed these broad spreads to beta heterogeneity (e.g. Blechschmidt et al., 2009; Parton et al., 2015a).

Beta heterogeneity has a greater impact in contexts where the concentrations of soil radionuclides are low (e.g. Mayya et al., 2006; Blechschmidt et al., 2009). Small ophiolitic clasts may act as localised radiation hotspots due to their enrichment in uranium and thorium (e.g. Parton et al., 2015). However, sediments from the Hajar region can also have high carbonate contents (e.g. Fuchs and Buerkert, 2008), as evidenced by the highly cemented nature of many of the units sampled in this study. By contrast to the hotspots of ophiolitic clasts, carbonates can shield some grains from being irradiated relative to other grains, producing lower D_e values (Degering and Degering, 2020). Beta heterogeneity may therefore explain both the very low and very high outlying D_e values observed for the majority of our samples (e.g. Figs.10.3, 10.4), as well as potentially the occurrence of saturated aliquots from samples <200 ka in samples with generally low (<1 Gy ka^{-1}) dose rates. Broad scatter in D_e distributions can also be caused by partial bleaching and post-depositional mixing (Kenworthy et al., 2014). Blechschmidt et al. (2009) tested signal resetting from sediments transported during a modern flash flood on a fan in the southern Hajar. They found only a small residual dose (<1 ka) from these sediments which would likely become negligible for Pleistocene-age sediments.

Based on these considerations, we do not think that partial bleaching is significant in samples with broad, gaussian-like distributions where there is no clear younger population of D_es and favour the CAM for calculating final D_es (Table 10.3). This follows the approach adopted by previous studies dating Hajar alluvium with broad, gaussian D_e distributions (e.g. Parton et al., 2015a; Mueller et al., 2022; Beuzen-Waller et al., 2022), as well as fan and fluvial sediments in other dryland contexts (e.g. Kenworthy et al., 2014; Durcan et al., 2019). Samples OM20/4/1 and OM20/5/2 are ascribed minimum ages based on CAM D_es due to being judged to be in saturation.

The second type of D_e distributions observed are those with skewed distributions with a modal group of lower values and 'tails' of higher outliers. These are judged to suggest partial bleaching (Rodnight et al., 2006). As such, MAM D_es are more appropriate for these samples (e.g. OM20/11/3;

Fig.10.4; Table 10.3). This approach also follows what has been applied to similar D_e distributions from alluvium in the region (e.g. Fuchs and Buerkert, 2008; Hoffmann et al., 2015; Mueller et al., 2022). A MAM D_e is also derived for OM20/6/3 (Fig.10.4), despite its low overdispersion (20%) and gaussian kernel density estimate (KDE) plot, as the doses produce a bimodal histogram falling into a higher and lower population around the CAM value. Applying a finite mixture model (FMM) shows that these two populations are statistically distinct (Galbraith et al., 1999), with k = 2 giving the lowest Bayesian Information Criterion (BIC) score (6.46). The lower dose component from the FMM (197.60 ± 15.60 Gy, proportion = 0.43) is within uncertainties of the MAM whilst the higher dose component (283.18 ± 20.02 Gy, proportion = 0.57) is higher than the CAM (Table 10.3). There is potential that this distribution could be an artefact of signal averaging through multi-grain dating (Arnold and Roberts, 2009), however the MAM age for this sample (300 ± 33 ka) corresponds well with the overlying CAM age of sample OM20/6/1 (294 ± 24 ka) which, based on the stratigraphy, is likely to be related to the same period of fan aggradation. A similar approach has been applied to fluvial samples with broad spreads in D_e distribution by Rodnight et al. (2006), whereby authors favour the lowest dose component with a proportion >0.1.

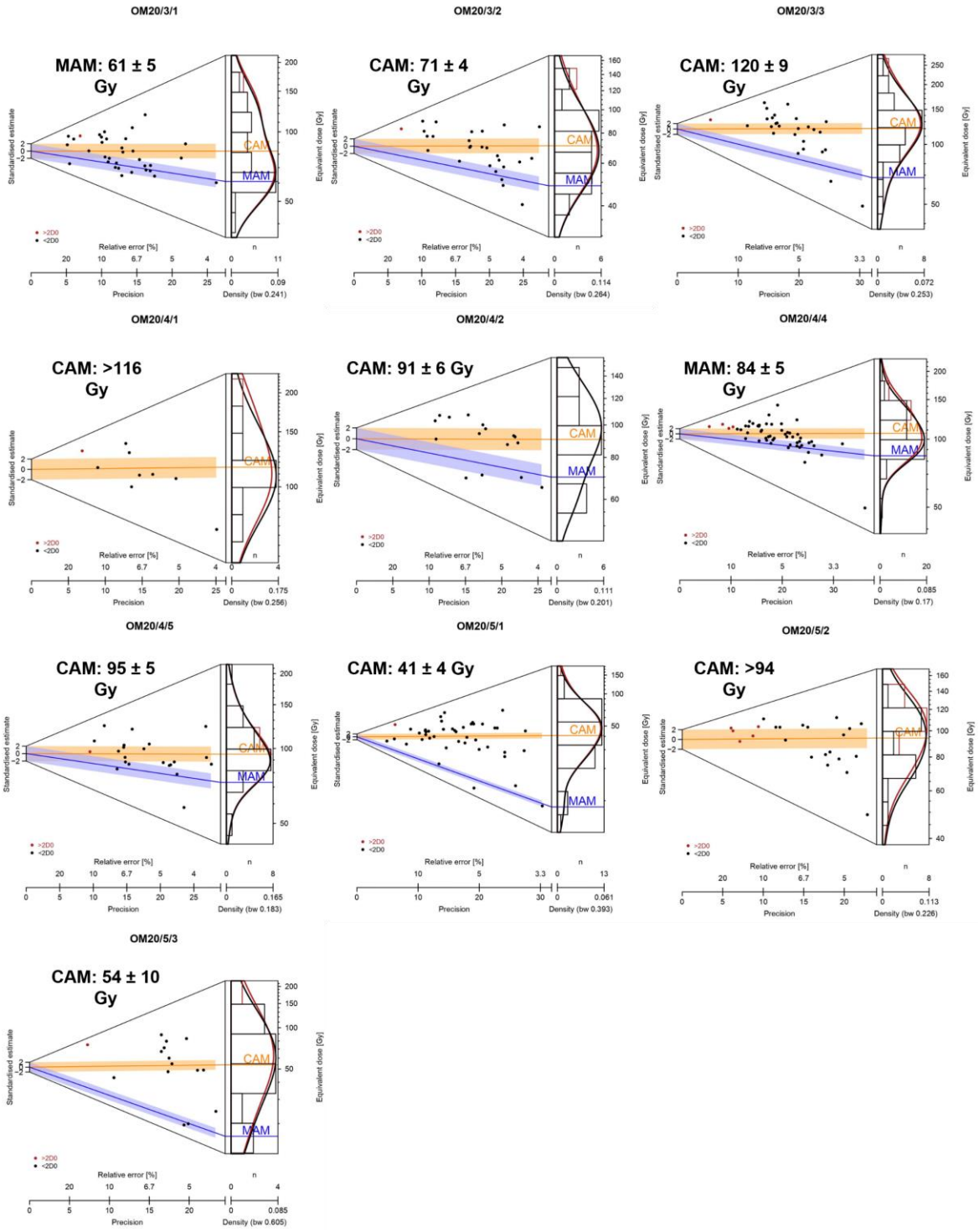

Figure 10.3. Abanico plots of samples dated along Wadi Sahtan and the proximal Rustaq fan. Age model results are shown CAM (orange line) and MAM (blue line; see Table 10.3 for full results). No MAM result is shown for OM20/4/1 or OM20/5/2 as they are ascribed minimum ages based on CAM due to issues of signal saturation.

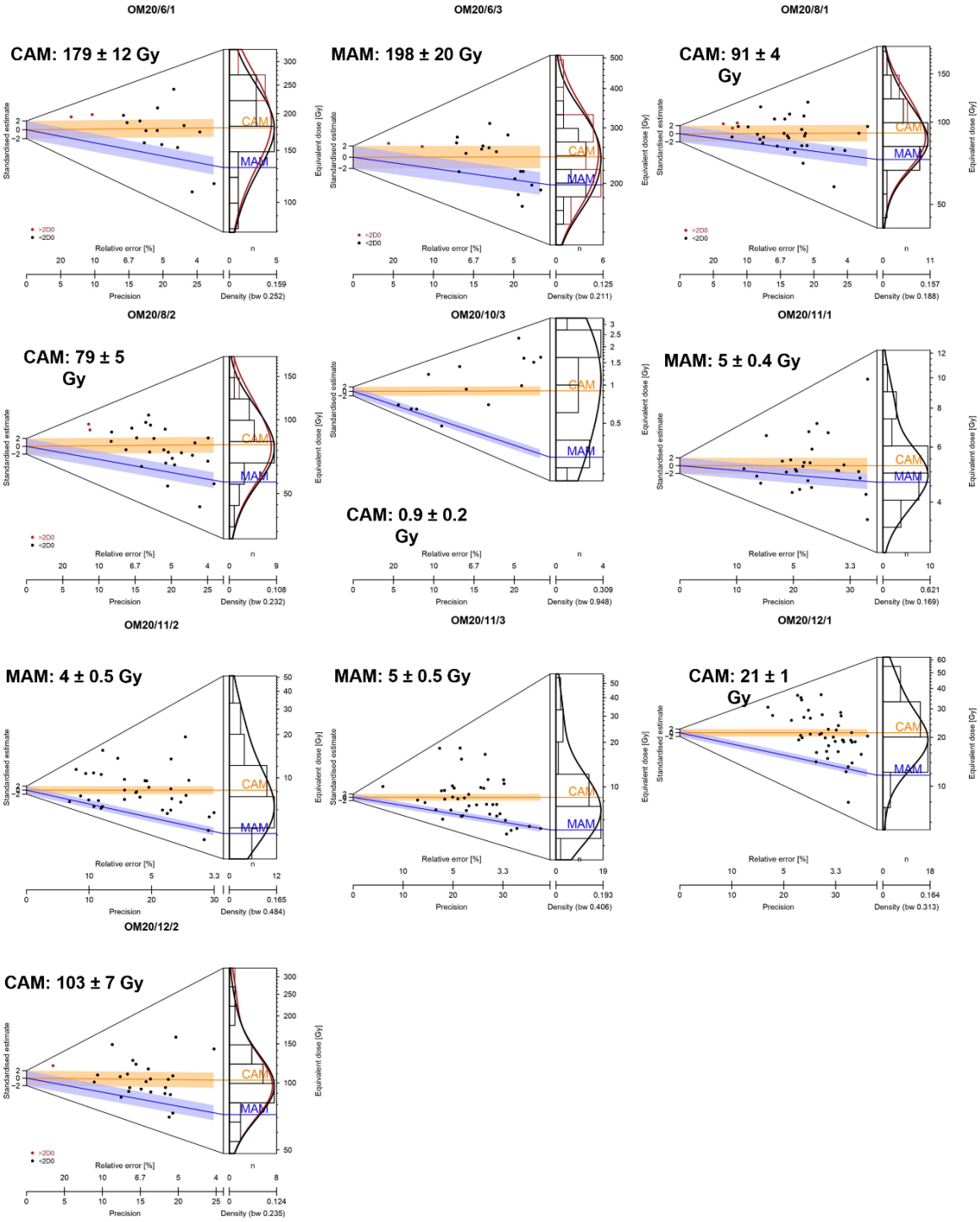

Figure 10.4. Abanico plots of samples dated along the Ibri and Dhank fans. Age model results are shown: CAM (orange line) and MAM (blue line; see Table 10.3 for full results).

Table 10.3. Sample depth, the grain size fraction selected for dating, the number of aliquots both measured and accepted, the overdispersion and final D_e determinations derived from the central age model (CAM: Galbriath et al 1999) and the minimum age model (MAM: Galbraith and Laslett (1993). Age model results in **bold** denote the final D_e selected for dating, based on the considerations discussed in the text. D_es are rounded to 2 d.p., apart from the saturated D_es from sample OM/4/1 and OM5/2 which are rounded to the nearest integer.

Sample	Depth (m)	Grain size (μm)	n[a]	Overdispersion (%)	CAM D_e (Gy)	MAM D_e (Gy)
OM20/3/1	10.30	90-150	34/96	28	82.55±5.12	**60.96±5.27**
OM20/3/2	10.80	90-210	27/48	21	**70.91±4.43**	48.41±4.87
OM20/3/3	12.30	150-210	27/70	43	**120.19±8.64**	68.09±7.71
OM20/4/1	8.50	150-210	9/48	28	**>116**	-
OM20/4/2	8.75	150-210	17/48	23	**90.55±5.76**	69.90±8.03
OM20/4/4	9.60	90-250	55/95	23	106.19±3.48	**84.45±5.46**
OM20/4/5	10.40	150-210	22/52	22	**94.91±5.48**	73.11±7.89
OM20/5/1	0.35	150-210	43/113	65	**40.71±4.13**	8.74±1.09
OM20/5/2	2.60	150-210	23/48	23	**>94**	-
OM20/5/3	4.50	150-210	15/40	62	**53.63±9.48**	16.15±2.7
OM20/6/1	1.50	180-210	16/32	23	**179.05±12.42**	131.24±15.6
OM20/6/3	4.80	125-180	19/34	20	242.51±12.91	**197.84±20.15**
OM20/8/1	0.50	150-210	33/47	21	**91.15±3.82**	73.02±6.16
OM20/8/2	0.90	150-250	27/47	28	**79.06±4.59**	55.73±5.39
OM20/10/3	1.80	150-180	13/48	83	**0.90±0.21**	0.27±0.05
OM20/11/1	0.30	150-180	28/48	24	5.23±0.26	**4.63±0.35**
OM20/11/2	0.75	150-180	36/48	63	8.19±0.87	**4.09±0.5**
OM20/11/3	1.40	150-180	41/48	56	8.49±0.75	**5.12±0.51**
OM20/12/1	0.30	150-180	44/48	42	**21.34±1.38**	11.70±1.02
OM20/12/2	2.60	90-150	25/32	29	**102.93±6.51**	72.11±8.73

[a] Number of aliquots accepted from rejection criteria / number of aliquots measured.

10.1.2. D_r calculation

Beta and gamma dose rate measurements: ICP-MS vs in-situ gamma spectrometry

Where possible, gamma dose rates were measured in-situ using a portable gamma spectrometer (GS). GS measurements were prioritised where samples were taken within close proximity (<30 cm) to stratigraphic boundaries with clastic units as these are likely to contribute to the gamma dose rate of the sample due to the range of gamma rays (~30 cm; Aitken, 1985). Potential gamma dose rate contributions from other sedimentary units would not be captured using radionuclide measurements of bulk sediments from the luminescence samples alone as these measurements only account for a much smaller range around the dated sample. However, beta dose rate estimations made from sample bulk sediments are more appropriate as the range of beta radiation is much smaller (~2 mm; Bailey et al., 2003).

Fig.10.5 compares the dose rates calculated using only ICP-MS measurements of radionuclides from bulk sediments removed from luminescence samples and those calculated based on beta dose rates derived from ICP-MS and gamma dose rates derived from field GS. Results show that for samples taken from within 30 cm of stratigraphic boundaries, or from units with gravel inclusions, that ICP-MS gamma dose rates are typically underestimated relative to dose rates which use field GS-derived gamma doses (Fig.10.5). The underestimation caused by using ICP-MS alone to derive dose rate is as much as 42% of the total dose rate in the case of sample OM20/12/2 which was taken from a thin sand lens within a heterogeneous conglomerate unit. Samples from homogeneous units away from stratigraphic boundaries show smaller differences between the two methods, typically lying closer to unity (Fig.10.5). From this, we hypothesise that the U and Th enrichment of clasts from the ophiolitic rock geology of the Hajar Mountains causes higher gamma dose rates where samples are taken within ~30 cm of conglomerate material (Parton et al., 2015a). Samples for which in-situ GS was not conducted in this study are not within 30 cm of stratigraphic boundaries, therefore we assume that the ICP-MS only approach is robust.

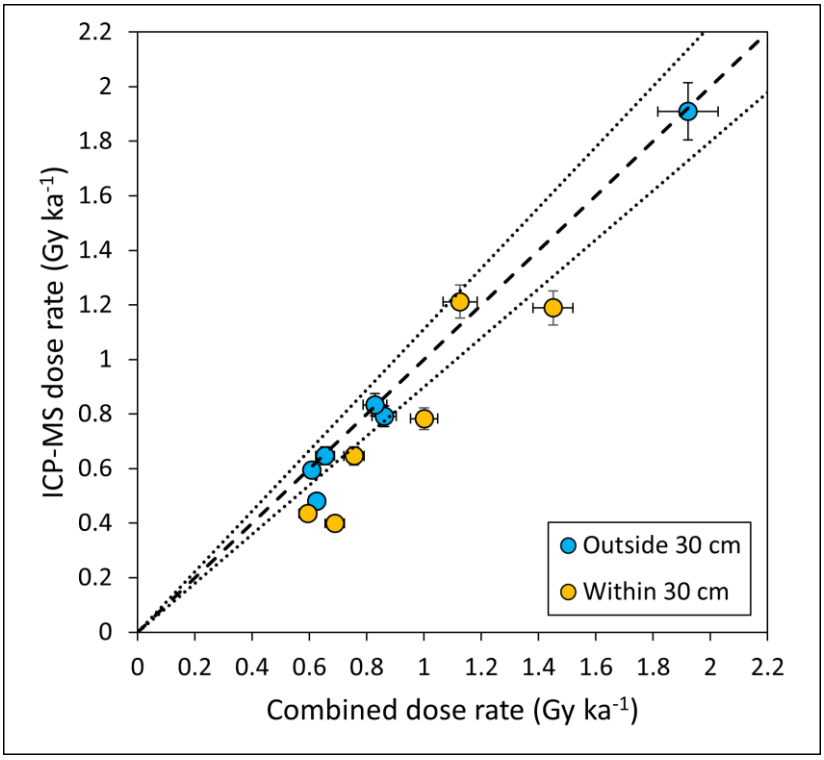

Figure 10.5. Comparison of dose rates derived using ICP-MS alone to calculate beta and gamma dose rates (y axis) and using ICP-MS to calculate beta dose rates and in-situ gamma spectrometry to calculate gamma dose rates. Results are grouped by whether samples were taken within 30 cm of a stratigraphic boundary or outside of 30 cm of a stratigraphic boundary. The black dashed line denotes unity, dotted lines denote ±10% of unity.

Carbonate attenuation factors

Alongside the more widely applied dose rate attenuation factors noted in the main text, a correction factor to account for the attenuating effect of carbonates within the sediment matrix was also incorporated using the approach of Nathan and Mauz (2008). Usually, the conversion from a 'dry' (not accounting for the attenuating effect of water within the sediment matrix) to a 'wet' (accounting for water attenuation) dose rate does not account for the presence of carbonate attenuation within the sediment matrix; calculated based on the following equation:

Equation 10.1. The conversion of 'dry' to 'wet' dose rate by incorporating an attenuation factor for water content.

$$Dose\ rate_{wet} = \frac{Dose\ rate_{dry}}{1 + x(\frac{W_c}{100})}$$

where w_c is the water content by percentage mass of sediment and *x* represents an attenuation factor of 1.25 or 1.14 for the beta and gamma dose rates, respectively (Zimmerman, 1971). Carbonate-corrected attenuation factors for the beta and gamma dose rates have previously been derived by Nathan and Mauz (2008) for a water content of 4% (within the range of 5±2% assumed for the samples in this study). We used log interpolation to generate bespoke values of *x* derived from the percentage carbonate content of sediments sampled in this study measured using the loss on ignition (LOI) method of Heiri et al. (2001). For the proportions of carbonate measured in samples, this correction made a negligible difference to overall beta and gamma dose rates (Table 10.4), with increases in the order of magnitude 10^{-2} Gy ka^{-1}.

Table 10.4. Percentage carbonate content for each sample and wet beta and gamma attenuation factors (*x*) and dose rates calculated using the standard attenuation factors of Zimmerman (1971) and those using the carbonate-corrected factors of Nathan and Mauz (2008).

Sample	Carbonate content (%)	x (β)	x (γ)	β dose rate (Gy ka^{-1})	Corrected β dose rate (Gy ka^{-1})	γ dose rate (Gy ka^{-1})	Corrected γ dose rate (Gy ka^{-1})
OM20/3/1	19	1.05	1.03	1.15±0.10	1.16±0.10	0.69±0.04	0.70±0.04
OM20/3/2	19	1.05	1.03	1.02±0.09	1.03±0.09	0.57±0.04[b]	0.57±0.04[b]
OM20/3/3	23	1.04	1.03	1.12±0.09	1.13±0.09	0.76±0.05[b]	0.77±0.05[b]
OM20/4/1	22[a]	1.04	1.03	0.70±0.06	0.71±0.06	0.34±0.02	0.34±0.02
OM20/4/2	23	1.04	1.03	0.88±0.07	0.89±0.07	0.53±0.03[b]	0.53±0.03[b]
OM20/4/4	21	1.04	1.03	0.83±0.07	0.84±0.07	0.49±0.03[b]	0.49±0.03[b]
OM20/4/5	23	1.04	1.03	0.69±0.06	0.70±0.06	0.67±0.04	0.68±0.04
OM20/5/1	20	1.04	1.03	0.27±0.02	0.27±0.02	0.26±0.02	0.26±0.02
OM20/5/2	33	1.03	1.03	0.39±0.03	0.40±0.03	0.31±0.02	0.31±0.02
OM20/5/3	30	1.03	1.03	0.22±0.02	0.22±0.02	0.29±0.02	0.29±0.02
OM20/6/1	35	1.03	1.03	0.26±0.02	0.26±0.02	0.18±0.01	0.18±0.01
OM20/6/3	29	1.03	1.03	0.33±0.03	0.34±0.03	0.20±0.01	0.20±0.01
OM20/8/1	20	1.04	1.03	0.37±0.03	0.38±0.03	0.44±0.03	0.44±0.03
OM20/8/2	26	1.04	1.03	0.17±0.01	0.17±0.01	0.27±0.02	0.27±0.02
OM20/10/3	18	1.05	1.03	0.69±0.06	0.70±0.06	0.34±0.02[b]	0.34±0.02[b]
OM20/11/1	11	1.06	1.03	0.92±0.09	0.93±0.09	0.37±0.03[b]	0.38±0.03[b]
OM20/11/2	18	1.05	1.03	0.55±0.05	0.55±0.05	0.28±0.02[b]	0.29±0.02[b]
OM20/11/3	15	1.05	1.03	0.30±0.03	0.31±0.03	0.15±0.01[b]	0.15±0.01[b]
OM20/12/1	26	1.04	1.03	0.38±00.03	0.38±0.03	0.30±0.02	0.30±0.02
OM20/12/2	35	1.03	1.03	0.16±0.01	0.16±0.01	0.37±0.02	0.38±0.02

[a] The carbonate content of sample OM20/4/1 is an average of the other samples from the same site (which all have similar values) as there was not enough sample available to conduct LOI analysis.

[b] The γ dose rates of these samples were calculated based on ICP-MS measurements of radionuclides and not in-situ gamma spectrometry.

The influence of varying cosmic dose on final ages

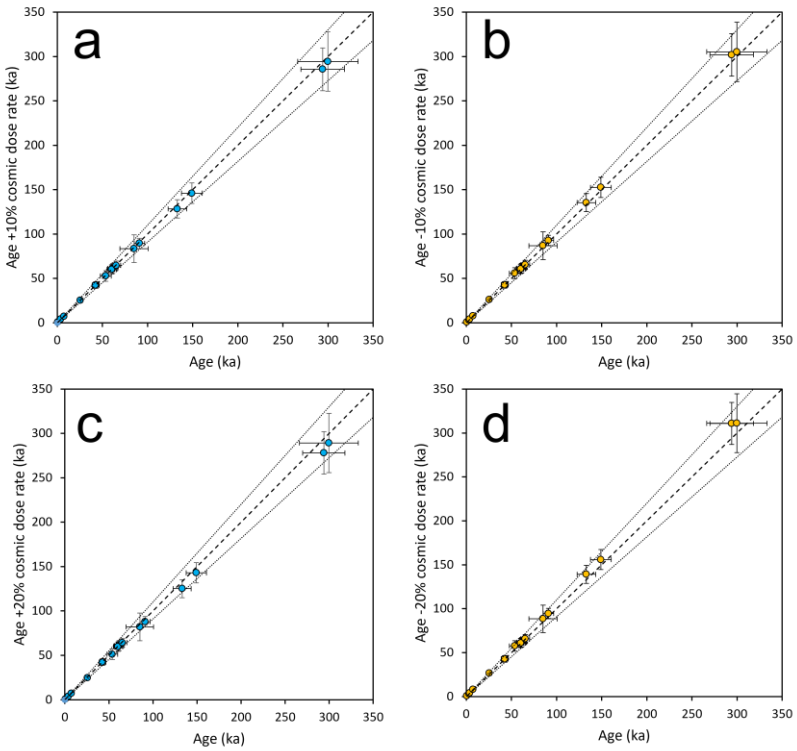

Figure 10.6. The influence of varying cosmic dose on resulting ages plotted against the age used as part of the chronology in Chapter 4 (x axis). **(a)** Increasing cosmic dose rate by 10%. **(b)** Decreasing cosmic dose rate by 10%. **(c)** Increasing cosmic dose rate by 20%. **(d)** Decreasing cosmic dose rate by 20%. Results show that age calculations are relatively insensitive to changing cosmic dose rates. The dashed line represents unity, with the dotted lines representing ±10%.

10.2. Hierarchical cluster analysis of literature age data

Table 10.5. Age data from alluvial and lacustrine deposits interpreted as being indicative of greater streamflow than present in the Hajar Mountains. Data used as input for hierarchical clustering analysis.

Reference	Age (ka)	Error (ka)	Method	Context
Atkinson et al. (2013)	12.3	0.7	OSL	Alluvial/fluvial
	12.7	0.8	OSL	Alluvial/fluvial
	73.9	3.5	OSL	Alluvial/fluvial
	76.7	8.5	OSL	Alluvial/fluvial
	79.5	8.5	OSL	Alluvial/fluvial
	84.9	9.3	OSL	Alluvial/fluvial
	89.3	9.4	OSL	Alluvial/fluvial
	92.2	9.9	OSL	Alluvial/fluvial
	109.5	6.4	OSL	Alluvial/fluvial
	120.2	11.2	OSL	Alluvial/fluvial
	131.6	11.3	OSL	Alluvial/fluvial
	136.5	11.9	OSL	Alluvial/fluvial
Beuzen-Waller et al. (2022)	6.6	0.7	OSL	Alluvial/fluvial
	11.4	1.3	OSL	Alluvial/fluvial
Blechschmidt et al. (2009)	45	5	OSL	Alluvial/fluvial
	194	18	OSL	Alluvial/fluvial
	213	46	OSL	Alluvial/fluvial
	214	19	OSL	Alluvial/fluvial
	220	24	OSL	Alluvial/fluvial

	225	22	OSL	Alluvial/fluvial
	227	27	OSL	Alluvial/fluvial
	229	37	OSL	Alluvial/fluvial
	232	21	OSL	Alluvial/fluvial
	233	26	OSL	Alluvial/fluvial
Dalongeville (1999)	4.7	0.15	C14	Alluvial/fluvial
	5.8	0.24	C14	Alluvial/fluvial
	7.8	0.13	C14	Alluvial/fluvial
	10.8	0.3	C14	Alluvial/fluvial
Farrant et al. (2012)	53.4	3.8	OSL	Alluvial/fluvial
	54.1	3.1	OSL	Alluvial/fluvial
Fuchs and Buerkert (2008)	7.6	0.42	OSL	Lacustrine
	7.9	0.59	OSL	Lacustrine
	8	0.57	OSL	Lacustrine
	8	0.58	OSL	Lacustrine
	8.1	0.58	OSL	Lacustrine
	8.3	0.6	OSL	Lacustrine
	8.6	0.59	OSL	Lacustrine
	8.7	0.62	OSL	Lacustrine
	8.8	0.66	OSL	Lacustrine
	9.6	0.73	OSL	Lacustrine
	9.9	0.74	OSL	Lacustrine
	10.6	0.76	OSL	Lacustrine
Moraetis et al. (2020)	159	7.9	OSL	Alluvial/fluvial

Mueller et al. (2022)	34	2	OSL	Alluvial/fluvial
	39	3	OSL	Alluvial/fluvial
	40	2	OSL	Alluvial/fluvial
	43	2	OSL	Alluvial/fluvial
	134	8	OSL	Alluvial/fluvial
	149	8	OSL	Alluvial/fluvial
	161	8	OSL	Alluvial/fluvial
Parker et al. (2006)	6	0.1	C14	Lacustrine
	7.7	0.04	C14	Lacustrine
	7.9	0.05	C14	Lacustrine
	8	0.08	C14	Lacustrine
	8.1	0.05	C14	Lacustrine
Parton et al. (2013)	57	8.8	OSL	Lacustrine
	58	15.8	OSL	Lacustrine
Parton et al. (2015a)	88	7.8	OSL	Alluvial/fluvial
	130	6.4	OSL	Alluvial/fluvial
	147	16.1	OSL	Alluvial/fluvial
	151	16.4	OSL	Alluvial/fluvial
	157	18	OSL	Alluvial/fluvial
	158	19.5	OSL	Alluvial/fluvial
	159	15.2	OSL	Alluvial/fluvial
	160	13.1	OSL	Alluvial/fluvial

Preston et al. (2015)	6.4	0.04	C14	Lacustrine
	7.8	0.06	C14	Lacustrine
	8.3	0.05	C14	Lacustrine
Purdue et al. (2019)	10.19	0.93	OSL	Alluvial/fluvial
Rosenberg et al. (2012)	103	9	OSL	Lacustrine
	104	7	OSL	Lacustrine
	108	8	OSL	Lacustrine
	112	8	OSL	Lacustrine
	112	7	OSL	Lacustrine
	116	7	OSL	Lacustrine
	118	7	OSL	Lacustrine
	120	8	OSL	Lacustrine
	132	8	OSL	Lacustrine
This thesis (Chapter 4)	42.95	3.56	OSL	Alluvial/fluvial
	42.44	3.62	OSL	Alluvial/fluvial
	61.51	5.53	OSL	Alluvial/fluvial
	53.85	6	OSL	Alluvial/fluvial
	85.13	15.58	OSL	Alluvial/fluvial
	294.01	23.99	OSL	Alluvial/fluvial
	299.76	33.43	OSL	Alluvial/fluvial
	133.1	10.22	OSL	Alluvial/fluvial
	7.53	0.82	OSL	Alluvial/fluvial
	14.1	1.4	OSL	Alluvial/fluvial
	104.51	13.44	OSL	Alluvial/fluvial

Table 10.6. Results of the hierarchical cluster analysis. The number of members (ages), mean age, mean error and upper and lower quartile bounds are shown for the nine resulting groups. No quartile range is given for Group 7 or 9 as they contain only one and two ages, respectively.

Group number	n	Mean age (ka)	Mean error (ka)	Lower quartile (ka)	Upper quartile (ka)
Group 1	30	8.5	0.5	7.7	9.7
Group 2	7	37.7	3.0	34.0	43.0
Group 3	7	56.8	6.8	53.9	58.0
Group 4	8	83.7	9.1	77.4	89.0
Group 5	10	112.3	7.9	107.0	118.5
Group 6	16	146.7	11.8	133.3	158.8
Group 7	1	194.0	18.0	NA	NA
Group 8	8	224.1	27.8	215.5	231.3
Group 9	2	297.0	28.5	NA	NA

11 | Appendix C: Supplementary material for Chapter 5 (Paper 2)

Table 11.1. References and locations of previous dryland fan morphometric studies shown in Figure 5.2. Latitude and longitude have been estimated from the information provided in original publications.

Study number	Latitude	Longitude	Study site	Location	Reference
1	37.27	-3.72	Grenada basin	Spain	Viseras et al. (2003)
2	37.06	-3.67	Padul depression	Spain	Viseras et al. (2003)
3	38.12	-0.82	Bajo Segura basin	Spain	Viseras et al. (2003)
4	37.57	-1.64	Almenara fans	Spain	Silva et al. (1992)
5	37.85	-1.33	Carrascoy fans	Spain	Silva et al. (1992)
6	37.56	-1.82	Pto. Lumbreras fans	Spain	Silva et al. (1992)
7	37.75	-1.6	Lorca Totanta fans	Spain	Silva et al. (1992)
8	37.86	-1.43	Alhama fans	Spain	Silva et al. (1992)
9	37.96	-1.29	Alcantarilla fans	Spain	Silva et al. (1992)
10	36.78	-2.15	Cabo de Gata	Spain	Harvey et al. (1999)
11	37.03	-2.4	Southern Murcia metamorphic region	Spain	Harvey (1987)
12	38.56	-0.13	Pre-Betic region	Spain	Harvey (1987)
13	37.61	-1.68	Southern Murcia sedimentary region	Spain	Harvey (1987)
14	37.83	-1.3	Carrascoy region	Spain	Harvey (1987)
15	36.97	-3.6	Sierra Nevada	Spain	Calvache et al. (1997)
16	37.2	-2.04	Betic zone	Spain	Mather et al. (2000)
17-19	37.81, 38.58, 37.59	-1.28, -0.17, -1.23	Northern group	Spain	Harvey (1990)
20-24	37.78, 37.52, 37.37, 37.27, 36.80	-1.50, -1.86, -1.89, -1.95, -2.18	Southern group (exclusing schists)	Spain	Harvey (1990)
25-28	37.47, 37.63, 36.96, 37.18	-1.69, -1.77, -2.25, -2.35	Southern group (schists)	Spain	Harvey (1990)
29	36.41	-120	Western Fresno County (shale), California	USA	Bull (1964)
30	36.64	-121	Western Fresno County (sandstone), California	USA	Bull (1964)
31	40.98	-118	Winnemuca, Nevada	USA	Hawley and Wilson (1965)
32	36.2	-117	Death Valley, California	USA	Denny (1965)
33	37.32	-118	Owens Valley, California	USA	Hooke (1968)
34	36.19	-118	Cactus Flats, California	USA	Hooke (1968)
35	36.12	-117	Death Valley east side, California	USA	Hooke (1968)
36	37.16	-118	Little Cowhorn Valley southeast side, California	USA	Hooke (1968)
37	36.2	-117	Death Valley west side, California	USA	Hooke (1968)
38	37.29	-118	Deep Springs Valley (quartzite and dolomite), California	USA	Hooke (1968)
39	37.29	-118	Deep Springs Valley (quartzite), California	USA	Hooke (1968)
40	37.16	-118	Little Cowhorn Valley, California	USA	Hooke and Rohrer (1977)
41	36.12	-117	Death Valley east side, California	USA	Hooke and Rohrer (1977)
42	36.1	-117	Death Valley west side, California	USA	Hooke and Rohrer (1977)
43	35.15	-116	Zzyzx, California	USA	(Harvey, 1990)
44	36.8	-117	South-western Bare Mountain, California	USA	Ferrill et al. (1996)
45	36.87	-117	Eastern Bare Mountain, California	USA	Ferrill et al. (1996)
46	37.79	-118	Northern White Mountains, California	USA	Whipple and Trayler (1996)
47	37.48	-118	Southern White Mountains, California	USA	Whipple and Trayler (1996)
48	36.7	-118	Western Bajada, California	USA	Whipple and Trayler (1996)
49	36.5	-118	Owens Lake, California	USA	Whipple and Trayler (1996)
50	39.67	-118	Stillwater, Nevada	USA	Harvey (2002)
51	39.43	-118	Cold Springs, Nevada	USA	Harvey (2002)
52	39.9	-118	Dixie, Nevada	USA	Harvey (2005)
53	40.66	-119	Gerlach, Nevada	USA	Harvey (2005)
54	37.41	-118	Western White Mountains (resistant), California	USA	Lecce (1991)
55	37.41	-118	Western White Mountains (erodible), California	USA	Lecce (1991)
56	33.44	48.48	Oshtorankooh Altitudes	Iran	Mokarram et al. (2014)
57	34.38	45.88	Danehkhoshk anticline	Iran	Bahrami (2013)
58	35.56	51.8	Elburz Mountains	Iran	Beaumont (1972)
59	37.61	23.37	Methana	Greece	Harvey (1990)
60	38.41	23.76	North Evoikos Gulf	Greece	Valkanou et al. (2013)
61	38.13	22.32	Gulf of Corinth	Greece	Karymbalis et al. (2018)
62	38.61	21.55	Lake Trichonis	Greece	Karymbalis et al. (2022)
63	25.77	56.04	Wadi al Bih mountain front	UAE	Al-Farraj and Harvey (2005)
64	25.83	56.11	Wadi al Bih tributary jubction	UAE	Al-Farraj and Harvey (2005)
65	-31.5	-69.5	San Juan River	Argentina	Milana and Ruzycki (1999)
66	31.58	-5.9	River Dades, High Atlas Mountains	Morocco	Stokes and Mather (2015)
67	16.85	-25	Sao Vincente	Cape Verde	Stokes and Gomes (2020)

Table 11.2. Summary of F_r v. C_a regression relationships for each study area. Bold p-values denote statistically significant relationships at the 95% confidence level.

Area	Coefficient x	Exponent y	R^2	Standard error	p-value
Musandam Peninsula	30.22	0.04	0.01	0.9	**0.00**
Rub' al Khali	30.15	0.25	0.62	0.57	**0.00**
Wahiba Sands	26.38	0.27	0.57	0.58	**0.00**
Batinah Coast	35.95	0.24	0.41	0.56	**0.00**

Table 11.3. Summary of F_g v. C_g regression relationships for each study area. Bold p-values denote statistically significant relationships at the 95% confidence level.

Area	Coefficient x	Exponent y	R^2	Standard error	p-value
Musandam Peninsula	0.00	0.78	0.08	1.02	**0.00**
Rub' al Khali	0.00	0.94	0.32	0.73	**0.00**
Wahiba Sands	0.00	0.30	0.15	0.39	**0.01**
Batinah Coast	193.72	0.56	0.17	0.53	**0.00**

Table 11.4. Summary of F_g v. C_{mr} regression relationships for each study area. Bold p-values denote statistically significant relationships at the 95% confidence level.

Area	Coefficient x	Exponent y	R^2	Standard error	p-value
Musandam Peninsula	0.04	0.69	0.25	0.92	**0.00**
Rub' al Khali	0.04	0.60	0.63	0.53	**0.00**
Wahiba Sands	0.02	0.36	0.24	0.37	**0.00**
Batinah Coast	0.01	0.23	0.21	0.37	**0.00**

Table 11.5. Summary of F_a v. C_{mr} regression relationships for each study area. Bold p-values denote statistically significant relationships at the 95% confidence level.

Area	Coefficient x	Exponent y	R^2	Standard error	p-value
Musandam Peninsula	0.22	-1.85	0.44	1.61	**0.00**
Rub' al Khali	0.08	-2.19	0.69	1.71	**0.00**
Wahiba Sands	0.40	-1.10	0.24	2.08	**0.00**
Batinah Coast	5.39	-0.69	0.12	1.58	**0.00**

Table 11.6. Summary of F_a v. C_r regression relationships for each study area. Bold p-values denote statistically significant relationships at the 95% confidence level.

Area	Coefficient x	Exponent y	R^2	Standard error	p-value
Musandam Peninsula	0.00	1.86	0.49	1.53	**0.00**
Rub' al Khali	0.00	2.35	0.43	2.33	**0.00**
Wahiba Sands	0.00	1.74	0.74	1.12	**0.00**
Batinah Coast	0.04	1.00	0.33	1.38	**0.00**

Table 11.7. Summary of F_g v. F_a regression relationships for each study area. Bold p-values denote statistically significant relationships at the 95% confidence level.

Area	Coefficient x	Exponent y	R^2	Standard error	p-value
Musandam Peninsula	0.03	-0.30	0.37	0.84	**0.00**
Rub' al Khali	0.02	-0.25	0.77	0.42	**0.00**
Wahiba Sands	0.01	-0.10	0.29	0.36	**0.00**
Batinah Coast	0.01	-0.16	0.40	0.33	**0.00**

Table 11.8. Morphometric relationships from Equations 2.1 and 2.2 and their associated R^2 values for mountain front (MF) and tributary junction (TJ) fans in different dryland contexts on Earth, Mars and Titan. These regression relationships are plotted in Figure 5.15 and study sites mapped in Figure 5.2.

Morphometric relationship						Fan setting	Study site	Location	Reference
$F_a = xC_a^y$			$F_g = xC_a^y$						
x	y	R^2	x	y	R^2				
0.21	0.86	0.91	0.13	-0.15	0.83	MF	Grenada basin	Spain	Viseras et al. (2003)
1.82	1.49	0.98	0.13	-0.26	0.92	MF	Padul depression	Spain	Viseras et al. (2003)
0.72	1.05	0.84	0.08	-0.1	0.26	MF	Bajo Segura basin	Spain	Viseras et al. (2003)
1.04	0.81	0.88	0.05	-0.3	0.84	MF	Almenara fans	Spain	Silva et al. (1992)
1.26	0.75	0.99	0.15	-0.48	0.98	MF	Carrascoy fans	Spain	Silva et al. (1992)
0.57	0.8	0.89	0.04	-0.26	0.84	MF	Pto. Lumbreras fans	Spain	Silva et al. (1992)
0.46	0.71	0.81	0.04	-0.31	0.55	MF	Lorca Totanta fans	Spain	Silva et al. (1992)
0.66	0.66	0.71	0.06	-0.16	0.39	MF	Alhama fans	Spain	Silva et al. (1992)
5.51	0.07	0.46	0.03	-0.06	0.68	MF	Alcantarilla fans	Spain	Silva et al. (1992)
0.84	0.75	0.92	0.058	-0.37	0.74	MF	Cabo de Gata	Spain	Harvey et al. (1999)
-	-	-	0.06	-0.25	0.84	MF	Southern Murcia metamorphic region	Spain	Harvey (1987)
-	-	-	0.1	-0.23	0.45	MF	Pre-Betic region	Spain	Harvey (1987)
-	-	-	0.05	-0.18	0.71	MF	Southern Murcia sedimentary region	Spain	Harvey (1987)
-	-	-	0.09	-0.29	0.37	MF	Carrascoy region	Spain	Harvey (1987)
1.82	1.49	0.97	0.13	-0.26	0.85	MF	Sierra Nevada, central and SE group	Spain	Calvache et al. (1997)
0.21	0.82	0.9	0.14	-0.13	0.8	MF	Sierra Nevada, NW group	Spain	Calvache et al. (1997)
1.38	1.23	0.83	0.068	-0.25	0.50	MF	Betic zone	Spain	Mather et al. (2000)
-	-	-	0.08	-0.20	0.32	MF	Northern group	Spain	Harvey (1990)
-	-	-	0.05	-0.20	0.69	MF	Southern group (exclusing schists)	Spain	Harvey (1990)
-	-	-	0.06	-0.26	0.84	MF	Southern group (schists)	Spain	Harvey (1990)
2.4	0.98	-	-	-	-	MF	Western Fresno County (shale), California	USA	Bull (1964)
1.3	0.88	-	-	-	-	MF	Western Fresno County (sandstone), California	USA	Bull (1964)
0.74	0.98	-	-	-	-	MF	Winnemuca, Nevada	USA	Hawley and Wilson (1965)
0.33	1.00	-	-	-	-	MF	Death Valley, California	USA	Denny (1965)
0.42	0.94	-	-	-	-	MF	Owens Valley, California	USA	Hooke (1968)
0.24	1.01	-	-	-	-	MF	Cactus Flats, California	USA	Hooke (1968)
0.15	0.9	-	-	-	-	MF	Death Valley east side, California	USA	Hooke (1968)

0.28	1.13	-	-	-	-	MF	Little Cowhorn Valley southeast side, California	USA	Hooke (1968)
1.05	0.76	-	-	-	-	MF	Death Valley west side, California	USA	Hooke (1968)
0.44	0.62	-	-	-	-	MF	Deep Springs Valley (quartzite and dolomite), California	USA	Hooke (1968)
0.16	0.75	-	-	-	-	MF	Deep Springs Valley (quartzite), California	USA	Hooke (1968)
0.2	1.07	-	-	-	-	MF	Little Cowhorn Valley, California	USA	Hooke and Rohrer (1977)
0.16	0.9	-	-	-	-	MF	Death Valley east side, California	USA	Hooke and Rohrer (1977)
0.95	0.89	-	-	-	-	MF	Death Valley west side, California	USA	Hooke and Rohrer (1977)
		-	0.08	0.347	0.61	MF	Zzyzx, California	USA	(Harvey, 1990)
2.05	0.7	-	-	-	-	MF	South-western Bare Mountain, California	USA	Ferrill et al. (1996)
0.55	0.92	-	-	-	-	MF	Eastern Bare Mountain, California	USA	Ferrill et al. (1996)
0.01	2.82	0.76	-	-	-	MF	Northern White Mountains, California	USA	Whipple and Trayler (1996)
1.66	0.34	0.33	-	-	-	MF	Southern White Mountains, California	USA	Whipple and Trayler (1996)
2.59	0.64	0.61	-	-	-	MF	Western Bajada, California	USA	Whipple and Trayler (1996)
0.64	0.47	0.81	-	-	-	MF	Owens Lake, California	USA	Whipple and Trayler (1996)
0.4	0.68	0.93	-	-	-	MF	Stillwater, Nevada	USA	Harvey (2002)
0.41	0.94	0.94	-	-	-	MF	Cold Springs, Nevada	USA	Harvey (2002)
0.36	0.97	0.94	-	-	-	MF	Dixie, Nevada	USA	Harvey (2005)
0.54	0.96	0.95	-	-	-	MF	Gerlach, Nevada	USA	Harvey (2005)
0.65	0.65	0.75	-	-	-	MF	Western White Mountains (resistant), California	USA	Lecce (1991)
0.7	1.22	0.80	-	-	-	MF	Western White Mountains (erodible), California	USA	Lecce (1991)
0.22	0.11	0.83	1.01	-0.38	0.86	MF	Oshtorankooh Altitudes	Iran	Mokarram et al. (2014)
0.06	0.55	0.43	13.52	-0.02	0.65	MF	Danehkhoshk anticline	Iran	Bahrami (2013)
1.18	0.95	-	-	-	-	MF	Elburz Mountains	Iran	Beaumont (1972)
0.14	-0.44	0.81	-	-	-	-	Methana	Greece	Harvey (1990)
0.12	0.7	0.89	0.06	-0.23	0.3	MF	North Evoikos Gulf	Greece	Valkanou et al. (2013)
0.17	0.64	0.64	0.09	-0.41	0.47	MF	Gulf of Corinth	Greece	Karymbalis et al. (2018)
0.23	0.1	0.94	0.05	-0.32	0.4	MF	Lake Trichonis	Greece	Karymbalis et al. (2022)
0.45	0.72	0.85	0.07	-0.13	0.53	MF	Wadi al Bih mountain front	UAE	Al-Farraj and Harvey (2005)
0.14	0.66	0.88	0.09	-0.12	0.5	TJ	Wadi al Bih tributary junction	UAE	Al-Farraj and Harvey (2005)
0.09	0.86	0.56	0.06	-0.37	0.42	MF	Musandam Peninsula fans	UAE/Oman	This study
0.83	1.02	0.89	0.02	-0.27	0.78	MF	Rub' al Khali fans	UAE/Oman	This study

1.36	0.8	0.82	0.01	-0.12	0.48	MF	Wahiba Sands fans	Oman	This study
2.21	0.66	0.6	0.01	-0.1	0.23	MF	Batinah Coast fans	Oman	This study
0.12	0.49	0.72	0.2	-0.23	0.53	TJ	San Juan River	Argentina	Milana and Ruzycki (1999)
0.00	0.34	0.27	0.02	-0.2	0.21	TJ	River Dades, High Atlas Mountains	Morocco	Stokes and Mather (2015)
0.86	0.29	0.75	0.15	-0.24	0.23	Mixed	Sao Vincente	Cape Verde	Stokes and Gomes (2020)
0.61	0.91	-	-	-	-	-	Global	Titan	Birch et al. (2016)
4.26	0.79	0.42	0.12	-0.22	0.23	-	0-30°S, 60-270°W (craters)	Mars	Moore and Howard (2005)
1.27	0.97	0.75	8.32	-0.20	0.51	-	Global (craters)	Mars	Morgan et al. (2022)
5.37	0.42	0.42	10.90	-0.10	0.27	-	Global (not in craters)	Mars	Morgan et al. (2022)

12 | Appendix D: Supplementary material for Chapter 6 (Paper 3)

Table 12.1. Palaeoclimate and sea level records around the Arabian Peninsula covering the period 0-20 ka. Numbers refer to Figures 6.1 and 6.2 in the text. Coordinates are given in decimal degrees.

Number	Name	Latitude	Longitude	Record type	Proxies	Chronological technique	Reference(s)
A	Hoti Cave	23.08	57.35	Speleothem	$\delta^{18}O$	U-Th	Burns et al. (1998); Burns et al. (2001); Neff et al. (2001); (Fleitmann et al., 2003)
B	Qunf Cave	17.17	54.30	Speleothem	$\delta^{18}O$	U-Th	Fleitmann and Matter (2009)
C	Moomi Cave	12.50	54.00	Speleothem	$\delta^{18}O$	U-Th	Shakun et al. (2007)
D	RC27-23	18.00	57.59	Marine core	*G. bulloides* abundance	^{14}C	Overpeck et al. (1996)
E	74KL	14.32	57.35	Marine core	$\delta^{18}O$	^{14}C	Sirocko et al. (1993)
F	M5-422	24.38	59.05	Marine core	% $CaCO_3$ % Dolomite	^{14}C	Cullen et al. (2000)
G	MD04-288	22.20	63.10	Marine core	XRF Br counts	Age model of Sinnighe Damste et al. (2002)	Ziegler et al. (2010)
H	Dosariyah	26.92	49.74	Sea level reconstruction	Sea level index points	OSL, ^{14}C	Parker et al. (2020)
I	KL11	18.77	39.33	Sea level reconstruction	$\delta^{18}O$	U-Th	Siddall et al. (2003)

Table 12.2. Palaeoenvironmental records compiled and assessed in the database from around the Arabian Peninsula, covering the period 0-20 ka. 'Site numbers' refer to Figure 6.2 in the text, 'Assessed site numbers' refer to Figure 6.6 in the text. Coordinates are given in decimal degrees. Sub-region codes are N (Nefud), AG/NR (Arabian Gulf/Northern Rub'al Khali), HM (Hajar Mountains), ASC (Arabian Sea Coast), RAK (Rub'al Khali), WA (Western Arabia), SA (Southern Arabia).

Site number	Assessed site number	Site name	Latitude	Longitude	Country	Sub-region	Record type(s)	Proxies	Number of ages	Chronological technique(s)	Reference(s)
1	1	Jubbah	28.00	40.94	Saudi Arabia	N	Lake, wetland	Geoproxy, diatoms	8	OSL, ^{14}C	Hilbert et al. (2014); Parton et al. (2018); Clark-Balzan et al. (2018)
2	2	Jebel Oraf	27.90	40.80	Saudi Arabia	N	Lake, wetland	Geoproxy	4	OSL	Guagnin et al. (2020)
3	-	An Nafud	27.36	38.5	Saudi Arabia	N	Lake	Geoproxy	1	^{14}C	Whitney et al. (1983)
4	3	Tayma	27.38	38.33	Saudi Arabia	N	Lake, wetland	Geoproxy, pollen	23	^{14}C	Engel et al. (2012); Dinies et al. (2015)
5	-	Wadi ad Dawasir 1	28.30	45.32	Saudi Arabia	N	Lake	Geoproxy	3	^{14}C	Zarins et al. (1979)
6	4	Wahalah	25.64	55.79	UAE	AG/NR	Lake, wetland, aeolian	Geoproxy, ostracods, geochemistry	30	OSL, ^{14}C	Atkinson et al. (2011); Preston et al. (2015); Parker et al. (2016)
7	5	Emirates Highway	25.63	55.83	UAE	AG/NR	Aeolian	Geoproxy	28	OSL	Atkinson et al. (2011); Leighton et al. (2013); Leighton et al. (2014)
8	6	Ramlat ash Shuruq	25.67	55.90	UAE	AG/NR	Aeolian	Geoproxy	3	OSL	Atkinson et al. (2011)
9	7	Al Ain	24.35	55.77	UAE	AG/NR	Aeolian	Geoproxy	11	OSL	Atkinson et al. (2011)
10	8	Tawi Amar 1	25.41	55.75	UAE	AG/NR	Fluvial	Geoproxy	2	OSL	Atkinson et al. (2013)
11	9	Tawi Amar 2	25.42	55.74	UAE	AG/NR	Aeolian	Geoproxy	7	OSL	Atkinson et al. (2013)
12	10	Awafi	25.72	55.95	UAE	AG/NR	Lake, wetland, aeolian	Geoproxy, pollen, geochemistry, phytoliths, $\delta^{13}C$	23	OSL, ^{14}C	Goudie et al. (2000); Parker et al. (2004); Parker et al. (2006); Parker et al. (2016)
13	11	Liwa 1	22.93	53.54	UAE	AG/NR	Aeolian	Geoproxy	12	OSL	Bray and Stokes (2004)
14	12	Liwa 2	22.92	53.54	UAE	AG/NR	Aeolian	Geoproxy	23	OSL	Stokes and Bray (2005)
15	13	Liwa 3	22.98	53.41	UAE	AG/NR	Aeolian	Geoproxy	2	OSL	Stokes and Bray (2005)
16	-	UAE7845	24.24	54.80	UAE	AG/NR	Aeolian	Geoproxy	9	OSL	Farrant et al. (2015)
17	-	UAE7947	24.11	55.4	UAE	AG/NR	Aeolian	Geoproxy	1	OSL	Farrant et al. (2015)
18	-	UAE7978	24.31	54.63	UAE	AG/NR	Aeolian	Geoproxy	1	OSL	Farrant et al. (2015)
19	-	UAE7984	24.17	54.57	UAE	AG/NR	Aeolian	Geoproxy	1	OSL	Farrant et al. (2015)
20	-	UAE8028	24.01	53.68	UAE	AG/NR	Aeolian	Geoproxy	1	OSL	Farrant et al. (2015)
21	-	UAE8510	24.07	54.13	UAE	AG/NR	Aeolian	Geoproxy	1	OSL	Farrant et al. (2015)
22	-	UAE6183	22.82	53.68	UAE	AG/NR	Aeolian	Geoproxy	1	OSL	Farrant et al. (2012)
23	-	UAE6330	24.40	55.03	UAE	AG/NR	Aeolian	Geoproxy	1	OSL	Farrant et al. (2012)
24	-	UAE6355	24.31	54.82	UAE	AG/NR	Aeolian	Geoproxy	1	OSL	Farrant et al. (2012)
25	-	UAE6357	24.40	54.95	UAE	AG/NR	Aeolian	Geoproxy	1	OSL	Farrant et al. (2012)
26	-	UAE6567	25.03	55.27	UAE	AG/NR	Aeolian	Geoproxy	1	OSL	Farrant et al. (2012)
27	-	UAE6581	23.43	55.41	UAE	AG/NR	Aeolian	Geoproxy	1	OSL	Farrant et al. (2012)
28	-	UAE6735	23.84	54.81	UAE	AG/NR	Aeolian	Geoproxy	1	OSL	Farrant et al. (2012)
29	-	UAE6916	24.34	54.70	UAE	AG/NR	Aeolian	Geoproxy	1	OSL	Farrant et al. (2012)
30	-	UAE6935	23.97	54.16	UAE	AG/NR	Aeolian	Geoproxy	1	OSL	Farrant et al. (2012)
31	-	UAE7102	23.97	53.93	UAE	AG/NR	Aeolian	Geoproxy	1	OSL	Farrant et al. (2012)
32	-	UAE7317	23.94	52.89	UAE	AG/NR	Aeolian	Geoproxy	1	OSL	Farrant et al. (2012)
33	-	UAE7347	24.07	52.50	UAE	AG/NR	Aeolian	Geoproxy	1	OSL	Farrant et al. (2012)
34	14	Dub 6	25.11	55.19	UAE	AG/NR	Shoreline, mangrove	Geoproxy, fossils	9	OSL, ^{14}C	Zander et al. (2007)

35	15	Dub 5	25.11	55.18	UAE	AG/NR	Shoreline	Geoproxy, fossils	7	OSL, ^{14}C	Zander et al. (2007)
36	-	Near Liwa Hotel	23.11	53.75	UAE	AG/NR	Aeolian	Geoproxy	1	OSL	Wood et al. (2003)
37	16	Dosariyah	26.92	49.74	Saudi Arabia	AG/NR	Aeolian, sabkha	Geoproxy, sea level reconstruction	14	OSL, ^{14}C	Parker et al. (2020)
38	-	Mussafah Channel	24.30	54.52	UAE	AG/NR	Sabkha	Geoproxy	3	OSL	Lokier et al. (2015)
39	-	Al Hasa 1	26.05	50.57	Bahrain	AG/NR	Palaeosol	Geoproxy	4	^{14}C	Larsen (1983)
40	-	Al Hasa 2	25.50	49.67	Saudi Arabia	AG/NR	Lake, palaeosol	Geoproxy	4	^{14}C	Al-Sayari and Zotl (1978); Sanlaville (1992)
41	-	Wadi Dhaid	25.35	55.38	UAE	AG/NR	Fluvial	Geoproxy	1	^{14}C	Sanlaville (1992)
42	17	UAE06-2	25.65	55.80	UAE	AG/NR	Aeolian	Geoproxy	5	^{14}C	Preston et al. (2015)
43	18	Al Jubail	24.13	54.10	UAE	AG/NR	Shoreline	Geoproxy	5	^{14}C	Wood et al. (2012)
44	-	Liwa	22.91	54.32	UAE	AG/NR	Spring	Geoproxy	5	^{14}C	Wood and Imes (1995)
45	19	Abu Dhabi Sabkha	24.09	54.06	UAE	AG/NR	Sabkha	Geoproxy, fossils	16	^{14}C	Lokier and Steuber (2008)
46	20	Kuwait Bay	29.57	48.11	Kuwait	AG/NR	Shoreline	Geoproxy, fossils	19	^{14}C	Reinink-Smith (2015)
47	21	Maqta	22.83	59.00	Oman	HM	Wetland	Geoproxy, fossils	46	OSL, ^{14}C	Fuchs and Buerkert (2008); Urban and Buerkert (2009)
48	22	Shu'ayb	24.80	55.80	UAE	HM	Aeolian	Geoproxy	18	OSL	Atkinson et al. (2011), Leighton et al. (2013)
49	23	Masafi	25.31	56.16	UAE	HM	Fluvial	Geoproxy	4	OSL, ^{14}C	Purdue et al. (2019)
50	24	Al Sibetah	24.33	55.76	UAE	HM	Aeolian	Geoproxy	2	OSL	Parton et al. (2015a)
51	-	Jebel Hafit	24.07	55.78	UAE	HM	Fluvial	Geoproxy	1	^{14}C	Gebel et al. (1989)
52	-	Al Ain	24.18	55.73	UAE	HM	Lake, fluvial	Geoproxy	5	^{14}C	Gebel et al. (1989)
53	25	Mleiha	25.12	55.86	UAE	HM	Fluvial	Geoproxy	2	^{14}C	Dalongeville (1999)
54	26	Qafeefah travertine	22.91	58.43	Oman	HM	Spring	Geoproxy, geochemistry, $\delta^{13}C$, $\delta^{18}O$	5	^{14}C	Mervine et al. (2014); Mervine et al. (2015)
55	27	Misht travertine	23.29	56.88	Oman	HM	Spring	Geoproxy, geochemistry, $\delta^{13}C$, $\delta^{18}O$	7	^{14}C	Mervine et al. (2014); Mervine et al. (2015)
56	28	Wadi Sudari travertine	23.96	56.44	Oman	HM	Spring	Geoproxy, geochemistry, $\delta^{13}C$, $\delta^{18}O$	2	^{14}C	Mervine et al. (2014); Mervine et al. (2015)
57	29	Wadi Uqaybah travertine	23.81	56.28	Oman	HM	Spring	Geoproxy, geochemistry, $\delta^{13}C$, $\delta^{18}O$	2	^{14}C	Mervine et al. (2014); Mervine et al. (2015)
58	-	Jill	22.86	57.52	Oman	HM	Spring	Geoproxy, geochemistry, $\delta^{13}C$, $\delta^{18}O$	3	^{14}C	Kelemen and Matter (2008)
59	-	'Duck' outcrop	22.81	57.84	Oman	HM	Spring	Geoproxy, geochemistry, $\delta^{13}C$, $\delta^{18}O$	2	^{14}C	Kelemen and Matter (2008)
60	-	Tuf	23.10	57.95	Oman	HM	Spring	Geoproxy, geochemistry, $\delta^{13}C$, $\delta^{18}O$	1	^{14}C	Kelemen and Matter (2008)
61	-	Falaij	22.85	58.06	Oman	HM	Spring	Geoproxy, geochemistry, $\delta^{13}C$, $\delta^{18}O$	4	^{14}C	Kelemen and Matter (2008)
62	-	Wadi Nassif	22.91	58.37	Oman	HM	Spring	Geoproxy, geochemistry, $\delta^{13}C$, $\delta^{18}O$	1	^{14}C	Kelemen and Matter (2008)
63	-	Khafifah-Dima	22.94	58.44	Oman	HM	Spring	Geoproxy, geochemistry, $\delta^{13}C$, $\delta^{18}O$	1	^{14}C	Kelemen and Matter (2008)
64	-	Wadi Dhuli	22.98	58.63	Oman	HM	Spring	Geoproxy, geochemistry, $\delta^{13}C$, $\delta^{18}O$	2	^{14}C	Kelemen and Matter (2008)
65	-	Batin	22.93	58.67	Oman	HM	Spring	Geoproxy, geochemistry, $\delta^{13}C$, $\delta^{18}O$	2	^{14}C	Kelemen and Matter (2008)
66	-	Nizwa	22.87	57.52	Oman	HM	Spring	Geoproxy, $\delta^{13}C$, $\delta^{18}O$	29	^{14}C	Clark and Fontes (1990)
67	-	N' Ra's Ruways	21.03	58.83	Oman	ASC	Aeolian	Geoproxy	4	IRSL	Preusser et al. (2002)
68	-	Ra's Ruways	20.98	58.80	Oman	ASC	Aeolian	Geoproxy	9	IRSL	Preusser et al. (2002)
69	-	Khuwayma	21.28	59.08	Oman	ASC	Aeolian	Geoproxy	8	IRSL	Preusser et al. (2002)
70	-	Qahid	21.16	58.93	Oman	ASC	Wetland	Geoproxy	8	IRSL	Preusser et al. (2002)
71	-	Qurun	21.47	59.26	Oman	ASC	Aeolian	Geoproxy	3	IRSL	Preusser et al. (2002)
72	30	Wahiba Sand Sea	21.88	58.88	Oman	ASC	Lake	Geoproxy, fossils	7	IRSL, ^{14}C	Radies et al. (2005)

73	-	OM12/13	21.21	58.96	Oman	ASC	Aeolian, wetland	Geoproxy	3	OSL	Glennie and Singhvi (2002)
74	-	WDR1	22.19	58.85	Oman	ASC	Aeolian	Geoproxy	1	IRSL	Preusser et al. (2002)
75	-	WDR2	22.31	58.86	Oman	ASC	Aeolian	Geoproxy	11	IRSL	Preusser et al. (2002)
76	31	Wadi Batha	22.35	59.03	Oman	ASC	Aeolian, fluvial	Geoproxy	4	OSL	Kocurek et al. (2020)
77	32	Ruways-C1	22.17	59.72	Oman	ASC	Sabkha	Geoproxy	2	OSL	Richard et al. (2020)
78	33	Daffah-C2	22.28	59.80	Oman	ASC	Sabkha	Geoproxy	2	OSL	Richard et al. (2020)
79	34	Khor al Jaramah C1/C2	22.49	59.76	Oman	ASC	Lagoon	Geoproxy	2	OSL	Richard et al. (2020)
80	-	Al-Haid	22.49	59.08	Oman	ASC	Palaeosol, wetland	Geoproxy	2	^{14}C	Lézine et al. (2010)
81	-	SWY-3	22.05	59.67	Oman	ASC	Mangrove, lagoon	Geoproxy, fossils, pollen	11	^{14}C	Lézine et al. (2002)
82	-	HD-6	22.50	59.81	Oman	ASC	Mangrove	Geoproxy, fossils	1	^{14}C	Lézine et al. (2002)
83	-	SWY-2	22.09	59.69	Oman	ASC	Mangrove	Geoproxy, fossils, pollen	2	^{14}C	Lézine et al. (2002)
84	-	SWY-11	22.10	59.71	Oman	ASC	Mangrove	Geoproxy, fossils, pollen	2	^{14}C	Lézine et al. (2002)
85	35	Suwayh	22.09	59.67	Oman	ASC	Mangrove, lagoon	Geoproxy, fossils, pollen	4	^{14}C	Lézine et al. (2002)
86	36	Quriyat	23.25	58.90	Oman	ASC	Mangrove, lagoon,	Geoproxy, fossils	6	^{14}C	Beuzen-Waller et al. (2019)
87	-	Bar al-Hikman	20.40	58.35	Oman	ASC	Mangrove	Geoproxy, fossils	1	^{14}C	Berger et al. (2013)
88	37	Alashkara	21.88	59.57	Oman	ASC	Mangrove, lagoon	Geoproxy, fossils	8	^{14}C	Berger et al. (2013)
89	38	Ra's al-Hamra	23.62	58.48	Oman	ASC	Mangrove	Geoproxy, fossils	12	^{14}C	Biagi and Nisbet (1992)
90	39	Filim	20.16	58.17	Oman	ASC	Mangrove	Geoproxy, pollen, fossils	8	^{14}C	Lézine et al. (2017)
91	40	Kwar al Jaramah	22.49	59.76	Oman	ASC	Mangrove	Geoproxy, pollen, fossils	7	^{14}C	Lézine et al. (2017)
92	41	B19.1	18.72	53.19	Oman	RAK	Wetland	Geoproxy	5	OSL	Matter et al. (2015)
93	42	B18.2	19.26	53.33	Oman	RAK	Wetland	Geoproxy	4	OSL	Matter et al. (2015)
94	43	Al Quwaiayh	24.36	45.63	Saudi Arabia	WA	Fluvial	Geoproxy	2	OSL	McLaren et al. (2009)
95	44	Wadi ad Dawasir 2	21.96	49.75	Saudi Arabia	WA	Fluvial	Geoproxy	3	OSL, ^{14}C	Matter et al. (2016)
96	45	Wadi ad Dawasir 3	22.05	49.82	Saudi Arabia	WA	Fluvial	Geoproxy	3	OSL, ^{14}C	Matter et al. (2016)
97	46	Wadi ad Dawasir 4	21.89	49.70	Saudi Arabia	WA	Fluvial	Geoproxy	4	OSL, ^{14}C	Matter et al. (2016)
98	47	Wadi ad Dawasir 5	22.11	49.90	Saudi Arabia	WA	Fluvial	Geoproxy	3	OSL, ^{14}C	Matter et al. (2016)
99	48	Wadi ad Dawasir 6	19.20	43.58	Saudi Arabia	WA	Fluvial	Geoproxy	1	OSL, ^{14}C	Matter et al. (2016)
100	49	Mundafan	18.54	45.37	Saudi Arabia	WA	Lake, wetland, aeolian	Geoproxy, fossils	29	OSL, ^{14}C	McClure (1976); Rosenberg et al. (2011)
101	-	Al Jirthamiya	20.60	43.82	Saudi Arabia	WA	Spring	Geoproxy	1	^{14}C	Sanlaville (1992)
102	-	Jabal Umm al Qunman- Wadi Maqab	16.87	42.97	Saudi Arabia	WA	Fluvial, aeolian	Geoproxy	2	^{14}C	Sanlaville (1992)
103	-	Al Sulb Cave	26.42	47.33	Saudi Arabia	WA	Spring	Geoproxy	1	^{14}C	Sanlaville (1992)
104	-	North Jeddah	21.73	39.12	Saudi Arabia	WA	Spring	Geoproxy	1	^{14}C	Sanlaville (1992)
105	-	Wadi Abu Saw	23.05	39.63	Saudi Arabia	WA	Fluvial	Geoproxy	1	^{14}C	Sanlaville (1992)
106	-	Wadi al Birk	18.20	41.55	Saudi Arabia	WA	Spring	Geoproxy	2	^{14}C	Sanlaville (1992)
107	-	Wadi Jizan	17.17	42.83	Saudi Arabia	WA	Fluvial, spring	Geoproxy	9	^{14}C	Zötl and Jado (1984); Sanlaville (1992)
108	-	Wadi al Luhy (Tuwayq Mountains)	24.33	46.67	Saudi Arabia	WA	Fluvial	Geoproxy	1	^{14}C	Al-Sayari and Zotl (1978)
109	-	N. as Sirr	26.10	44.19	Saudi Arabia	WA	Lake	Geoproxy	1	^{14}C	Whitney et al. (1983)
110	-	N. Urayq	25.35	42.40	Saudi Arabia	WA	Lake	Geoproxy	2	^{14}C	Whitney et al. (1983)
111	-	Harrat as Sarat	18.03	43.10	Saudi Arabia	WA	Fluvial	Geoproxy	2	^{14}C	Jado and Zötl (1984)
112	-	Wadi ad Dawasir 7	21.25	42.73	Saudi Arabia	WA	Fluvial	Geoproxy	2	^{14}C	Jado and Zötl (1984)
113	-	Wadi Jizan, Maloki Crater	17.02	42.92	Saudi Arabia	WA	Aeolian	Geoproxy	1	^{14}C	Jado and Zötl (1984)
114	50	Al-Kharrar	22.99	38.84	Saudi Arabia	WA	Coastal	Geoproxy, pollen	3	^{14}C	Bantan et al. (2019)
115	51	Shuaiba	20.76	39.50	Saudi Arabia	WA	Coastal	Geoproxy, pollen	6	^{14}C	Abu-Zied and Bantan (2015)

116	52	Khawr al Balid	17.01	54.14	Oman	SA	Fluvial	Geoproxy	5	^{14}C	Hoorn and Cremaschi (2004)
117	53	Khawr Rawri	17.04	54.43	Oman	SA	Fluvial	Geoproxy	4	^{14}C	Hoorn and Cremaschi (2004)
118	54	Wadi Darbat	17.07	54.45	Oman	SA	Fluvial	Geoproxy	1	^{14}C	Hoorn and Cremaschi (2004)
119	55	Al Hawa	15.87	46.72	Yemen	SA	Lake, wetland	Geoproxy, pollen, fossils	18	^{14}C	Lézine et al. (2010); Lézine et al. (1998); Lézine et al. (2007)
120	56	Ghazwan	14.37	44.36	Yemen	SA	Palaeosol, lake	Geoproxy	6	^{14}C	Wilkinson (2005)
121	-	Sedd Adhra'ah 1	14.53	44.38	Yemen	SA	Palaeosol, lake	Geoproxy	4	^{14}C	Wilkinson (2005)
122	-	Pit 57 nr Dhamar	14.54	44.40	Yemen	SA	Palaeosol	Geoproxy	1	^{14}C	Wilkinson (2005)
123	-	Pit 24 Risabar	14.70	44.35	Yemen	SA	Palaeosol	Geoproxy	1	^{14}C	Wilkinson (2005)
124	-	Zebl 1	14.55	44.53	Yemen	SA	Lake	Geoproxy	3	^{14}C	Wilkinson (2005)
125	-	Pit 22 Qa Jahran	14.63	44.40	Yemen	SA	Lake	Geoproxy	1	^{14}C	Wilkinson (2005)
126	-	Al-Adhla (WP 333)	14.50	44.27	Yemen	SA	Lake	Geoproxy	1	^{14}C	Wilkinson (2005)
127	57	Rada	14.43	44.82	Yemen	SA	Lake	Geoproxy, pollen	3	^{14}C	Lézine et al. (2010)
128	58	Saada	17.00	43.75	Yemen	SA	Lake, wetland	Geoproxy	2	^{14}C	Lézine et al. (2010)
129	59	Shabwa	15.53	46.92	Yemen	SA	Wetland	Geoproxy	1	^{14}C	Lézine et al. (2010)
130	-	Sana	15.35	44.19	Yemen	SA	Palaeosol	Geoproxy	1	^{14}C	Nettleton and Chadwick (1996)
131	-	Wadi Sana	15.84	49.00	Yemen	SA	Palaeosol	Geoproxy	4	^{14}C	McCorriston et al. (2002)
132	60	Wadi Idim	15.81	48.67	Yemen	SA	Spring	Geoproxy	4	^{14}C	McCorriston et al. (2002)
133	61	Arda	16.16	49.30	Yemen	SA	Fluvial	Geoproxy	3	^{14}C	Berger et al. (2012)
134	62	Masila	16.05	49.72	Yemen	SA	Fluvial, palaeosol	Geoproxy	5	^{14}C	Berger et al. (2012)
135	63	Bayt Nahmi	14.42	44.52	Yemen	SA	Wetland	Geoproxy, fossils	6	^{14}C	Davies (2006)
136	64	Zebl 2	14.28	44.58	Yemen	SA	Palaeosol, wetland	Geoproxy, fossils	3	^{14}C	Davies (2006)
137	65	Sedd Adhra'ah 2	14.35	44.63	Yemen	SA	Palaeosol	Geoproxy, fossils	3	^{14}C	Davies (2006)
138	66	Matafah	17.69	53.58	Oman	SA	Fluvial	Geoproxy	3	OSL	Rose et al. (2019)

13 | Appendix E: Statement of authorship

Author contributions to the research papers comprising this thesis

The vast majority of the work presented in this thesis was carried out by the author, Sam Woor (SW). There were also small contributions from the co-authors on each of the papers comprising chapters 4-6. These contributions were as follows:

Paper 1 (Chapter 4)

Project conception was led by SW, through discussions with David Thomas (DT) and Ash Parton (AP). Fieldwork was conducted in Oman in January 2020 by SW, DT and AP. Sample preparation, measurement and data analysis for luminescence dating was undertaken by SW under the supervision of Sallie Burrough (SB) and Julie Durcan (JD). Grain size measurements, statistical analyses and the drawing of all figures was conducted by SW. SW wrote the original draft of the manuscript, which was then edited by DT, JD and SB. All authors were involved in discussing and interpreting results.

Paper 2 (Chapter 5)

Project conception was led by SW, through discussions with DT and AP. All data processing, mapping, morphometric measurements, data analyses and figure drawing was conducted by SW. Results were discussed with DT, AP and Anya Leenman (AL), with all authors contributing to their interpretation. The original draft of the manuscript was written by SW, which was then edited by DT, AL and AP.

Paper 3 (Chapter 6)

Project conception was led by SW, through discussions with DT, AP and Catherine Buckland (CB). SW compiled all records within the database, conducted all data analysis and prepared all figures. Results were then discussed with DT, AP and CB, with all authors contributing to their interpretation. The original draft of the manuscript was written by SW and then edited by DT, AP and CB.

Paper 4 (Appendix 1)

Project conception was led by SW in discussion with JD, SB, DT and AP. All sample preparation and measurement in the luminescence laboratory was conducted by SW under the supervision of JD and SB. XRD analysis was conducted commercially in the Department of Earth Sciences, University of Oxford. SW was responsible for all data analysis, figure drawing and writing the original draft of the manuscript. Results were discussed and interpreted by all authors. The manuscript was edited by JD, SB and DT.

Signature:  **Date: 16/06/23**

Samuel Woor

Signature: 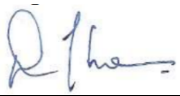 **Date: 16/06/23**

Professor David Thomas

Signature:  **Date: 16/06/23**

Dr Ash Parton

Signature: 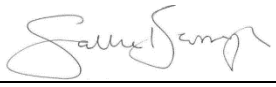 **Date: 16/06/23**

Dr Sallie Burrough

Signature: 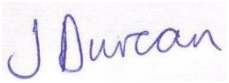 **Date: 16/06/23**

Dr Julie Durcan

Signature:  **Date: 16/06/23**

Dr Anya Leenman

Signature:  **Date: 16/06/23**

Dr Catherine Buckland